BIOPOLYMER THIN FILMS AND COATINGS

EDITED BY: Stefan Spirk, Tiina Nypelö and Eero Kontturi
PUBLISHED IN: Frontiers in Chemistry

frontiers Research Topics

frontiers

ISSN 1664-8714
ISBN 978-2-88963-333-3
DOI 10.3389/978-2-88963-333-3

About Frontiers

Frontiers is more than just an open-access publisher of scholarly articles: it is a pioneering approach to the world of academia, radically improving the way scholarly research is managed. The grand vision of Frontiers is a world where all people have an equal opportunity to seek, share and generate knowledge. Frontiers provides immediate and permanent online open access to all its publications, but this alone is not enough to realize our grand goals.

Frontiers Journal Series

The Frontiers Journal Series is a multi-tier and interdisciplinary set of open-access, online journals, promising a paradigm shift from the current review, selection and dissemination processes in academic publishing. All Frontiers journals are driven by researchers for researchers; therefore, they constitute a service to the scholarly community. At the same time, the Frontiers Journal Series operates on a revolutionary invention, the tiered publishing system, initially addressing specific communities of scholars, and gradually climbing up to broader public understanding, thus serving the interests of the lay society, too.

Dedication to Quality

Each Frontiers article is a landmark of the highest quality, thanks to genuinely collaborative interactions between authors and review editors, who include some of the world's best academicians. Research must be certified by peers before entering a stream of knowledge that may eventually reach the public - and shape society; therefore, Frontiers only applies the most rigorous and unbiased reviews.
Frontiers revolutionizes research publishing by freely delivering the most outstanding research, evaluated with no bias from both the academic and social point of view. By applying the most advanced information technologies, Frontiers is catapulting scholarly publishing into a new generation.

What are Frontiers Research Topics?

Frontiers Research Topics are very popular trademarks of the Frontiers Journals Series: they are collections of at least ten articles, all centered on a particular subject. With their unique mix of varied contributions from Original Research to Review Articles, Frontiers Research Topics unify the most influential researchers, the latest key findings and historical advances in a hot research area! Find out more on how to host your own Frontiers Research Topic or contribute to one as an author by contacting the Frontiers Editorial Office: researchtopics@frontiersin.org

BIOPOLYMER THIN FILMS AND COATINGS

Topic Editors:
Stefan Spirk, Graz University of Technology, Austria
Tiina Nypelö, Chalmers University of Technology, Sweden
Eero Kontturi, Aalto University, Finland

In science as well as in industry, the impetus of research on bio-based polymers has recently expanded into new terrains. The need to replace fossil-based materials with sustainable and renewable sources is one of the main drivers for the emergence and the development of new and environmentally friendly materials. While some materials applications of bio-based polymers are already very well established, for instance, in paper and textiles, others have just emerged with thin films and coatings being a recent and particular area of interest. Thin films in general are an enormous field of research both fundamentally and from an applied perspective, with uses ranging from corrosion resistance to photovoltaics and sensors. Since bio-based materials are a relatively novel source material for thin films, the research in this area is at a fresh, exciting stage at the moment.

Citation: Spirk, S., Nypelö, T., Kontturi, E., eds. (2020). Biopolymer Thin Films and Coatings. Lausanne: Frontiers Media SA. doi: 10.3389/978-2-88963-333-3

Table of Contents

frontiers in Chemistry

EDITORIAL
published: 25 October 2019
doi: 10.3389/fchem.2019.00736

Editorial: Biopolymer Thin Films and Coatings

Stefan Spirk [1], Tiina Nypelö [2,3] and Eero Kontturi [4]*

[1] Institute of Paper, Pulp and Fiber Technology, Graz University of Technology, Graz, Austria, [2] Department of Chemistry and Chemical Engineering, Chalmers University of Technology, Gothenburg, Sweden, [3] Wallenberg Wood Science Center, Gothenburg, Sweden, [4] Department of Bioproducts and Biosystems, Aalto University, Espoo, Finland

Keywords: thin films, biopolymer, cellulose, chitosan, lignin, coatings, proteins

Editorial on the Research Topic

Biopolymer Thin Films and Coatings

The development of thin film technology has played a decisive role in the manufacturing of high-tech devices and products such as computers, mobile phones, solar cells, sensors, and displays. With polymer materials, synthetic polymers are still mostly applied while the use of bio-based materials for thin coatings and films is still at an early stage. Of these, particularly thin films of natural polysaccharides have been at the forefront of the research scene for the past 10–15 years. Although the main problems in film preparation, such as sparing solubility, have been largely overcome, many issues affecting the film performance are still not fully understood. One of the pressing issues is the influence of water on the film structure and behavior, given the special relationship that many biopolymers share with water. Other open questions include the stability and the general structural order of the films. In this special issue, we have assembled the frontiers of biopolymer ultrathin films: topical studies on water interactions, protein adsorption, and film structure among many others. The materials choices in the thin films include cellulose, cellulose derivatives, lignin, alginate, and chitosan.

The special issue contains two review and 10 original research articles. The reviews yield insight into general materials perspectives (Kontturi and Spirk) as well as to the current state of ultrathin cellulose films to act as a biointerface (Raghuwanshi and Garnier). These are important emerging areas particularly with polysaccharide thin films where the research has generally been focused on their use as model systems (model surfaces). The 10 research articles, on the other hand, focus on different, mainly fundamental and materials-related aspects, such as composition, morphology and accessibility, crosslinking and interaction with biomolecules. The contribution of Kargl et al. presents affinity of proteins on cellulose, and other surfaces, and contributes to the quest for identifying the reasons behind selectivity of protein attachment on surfaces. Quantification of protein adsorption on surfaces in aqueous media is limited by the physics of the analytical techniques but also of data analysis. This contribution among others, utilizes a combination of analytical methods to cover the limitations of the individual techniques and models.

Czibula et al. investigate mixtures of two biopolymers in a film. They present film formation from cellulose derivate blends, leading to control of hydrophobic and hydrophilic domains, combined with surface roughness and structure periodicity. There is something curious about proteins adsorbing on textured surfaces that lead often to an unexpected increase in the adsorbed amount at certain compositions, as seen in previous accounts. The contribution by Czibula contributed to this topic by adding friction force morphology as a tool to screen interactions besides conventional tools such as QCM-D and SPR. Nau et al., on the other hand, focused on film formation by cross-linking hydroxypropyl cellulose that had been modified with fatty acid esters. Cross-linking and simultaneous binding on the surface was realized with a photo-induced radical cross-linker and the film properties were carefully and comprehensively monitored.

Edited and reviewed by:
Pellegrino Musto, Italian National Research Council (CNR), Italy

****Correspondence:***
Stefan Spirk
stefan.spirk@tugraz.at

Specialty section:
This article was submitted to Polymer Chemistry, a section of the journal Frontiers in Chemistry

Received: *03 October 2019*
Accepted: *15 October 2019*
Published: *25 October 2019*

Citation:
Spirk S, Nypelö T and Kontturi E (2019) Editorial: Biopolymer Thin Films and Coatings. Front. Chem. 7:736. doi: 10.3389/fchem.2019.00736

Besides macromolecular interaction, adsorption of small molecules (other than water) has been probed relatively little with cellulose thin films. Henögl et al. looked at the deposition of small molecules on cellulose surfaces with regard to their interaction capacity. They used as model compounds n-decane and deuterated methanol and found that although both molecules adsorb, the interaction of methanol with the cellulose surfaces is stronger, and supported the observation with thermodynamic data. On the other hand, the work by Sampl et al. looked more on the order and density of such cellulose thin films. The paper reveals that there are different areas in the films that feature lower density, i.e., at the air-film interface and at the film-substrate interface. Maver et al. also look into the structural feature of films, specifically hydrophilic multi-layered thin films. They further apply them as a model drug-carrier and time-dependent release system aiming for new functional and active 3D materials to be used in regenerative medicine.

Hua et al. had a more pragmatic approach to coat hydrophobic films on down-to-earth substrates like glass or Kraft pulp sheets, resulting in increased surface hydrophobicity of these materials. The lignin coating was performed using microparticles whose formation was made feasible by esterification of lignin hydroxyl groups. Likewise, Chemin et al. had their eye on utilizing thin films for genuine applications. In their work, hybrid films of cellulose nanocrystals and Gibbsite nanoplatelet films were constructed by layer-by-layer technique onto substrates in packaging applications, such as cardboard. The resulting materials exhibited improved oxygen barrier properties. Electrostatic interaction was also utilized in a different fashion by Zou et al. who used chitosan to attach as an ultrathin biofilm on negatively charged colloidal lignin nanoparticles. Such nanoparticles were especially suited for stabilizing oil-in-water Pickering emulsions for, e.g., food applications. Work of Zieglowski et al. also utilizes lignin. They provide insight in reactivity and isocyanate structure linked to Kraft lignin on polyurethane formation. Polyurethanes are an important material for coatings and use of lignin enables incorporation of the biomacromolecule into a highervalue polymer material. The rational choice of the isocyanate for pre-functionalization of lignin assists to prepare materials with better mechanical performance.

The contributions in this special issue of Biopolymer Thin Films and Coatings highlight that mastering the fundamentals of film formation and characterization already enables to reach toward utilization. The applications covered in this special issue, supported by the state-of-the-art analysis, provide a dissection of the status of the biopolymer thin film and coating field. We hope that the issue will inspires the readers to further contribute to this exciting field of fundamental and applied endeavors.

AUTHOR CONTRIBUTIONS

All authors listed have made a substantial, direct and intellectual contribution to the work, and approved it for publication.

ACKNOWLEDGMENTS

SS acknowledges the Christian Doppler Laboratory for Fiber Swelling and Paper Performance for financial support of the Austrian Federal Ministry of Economy, Family and Youth, and the National Foundation for Research, Technology and Development. TN acknowledges financial support of Wallenberg Wood Science Center (WWSC) and Area of Advance Materials at Chalmers University of Technology. EK acknowledges Academy of Finland (grant no. 303452) for funding.

Conflict of Interest: The authors declare that the research was conducted in the absence of any commercial or financial relationships that could be construed as a potential conflict of interest.

frontiers in Chemistry

ORIGINAL RESEARCH
published: 09 April 2019
doi: 10.3389/fchem.2019.00217

Polysaccharide Thin Solid Films for Analgesic Drug Delivery and Growth of Human Skin Cells

Tina Maver[1,2]*, *Tamilselvan Mohan*[1]*, *Lidija Gradišnik*[3], *Matjaž Finšgar*[4], *Karin Stana Kleinschek*[1,5] *and Uroš Maver*[2,3]

[1] *Laboratory for Characterization and Processing of Polymers, Faculty of Mechanical Engineering, University of Maribor, Maribor, Slovenia,* [2] *Department of Pharmacology, Faculty of Medicine, University of Maribor, Maribor, Slovenia,* [3] *Faculty of Medicine, Institute of Biomedical Sciences, University of Maribor, Maribor, Slovenia,* [4] *Faculty of Chemistry and Chemical Engineering, University of Maribor, Maribor, Slovenia,* [5] *Institute for Chemistry and Technology of Materials, Graz University of Technology, Graz, Austria*

Chronic wounds not only lower the quality of patient's life significantly, but also present a huge financial burden for the healthcare systems around the world. Treatment of larger wounds often requires the use of more complex materials, which can ensure a successful renewal or replacement of damaged or destroyed tissues. Despite a range of advanced wound dressings that can facilitate wound healing, there are still no clinically used dressings for effective local pain management. Herein, alginate (ALG) and carboxymethyl cellulose (CMC), two of the most commonly used materials in the field of chronic wound care, and combination of ALG-CMC were used to create a model wound dressing system in the form of multi-layered thin solid films using the spin-assisted layer-by-layer (LBL) coating technique. The latter multi-layer system was used to incorporate and study the release kinetics of analgesic drugs such as diclofenac and lidocaine at physiological conditions. The wettability, morphology, physicochemical and surface properties of the coated films were evaluated using different surface sensitive analytical tools. The influence of *in situ* incorporated drug molecules on the surface properties (e.g., roughness) and on the proliferation of human skin cells (keratinocytes and skin fibroblasts) was further evaluated. The results obtained from this preliminary study should be considered as the basis for the development "real" wound dressing materials and for 3D bio-printing applications.

Keywords: thin (blend) films, alginate, carboxymethyl cellulose, diclofenac, lidocaine, keratinocytes, skin fibroblasts

OPEN ACCESS

Edited by:
Stefan Spirk,
Graz University of Technology, Austria

Reviewed by:
Sergiu Coseri,
Institute of Macromolecular Chemistry "Petru Poni", Romania
Mirjana Kostic,
University of Belgrade, Serbia

***Correspondence:**
Tina Maver
tina.maver@um.si
Tamilselvan Mohan
tamilselvan.mohan@um.si

Specialty section:
This article was submitted to Polymer Chemistry, a section of the journal Frontiers in Chemistry

Received: *14 February 2019*
Accepted: *19 March 2019*
Published: *09 April 2019*

Citation:
Maver T, Mohan T, Gradišnik L, Finšgar M, Stana Kleinschek K and Maver U (2019) Polysaccharide Thin Solid Films for Analgesic Drug Delivery and Growth of Human Skin Cells. Front. Chem. 7:217. doi: 10.3389/fchem.2019.00217

INTRODUCTION

Thin films from polymeric materials present an emerging platform for various types of applications, including drug delivery (Maver et al., 2015b; Karki et al., 2016; Stana et al., 2017), sensors, microarray preparations (Mohan et al., 2012), etc. They also hold a huge scientific interest for several solid-liquid interface studies, especially for the adsorptive interaction of nanoparticles (Taajamaa et al., 2013), polyelectrolytes (Mohan et al., 2015, 2017), biomolecules (Kargl et al., 2015), etc. While significant efforts have been made to formulate drug delivery platforms from organo-soluble synthetic polymers (Vendra et al., 2011; Ponnusamy et al., 2012), the use of natural polymers

(e.g., polysaccharides) for such applications is limited and have recently gained a paramount of interest (Zelikin, 2010; Park K. et al., 2018; Park S. et al., 2018). Due to their high compatibility, bio-inertness, diverse physicochemical properties and ease of handling during manufacturing, polysaccharide thin films are excellent candidates for skin-related applications, where a controlled and targeted delivery of pain-relieving analgesic drugs are prerequisite (Miao et al., 2018). Skin is the largest organ of the integumentary system and it plays a vital protective role of the human body against pathogens. Thus, any major injury (wound) that results in the loss of its integrity, can lead to significant patient disability or even death (Singer and Clark, 1999). Such injury/wounds are often further associated with severe pain that represents a stress for the patient and is therefore a potential factor in delaying the physiological process of wound healing (McGuire et al., 2006; Guo and Dipietro, 2010). Optimizing the analgesic treatment of injured patients is thus of major importance. In order to avoid several side effects that analgesic drugs have, the local application could be a good alternative (Palao i Domenech et al., 2008; Marques et al., 2014). However, there are difficulties in quantitively controlling and prolonging the release of analgesic drug molecules such as lidocaine (LID) and diclofenac (DCF), when they are employed without any supporting matrices. Several attempts have been made to incorporate LID and DCF into nanoscale multi-layered thin films for controlling their loading capacity and release profiles (Loo et al., 2010; Jeganathan et al., 2016). LID is among the most widely used local anesthetics due to its rapid action (the effect is noticed immediately), making it suitable to alleviate the pain, caused by dressing change (Zhao et al., 2018), while DCF is a long lasting non-steroidal anti-inflammatory drug, which can provide a longer-lasting pain reduction, caused by the injury itself (Altman et al., 2015).

Since LID and DCF are both water soluble and hydrophilic, their incorporation into thin films derived from hydrophobic polymers, are still challenging. Therefore, the polysaccharides [e.g., alginate (ALG) and carboxymethyl cellulose (CMC)], which are both inherently hydrophilic and water soluble, seem suitable candidates to incorporate large amounts of both mentioned drugs in a uniform fashion. ALG is the most commonly used mucoadhesive polymer in wound healing applications, owing to its excellent water uptake capacity, non-toxicity and abundance in nature (Pawar and Edgar, 2012). It is derived from brown algae and bacteria and is classified as a linear anionic polysaccharide, composed of repeating units of β-1,4-linked D-mannuronic acid (M) and L-guluronic acid (G) in varying ratios. Depending on the type of ALG, its composition leads to the formation of tight ionically cross-linked network structures; contributing to a prolonged drug release (Paques et al., 2014). CMC, a derivative of the most abundant natural polymer cellulose, is also anionic, weakly charged and water soluble. Both were already proven to be efficient film-forming polymers and have found use in erodible and other drug formulations (Palmer et al., 2011).

Until now, the layer-by-layer (LbL) self-assembly technique has been largely used to create nanoscale multi-layered systems, which are of interest for targeted drug delivery applications (Stana et al., 2017; Park K. et al., 2018), where the simplicity and versatility of the preparation procedure lower the overall drug delivery system costs. In general, the LbL technique exploits the alternating deposition of oppositely charged substances (e.g., polyelectrolytes, polypeptides, etc.), which enables surface and bulk material decoration with a wide range of functional groups, in the final multi-layer structure (Liu et al., 2019; Zhang et al., 2019). However, the application of this technique to create multi-layered nanofilms from a single polymer or mixture of polymers with the same ionic/functional groups, and the use of the latter system in the release of therapeutic drug molecules is still only scarcely reported (Finšgar et al., 2016; Stana et al., 2017). Amongst several other fabrication techniques, spin coating is the commonly used technique for the design of multi-layered structures. Its main advantages include a high reproducibility, reliability, rapid film formation, and simultaneous solvent evaporation. On top of the mentioned, it allows to control the thickness, morphology and surface properties of the final material (Stana et al., 2017). The challenges in the fabrication of multi-layered nanofilms from water soluble and hydrophilic polymers (with similar overall properties) such as ALG, CMC, and the ALG-CMC combination by spin-assisted LbL technique was not yet explored in a systematic way. Furthermore, the potential application of these self-assembled polysaccharide multi-layers for incorporation and controlled release of LID and DCF were also not yet investigated in detail.

The motivations for this work, therefore, was to create a nanoscale multi-layered thin films, as a model drug-carrier system, in a systematic way from hydrophilic ALG and CMC. In addition, this work also aims to gain a deeper understanding of the surface and physiochemical properties of the developed multilayered system. For this purpose, aqueous solutions of ALG, CMC, and the mixture of ALG-CMC with incorporated DCF or LID drugs were used to fabricate multi-layered thin films on different solid substrates by the spin-assisted LBL coating technique. The wettability, thickness, morphology, and roughness of the multi-layered films were characterized using several surface sensitive methods. The time-dependent release of drugs from the multi-layer at body temperature and at physiological pH were also determined. The obtained release profiles were further fitted with various kinetic models to discern the release mechanism of the drugs. Finally, the influence of the multi-layer films with *in situ* included drugs on the proliferation of human skin cells (keratinocytes and skin fibroblasts) was evaluated. The results obtained from this preliminary study should be considered as the basis for the development of new functional and active 3D materials to be used in regenerative medicine.

EXPERIMENTAL SECTION

Materials and Methods

All chemicals used for the preparation of multi-layered thin films (ALG: viscosity: 0.015–0.025 Pa s, CMC: Viscosity: 2.5–6 Pa s, DCF and LID) were purchased from Sigma-Aldrich, Germany. The tetrazolium salt MTT [3(4, 5 dimethylthiazolyl-2)-2, 5-diphenyltetrazolium bromide] for the biocompatibility testing was purchased from Sigma-Aldrich, Germany. Advanced

Dulbecco's Modified Eagle's Medium (ADMEM) and Fetal Bovine Serum (FBS) were purchased from ThermoFisher, Germany. Keratinocytes, an aneuploid immortal keratinocyte cell line (HACAT) from adult human skin was kindly provided by Prof. Dr. Elsa Fabbretti (Centre for Biomedical Sciences and Engineering, University of Nova Gorica, Slovenia). Human derived skin fibroblasts (ATCC CCL-119, Detroit 551, LGC Standard) were purchased from ATCC, UK. For all experiments, ultra-pure water (18.2 MΩ cm at 25°C) was used, prepared from a ELGA Purelab water purification system (Veolia Water Technologies, UK).

Sample Preparation

Three types of solutions were prepared for spin-coated. **Type I** (ALG-DCF or ALG-LID, 0.5/0.1%, w/v): 500 mg ALG was added to DCF or LID (0.1%, w/v, dissolved in water), stirred overnight with a mechanical stirrer. ALG (0.5%, w/v) was prepared in the same way without DCF or LID. **Type II**: (CMC-DCF or CMC-LID), CMC with and without DCF or LID with the same concentrations as mentioned in Type I were prepared. **Type III**. ALG-CMC-DCF or ALG-CMC-LID: ALG and CMC with DCF or LID were mixed together in a ratio of 1:1. The final concentration of the polymers and drugs in the final solution are 0.25 and 1 mg/mL, respectively. All solutions were prepared freshly before use.

Multi-Layered Thin Film Preparation and Drug Incorporation

Silicon wafers were used as base-substrates for multi-layered thin film preparation. Prior to spin-coating, the silicon wafers were cut into pieces of 1 × 1 cm^2, soaked into a "piranha solution" [H_2O_2 (30 wt. %)/H_2SO_4 (conc.): 1:7 (v/v)], rinsed with ultra-pure water and blow dried in a stream of dry nitrogen of high purity (99.999%). For creating multi-layers, the above-mentioned three types of polymer solutions with and without drugs were used. For spin-coated, 50 μL of ALG or CMC or ALG-CMC mixture with DCF or LID was deposited on the static substrate and spin-coated with a spinning speed of 4,000 revolutions per minute (rpm) and an acceleration of 2,500 rpm s^{-1} for 60 s. This procedure was repeated three times for each sample. In this way, three layers of the same material were created. These spin-coated final three layers from ALG, CMC, and ALG-CMC are designated as ALG 3, CMC 3, and ALG-CMC 3, respectively, without incorporated drugs. The drug incorporated and spin-coated three layers are designated as CMC-DCF 3 (or LID 3), ALG-DCF 3 (or LID 3), or ALG-CMC-DCF 3 (or LID 3).

Atomic Force Microscope (AFM)

AFM was used for the topographical and surface roughness analysis of spin-coated multi-layered thin films. Prior to analysis using the Keysight 7500 AFM (Keysight Technologies, USA), the samples were attached onto round shaped metal disc sample holders. Topography images were acquired using the acoustic AC AFM mode. Silicon AFM tips (Nanosensors, Switzerland) with a nominal spring constant 12–110 N/m and a nominal resonance frequency of 210–490 kHz, were used for imaging purposes for all samples. Images of 1 × 1 μm^2 were recorded, with a resolution of at least 524 × 524 pixels. All images were processed, and the corresponding roughness was calculated using freeware Gwyddion software package. For thickness determination, a straight line was created on the spin-coated sample by scratching with a sharp scalpel. Subsequently, a profile was created along the scratched straight line. This profile was then used to estimate the thickness of each spin-coated layer.

Attenuated Total Reflection-Fourier Transform Infrared (ATR-FTIR) Analysis

The ATR-FTIR spectra of spin coated samples were measured using a Perkin Elmer FTIR System Spectrum GX Series-73565 at a wavenumber range of 4,000–650 cm^{-1}. A total of 32 scans were performed for all measurements with a resolution of 4 cm^{-1}. QCM quartz crystals (QSX301, LOT-Oriel, Germany) coated with a gold layer were used as substrates for ATR-FTIR measurements. The spin coating of polymer solutions with and without drugs were performed in the same way as with silicon wafers.

Contact Angle Measurements

The wettability of spin-coated multi-layers was determined using a OCA15+ goniometer system (Dataphysics, Germany) with the sessile drop method. Static contact angle (SCA) measurements were carried out using ultra-pure water at ambient temperature. All measurements were carried out on at least two independent surfaces with a drop volume of 2 μL. Each SCA value was the average of at least five drops of liquid per surface.

In vitro Release Studies

The release of DCF and LID from the multi-layered thin films was studied using an Automated Transdermal Diffusion Cells Sampling System (Logan System 912-6, Somerset, USA). For this purpose, each spin-coated wafer (1 × 1 cm^2) was transferred to a 15 mL Franz diffusion Cell, filled with phosphate buffered saline (PBS, Sigma-Aldrich, Germany) with pH of 7.4. Its temperature was maintained at 37°C all the time. Samples were collected over a period of 24 h at different time intervals. The absorbances were determined using a UV-Vis spectrophotometer (Cary 60 UV/VIS, Agilent, Germany), and the released amounts calculated by quantification of the absorption bands at 276 nm (DCF) and 204 nm (LID), using the Beer-Lambert law. The withdrawn sample volumes were replaced by fresh PBS. During the release profile calculations, this dilution was accounted for. The release measurements of at least three parallels of each sample were conducted and the results are reported as average value with ± standard error.

To evaluate the release profiles further, the results from the *in vitro* drug release test were fitted using three known models (first-order, Higuchi-model, and Korsmeyer-Peppas model). Using these models (Costa and Sousa Lobo, 2001), the release mechanisms of the respective drugs from the multi-layers were analyzed.

First-order kinetics (1) is used to describe the release of the drug where the release rate is concentration depended.

$$\log Q = \log Q_0 - K_t/2.303 \quad (1)$$

where Q is the amount of released drug in time "*t*," Q_0 is the initial concentration of the drug and *K* is the first-order rate constant.

Higuchi-model (2) is used to express the drug release from an insoluble matrix as a square root of time dependent process based on the Fick's diffusion:

$$Q = Kt^{1/2} \quad (2)$$

where *Q* is the amount of drug released at time "t" and K is the Higuchi constant.

The Korsmeyer-Peppas model (3) describes the release of drugs from polymeric systems, which has been successfully applied to describe the release from different modified release dosage forms:

$$Q_t/Q_\infty = Kt^n \quad (3)$$

where Q_t is the amount of drug released in time "t," Q_∞ is the amount of drug released after infinite time, K is the constant, and n is the diffusional exponent. If the n value is equal 0.5, then the release mechanism is Fickian diffusion, if $0.45 < n < 0.89$, then it is called non-Fickian or anomalous diffusion. In the case of "*n*" is between 0.89 and 1, and above 1, the drug release is the combination of both diffusion and erosion-controlled processes.

Biocompatibility Testing

In order to test the influence of added DCF and LID on cell viability, the latter was evaluated via the reduction reaction of the tetrazolium salt MTT [3(4,5 dimethylthiazolyl-2)-2,5-diphenyltetrazolium bromide], purchased from Sigma Aldrich, Germany. This is a commonly used and reliable method to evaluate cell proliferation (Finšgar et al., 2016; Maver et al., 2018). It is based on the reduction of the yellow MTT by metabolically active cells (e.g., in part by dehydrogenase enzymes), which results in the formation of nicotinamide adenine dinucleotide and/or nicotinamide adenine dinucleotide phosphate (Maver et al., 2017). During this reaction, a purple formazan is formed intracellularly, which can be solubilized and quantified by spectrophotometric means. Thin films on silicon wafers (1×1 cm^2) were exposed to the UV light for 30 min (i.e., sterilization). Further, the samples were soaked into 1.5 mL of Advanced Dulbecco's Modified Eagle's Medium (ADMEM; ThermoFisher, Germany), supplemented with 5 wt.% Fetal Bovine Serum (FBS; ThermoFisher, Germany), and incubated for 24 h at 37°C in an atmosphere containing 5 wt.% CO_2. The HaCaT and Skin Fibroblast cells (10,000 cells/well) were seeded into a 96-well microtiter plate with a final volume of 100 μL of ADMEM medium supplemented with 5 wt.% FBS. The material samples (supernatants of the starting samples) were added to the cells after 24 h of incubation at 37°C in an atmosphere containing 5 wt.% CO_2 in four parallels. As control, ADMEM medium supplemented with 5 wt.% FBS was added to the cells. After 24 h of treatment, cell viability was determined using the standard reduction of the tetrazolium salt MTT (Stergar et al., 2017; Maver et al., 2018b).

Statistical Analysis

All numerical values are given as average values ± standard deviation. Statistical analysis was performed using SPSS Statistics 25 (IBM Corp. Armonk, NY, USA). By using the Shapiro–Wilk test it was determined that all experimental data was normally distributed, allowing the use of one-way ANOVA. $P < 0.05$ were considered statistically significant (these are marked with an asterisk * in respective graphs).

RESULTS AND DISCUSSION

Surface Morphology, Layers Thickness, and Wettability

Surface Morphology

The surface morphology and roughness of the spin-coated multi-layer films based on ALG, CMC, and the ALG-CMC mixture were characterized using atomic force microscopy (AFM). For clarity reasons, only the results obtained from the final (top) layers are shown in this section, since the same system is used for the release of DCF and LID drugs (section *In vitro* Release Studies). While smooth morphologies with a low surface roughness value (below 1 nm) are observed for both drug-free ALG 3 and CMC 3 coated films, the ALG-CMC mixture prepared at 1:1 ratio (top right image in **Figure 1**) did show some different surface features. Interestingly, the surface roughness of both ALG and CMC 3 samples is lower when compared to its layer thickness (see **Figure 2**). This is most likely due to tight packing and more self-organization of polymer molecules within the film structure. Surfaces with a phase separated morphology are detected for the two-component system that are composed of same charges i.e., ALG-CMC 3. Such phase separation is already noticed for the first ALG-CMC layer (**Figure S1**).

The reports on the phase separation of polymer blends from (organo-soluble) hydrophobic polymers upon spin-coating are manifold (Taajamaa et al., 2011; Strasser et al., 2016). Whereas, no studies on the formation of blend surfaces from spin-coated polysaccharides, which are hydrophilic and water-soluble, can be found to the best of our knowledge. Therefore, maximum efforts are made to explain the observed lateral phase separation in the ALG-CMC 3 multi-layered system and not to overinterpret the results at the same time. At low solute (polymer) concentration, the polymer-polymer blend in solution stays in one phase only (Doublier et al., 2000; Keating, 2012; van de Velde et al., 2015). Upon spin-coating, the increase of solute concentration will push the system into two phases with each phase enhanced in its respective component. The formation of two phases (i.e., phase separation) is often a complex phenomenon, leading to the formation of non-equilibrium morphologies, due to the rapid removal of solvent during the spin-coating process. Usually, this leads to different structures/morphology on the nano- to micro-meter scale (Walheim et al., 1997). This nano- and micro-phase separation can be classified into associate and segregate, which in turn dependent on the affinity between polymers and solvent. The associate phase separation arises when both polymers are oppositely charged, and both polymers are intensified in one of the separating phases while leaving the other phases mostly with

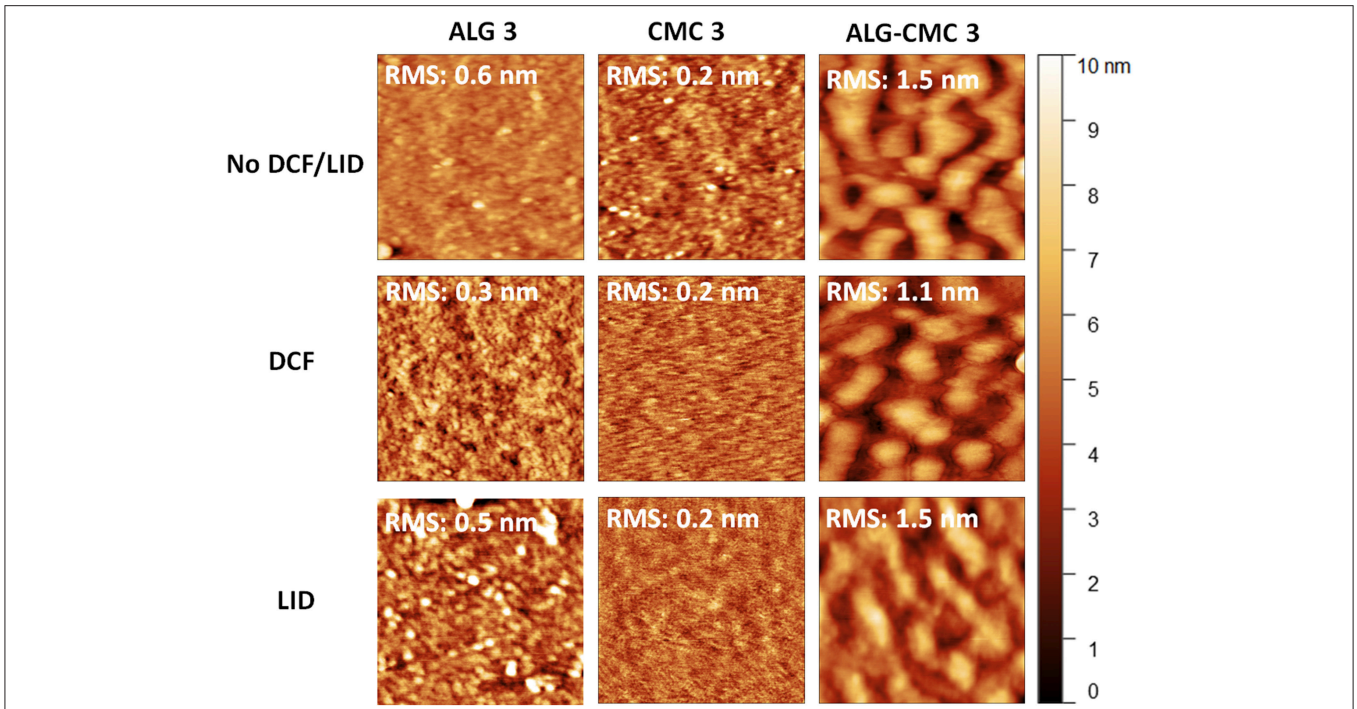

FIGURE 1 | AFM height images (size: 1 × 1 μm^2) of polysaccharide nanofilms, without drugs **(top)**, with DCF **(middle)**, and with LID **(bottom)**.

solvent. In the case of segregate phase separation, two polymers with same charges are separated into two different phases (Fang et al., 2006). The segregate phase separation is well-known for water soluble polymers (e.g., proteins- polysaccharides) for several years (Doublier et al., 2000), but not reported for spin-coated blend films. Keeping this mind, we believe that the lateral phase separation that occurred in the case of ALG-CMC blend, which stays in one phase in water, is of the segregate type, which can be explained by the transient bilayer theory (Heriot and Jones, 2005; Taajamaa et al., 2011).

According to the transient bilayer theory, the formation of the lateral phase separated structures/morphologies during spin-coating, occurs because of de-wetting and interfacial instabilities between the two polymers (ALG and CMC in this study). The instability at the interface is presumably caused by the solvent-concentration gradient within the film. Usually, the evaporation of the solvent is faster at the film surface than in the bulk phase, leading to a lower solvent concentration at the surface than at the polymer-substrate interface. Thus, the instability, caused by the interfacial tension at a polymer-polymer interface is a function of solvent concentration. Concretely this means that if one of the polymers out of the two polymer blend exhibits a strong interaction with the substrate, the phase separation is initiated in a surface-oriented fashion, resulting in a transient bilayer (Geoghegan et al., 1994; Walheim et al., 1997). With the evaporation of more solvent from the film, the upper layer of the film gets unstable with the formation of holes. The latter is then filled with the lower (liquid phase) layer as it is shown for ALG-CMC coated (first) layer (**Figure S1**) (Taajamaa et al., 2011). Interestingly, the phase separation is retained even after the third layer (**Figure 1**, top row and **Figure S2**). Using the phase image (**Figure S2**), the existence of two phases, with a thicker region surrounded by a thinner one, from the two-component system can be easily seen. However, we are aware of the fact that it is difficult to confirm the thicker or major phase is either ALG or CMC; which needs further investigation. From the above discussion, it is proposed that the lateral phase separation occurs upon spin-coating for the hydrophilic polysaccharides that carry similarly charged chains. The detailed understanding of these phenomenon at different ALG-CMC ratios (in water) and humidity' s is currently in progress and is out of the scope of this work. The addition of drugs (LID and DCF) leads to a change in surface morphology for both ALG 3 and CMC 3 coated layers (but not for the ALG-CMC 3 mixture). Especially, particle-like features are visible for LID incorporated ALG 3 sample, whereas a featureless and even more smooth morphology is noticed for both DCF and LID incorporated CMC 3 sample. This can be due, on one hand, an enhanced interaction between LID and functional groups in the multilayer system (as confirmed by IR) and on the other hand, potentially significant inter-diffusion of small, hydrophilic LID molecules within the entire film architecture during the film formation, which occurs during the spin-coating process. In the case of drug incorporated ALG-CMC 3 blend, the phase-separation is still visible with only minimal changes in the morphology. This could be due to the enrichment of drugs in both phases, as confirmed by ATR-FTIR and *in vitro* release studies, where the peaks correspond to DCF and LID and a successful release of both drugs is observed (see below).

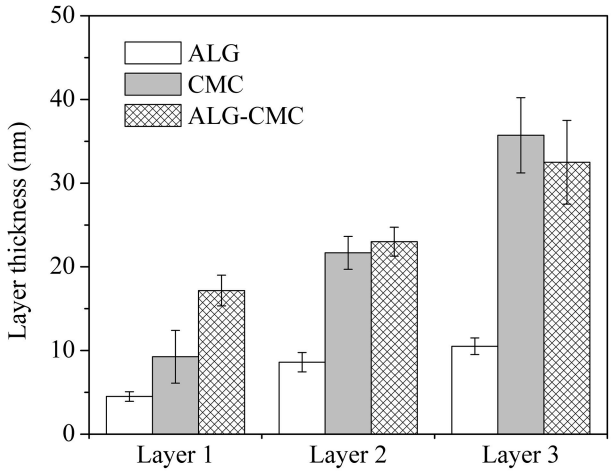

FIGURE 2 | Layer thickness of spin-coated films determined using AFM.

Layer Thickness

The thicknesses of each spin-coated layer (for respective samples) are shown in **Figure 2**. Expectedly, the layer thickness increased with the number of layers deposited for all spin-coated samples. However, there is a difference among the spin-coated materials. For ALG based samples, a layer thickness of only ∼10 nm is measured even after the spin-coated of the third layer. Whereas, a value close to 10 nm is already obtained for the first layer in CMC based samples. With the second and the third layers, the thickness value for this sample is increased from ∼22 to ∼35 nm, respectively. This can be (at least partially) explained by a higher molecular weight (700 kDa) and viscosity (2.5–6 Pa s) of the CMC solution, leading to deposition of higher polymer masses on the surface upon spin-coating. As can be seen in **Figure 2**, the thickness of the first layer of ALG-CMC blend is considerably higher when compared to the first layer of single component ALG and CMC (ALG-CMC: 17 nm > CMC: 9 nm > ALG: 5 nm). These results demonstrate that a multi-layer can be fabricated from a single or mixture of polysaccharides with the same functional groups (i.e., –COOH). In addition, it has to be pointed out that the layer thickness of drug-incorporated spin-coated films (of ALG, CMC or ALG-CMC blend) did not increase considerably compared to films prepared without drugs (data not shown). This could be due to lower concentration (see **Figure 5**) and homogenous incorporation of the drugs into the spin-coated layer. This gained knowledge, in future, can exclude the use of oppositely charged components, such as carboxymethyl cellulose—chitosan (Mohan et al., 2015), hyaluronic acid- chitosan (Pérez-Álvarez et al., 2019), alginate-chitosan (Stana et al., 2017; Criado-Gonzalez et al., 2019), etc., to create multi-layered system.

Wettability

The contact angle values directly reflect surface wettability and are sensitive to chemical functionalities of the outermost layer (Stana et al., 2017). The surface wettability of spin-coated multi-layers, incorporated with and without drugs, were measured by the static water contact angle [SCA(H_2O)] measurements and the results are depicted in **Table 1** (also see in **Table S1**). It shows that the spin-coated layers of ALG 3, CMC 3 or their combination are hydrophilic [obtained SCA(H_2O) values << 90°] (Yuan and Lee, 2013). For all three spin-coated samples, higher SCA(H_2O) values are observed compared to the SCA(H_2O) values of the substrate used for spin-coated [Si-wafers; SiO_2 surface (10 ± 0.2°)] (Stana et al., 2017). The changes in the SCA(H_2O) indirectly also confirm a successful deposition of the spin-coated polysaccharide materials. Compared to ALG 3 alone, slightly increased SCA(H_2O) values for CMC 3 and the ALG-CMC 3 blend are observed, which can be related to the rougher and thicker surfaces of the latter samples (**Figures 1**, **2**). Another important observation based on these results is that no further (major) changes in the SCA(H_2O) values resulted for the incorporation of either of the drugs. Namely, hydrophilic and highly wettable surfaces are already on their own beneficial for wound healing of specific (e.g., chronic) wounds and changes toward more hydrophobic values would potentially limit their therapeutic efficiency. Furthermore, such surfaces can even enhance the drug release efficiency by allowing penetration of body fluids and thus enabling the dissolution and/or diffusion of the drugs from the materials to the wound area (Maver et al., 2018a).

TABLE 1 | SCA(H_2O) values of ALG, CMC, and ALG-CMC spin-coated multi-layers, incorporated with and without drugs.

	ALG 3 [°]	CMC 3 [°]	ALG-CMC 3 [°]
No drug	21 ± 1	29 ± 3	30 ± 2
DCF	23 ± 2	36 ± 1	33 ± 2
LID	24 ± 2	34 ± 3	31 ± 1

Surface Composition

The surface composition of spin-coated multi-layers incorporated with and without drugs was analyzed using ATR-FTIR spectroscopy. **Figure 3A** shows characteristic peaks of pure ALG and CMC. For ALG, the observed peaks at 3,360, 2,903, and 1,625 cm^{-1} are attributed to O-H stretching, -CH stretching, the asymmetric and symmetric vibrations of -COO and C-O-C stretching, respectively. Whereas, all major peaks of CMC are observed at 3,411, 2,916, 1,583, 1,420, and 1,324 cm^{-1}, which are assigned to O-H and –CH stretching, and the asymmetrical and symmetrical vibrations of carboxyl groups in the CMC, respectively. Although no additional new peaks are noticed for ALG-CMC 3 coated layers, all the characteristic peaks, as shown above, of ALG and CMC are detected. These results suggest that the ALG-CMC 3 layer is composed fully of both polymers and no new bindings/interactions are involved between the functional groups.

The spectra of sodium salt of DCF and DCF loaded polymers are shown in **Figure 3B**. Characteristic DCF peaks include at 3,253 cm^{-1} the NH stretching of the secondary amine, at 1,571 cm^{-1} the –C=O stretching of the carboxyl ion, at 1,500 cm^{-1} the C=C ring stretching, at 1,450 cm^{-1} the -CH_2 bending,

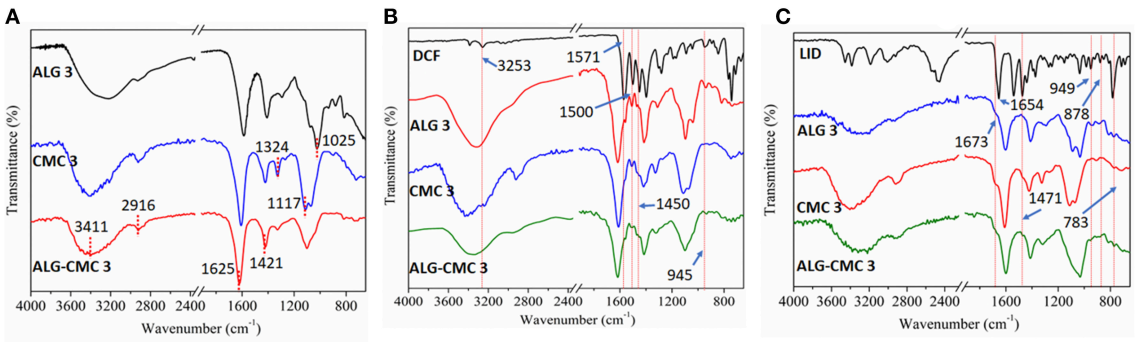

FIGURE 3 | ATR-FTIR spectra of drug-free **(A)**, DCF-loaded **(B)**, and LID-loaded **(C)** polymers.

at 945 cm^{-1} the -C-O-C stretching, and at 746 cm^{-1} the C-Cl stretching. All these peaks are also present for all samples (ALG, CMC, and the ALG-CMC blends). **Figure 3C** shows the characteristic peaks of LID at 1,673 cm^{-1} for the stretching of carbonyl group, and at 1,541 cm^{-1} the in-plane bending of the N-H group. Also, in the case of the LID, most of these peaks are detected for all the polysaccharide based multi-layer samples. Interestingly, the -C=O peak position of CMC and ALG is altered after the incorporation of both drugs. The -C=O peak is shifted from 1,625 to 1,604 cm^{-1} and from 1,583 to 1,613 cm^{-1} for ALG and CMC, respectively. These peak shifts indicate that both drugs are involved in some sort of interactions, most likely ionic or H-bonding. Such a scenario is mostly favorable and desired for applications, especially for prolonging the release rate of the drugs. In addition, the drug molecules could also be physically incorporated, which has other advantageous that drug molecules could simply diffuse through the layers and be released into the medium or at the wound site without any hinderance from the polysaccharide in which the drugs are incorporated. It can be concluded that the ATR-FTIR results confirmed the presence, and hence a successful incorporation of both used drugs into the formed multi-layer systems regardless of their compositions. Therefore, the next step was a thorough drug release analysis of all drug incorporated samples.

In vitro Release Studies

Controlled and local release of pain relieving, and anti-inflammatory drugs presents an important step toward a more successful chronic wound healing. Such drugs can not only diminish the pain from the wound itself, but also reduce the pain induced stress, which is known to hinder the healing efficiency, especially in the long term (Maver et al., 2015a). The used drugs herein (LID and DCF), come from different pharmacodynamic groups (LID is a local anesthetic and DCF a non-steroidal anti-inflammatory drug), and hence lower the sensation of pain through different mechanisms, improving the overall therapeutic potential of the developed multi-layered materials even further (Maver et al., 2017). Since they are both water soluble, DCF and LID can be easily mixed and homogeneously incorporated within the herein used hydrophilic host materials (ALG and CMC). Altogether, such systems provide an excellent platform for rapid design of novel multifunctional wound dressing materials as was shown before (Maver et al., 2019). In this study, novel polysaccharide drug loaded multi-layer thin film systems were fabricated that serve as a representative model of "real" dressing materials, enabling their optimization already during development. Since it is important to ensure an efficient pharmacotherapy i.e., controlled drug delivery for the newly developed systems, a lot of emphasis has been put on the evaluation of the results obtained from the *in vitro* drug release studies.

The DCF and LID release profiles from the different polysaccharide multi-layers are shown in **Figure 4**. The release of both drugs is performed at physiological pH with PBS buffer and at a simulated body temperature (37°C) using the "Franz-diffusion" cell-based drug release system, which is the best currently available system to simulate the release from wound dressings. The released mass of DCF as a function of time is depicted in **Figure 4A**. Immediately it can be observed that there are notable differences in the released mass of DCF from the three systems. As it seems, the DCF release is favored from the "pure" ALG multi-layers, which is not really surprising considering that DCF is in its essence an "acid." Whereas, CMC can exhibit multiple carboxylic groups per one sugar unit, this is not the case with ALG, which has only one such group in its structure. Therefore, increased repulsive forces could be present in the case of CMC multi-layer systems, which probably led already in the preparation steps to smaller incorporated DCF amounts, hence finally contributed to a smaller overall DCF release. In addition, as can be seen from the calculated first derivatives of the release data (**Figure 4B**), the profiles of all systems show that multiple mechanisms might be involved in the release of DCF as the time progresses (breaks in the curves of first derivatives). This corresponds to the fact that release of hydrophilic drugs from hydrophilic multi-layer thin films present not just a "simple" diffusion-controlled mechanism but is often further accompanied by a combination of swelling and erosion of polymer chains upon contact with a buffer solution. As soon as the drug becomes soluble and polymer chains becomes mobile, the diffusion of drugs through the multi-layered films occurs with a different rate. A careful evaluation of the release profiles shows a fast (burst) release (∼45%) within the first 30 min,

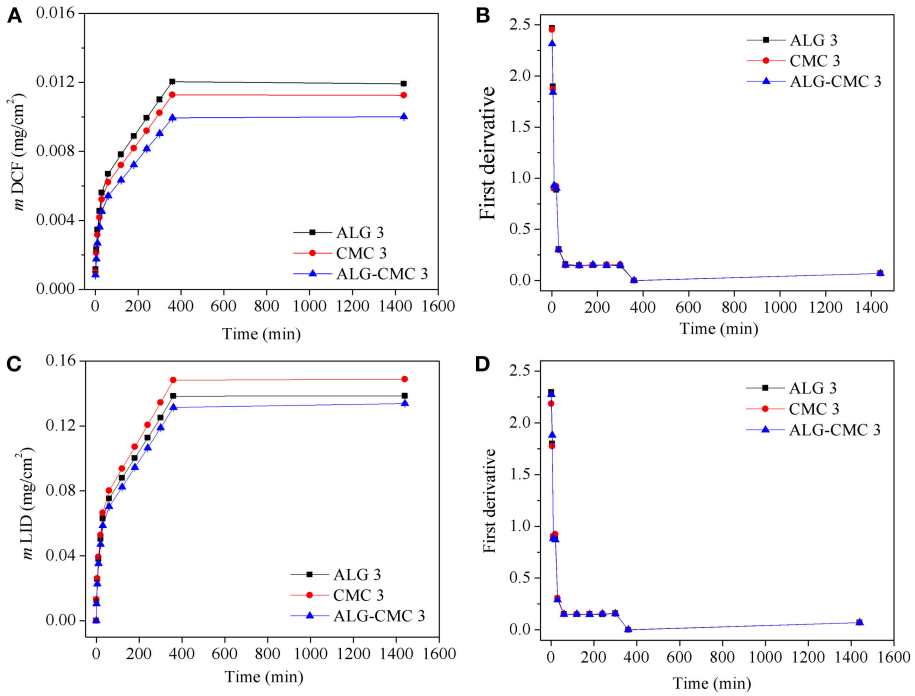

FIGURE 4 | *In vitro* release studies of DCF and LID from the spin-coated multi-layers of alginate (ALG 3), carboxymethyl cellulose (CMC 3) and ALG-CMC 3 blend. Dissolution profiles of DCF **(A)** and LID **(C)** of mass change as a function of time. First derivative of the release data of DCF **(B)** and LID **(D)**.

which most likely corresponds to the release and dissolution of "trapped" or unbound drug molecules within the polymer structure. The latter is followed by a slower and prolonged release (∼50%) for the next 6 h (360 min), which is related to the combination of swelling and partial erosion (mentioned above). The last release stage is the so called "plateau," which present a diffusion-controlled release of the remainder of the drug from the remaining (mostly intact) part of the multi-layer system. Another important observation based on the obtained release results is that regardless of the composition, all three different samples seems to follow the same combined release mechanism (confirmed by the calculation of the first derivatives shown in **Figure 4B**). This has another implication for the potential clinical use of such materials. Namely, by simply choosing another polymer (or the combination thereof), the physician can also control the overall used/delivered drug dose to the wound. Further studies would be necessary to show how we can further control the released drug amount by changing the incorporated drug amount, but this is out of the scope of this study. Developing the thought about the potential clinical application of such materials further, it can be said that such a release profile is essentially as desired in release of analgesic drugs in chronic wound treatment. Whereas, the initial "large" released amount of the analgesic drug is essential to provide a strong pain-relieving action as soon as possible, the sustained release is important to lower the pain sensation until the dressing is changed. The sustained drug release further improves the quality of life of the patient in long-term during treatment.

Similar deductions about the release mechanism can be made for the system with incorporated drug LID, although there is a different order of the systems in regard of the total release LID amount. Namely, here the CMC based system show the highest release amount, which is most likely again connected with the polymer and drug molecular structure. LID presents an amide, which has another secondary amine in its structure. The latter is capable to form interactions (e.g., ionic bonds) with carboxylic groups, which might have contributed to a higher incorporated dose of the drug during the preparation step (i.e., spin-coating). Since CMC has a higher amount of such groups, more of the drug could have been interacting with the polymer chains in the multi-layer film structure. This data fits with the ATR-IR results where the shift of -C=O peaks of polymers are observed as the result of ionic interactions. Two more conclusions can be made based on the results shown in **Figure 4**. Firstly, the multi-layer systems with incorporated LID had a higher overall incorporated amount of the drug. And secondly, regardless of the drug type, the combined polymer system (ALG-CMC) has shown the most sustained release. To ease further discussions of the latter, the overall released mass of DCF and LID from three types of multi-layers are compared and the results are shown in **Figure 5**. The total released mass of DCF is higher for ALG 3 with a thickness of *ca.*11 nm than the other two multi-layers (CMC 3: 36 nm, ALG-CMC 3: 33 nm). It is suggested that the DCF as a small molecule with a molecular weight of 296.2 g/mol is expected to diffuse faster in and out of the thin multi-layer films. From this release result, it can be stated that even the thinnest multi-layer films can be used to incorporate and release

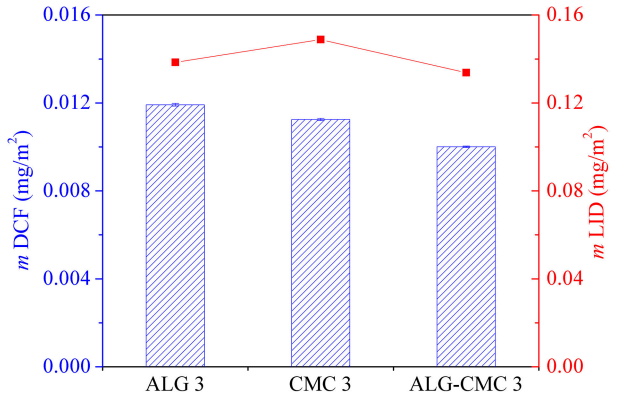

FIGURE 5 | Total amount of released drug mass from different spin-coated polysaccharide multi-layered thin films.

drugs in therapeutic doses in a controlled manner similar to that of three times thicker CMC 3 or ALG-CMC 3 films. Among other two multi-layers, a slightly lower mass is found for ALG-CMC 3. A reason can be that the diffusion of DCF through the thicker ALG-CMC 3 and hierarchically structured film from the two polymer components is prevented, and thus the overall released mass is lower. However, a different trend is observed for LID incorporated multi-layers. While ALG 3 and ALG-CMC 3 showed almost the same amount of the released mass, CMC 3 multi-layers showed a slightly higher mass release, which is the opposite to the results observed for DCF incorporated CMC 3 multi-layer. For LID incorporated layers (**Figure 4C**), although the release profile is similar to DCF, the overall released mass is 10 times higher when compared to DCF. This can be related to differences in the solubility of both drugs. It is suggested that upon contact with water, compared to DCF (solubility in water: 0.005 mg/mL), the hydrochloride form of LID (used in this study, solubility in water: 0.6 mg/mL) incorporated within the hydrophilic ALG-CMC 3 matrix dissolves and diffuses quicker through the film, and thus a larger amount of drug is released over time. Overall, the data show that it is possible to carefully tune the release rate of drug using one particular system, as it is demonstrated by several others (Vasilev et al., 2011; Wang et al., 2016; Maver et al., 2018a; Speer et al., 2019). Using thinner and thicker multi-layer coatings, the release rate can be extended even further (desired in treatment of chronic wounds is for multiple days).

To further evaluate the kinetics and mechanisms of drug (DIC and LID) release from the multi-layers, the *in vitro* release data were fitted by linear regression analysis according to different kinetic models. Although different kinetic models were considered, only the models (First-order, Higuchi-model, and Korsmeyer-Peppas model, see **Table 2**) that gave reasonable fits for the release data were selected [based on the square of the correlation coefficient (r^2) value]. The kinetic model that resulted in the highest r^2 value was considered as the best fit for the release data. Among the tested three kinetic models, the Korsmeyer–Peppas model had the best fit with the highest r^2 value for all multi-layers. Slightly lower r^2 values were calculated

TABLE 2 | The values of correlation coefficient (r^2) and release exponent (n) calculated from different kinetic models for DCF and LID loaded system.

Samples	First order	Higuchi model	Korsmayer-Peppas model	
	r^2	r^2	r^2	*n*
ALG 3	0.900	0.966	0.984	1.05
CMC 3	0.878	0.966	0.981	1.02
ALG-CMC 3	0.816	0.969	0.981	0.99
ALG 3	0.683	0.969	0.985	1.02
CMC 3	0.786	0.972	0.985	0.99
ALG-CMC 3	0.881	0.972	0.979	0.97

for the Higuchi-model (reflected in **Table 2** and **Figure 6**). Since the first-order model resulted in much lower r^2 values, it was not considered for further interpretation and discussion of the results. Considering the best fit (highest r^2 value in **Table 2**), as well as considering the calculated first derivative results based on the release data (shown in **Figures 4B,D**), it can be assumed that more than one mechanism is involved in the release of the drug from all three multi-layers (Keny et al., 2009). For the fitting of the results, the release data from 0 to 360 min were used. The best fit was obtained with Korsmeyer-Peppas model, which is among the most common models to describe the drug release kinetics from polymeric systems, when the release mechanism is unknown, or more than one release phenomena is involved. The release component "*n*" value from the Korsmeyer–Peppas Equation (3) was shown to be related (at least partially) to different release mechanisms and can therefore be used for an estimation of the latter. From **Table 2** it can be seen that the "*n*" value is found to vary with type of multi-layers used, whereas the absolute value is in all cases above 0.89 for both drugs. This calculation leads to the conclusion that the release of both drugs from all system is an anomalous non-Fickian diffusion transport (super case-II transport mechanism). This means that the drug molecules are released through a diffusion process in a highly hydrated polysaccharide matrix that involved in the dissolution or relaxation of polymer chains (might be either swelling, erosion, or both) (Nayak and Pal, 2013). Since the Higuchi model came close to the best fit (r^2: 0.96–0.97), let us consider what it would mean, if the latter model would hold. Considering that the Higuchi model presents the derivation of an equation that allowed for the quantification of drug release from thin ointment films, containing finely dispersed drug (applicable in perfect sink conditions), this model could also potentially be used to explain the release mechanism in this study. For example, the obtained r^2 values suggest that the release of drugs from the multi-layered system is controlled by diffusion, which is totally opposite to non-Fickian diffusion approach. Therefore, according to the best fit and highest r^2 value, we believe that the release of both drugs from all three multi-layered system follows Korsmeyer–Peppas model and no other kinetic models.

Biocompatibility Testing

In vitro biocompatibility testing with human skin cells is an important indication for developed material safety and (depending on the type of material and purpose) to some extent

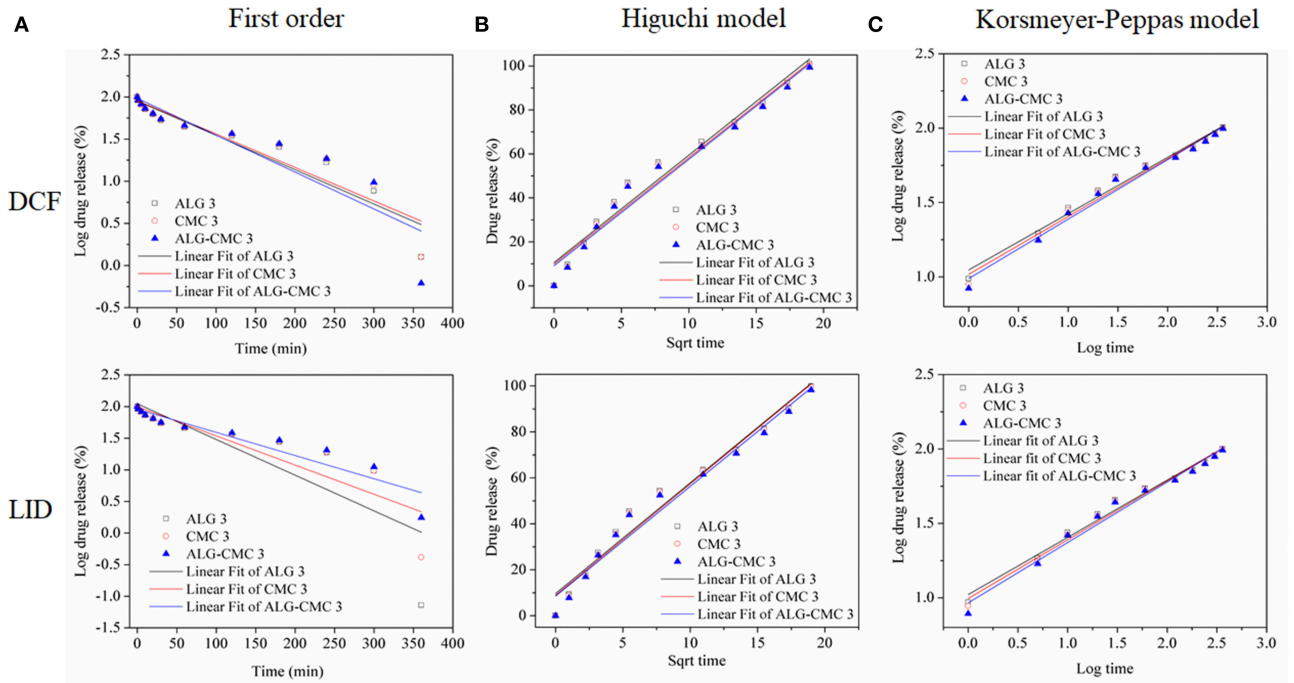

FIGURE 6 | Drug release data of DCF and LID loaded polymers fitted to various kinetic models.

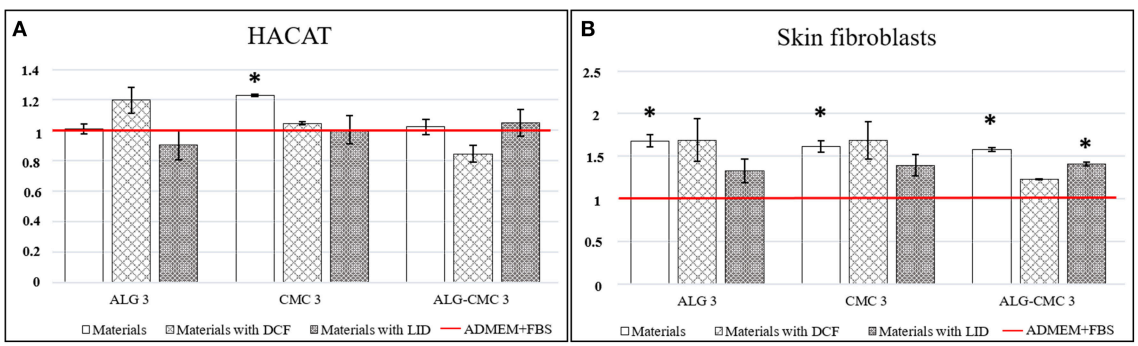

FIGURE 7 | (A) HaCaT cells' viability determination using the MTT assay for all samples and the control; ADMEM + FBS (red line in graph), **(B)** Skin Fibroblast cells' viability determination using the MTT assay for all samples and the control; ADMEM + FBS (red line in graph). Error bars represent standard deviation of the replicate measurements. Statistical significance is defined as $^{*}P < 0.05$ (ANOVA test) for all samples compared to the control.

efficiency for wound application. In comparison to most available studies, where animal-derived or cancer-transformed cells are used, the results obtained using human cells can serve as a much better approximation of the actual influence of the developed materials in clinical use (Stana et al., 2017). The viability of keratinocytes (HaCaT) and skin fibroblasts (SF) with the drug incorporated multi-layers was tested to confirm the potential of prepared materials for wound care applications. Since extracts of the developed materials were tested against the skin cells, pure cell growth media (ADMEM + FBS) was used as the control sample. From **Figure 7**, which show the obtained results of this testing, it is immediately apparent that all samples with one exception among each of the developed drug filled multi-layer systems, outperformed the control sample. The exception is LID incorporated ALG3 and DCF incorporated ALG-CMC3 multi-layer; however, no significant deviation was measured even in these samples, as well as no differences in the cell morphology was detected for neither of these samples, indicating that no toxicity whatsoever is present. Important conclusions, which can be made here; no toxic degradation products are formed in neither of the samples (namely, these would significantly affect the cell growth in a negative sense), and the tested multi-layers promoted the growth of cells, especially the skin fibroblasts (**Figure 7B**). After 48 h, the viability of skin fibroblasts significantly increased in almost all cases, whereas the best results were obtained for the drug-free and DCF included ALG3 multi-layer. Unexpectedly, the incorporation of LID did partially lower the viability of the cells compared to the drug free materials, although the values

still remained above the control. Similar results were acquired for skin fibroblasts exposed to CMC 3 with and without included drugs. In the case of ALG-CMC 3, the viability decreased a little after addition of DCF, but nevertheless it remained above the one measured for the control sample. Similar results, only with somewhat lower values, were obtained in the case of HaCaT cells.

Altogether, the obtained results prove that regardless of the polymer-drug combinations used in this study, especially when considering the different mechanisms of action of the LID and DCF drugs, they did not exhibit any toxic effect on neither of the most abundant human skin cells (keratinocytes and fibroblasts). Therefore, we can conclude that tested materials with and without included drugs are biocompatible. The measured higher viabilities in most sample cases compared to the control, require further studies to evaluate the physiological mechanism behind, whereas at the moment, the obtained results indicate that the developed materials are very suitable for use in wound care.

CONCLUSIONS

A simple and rapid method to fabricate nanoscale multi-layered system from water soluble polysaccharides using the combination of spin-coated and LBL techniques is demonstrated. The potential application of multi-layered thin films created from ALG and CMC for the effective incorporation and controlled release of two analgesic drug molecules (DIC and LID) at a physiological condition is investigated in detail. Upon spin-coating, the phase separation occurred for the ALG-CMC mixture, which could not be seen for either ALG or CMC. Such phase separated features are not influenced by the incorporation of either DIC or LID. The presence of latter can be confirmed by ATR-FTIR measurements; however, no substantial changes in the surface wettability are observed before and after the incorporation of drug molecules. Although the film thickness is increased for all three system with a number of deposition steps, a thicker film (highly adsorbed mass) is formed for both CMC and ALG-CMC. A rapid "burst" release followed by a prolonged release kinetics are observed for both drugs regardless of the multilayered system, while the overall released mass is lower for ALG-CMC compared to either ALG or CMC coated surfaces alone. The release properties of both drugs are suited for Korsmeyer–Peppas model, which showed a best fit and the highest "r^2 value" when compared to other two models. The release behavior is predicted to be non-Fickian based on the exponent "n" value which is above 0.89 in all cases. Although the influence of incorporated drugs in the multi-layered thin films is not significant in the growth of both tested skin cells, a pounced growth of skin fibroblast cells is detected already for drug-free multi-layered films. Overall, the knowledge gained through this study is highly beneficial not only to develop a highly multifunctional materials but also for applications related to targeted drug-delivery and tissue engineering, in general.

DATA AVAILABILITY

All datasets generated for this study are included in the manuscript and/or the **Supplementary Files**.

AUTHOR CONTRIBUTIONS

TiM performed all experiments and contributed substantially to the writing of this manuscript. TaM contributed substantially to the writing, handled submission and revising of the manuscript. LG performed experimental work related to cell testing. MF, KS, and UM contributed to writing and revising of the manuscript.

ACKNOWLEDGMENTS

The authors acknowledge the financial support from the Slovenian Research Agency for Research (grant numbers: P2-0118, P3-0036, P2-0032, J1-9169, I0-0029, and Z2-8168).

SUPPLEMENTARY MATERIAL

The Supplementary Material for this article can be found online at: https://www.frontiersin.org/articles/10.3389/fchem.2019.00217/full#supplementary-material

REFERENCES

Altman, R., Bosch, B., Brune, K., Patrignani, P., and Young, C. (2015). Advances in NSAID development: evolution of diclofenac products using pharmaceutical technology. *Drugs* 75, 859–877. doi: 10.1007/s40265-015-0392-z

Costa, P., and Sousa Lobo, J. M. (2001). Modeling and comparison of dissolution profiles. *Eur. J. Pharm. Sci.* 13, 123–133. doi: 10.1016/S0928-0987(01)00095-1

Criado-Gonzalez, M., Fernandez-Gutierrez, M., San Roman, J., Mijangos, C., and Hernández, R. (2019). Local and controlled release of tamoxifen from multi (layer-by-layer) alginate/chitosan complex systems. *Carbohydr. Polym.* 206, 428–434. doi: 10.1016/j.carbpol.2018.11.007

Doublier, J. L., Garnier, C., Renard, D., and Sanchez, C. (2000). Protein–polysaccharide interactions. *Curr. Opin. Colloid Interface Sci.* 5, 202–214. doi: 10.1016/S1359-0294(00)00054-6

Fang, Y., Li, L., Inoue, C., Lundin, L., and Appelqvist, I. (2006). Associative and segregative phase separations of gelatin/κ-carrageenan aqueous mixtures. *Langmuir* 22, 9532–9537. doi: 10.1021/la061865e

Finšgar, M., Uzunalić, A. P., Stergar, J., Gradišnik, L., and Maver, U. (2016). Novel chitosan/diclofenac coatings on medical grade stainless steel for hip replacement applications. *Sci. Rep.* 6:26653. doi: 10.1038/srep26653

Geoghegan, M., Jones, R. A. L., Payne, R. S., Sakellariou, P., Clough, A. S., and Penfold, J. (1994). Lamellar structure in a thin polymer blend film. *Polymer* 35, 2019–27. doi: 10.1016/0032-3861(94)90223-2

Guo, S., and Dipietro, L. A. (2010). Factors affecting wound healing. *J. Dent. Res.* 89, 219–229. doi: 10.1177/0022034509359125

Heriot, S. Y., and Jones, R. A. L. (2005). An interfacial instability in a transient wetting layer leads to lateral phase separation in thin spin-cast polymer-blend films. *Nat. Mater.* 4, 782–786. doi: 10.1038/nmat1476

Jeganathan, B., Prakya, V., and Deshmukh, A. (2016). Preparation and evaluation of diclofenac sodium tablet coated with polyelectrolyte multilayer film using hypromellose acetate succinate and polymethacrylates for ph-dependent, modified release drug delivery. *AAPS PharmSciTech.* 17, 578–587. doi: 10.1208/s12249-015-0385-y

Kargl, R., Vorraber, V., Ribitsch, V., Köstler, S., Stana Kleinschek, K., and Mohan, T. (2015). Selective immobilization and detection of DNA on biopolymer supports for the design of microarrays. *Biosens. Bioelectron.* 68, 437–441. doi: 10.1016/j.bios.2015.01.038

Karki, S., Kim, H., Na, S.-J., Shin, D., Jo, K., and Lee, J. (2016). Thin films as an emerging platform for drug delivery. *Asian J. Pharm. Sci.* 11, 559–574. doi: 10.1016/j.ajps.2016.05.004

Keating, C. D. (2012). Aqueous phase separation as a possible route to compartmentalization of biological molecules. *Acc. Chem. Res.* 45, 2114–2124. doi: 10.1021/ar200294y

Keny, R. V., Mankame, S. A., and Lourenco, C. F. (2009). Formulation and evaluation of once daily minocycline hydrochloride extended release matrix tablets. *Indian J. Pharm. Sci.* 71, 295–302. doi: 10.4103/0250-474X.56034

Liu, T., Wang, Y., Zhong, W., Li, B., Mequanint, K., Luo, G., et al. (2019). Biomedical applications of layer-by-layer self-assembly for cell encapsulation: current status and future perspectives. *Adv. Healthc. Mater.* 8:1800939. doi: 10.1002/adhm.201800939

Loo, S. C. J., Tan, Z. Y. S., Chow, Y. J., and Lin, S. L. I. (2010). Drug release from irradiated PLGA and PLLA multi-layered films. *J. Pharm. Sci.* 99, 3060–3071. doi: 10.1002/jps.22079

Marques, E. M., Jones, H. E., Elvers, K. T., Pyke, M., Blom, A. W., and Beswick, A. D. (2014). Local anaesthetic infiltration for peri-operative pain control in total hip and knee replacement: systematic review and meta-analyses of short- and long-term effectiveness. *BMC Musculoskelet. Disord.* 15:220. doi: 10.1186/1471-2474-15-220

Maver, T., Gradišnik, L., Kurečič, M., Hribernik, S., Smrke, D. M., Maver, U., et al. (2017). Layering of different materials to achieve optimal conditions for treatment of painful wounds. *Int. J. Pharm.* 529, 576–588. doi: 10.1016/j.ijpharm.2017.07.043

Maver, T., Hribernik, S., Mohan, T., Smrke, D. M., Maver, U., and Stana Kleinschek, K. (2015a). Functional wound dressing materials with highly tunable drug release properties. *RSC Adv.* 5, 77873–77884. doi: 10.1039/C5RA11972C

Maver, T., Maver, U., Mostegel, F., Griesser, T., Spirk, S., Smrke, D. M., et al. (2015b). Cellulose based thin films as a platform for drug release studies to mimick wound dressing materials. *Cellulose* 22, 749–761. doi: 10.1007/s10570-014-0515-9

Maver, T., Maver, U., Pivec, T., Kurečič, M., Peršin, Z., Stana Kleinschek, K., et al. (2018a). Advanced wound care. *Bioact. Polysacch. Mater. Modern Wound Heal.* 1–8. doi: 10.1007/978-3-319-89608-3_1

Maver, T., Smrke, D. M., Kurečič, M., Gradišnik, L., Maver, U., and Stana Kleinschek, K. (2018b). Combining 3D printing and electrospinning for preparation of pain-relieving wound-dressing materials. *J. Sol-Gel Sci. Technol.* 88, 33–48. doi: 10.1007/s10971-018-4630-1

Maver, U., Milojević, M., Štos, J., Adrenšek, S., and Planinšek, O. (2019). Matrix tablets for controlled release of drugs incorporated using capillary absorption. *AAPS PharmSciTech* 20:91. doi: 10.1208/s12249-019-1303-5

Maver, U., Xhanari, K., Zizek, M., Korte, D., Gradisnik, L., Franko, M., et al. (2018). A combination of interdisciplinary analytical tools for evaluation of multi-layered coatings on medical grade stainless steel for biomedical applications. *Eur. J. Pharm. Biopharm.* 128, 230–246. doi: 10.1016/j.ejpb.2018.05.002

McGuire, L., Heffner, K., Glaser, R., Needleman, B., Malarkey, W., Dickinson, S., et al. (2006). Pain and wound healing in surgical patients. *Ann. Behav. Med.* 31, 165–172. doi: 10.1207/s15324796abm3102_8

Miao, T., Wang, J., Zeng, Y., Liu, G., and Chen, X. (2018). Polysaccharide-based controlled release systems for therapeutics delivery and tissue engineering: from bench to bedside. *Adv. Sci.* 5, 1700513–1700513. doi: 10.1002/advs.201700513

Mohan, T., Kargl, R., Köstler, S., Doliška, A., Findenig, G., Ribitsch, V., et al. (2012). Functional polysaccharide conjugates for the preparation of microarrays. *ACS Appl. Mater. Interfaces* 4, 2743–2751. doi: 10.1021/am300375m

Mohan, T., Kargl, R., Tradt, K. E., Kulterer, M. R., Bračić, M., Hribernik, S., et al. (2015). Antifouling coating of cellulose acetate thin films with polysaccharide multilayers. *Carbohydr. Polym.* 116, 149–158. doi: 10.1016/j.carbpol.2014.04.068

Mohan, T., Niegelhell, K., Nagaraj, C., Reishofer, D., Spirk, S., Olschewski, A., et al. (2017). Interaction of tissue engineering substrates with serum proteins and its influence on human primary endothelial cells. *Biomacromolecules* 18, 413–421. doi: 10.1021/acs.biomac.6b01504

Nayak, A. K., and Pal, D. (2013). Formulation optimization and evaluation of jackfruit seed starch–alginate mucoadhesive beads of metformin HCl. *Int. J. Biol. Macromol.* 59, 264–272. doi: 10.1016/j.ijbiomac.2013.04.062

Palao i Domenech, R., Romanelli, M., Tsiftsis, D. D., Slonkova, V., Jortikka, A., Johannesen, N., et al. (2008). Effect of an ibuprofen-releasing foam dressing on wound pain: a real-life RCT. *J. Wound Care* 342, 344–348. doi: 10.12968/jowc.2008.17.8.30797

Palmer, D., Levina, M., Nokhodchi, A., Douroumis, D., Farrell, T., and Rajabi-Siahboomi, A. (2011). The influence of sodium carboxymethylcellulose on drug release from polyethylene oxide extended release matrices. *AAPS PharmSciTech* 12, 862–871. doi: 10.1208/s12249-011-9648-4

Paques, J. P., Van Der Linden, E., Van Rijn, C. J. M., and Sagis, L. M. C. (2014). Preparation methods of alginate nanoparticles. *Adv. Colloid Interface Sci.* 209, 163–171. doi: 10.1016/j.cis.2014.03.009

Park, K., Choi, D., and Hong, J. (2018). Nanostructured polymer thin films fabricated with brush-based layer-by-layer self-assembly for site-selective construction and drug release. *Sci. Rep.* 8:3365. doi: 10.1038/s41598-018-21493-9

Park, S., Han, U., Choi, D., and Hong, J. (2018). Layer-by-layer assembled polymeric thin films as prospective drug delivery carriers: design and applications. *Biomater. Res.* 22, 29–29. doi: 10.1186/s40824-018-0139-5

Pawar, S. N., and Edgar, K. J. (2012). Alginate derivatization: a review of chemistry, properties and applications. *Biomaterials* 33, 3279–3305. doi: 10.1016/j.biomaterials.2012.01.007

Pérez-Álvarez, L., Ruiz-Rubio, L., Azua, I., Benito, V., Bilbao, A., and Vilas-Vilela, J. L. (2019). Development of multiactive antibacterial multilayers of hyaluronic acid and chitosan onto poly(ethylene terephthalate). *Eur. Polym. J.* 112, 31–37. doi: 10.1016/j.eurpolymj.2018.12.038

Ponnusamy, T., Lawson, L. B., Freytag, L. C., Blake, D. A., Ayyala, R. S., and John, V. T. (2012). *In vitro* degradation and release characteristics of spin coated thin films of PLGA with a "breath figure" morphology. *Biomatter* 2, 77–86. doi: 10.4161/biom.20390

Singer, A. J., and Clark, R. A. (1999). Cutaneous wound healing. *N. Engl. J. Med.* 341, 738–746. doi: 10.1056/NEJM199909023411006

Speer, I., Lenhart, V., Preis, M., and Breitkreutz, J. (2019). Prolonged release from orodispersible films by incorporation of diclofenac-loaded micropellets. *Int. J. Pharm.* 554, 149–160. doi: 10.1016/j.ijpharm.2018.11.013

Stana, J., Stergar, J., Gradišnik, L., Flis, V., Kargl, R., Fröhlich, E., et al. (2017). Multilayered polysaccharide nanofilms for controlled delivery of pentoxifylline and possible treatment of chronic venous ulceration. *Biomacromolecules* 18, 2732–2746. doi: 10.1021/acs.biomac.7b00523

Stergar, J., Ban, I., Gradišnik, L., and Maver, U. (2017). Novel drug delivery system based on NiCu nanoparticles for targeting various cells. *J. Sol-Gel Sci. Technol.* 88, 57–65. doi: 10.1007/s10971-017-4513-x

Strasser, S., Niegelhell, K., Kaschowitz, M., Markus, S., Kargl, R., Stana-Kleinschek, K., et al. (2016). Exploring nonspecific protein adsorption on lignocellulosic amphiphilic bicomponent films. *Biomacromolecules* 17, 1083–1092. doi: 10.1021/acs.biomac.5b01700

Taajamaa, L., Rojas, O. J., Laine, J., and Kontturi, E. (2011). Phase-specific pore growth in ultrathin bicomponent films from cellulose-based polysaccharides. *Soft Matter* 7, 10386–10394. doi: 10.1039/c1sm06020a

Taajamaa, L., Rojas, O. J., Laine, J., Yliniemi, K., and Kontturi, E. (2013). Protein-assisted 2D assembly of gold nanoparticles on a polysaccharide surface. *Chem. Commun.* 49, 1318–1320. doi: 10.1039/c2cc37288f

van de Velde, F., de Hoog, E. H., Oosterveld, A., and Tromp, R. H. (2015). Protein-polysaccharide interactions to alter texture. *Annu. Rev. Food Sci. Technol.* 6, 371–388. doi: 10.1146/annurev-food-022814-015558

Vasilev, K., Poulter, N., Martinek, P., and Griesser, H. J. (2011). Controlled release of levofloxacin sandwiched between two plasma polymerized layers on a solid carrier. *ACS Appl. Mater. Interfaces* 3, 4831–4836. doi: 10.1021/am201320a

Vendra, V. K., Wu, L., and Krishnan, S. (2011). "Polymer thin films for biomedical applications," in *Nanotechnologies for the Life Sciences*, eds C. S. S. R. Kumar (Weinheim: WILEY-VCH Verlag GmbH & Co.), 1–39.

Walheim, S., Böltau, M., Mlynek, J., Krausch, G., and Steiner, U. (1997). Structure formation via polymer demixing in spin-cast films. *Macromolecules* 30, 4995–5003. doi: 10.1021/ma9619288

Wang, B., Jin, T., Xu, Q., Liu, H., Ye, Z., and Chen, H. (2016). Direct loading and tunable release of antibiotics from polyelectrolyte multilayers to reduce bacterial adhesion and biofilm formation. *Bioconjug. Chem.* 27, 1305–1313. doi: 10.1021/acs.bioconjchem.6b00118

Yuan, Y., and Lee, T. R. (2013). "Contact angle and wetting properties," in *Surface Science Techniques*, eds. G. Bracco and B. Holst. (Berlin; Heidelberg: Springer), 3–34.

Zelikin, A. N. (2010). Drug releasing polymer thin films: new era of surface-mediated drug delivery. *ACS Nano* 4, 2494–2509. doi: 10.1021/nn100634r

Zhang, X., Xu, Y., Zhang, X., Wu, H., Shen, J., Chen, R., et al. (2019). Progress on the layer-by-layer assembly of multilayered polymer composites: Strategy, structural control and applications. *Prog. Polym. Sci.* 89, 76–107. doi: 10.1016/j.progpolymsci.2018.10.002

Zhao, X., Sun, Y., and Li, Z. (2018). Topical anesthesia therapy using lidocaine-loaded nanostructured lipid carriers: tocopheryl polyethylene glycol 1000 succinate-modified transdermal delivery system. *Drug Des. Dev. Ther.* 12, 4231–4240. doi: 10.2147/DDDT.S187177

Conflict of Interest Statement: The authors declare that the research was conducted in the absence of any commercial or financial relationships that could be construed as a potential conflict of interest.

frontiers in Chemistry

ORIGINAL RESEARCH
published: 16 April 2019
doi: 10.3389/fchem.2019.00251

Multilayer Density Analysis of Cellulose Thin Films

Carina Sampl[1,2†], *Katrin Niegelhell*[1,2†], *David Reishofer*[1†], *Roland Resel*[3†], *Stefan Spirk*[1,2*†] *and Ulrich Hirn*[1,2†]

[1] Institute for Paper, Pulp and Fibre Technology, Graz University of Technology, Graz, Austria, [2] CD-Laboratory for Fibre Swelling and Paper Performance, Graz University of Technology, Graz, Austria, [3] Institute of Solid State Physics, Graz University of Technology, Graz, Austria

An approach for the multilayer density analysis of polysaccharide thin films at the example of cellulose is presented. In detail, a model was developed for the evaluation of the density in different layers across the thickness direction of the film. The cellulose thin film was split into a so called "roughness layer" present at the surface and a "bulk layer" attached to the substrate surface. For this approach, a combination of multi-parameter surface plasmon resonance spectroscopy (SPR) and atomic force microscopy (AFM) was employed to detect changes in the properties, such as cellulose content and density, thickness and refractive index, of the surface near layer and the bulk layer. The surface region of the films featured a much lower density than the bulk. Further, these results correlate to X-ray reflectivity studies, indicating a similar layered structure with reduced density at the surface near regions. The proposed method provides an approach to analyse density variations in thin films which can be used to study material properties and swelling behavior in different layers of the films. Limitations and challenges of the multilayer model evaluation method of cellulose thin films were discussed. This particularly involves the selection of the starting values for iteration of the layer thickness of the top layer, which was overcome by incorporation of AFM data in this study.

Keywords: multilayer analysis, surface plasmon resonance, atomic force microscopy, cellulose thin film, X-ray reflectivity

OPEN ACCESS

Edited by:
Giuseppe Mensitieri, University of Naples Federico II, Italy

Reviewed by:
Ram Gupta, Pittsburg State University, United States
Marino Lavorgna, Institute of Polymers, Composite and Biomaterials, Italian National Research Counci, Italy

****Correspondence:***
Stefan Spirk
stefan.spirk@tugraz.at

[†] Members of NAWI Graz and the European Polysaccharide Network of Excellence (EPNOE)

Specialty section:
This article was submitted to Polymer Chemistry, a section of the journal Frontiers in Chemistry

Received: *22 January 2019*
Accepted: *27 March 2019*
Published: *16 April 2019*

Citation:
Sampl C, Niegelhell K, Reishofer D, Resel R, Spirk S and Hirn U (2019) Multilayer Density Analysis of Cellulose Thin Films. Front. Chem. 7:251. doi: 10.3389/fchem.2019.00251

INTRODUCTION

The past decades have seen tremendous efforts to explore and to understand processes occurring at surfaces of materials, which was accompanied by the development of new surface sensitive techniques and methodologies. These techniques are either capable of determining the surface properties such as morphology, topography, chemical structure, and composition, or they are utilized to monitor dynamic phenomena taking place at interfaces, such as adsorption, modification, or wetting, to name a few (Vickerman and Gilmore, 2009; Zaera, 2011).

Atomic force microscopy (AFM) (Binnig et al., 1986), for instance, is an imaging technique for the investigation of surfaces on an atomic scale by scanning the surface using a cantilever with a sharp tip while it is maintained at a constant force or a constant height above the sample. Nowadays, the observation of surfaces in real-time using fast scanning devices (one frame per second and faster) allows for visualizing dynamic biological processes at interfaces. For example, enzymatic degradation of biopolymers such as cellulose can be monitored and videos of the degradation process can be acquired (Giessibl, 2003; Jalili and Laxminarayana, 2004; Niegelhell et al., 2016).

Surface plasmon resonance (SPR) spectroscopy is a surface sensitive technique that is able to monitor processes in real-time as well. In contrast to atomic force microscopy, it detects changes

in the chemical environment, i.e., the refractive index *n*, near a metal surface (∼100 nm) (Raether, 1977). The technique is based on the resonance of surface plasmons, which originates from the oscillation of charge densities on the metal surface caused by freely moving electron gas (Ritchie, 1957). Acquisition of SPR spectra is accomplished by focusing a *p*-polarized light source onto a metal surface (e.g., a glass slide coated with a thin gold layer) and recording the intensity of the reflected light by a detection system (e.g., photodiode array detectors). State of the art multi-parameter SPR devices, acquire spectra in dependence of the incidence angle of the light, which allows for the investigation of processes in real-time and in varying ambient media (i.e., gas or liquid) at different wavelengths (i.e., 670 and 785 nm) in a single experiment. The resulting curves are evaluated by a multilayer fitting procedure, whereby thickness (*d*) and refractive index (*n*) of the examined layers are derived (Geddes et al., 1994). In a standard SPR spectrometer, where the measurement is performed with only a single wavelength, determination of both -layer thickness and refractive index- is not possible without assuming or knowing one of the values. Multi-parameter SPR (MP-SPR) systems measuring at two or more wavelengths overcome this problem (Peterlinz and Georgiadis, 1996; Liang et al., 2010).

When observing phenomena with SPR spectroscopy in real-time, the change in refractive index related to the whole sample is detected. In most cases, this information is sufficient because it allows for monitoring adsorption processes at the interfaces, in terms of deposited mass and adsorption kinetics. Many examples do exist which investigate biomolecule deposition on cellulose thin films mainly with the aim to establish sensor systems or antifouling surfaces (Orelma et al., 2011, 2012; Niegelhell et al., 2016, 2017, 2018; Strasser et al., 2016; Mohan et al., 2017; Weißl et al., 2018). Since water incorporation into the film changes its refractive index, swelling has been investigated by SPR as well for the whole film (Kontturi et al., 2013). However, when it comes to more complex questions, i.e., whether the swelling of such a thin film is different on the "surface" than in the "bulk," other approaches with more complex fitting procedures are required. Up to now, the fitting procedures used in SPR data evaluation have only been used to describe the cellulose film as a single layer. When splitting the film into more than one layer, more information is required for the fitting procedure.

Herein, the investigation of such a multilayer analysis approach to evaluate density variations of different layers in thin films, at the example of cellulose, is presented. A model describing the cellulose thin film as a multilayer system was developed. The implementation of AFM data into the multilayer fitting model was of outmost importance in order to obtain starting values for the fitting procedure concerning thickness of bottom and top layer. This combination of analysis methods and the presented multilayer density analysis approach yielded spatial resolution along the z-axis of the examined films. Compositions of the entire films as well as differences between the surface regions and the bulk were evaluated. The approach was compared to X-ray reflectivity (XRR) measurements of cellulose thin films, which were also analyzed to obtain thickness and density data for a multilayer cellulose film system.

THEORETICAL BACKGROUND

Determination of Thickness and Refractive Index of Cellulose Thin Films: The 2-Wavelength Method (2-λ-Method)

The simulation of a sample measured at a single wavelength provides a refractive index (*n*)—thickness (*d*) continuum (*n* decreases when *d* increases) without a unique solution, since the surface plasmon wave vector k_{sp} is dependent on both entities.

$$k_{SP} \propto n * d \tag{1}$$

In order to determine a unique solution, measurements at two wavelengths resulting in two different sets of *n* - *d* continua are required. Since the refractive index is dependent on the wavelength, the *n* - *d* continuum measured at one wavelength can be shifted to the other wavelength (Peterlinz and Georgiadis, 1996). The unique solution is found at the intersection of these continuum solutions.

$$k_{SP1} = n_{\lambda 1} * d \ and \tag{2}$$

$$k_{SP2} = n_{\lambda 2} * d \tag{3}$$

where

$$n_{\lambda 2} = \left(n_{\lambda 1} + \frac{dn}{d\lambda} (\lambda_2 - \lambda_1) \right) and \tag{4}$$

$$k_{SP1} = n_{\lambda 1} * d \ and \tag{5}$$

$$k_{SP2} = \left(n_{\lambda 1} + \frac{dn}{d\lambda} (\lambda_2 - \lambda_1) \right) * d \tag{6}$$

The dependence of refractive index on the wavelength, i.e., chromatic dispersion ($dn/d\lambda$), is approximated to be linear for relatively small wavelength changes (a few hundred nm).

For cellulose, the $dn/d\lambda$ at 670 and 785 nm is −0.0338 and −0.0204 μm^{-1}, respectively (Kasarova et al., 2007). The average, −0.0271 μm^{-1}, was used in the calculations as a chromatic dispersion value of pure cellulose. The corresponding value for air is −0.00000856 μm^{-1} (Ciddor, 1996). The *n* - *d* curves of the cellulose thin films obtained by the two wavelengths were plotted in the same graph. The *n* - *d* curve of the measurement performed at 785 nm was shifted by the $dn/d\lambda$ value of cellulose and by the $dn/d\lambda$ value of the ambient medium (air). The intersection points of the shifted curves (air and cellulose) measured at 785 nm with the curve measured at 670 nm results in two unique solutions. An average (n_{film}) of the *n* values obtained by the intersection points was determined. The proportion of cellulose of the volume of the film, *a* corresponding to the obtained n_{film} value, was calculated according to Equation (7):

$$n_{film} = a \cdot n_{cellulose} + (1 - a) \cdot n_{medium} \tag{7}$$

where $n_{cellulose}$ is 1.466 (Kasarova et al., 2007) and n_{medium} is 1.00028 for air (Ciddor, 1996).

Based on a, the value of $dn/d\lambda$ was corrected by Equation (8) (Kontturi et al., 2013):

$$dn/d\lambda_{film} = a \cdot dn/d\lambda_{cellulose} + (1 - a) \cdot dn/d\lambda_{medium} \tag{8}$$

Then, the intersection point of the n - d curve measured at 670 nm and the n - d curve shifted from 785 to 670 nm with the new $dn/d\lambda$ results in the unique solution (n and d) of the cellulose thin film (for a detailed example see **Figure 4** in section results and discussion). The composition a of the film was determined by Equation (7). The densities of the films were calculated from the composition and the density values of pure cellulose and air (see **Supplementary Material**) similar to Equation (7).

Multilayer Analysis of Cellulose Thin Films

The procedure to obtain thickness d and the density (via refractive index n) of a thin film has been described in detail in the last section (Theoretical Background). These MP-SPR measurements are the basis for the multilayer analysis of thin film samples (**Figure 1**). The investigated film is split into two layers, namely the roughness layer (*RL*) and the bulk layer (*BL*). Thickness and density are determined for each layer.

The roughness layer *RL* describes the layer that contains the boundary between the film and the ambient medium i.e., the roughness of the film. The *RL* is composed of cellulose and air, the material fraction (mf) refers to the percentage of material within the volume of the *RL*.

Thin film data required to make use of the model is attained by MP-SPR spectroscopy. This data does not contain information on surface roughness, i.e., the roughness layer *RL* is treated as a flat layer with thickness d_t and density ρ_m^t. The roughness layer thickness (RLT^{AFM}) as well as its material fraction (mf_{RL}^{AFM}) were acquired from AFM topography experiments. AFM data was evaluated as illustrated in **Figure 2** and implemented into simulations. A detailed description of the AFM evaluations is shown in the experimental section and in the **Supplementary Material**.

Multilayer Data Analysis for 2-Layer Thin Films Analysis

We are using the modeling software Winspall to analyze film thickness and refractive index (density) from SPR measurements. The key approach of performing multilayer analysis is modeling the thickness for two layers of material instead of one layer of material in Winspall, in combination with the 2-λ method for determining n and d of the respective layers. Starting from a 1-layer analysis and using the AFM measurement results as starting values for the roughness layer thickness as starting values for the iteration a sequence of models is built to successively refine and confirm the results for refractive index (density) and film thickness in top- and bottom layer of the thin film. A step-by step description for this modeling procedure is shown in **Figure 3**. Finally, equations 9 to 12 are used to calculate the final results.

$$\rho_{RL}^{AFM} = \frac{mf^{AFM}\ [\%]}{100} \cdot \rho_m^t \tag{9}$$

$$RTL^{SPR} = \frac{d_t \cdot 100}{cellulose\ content\ [\%]} \tag{10}$$

$$\rho_{RL}^{SPR} = \frac{mf^{SPR}\ [\%]}{100} \cdot \rho_m^t \tag{11}$$

$$mf^{SPR} = \frac{d_t \cdot 100}{RLT^{AFM}}. \tag{12}$$

Here $\rho_{RL}^{AFM/SPR}$ is the density of the roughness layer and $mf^{AFM/SPR}$ is the material fraction calculated from AFM or MP-SPR data. RLT is the roughness layer thickness, d_t is the thickness of the top layer and ρ_m^t is the density of the top layer from MP-SPR multilayer evaluation.

The nine steps of the 2-layer analysis as shown in **Figure 3** are described below. Notation is explained in the caption of **Figure 3**. For a detailed example over all 9 steps of the analysis of a cellulose thin film, see **Table S1**.

STEP 1: Starting point is a 1-layer analysis of the entire film according to the 2-λ method. The result is thickness d^{SPR} and density ρ^{SPR} (refractive index n^{SPR}, respectively) for the entire cellulose film.

STEP 2: The film is split into two layers –the top and bottom layer- denoted as d_t^0 and d_b^0. Whereas, the starting d_t^0 values for evaluation are derived from AFM data with $d_t^0 = RLT^{AFM}/2$. Starting d_b^0 value is set to d^{SPR}—d_t^0. The refractive index of the entire cellulose thin film n^{SPR} is chosen as starting refractive index value for both, top (n_t^0) and bottom layer (n_b^0).

STEP 3: Iteration for the corresponding refractive indices; Result: refractive indices n_t^0 and n_b^0.

STEP 4: Evaluation of the bottom layer by 2-λ method yielding d_b^1 and n_b^1, while keeping the values for the top layer (d_t^0, n_t^0) constant.

STEP 5: The roughness layer thickness obtained from AFM imaging (RLT^{AFM}) is implemented into the model as new thickness value for the top layer (d_t^1).

STEP 6 and 7: The corresponding refractive index (n_t^1) is iterated in the simulation program and d_t^2 and n_t^2 of the top layer is evaluated by the 2-λ method, while the bottom layer values (d_b^1, n_b^1) are kept constant.

STEP 8: Evaluation of the bottom layer by the 2-λ method while keeping the new values for the top layer (d_t^2, n_t^2) constant, in order to validate the simulations.

STEP 9: To calculate the roughness layer's thickness (RLT), the density ($\rho_{RL}^{SPR/AFM}$) and the material fraction ($mf^{SPR/AFM}$) data from AFM and SPR as iterated above are calculated using Equations (9–12).

EXPERIMENTAL

Materials

Trimethylsilyl cellulose (TMSC, DS_{Si} = 2.8, Avicel, M_w = 185.000 g·mol^{-1}, M_n = 30.400 g·mol^{-1}, PDI = 6.1 determined by SEC in chloroform) was purchased from TITK (Rudolfstadt, Germany). Chloroform ($CHCl_3$, 99.3%), hydrochloric acid (HCl, 37 %), hydrogen peroxide (H_2O_2, 30% in water) and sulfuric acid (H_2SO_4, 95%) were purchased from Sigma Aldrich and used as received. MilliQ water (resistivity = 18 MΩ·cm) from a Millipore water purification system (Millipore, USA) was used for all experiments. A total of three films was measured with SPR and AFM and the 2-layer analysis was performed.

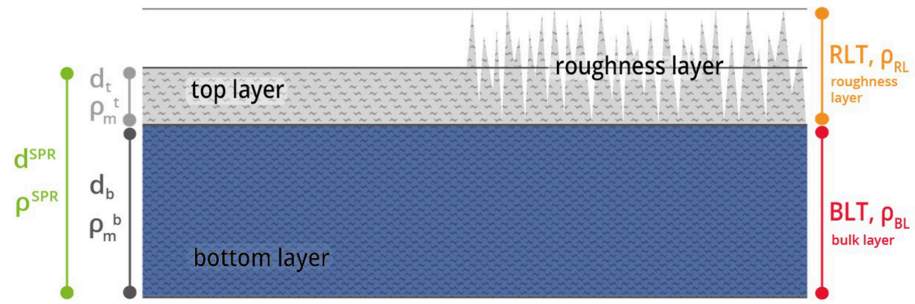

FIGURE 1 | Graphic description of the multilayer analysis model. The film consist of a roughness layer *RL* (gray) and a bulk layer *BL* (blue) with certain thickness *d* and density ρ. The thickness d^{SPR} and density ρ^{SPR} of the entire film are obtained via MP-SPR spectroscopy. The film is then split into a top layer (d_t, ρ_m^t) and a bottom layer (*BL*, d_b, ρ_m^b).

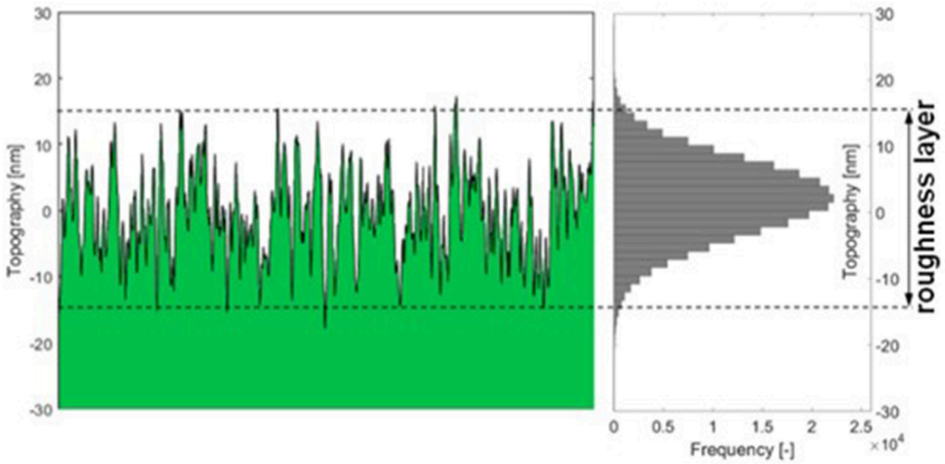

FIGURE 2 | Graphic description of AFM data evaluation: the thickness of the roughness layer (*RLT*) comprises 95% of the topography range measured with the AFM. The material fraction mf_{RL}^{AFM} is the percentage of material (green) within the roughness layer.

Substrate Cleaning and Film Preparation

SPR sensor slides—glass sensors with chromium adhesion layer (∼5 nm) and gold coating (∼50 nm) (CEN102Au)—were obtained from Cenibra, (Bramsche, Germany). In order to remove adventitious carbon, SPR sensors were cleaned before use by treatment with piranha solution (freshly prepared from sulfuric acid and hydrogen peroxide in a 3:1 (v/v) ratio) over a period of 10 min. Afterwards the SPR slides were extensively rinsed with MilliQ water and dried in a stream of nitrogen. The silicon wafer substrates (native oxide layer, 1.4 × 1.4 cm²) for the XRR measurements were cleaned with "piranha" acid [H_2SO_4:H_2O_2 = 7:3 (v/v)] for 30 min and neutralized afterwards with distilled water.

Cellulose thin films were prepared by spin coating trimethylsilyl cellulose (0.75 wt% in $CHCl_3$) onto the gold slides. One hundred microliters of TMSC-solution were deposited on the substrate and then rotated for 60 s at a spinning speed of 4,000 rpm and an acceleration of 2,500 rpm·s^{-1}. TMSC was converted to cellulose by treatment with hydrochloric acid (HCl) vapor. The TMSC films were placed into a petri dish (diameter 5 cm) containing 3 ml of 10% HCl. The dish was covered with its cap and the films were exposed to the HCl vapors for 15 min. The regeneration was verified by water contact angle and ATR-IR measurements as reported elsewhere (Kontturi et al., 2003; Woods et al., 2011; Mohan et al., 2012a,b).

Multi-Parameter Surface Plasmon Resonance (MP-SPR) Spectroscopy

Two-wavelength MP-SPR spectroscopy experiments were performed with an MP-SPR Navi^{TM} 210A Vasa instrument (by BioNavis Ltd., Tampere, Finland) equipped with two light source pairs providing 670 and 785 nm in each of the two measurement channels. All measurements were performed using a full angular scan (39−78°, scan speed: 8°·s^{-1}) in three parallels. SPR data was processed with BioNavis Dataviewer software. The full angular scans were simulated with the optical fitting software Winspall 3.01 (which is freely available from the Max-Planck Institute for Polymer Research (Mainz, Germany), http://www2.mpip-mainz.mpg.de/groups/knoll/software, 12.6.2013). The multilayer fitting approach is based on the Fresnel equations and the recursion formalism. The SPR signal of the pure sensor surface was simulated first in order to obtain the background

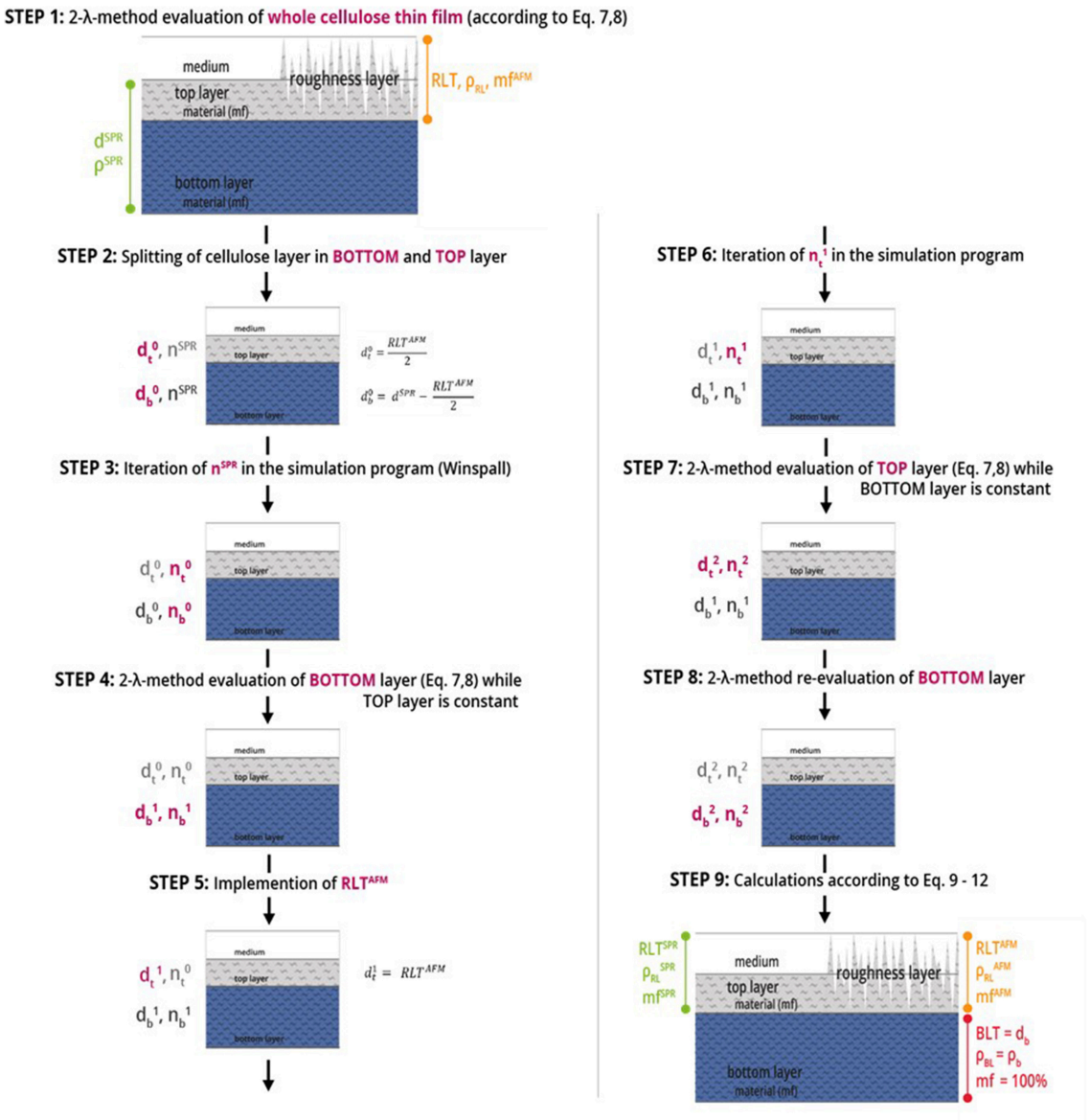

FIGURE 3 | Steps of multilayer analysis of cellulose thin films performed by means of MP-SPR spectroscopy, where *d* refers to the thickness [nm], *n* is the refractive index, *RL* is the roughness layer, *RLT* is the roughness layer thickness, *mf* is the material fraction [%], *BL* is the bulk layer, *BLT* is the bulk layer thickness and ρ is the density [g·cm^{-3}]. The indices *t*, *b* (subscript), *AFM* and *SPR* (superscript) stand for top layer and bottom layer. The number of iteration is given in the superscript, e.g., for thickness *d* as d^0, d^1, *and* d^2. Red text refers to the values changed in the respective evaluation step.

for the subsequent evaluation of the cellulose thin film. The two wavelengths cross point analyses were performed both using Microsoft Office Excel 2010 and Origin 8.6.

Atomic Force Microscopy (AFM)

AFM imaging was performed in atomic force microscopy tapping mode with a Veeco multimode scanning probe microscope (Bruker, USA). The images were scanned using silicon cantilevers (NCH-VS1-W, Nanoworld, Switzerland) with a resonance frequency of 320 kHz and a force constant of 42 N·m^{-1}. All images were processed using Nanoscope software package (V7.30r1sr3, Veeco).

The roughness layer thickness RLT^{AFM} is evaluated from the topography images measured by AFM, compare **Figure 2**. The roughness layer is the region of the cellulose film where both, material and ambient medium (water or air) are found, i.e., the region containing the boundary between cellulose film and surrounding. The thickness of this region depends on the roughness of the film. We have defined the roughness layer as the z-directional layer containing 95% of the surface roughness. For calculation, the histogram of the topography distribution is evaluated. From each edge of the histogram, 2.5% of the topography values are clipped off, the topography range comprising the remaining

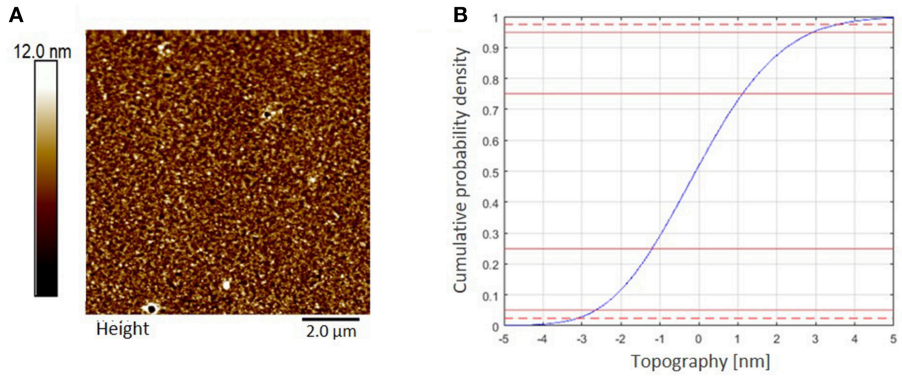

FIGURE 4 | (A) AFM topography image (10 × 10 μm^2) of a cellulose thin film spin coated from $CHCl_3$ measured in air at ambient conditions, z-scale 30 nm. RMS roughness (R_q) is 1.7 nm. **(B)** AFM topography evaluation. Roughness layer thickness RLT^{AFM} = 6.4 nm, 95% of the topography range are indicated by the dashed red lines in the cumulative topography distribution.

95% of height values is defined as the roughness layer thickness. We are not using 100% of the values because the topography distribution is close to normally distributed which means there are always some far outliers which would bloat the roughness layer beyond the true surface interaction range.

X-Ray Reflectivity XRR

X-ray reflectivity measurements were performed using a PANalytical Empyrean goniometer system with radiation produced by a copper sealed tube (λ = 0.154178 nm). The primary side of the reflectometer was equipped with a 20 mm beam mask, a multilayer mirror, a 1/32° slit, and an automatic beam attenuator. On the secondary side, a receiving slit of 0.1 mm and a Soller slit of 0.02 rad were used in front the PANalytical PIXEL3D point detector. The sample stage was a domed DHS 900 from Anton Paar (Resel et al., 2003), equipped with a SHT15 humidity sensor to monitor the relative humidity and the temperature during the measurements. The relative humidity (RH) was controlled using a S-503 humidity generator from Michell instruments. For each humidity step an equilibration time of 30 min was accomplished. XRR measurements were performed in the 2θ region 0.030–9.999° with a step size of 0.006°. The evaluation of the data was performed with the X'Pert Reflectivity (Panalytical, $C_6H_{10}O_5$ for cellulose was used) software package providing information on the electron density, layer thickness, and the roughness of the films by applying (Parratt, 1954) formalism and the disturbance term of Nevot–Croce(Nevot and Croce, 1980). A three layer model was required to fit the experimental data of the cellulose film (50% relative humidity, same as in laboratory where the SPR spectrometer is located), resulting in a very thin layer at the Si-cellulose interface (d = 0.6 nm, ρ = 0.8 g cm^{-3}), a bulk layer (d = 43.9 nm, ρ = 1.39 g cm^{-3}) and a surface layer (d = 4.2 nm, ρ = 1.09 g cm^{-3}). Total film thickness was 48.7 nm, with a density of 1.41 g cm^{-3} at 50% relative humidity. For the sake of comparison, data obtained at other humidity levels (0, 25, and 70% was acquired. The difference in layer thickness compared to the gold substrate stems from the different wettability of the silicon wafer (which is required for XRR) leading to higher thicknesses.

RESULTS AND DISCUSSION

Characterization and Preparation of Cellulose Thin Films

Cellulose thin films were prepared by spin coating of trimethylsilyl cellulose (TMSC), dissolved in chloroform ($CHCl_3$), and subsequent conversion to cellulose by a regeneration step completed with HCl vapors, cleaving off the silyl-groups by formation of TMSCl (Kontturi et al., 2003; Kontturi and Lankinen, 2010). The completed conversion to cellulose was proven by ATR-IR spectroscopy, proving the disappearance of bands related to the TMS group (υ_{SiC}, δ_{SiOC} at 1,250 and 852 cm^{-1}) while the typical OH stretching vibrations (υ_{OH}) for cellulose at 3,200–3,600 cm^{-1} appeared (Ehmann et al., 2015). The AFM images display smooth, homogeneous surface topography (**Figure 4**). Evaluation of thickness from AFM-imaging results in a *RLT* (roughness layer thickness) of 6.4 nm and a cellulose material fraction (mf^{AFM}) of 47.9 % in that film.

2-Layer Analysis of Thickness and Density in Thin Films

Thickness and refractive indices of three individual cellulose thin films were first determined for the entire film using the 2-λ method (**Figure 5**) as described above. In principle, cellulose thin films can be prepared with high reproducibility and only slight variations in film thickness. For example, the thickness evaluation of three thin films applying the 2-λ method led to just minor deviations (d^{SPR} of 36.4 ± 0.5 nm). The refractive indices at 785 and 670 nm are 1.408 ± 0.028 and 1.410 ± 0.024, respectively, which can be used to determine the cellulose content a in the whole film (Equation 7, 88.8 ± 0.1%). Based on that result, the film was subjected to multilayer density analysis as outlined in the previous sections (**Figure 3**). The first result was that the

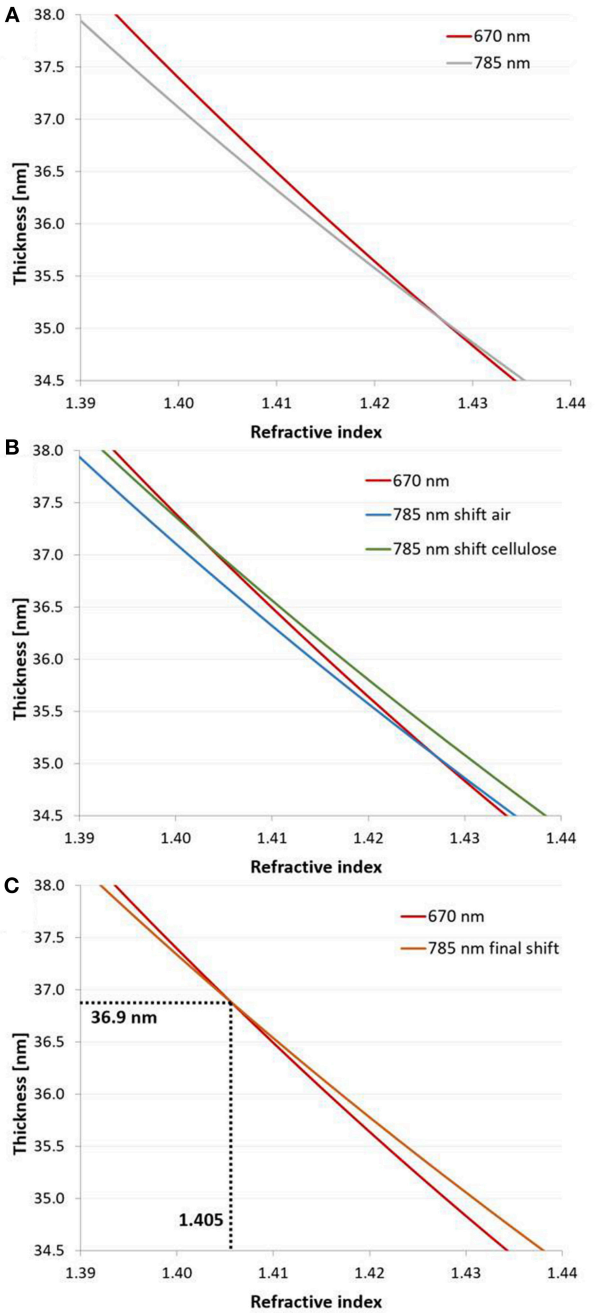

FIGURE 5 | 2-λ method: **(A)** Continuous solutions ($n - d$ curves) obtained at 670 and 785 nm at the example of a dry cellulose thin film (film 1 in **Table S3**) spin coated from $CHCl_3$. **(B)** The curve measured at 785 nm was shifted by the $dn/d\lambda$ of air ($-0.00000856\ \mu m^{-1}$) and cellulose ($-0.0271\ \mu m^{-1}$) in order to determine the composition of the film. The new $dn/d\lambda$ value for the film consisting of air and cellulose was re-estimated from the composition (average of refractive indices at both intersection points) with equations 7–8. **(C)** The $n - d$ curve recorded at 785 nm was shifted by the resulting $dn/d\lambda$ to obtain the unique solution ($d = 36.9$ nm, $n = 1.406$, $a = 89$ % cellulose) for the investigated thin film.

refractive indices of the top and bottom layer did not yield the same result. We found much smaller values for the top layer

TABLE 1 | Comparison of results determined by MP-SPR spectroscopy (see **Table S3**), AFM and XRR of cellulose thin films measured in air (average from three films).

	AFM	MP-SPR	XRR
d_b[nm]	–	33.7 ± 0.7	43.9 ± 0.3
ρ_m^b [g·cm^{-3}]	–	1.39 ± 0.04	1.39 ± 0.10
d_t [nm]	–	2.8 ± 0.2	4.2 ± 0.1
ρ_m^t [g·cm^{-3}]	–	0.76 ± 0.10	1.05 ± 0.10
RLT [nm]	6.4 ± 0.2	5.5 ± 1.4	–
ρ_{RL} [g·cm^{-3}]	0.37 ± 0.06	0.33 ± 0.07	–
mf [%]	48 ± 2	43 ± 7	–

RLT^{SPR}, mf^{SPR} and $\rho_{RL}^{SPR/AFM}$ were calculated according to Equations (9-−12). Note that for XRR, films featured a different thickness due to the use of a different substrate and the values that have been given in the table were obtained at 50% relative humidity.

($n_t = 1.237 \pm 0.034$ at 670 nm; 1.242 ± 0.030 at 785 nm) than for the bottom layer ($n_b = 1.421 \pm 0.012$ for 670 and 1.420 ± 0.011 for 785 nm). As a consequence, the cellulose content in the bottom layer ($a_b^{SPR} = 91.8 \pm 0.1$ %) is much larger than in the top layer ($a_t^{SPR} = 52.2 \pm 0.1$ %). The thickness of the entire films and the sum of the top and bottom layer thicknesses obtained by our multilayer analysis are consistent (one layer analysis: $d^{SPR} = 36.4 \pm 0.5$ vs. two layer analysis 36.5 ± 0.6 nm (bottom $d_b = 33.7 \pm 0.7$ and top layer $d_t = 2.8 \pm 0.2$ nm). Further, the density of the whole film ($\rho^{SPR} = 1.34 \pm 0.09$ g·cm^{-3}) is very well-represented by the individual densities of the top and bottom layers (bottom $\rho_m^b = 1.39 \pm 0.04$ g·cm^{-3} and top $\rho_m^t = 0.76 \pm 0.10$ g·cm^{-3}). The results from the multilayer density analysis using data obtained from AFM and MP-SPR spectroscopy experiments are depicted in **Table 1.** Evaluation results of the three cellulose thins films are shown in **Table S2**. Further, each individual thin film is evaluated in a multiple manner and compared to the other films, in order to demonstrate stability of the fitting approach and indicate deviations (see **Table S3**).

Comparison of AFM, SPR, and XRR Data

The resulting data from AFM, MP-SPR spectroscopy, and XRR was compared to validate the employed strategy for multilayer analysis. The material fraction (*mf*, composed of cellulose and air) and *RLT* were acquired by AFM. The cellulose content, i.e., the density of the material (ρ_m^t), and the thickness of the layer consisting of material, i.e., the top layer (d_t), were obtained from MP-SPR spectroscopy. For each technique, values which correspond to the same parameter determined by the other technique (ρ_{RL}^{AFM}, ρ_{RL}^{SPR}, RLT^{SPR}, and mf^{SPR}) were calculated from the measured results (mf^{AFM}, RLT^{AFM}, d_t and ρ_m^t), according to Equations (9–12). The outcome of these calculations is summarized in **Table 1**. While there are some minor deviations, the results are very consistent for AFM and 2-layer MP-SPR approach. The deviations can to some extent be attributed to the different measurement areas of the applied techniques and small variations in the cellulose thin films. For instance, AFM covers an area of $10 \times 10\ \mu m^2$, whereas the area of the MP-SPR spectroscopy lasers ($\varnothing = 0.6$ mm) is ~0.28 mm^2.

X-Ray reflectivity was employed to further validate the approach. However, the results are not directly comparable in terms of absolute layer thicknesses since gold substrates (used in SPR spectroscopy) cannot be used for that technique. Instead, films have been deposited on silicon wafers which have a different surface free energy, leading to different cellulose film thickness. Further, the film thickness is a function of humidity level; by increasing humidity levels, layer thickness increases (from 0 to 70% r.h. thickness increase by 14%, see **Table S4**, for full data and **Figure 6A** for the XRR curves including fitting). At the same humidity levels as in the labs where the AFM and the SPR spectrometer are located (50% r.h.), we observed a surface layer with reduced density (thickness: 4.2 nm, ρ: 1.05 g·cm^{-3}) as well as a bulk layer with a higher density (thickness: 43.9 nm, ρ: 1.39 g cm^{-3}). The share of the top layer on the overall layer thickness is 7.7 and 9.1% for cellulose thin films on gold and silicon wafers, respectively. Given the different experimental setup and the difference in the substrates, the XRR data is in excellent agreement with the multilayer density approach using AFM/SPR. The densities of the prepared films are in the range of molecular dynamics simulations on amorphous cellulose (1.34–1.39 g cm^{-3}) (Mazeau and Heux, 2003; Chen et al., 2004) but significantly lower than those of reported bulk amorphous substrates (1.48 g cm^{-3}) (Mark, 1982). It should be noted that XRR revealed a thin layer (0.6 nm) at the cellulose-Si interface with rather low density (0.8 g cm^{-3}). This is a known phenomenon for many polymer films but could not be revealed by SPR spectroscopy. The density profile of the layered system obtained by XRR is depicted in **Figure 6B**.

In summary both, MP-SPR and XRR yield a similar layer structure of the cellulose films, with a lower material density in a few nanometers thick top layer of the film and a higher density in the bulk of the film.

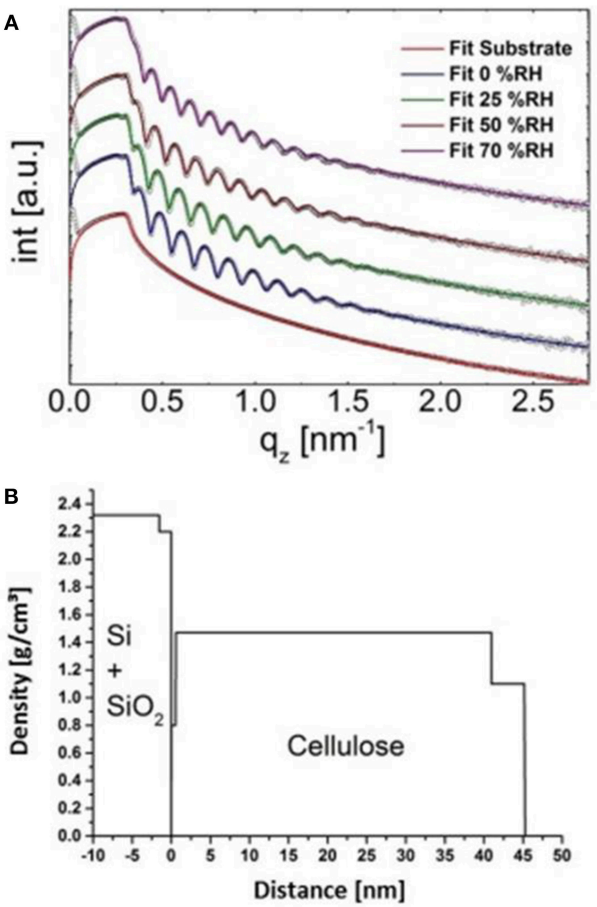

FIGURE 6 | Fits of the XRR curves of the cellulose thin film at different humidity levels **(A)** and concomitant density profile through the layer (at 0% humidity, **B**).

Potential and Limitations of the Method

Finally, the limitations and requirements of the multilayer density analysis approach need to be elucidated. The crucial point in the presented multilayer approach is to have appropriate starting values for the thickness of the bottom and the top layer (d_t^0 and d_b^0) for the data analysis in order to obtain physically meaningful results. Unique solutions for given *RLT/2* values were only obtained when the starting values for the thickness were in between d^{SPR} and the value obtained by iteration of the simulation program (d_t^0). A randomly chosen starting value for the *RLT* does not lead to a result corresponding to the real *RLT* of the thin film. Furthermore, some randomly chosen starting values of the *RLT* did not even yield intersection points of the *n* - *d* curves. However, by using AFM data providing starting values for *RLT*, physically meaningful results can be obtained, which was confirmed by XRR. The importance of implementing AFM data as starting values for the fitting process is shown in more detail in **Table S1**. Comparability of fitting results and deviations within multiple evaluations of the individual thin films is described in **Table S3** (**Supplementary Material**). The main advantage of SPR is that it can be used with a wide range of liquids while by XRR this is a rather challenging task. The multilayer analysis of thin films to explore swelling processes in different liquids is a potentially powerful application and will be applied in future reports.

CONCLUSION

We demonstrated a multilayer density analysis of thin films at the example of cellulose in air. We showed that the combination of AFM and SPR data allows for analyzing the density variation and thickness in surface near regions of cellulose thin films. The key finding, a layer with reduced density and a thickness of a few nanometers at the top of the cellulose film, was confirmed by XRR measurements on similar films. We believe that this approach has the potential to reveal the density in multilayer structures of a wide range of materials (biopolymer films, porous thin films), e.g., for density analysis in thin film structures or for water uptake during swelling of cellulose with different types of liquids. Still, the approach features some limitations and further improvements need to be accomplished. A major shortcoming is that the starting values used for the splitting of the layer are very important to get meaningful results in the fitting procedure, i.e., an educated guess is required, which was provided by AFM in this

study. A further limitation is the used modeling software which seems to have minor problems with numerical stability (see **Tables S2, S3**), when inappropriate starting values were used. Further improvements of the approach in future studies will focus on more robustness toward the starting values used for the fitting procedures. A promising approach is to employ 4- or 6- different wavelengths in MP-SPR measurements and to use this additional information together with adequate modeling software for an improved multilayer analysis of thin films.

AUTHOR CONTRIBUTIONS

All authors listed have made a substantial, direct and intellectual contribution to the work, and approved it for publication.

FUNDING

Federal Ministry of Economy, Family and Youth and the National Foundation for Research, Technology and Development, Austria.

ACKNOWLEDGMENTS

The financial support of the Federal Ministry of Economy, Family and Youth and the National Foundation for Research, Technology and Development, Austria, is gratefully acknowledged. We also thank the industrial partners Mondi, Océ, Kelheim, and SIG Combibloc for their support. Martin Steer, Jakob Häglsperger, and Johannes Rögner are gratefully acknowledged for providing inspiration for this work.

SUPPLEMENTARY MATERIAL

The Supplementary Material for this article can be found online at: https://www.frontiersin.org/articles/10.3389/fchem.2019.00251/full#supplementary-material

Supplementary Material | Supporting information is available including AFM topography evaluation, background MP-SPR curves,additional simulation experiments for multilayer analysis, results of multilayer analysis and comparison of multiple evaluations.

REFERENCES

Binnig, G., Quate, C. F., and Gerber, C. (1986). Atomic force microscope. *Phys. Rev. Lett.* 56, 930–933. doi: 10.1103/PhysRevLett.56.930

Chen, W., Lickfield, G. C., and Yang, C. Q. (2004). Molecular modeling of cellulose in amorphous state. Part I: model building and plastic deformation study. *Polymer* 45, 1063–1071. doi: 10.1016/j.polymer.2003.11.020

Ciddor, P. E. (1996). Refractive index of air: new equations for the visible and near infrared. *Appl. Opt.* 35, 1566–1573. doi: 10.1364/AO.35.001566

Ehmann, H. M. A., Werzer, O., Pachmajer, S., Mohan, T., Amenitsch, H., Resel, R., et al. (2015). Surface-sensitive approach to interpreting supramolecular rearrangements in cellulose by synchrotron grazing incidence small-angle x-ray scattering. *ACS Macro Lett.* 4, 713–716. doi: 10.1021/acsmacrolett.5b00306

Geddes, N. J., Martin, A. S., Caruso, F., Urquhart, R. S., Furlong, D. N., Sambles, J. R., et al. (1994). Immobilisation of IgG onto gold surfaces and its interaction with anti-IgG studied by surface plasmon resonance. *J. Immunol. Methods* 175, 149–160. doi: 10.1016/0022-1759(94)90358-1

Giessibl, F. J. (2003). Advances in atomic force microscopy. *Rev. Modern Phys.* 75, 949–983. doi: 10.1103/RevModPhys.75.949

Jalili, N., and Laxminarayana, K. (2004). A review of atomic force microscopy imaging systems: application to molecular metrology and biological sciences. *Mechatronics* 14, 907–945. doi: 10.1016/j.mechatronics.2004.04.005

Kasarova, S. N., Sultanova, N. G., Ivanov, C. D., and Nikolov, I. D. (2007). Analysis of the dispersion of optical plastic materials. *Opt. Mater.* 29, 1481–1490. doi: 10.1016/j.optmat.2006.07.010

Kontturi, E., and Lankinen, A. (2010). Following the kinetics of a chemical reaction in ultrathin supported polymer films by reliable mass density determination with x-ray reflectivity. *J. Am. Chem. Soc.* 132, 3678–3679. doi: 10.1021/ja100669w

Kontturi, E., Thüne, P. C., and Niemantsverdriet, J. W. (2003). Cellulose model surfaces simplified preparation by spin coating and characterization by x-ray photoelectron spectroscopy, infrared spectroscopy, and atomic force microscopy. *Langmuir* 19, 5735–5741. doi: 10.1021/la0340394

Kontturi, K. S., Kontturi, E., and Laine, J. (2013). Specific water uptake of thin films from nanofibrillar cellulose. *J. Mater. Chem. A* 1, 13655–13663. doi: 10.1039/c3ta12998e

Liang, H., Miranto, H., Granqvist, N., Sadowski, J. W., Viitala, T., Wang, B., et al. (2010). Surface plasmon resonance instrument as a refractometer for liquids and ultrathin films. *Sens. Actuat. B* 149, 212–220. doi: 10.1016/j.snb.2010.05.048

Mark, H. (1982). Encyclopedia of *Polymer Science* and *Technology-Plastics*, *Resins*, *Rubbers*, *Fibers*. New York, NY: Wiley.

Mazeau, K., and Heux, L. (2003). Molecular dynamics simulations of bulk native crystalline and amorphous structures of cellulose. *J. Phys. Chem. B* 107, 2394–2403. doi: 10.1021/jp0219395

Mohan, T., Niegelhell, K., Nagaraj, C., Reishofer, D., Spirk, S., Olschewski, A., et al. (2017). Interaction of tissue engineering substrates with serum proteins and its influence on human primary endothelial cells. *Biomacromolecules* 18, 413–421. doi: 10.1021/acs.biomac.6b01504

Mohan, T., Spirk, S., Kargl, R., Doliška, A., Ehmann, H. M. A., Köstler, S., et al. (2012a). Watching cellulose grow – kinetic investigations on cellulose thin film formation at the gas–solid interface using a quartz crystal microbalance with dissipation (QCM-D). *Colloids Surfaces A* 400, 67–72. doi: 10.1016/j.colsurfa.2012.02.053

Mohan, T., Spirk, S., Kargl, R., Doliska, A., Vesel, A., Salzmann, I., et al. (2012b). Exploring the rearrangement of amorphous cellulose model thin films upon heat treatment. *Soft Matter* 8, 9807–9815. doi: 10.1039/C2SM25911G

Nevot, L., and Croce, P. (1980). Characterization of surfaces by grazing X-Ray reflection - application to study of polishing of some silicate-glasses. *Revue Physi. Appli.* 15, 761–779.

Niegelhell, K., Chemelli, A., Hobisch, J., Griesser, T., Reiter, H., Hirn, U., et al. (2018). Interaction of industrially relevant cationic starches with cellulose. *Carbohydr. Polym.* 179, 290–296. doi: 10.1016/j.carbpol.2017.10.003

Niegelhell, K., Süßenbacher, M., Jammernegg, K., Ganner, T., Schwendenwein, D., Schwab, H., et al. (2016). Enzymes as biodevelopers for nano- and micropatterned bicomponent biopolymer thin films. *Biomacromolecules* 17, 3743–3749. doi: 10.1021/acs.biomac.6b01263

Niegelhell, K., Süßenbacher, M., Sattelkow, J., Plank, H., Wang, Y., Zhang, K., et al. (2017). How bound and free fatty acids in cellulose films impact nonspecific protein adsorption. *Biomacromolecules* 18, 4224–4231. doi: 10.1021/acs.biomac.7b01260

Orelma, H., Filpponen, I., Johansson, L.-S., Laine, J., and Rojas, O. J. (2011). Modification of cellulose films by adsorption of CMC and chitosan for controlled attachment of biomolecules. *Biomacromolecules* 12, 4311–4318. doi: 10.1021/bm201236a

Orelma, H., Teerinen, T., Johansson, L.-S., Holappa, S., and Laine, J. (2012). CMC-modified cellulose biointerface for antibody conjugation. *Biomacromolecules* 13, 1051–1058. doi: 10.1021/bm201771m

Parratt, L. G. (1954). Surface Studies of Solids by Total Reflection of X-Rays. *Phys. Rev.* 95, 359–369. doi: 10.1103/PhysRev.95.359

Peterlinz, K. A., and Georgiadis, R. (1996). Two-color approach for determination of thickness and dielectric constant of thin films using

surface plasmon resonance spectroscopy. *Opt. Commun.* 130, 260–266. doi: 10.1016/0030-4018(96)00238-6

Raether, H. (1977). Surface plasma oscillations and their applications. *Phys. Thin Films* 9, 145–261.

Resel, R., Tamas, E., Sonderegger, B., Hofbauer, P., and Keckes, J. (2003). A heating stage up to 1173 K for X-ray diffraction studies in the whole orientation space. *J. Appl. Cryst.* 36, 80–85. doi: 10.1107/S0021889802019568

Ritchie, R. H. (1957). Plasma losses by fast electrons in thin films. *Phys. Rev.* 106, 874–881. doi: 10.1103/PhysRev.106.874

Strasser, S., Niegelhell, K., Kaschowitz, M., Markus, S., Kargl, R., Stana-Kleinschek, K., et al. (2016). Exploring nonspecific protein adsorption on lignocellulosic amphiphilic bicomponent films. *Biomacromolecules* 17, 1083–1092. doi: 10.1021/acs.biomac.5b01700

Vickerman, J. C., and Gilmore, I. (2009). *Surface Analysis - The Principle Techniques.* New York, NY: Wiley.

Weißl, M., Niegelhell, K., Reishofer, D., Zankel, A., Innerlohinger, J., and Spirk, S. (2018). Homogeneous cellulose thin films by regeneration of cellulose xanthate: properties and characterization. *Cellulose* 25, 711–721. doi: 10.1007/s10570-017-1576-3

Woods, D. A., Petkov, J., and Bain, C. D. (2011). Surfactant adsorption by total internal reflection raman spectroscopy. Part III: adsorption onto cellulose. *Colloids Surf. A* 391, 10–18. doi: 10.1016/j.colsurfa.2011.07.027

Zaera, F. (2011). Surface chemistry at the liquid/solid interface. *Surf. Sci.* 605, 1141–1145. doi: 10.1016/j.susc.2011.04.021

Conflict of Interest Statement: The authors declare that the research was conducted in the absence of any commercial or financial relationships that could be construed as a potential conflict of interest.

frontiers in Chemistry

ORIGINAL RESEARCH
published: 03 May 2019
doi: 10.3389/fchem.2019.00239

Design of Friction, Morphology, Wetting, and Protein Affinity by Cellulose Blend Thin Film Composition

Caterina Czibula[1,2†], Gundula Teichert[3†], Maximilian Nau[4], Mathias Hobisch[3], Chonnipa Palasingh[5], Markus Biesalski[4], Stefan Spirk[2,3], Christian Teichert[1,2] and Tiina Nypelö[5,6*]*

[1] Institute of Physics, Montanuniversität Leoben, Leoben, Austria, [2] Christian Doppler Laboratory for Fiber Swelling and Paper Performance, Graz University of Technology, Graz, Austria, [3] Institute of Paper, Pulp and Fiber Technology, Graz University of Technology, Graz, Austria, [4] Macromolecular Chemistry and Paper Chemistry, Technical University Darmstadt, Darmstadt, Germany, [5] Division of Applied Chemistry, Department of Chemistry and Chemical Engineering, Chalmers University of Technology, Gothenburg, Sweden, [6] Wallenberg Wood Science Center, Gothenburg, Sweden

OPEN ACCESS

Edited by:
Giuseppe Mensitieri,
University of Naples Federico II, Italy

Reviewed by:
Artur J. M. Valente,
University of Coimbra, Portugal
Ram Gupta,
Pittsburg State University,
United States

***Correspondence:**
Christian Teichert
christian.teichert@unileoben.ac.at
Tiina Nypelö
tiina.nypelo@chalmers.se

[†]These authors have contributed equally to this work

Specialty section:
This article was submitted to Polymer Chemistry, a section of the journal Frontiers in Chemistry

Received: 28 January 2019
Accepted: 26 March 2019
Published: 03 May 2019

Citation:
Czibula C, Teichert G, Nau M, Hobisch M, Palasingh C, Biesalski M, Spirk S, Teichert C and Nypelö T (2019) Design of Friction, Morphology, Wetting, and Protein Affinity by Cellulose Blend Thin Film Composition. Front. Chem. 7:239. doi: 10.3389/fchem.2019.00239

Cellulose derivate phase separation in thin films was applied to generate patterned films with distinct surface morphology. Patterned polymer thin films are utilized in electronics, optics, and biotechnology but films based on bio-polymers are scarce. Film formation, roughness, wetting, and patterning are often investigated when it comes to characterization of the films. Frictional properties, on the other hand, have not been studied extensively. We extend the fundamental understanding of spin coated complex cellulose blend films via revealing their surface friction using Friction Force Microscopy (FFM). Two cellulose derivatives were transformed into two-phase blend films with one phase comprising trimethyl silyl cellulose (TMSC) regenerated to cellulose with hydroxyl groups exposed to the film surface. Adjusting the volume fraction of the spin coating solution resulted in variation of the surface fraction with the other, hydroxypropylcellulose stearate (HPCE) phase. The film morphology confirmed lateral and vertical separation and was translated into effective surface fraction. Phase separation as well as regeneration contributed to the surface morphology resulting in roughness variation of the blend films from 1.1 to 19.8 nm depending on the film composition. Friction analysis was successfully established, and then revealed that the friction coefficient of the films could be tuned and the blend films exhibited lowered friction force coefficient compared to the single-component films. Protein affinity of the films was investigated with bovine serum albumin (BSA) and depended mainly on the surface free energy (SFE) while no direct correlation with roughness or friction was found. BSA adsorption on film formed with 1:1 spinning solution volume ratio was an outlier and exhibited unexpected minimum in adsorption.

Keywords: blend films, spinodal decomposition, cellulose, friction, protein adsorption, adhesion

INTRODUCTION

Spinodal decomposition of polymer blends can generate thin films with multi-phase surface composition, and often, complex morphology (Heriot and Jones, 2005). Lateral separation of the phases on a substrate results in patterns where islands of one phase reside within the other phase. Vertical separation can lead to heterogeneous distribution in the film's z-direction induced by surface energy differences of the components and can influence the surface morphology (Karim et al., 1998).

An intriguing area of research is the exploration of blend thin films obtained with spin coating. During the spin coating step, macroscopically homogeneous solutions of two polymers phase separate into the domains (Dalnoki-Veress et al., 1997). The ratio of the two polymers, molecular weight, solvent and spin coating conditions define the feature sizes and shapes (Xue et al., 2012). Synthetic polymer phase separation is exploited in coatings and organic electronics (Halls et al., 1995), while for biopolymer blend thin films their utilization and fundamentals, are still in their origins.

Cellulose synthetized by nature is notorious for insolubility having only few one-component solvents such as N-methylmorpholine-N-oxide (Medronho et al., 2012). In industrial fiber production, cellulose insolubility has been circumvented by derivatization followed by conversion to cellulose commonly referred to as regeneration. Similar approaches have been applied in thin film manufacturing involving derivatization, dissolution, film formation, and regeneration of the derivatized film to cellulose (Schaub et al., 1993; Kontturi et al., 2003a,b). Spin coating, and propagation of repeating submicron patterns, requires volatile and good solvents for the blend components. Trimethylsilyl cellulose (TMSC) dissolved in toluene or chloroform has been used for single-component cellulose films as well as for blend films (Kontturi et al., 2009, 2010; Nyfors et al., 2009; Niegelhell et al., 2016, 2017; Strasser et al., 2016). Regeneration takes place upon exposure to hydrochloric acid vapor (Schaub et al., 1993).

Cellulose in products is often an inert component intended to protect or seal, such as package products, or to carry functionalities as in paper-based diagnostics (Pelton, 2009). As a substrate it can be used to accommodate follow-up chemistries, for example, to bind peptides to further tune it for specific protein or antibody affinity and sensing of biological molecules (Orelma et al., 2012a,b; Zhang et al., 2013). In addition to detection, protein adsorption is a way to design medical materials or to control fouling of surfaces. The inhibition of protein deposition, on the other hand, is an asset when bacterial growth and biofilm formation are required to be blocked.

Biofilm formation on surfaces takes place in two phases where the first one includes reversible physical attachment of bacteria and the second irreversible, cellular phase. Surface roughness, wetting and surface configuration have been identified as key parameters for bacterial adhesion (An and Friedman, 1998). The effect of hydrophobicity is directly in connection with the properties of the bacteria while with respect to roughness there is direct evidence that increase in roughness—and hence, in the surface area—promotes bacterial adhesion. Roughness is different from surface configuration that refers to patterning on the surface. The periodicity and size of surface patterns has been found to be a parameter to inhibit bacterial adhesion. While bacteria preferentially adhere to irregularities that conform to their size since this maximizes bacteria-surface area (Katsikogianni and Missirlis, 2004), there is evidence that specific surface pattern design can prevent the attachment. A pattern mimicking a skin of shark was able to significantly reduce biofilm formation (Chung et al., 2007). The key parameters of the biofilm inhibiting films are non-random patterns with a hierarchy where the size is optimized to the size of a specific bacteria (Schumacher et al., 2007a,b). Here, we apply spinodal separation to generate periodical cellulose blend film hierarchies and evaluate the morphology and configuration and discuss their relation to antifouling surfaces.

Atomic force microscopy (AFM) is a non-destructive analytical tool applying low forces and is therefore suited for nanoscale characterization of soft polymer and biological surfaces. Apart from morphology studies, phase contrast in tapping mode imaging (Tamayo and Garcia, 1996), chemical contrast with functionalized AFM tips (Frisbie et al., 1994), and mechanical contrasts (Chyasnavichyus et al., 2015; Kocun et al., 2017) are established investigation routines. Phase and adhesion contrast measurements have been explored also on cellulosic films to achieve chemical contrast with functionalized probes (Ganser et al., 2016). Friction behavior of blend films can be studied on the nanoscale by friction force microscopy (FFM) (Mate et al., 1987; Marti et al., 1990; Meyer and Amer, 1990). In FFM, the AFM tip scans in contact mode normal to the cantilever's long axis, and the resulting cantilever torsion is related to the friction coefficient. Friction contrast for polymers by FFM has been demonstrated for phase-separated thin organic films (Overney et al., 1992, 1994) where differences in the friction signal between hydrocarbon and fluorocarbon containing domains were found. More recently, FFM was employed to correlate friction to viscoelastic relaxation (Hammerschmidt et al., 1996; Sondhauß et al., 2015) and to characterize photoreactive organic surface patterns of spin casted thin films (Hlawacek et al., 2009; Shen et al., 2014). Polyisoprene and polystyrene blend coatings were recently reported to show an unexpected tribological synergy (Emerson et al., 2017). By varying the composition of the blend films, it was possible to tune the tribological properties and achieve friction coefficients which are much lower than for the pure films.

A blend of TMSC (regenerable to cellulose) and hydroxypropylcellulose stearate (HPCE) resulted in micropatterned films with varying aliphatic surface concentration. HPCE, a cellulose derivative, exhibits long alkyl side chains which may act as brushes and in combination with cellulose impact, wetting, adhesion, and protein adsorption. The surface morphology, roughness and lateral correlation length, of the films was quantitatively studied using AFM. The friction behavior was analyzed by FFM and compared to the adhesive properties of the surfaces of the pure and blend films obtained from AFM force spectroscopy. Finally, the comprehensive information obtained by surface characterization was employed to determine the influence of adhesive and

tribological surface properties of the cellulose-HPCE blend films on bovine serum albumin (BSA) adsorption investigated by surface plasmon resonance spectroscopy (SPR) and Quartz Crystal Microbalance with Dissipation monitoring (QCM-D).

MATERIALS AND METHODS

Materials

Hydroxypropylcellulose stearate (HPCE, M_w 134,700 g mol^{-1}, M_n 107,400 g mol^{-1}, polydispersity index 1.25, degree of substitution (DS) 3.0) was synthesized according to a literature protocol (Nau et al., 2018). Trimethylsilyl cellulose (TMSC, From Avicel, M_w 185,000 g mol^{-1}, M_n 30,400 g mol^{-1}, polydispersity index 6.1, DS 2.8) was purchased from TITK (Thuringian Institute of Textile and Plastics Research, Germany). The structures are shown in **Figure 1**. Chloroform (99.3%), disodium phosphate heptahydrate ($Na_2HPO_4{\cdot}7H_2O$), sodium dihydrogen phosphate monohydrate ($NaH_2PO_4{\cdot}H_2O$), hydrochloric acid (37%), and bovine serum albumin (BSA) were purchased from Sigma-Aldrich and were used as received. Silicon wafers used as film substrates were cut 1 cm × 2 cm. Surface plasmon resonance (SPR) gold sensor slides (CEN102 AU) were purchased from Cenibra (Germany). Milli-Q water (resistivity = 18.2 Ω^{-1} cm^{-1} at 25°C) from a Millipore water purification system (Millipore, U.S.A.) was used for contact angle, SPR, and QCM-D investigations.

Substrate Cleaning and Film Preparation

The film substrates were cleaned by immersing them in an *in-situ* produced peroxymonosulfuric acid containing H_2O_2 (30 wt%)/ H_2SO_4 (1:3 v/v) for 10 min for SPR spectroscopy slides or 30 min for silicon wafers, respectively. After rinsing with deionized water, the wafers were dried with nitrogen gas, rinsed and stored in deionized water. TMSC and HPCE were dissolved in chloroform in a concentration of 0.75 wt%, using a water bath heated to 30°C, and 120 h on a magnetic stirrer. Right before use the solutions were filtered through 0.45 µm PVDF filters (Chromafil) and mixed in volumetric ratios labeled further on as TMSC:HPCE 1:0, 1:3, 1:1; 3:1, and 0:1. A volume of 100 µl was used for spin coating and operated for 60 s with an acceleration of 2,500 rpm s^{-1} and a speed of 4,000 rpm.

The conversion of TMSC into cellulose was implemented in a polystyrene petri dish (5 cm in diameter) containing 3 ml of 10 wt% HCl. The substrates were exposed to HCl vapor for 12 min. The regeneration of cellulose from TMSC was verified by contact angle and ATR-IR measurements (Alpha FT-IR spectrometer, Bruker, U.S.A.) using an attenuated total reflection attachment and obtaining spectra between 4,000 and 400 cm^{-1} with 48 scans and a resolution of 4 cm^{-1}. The data was analyzed with OPUS 4.0 software.

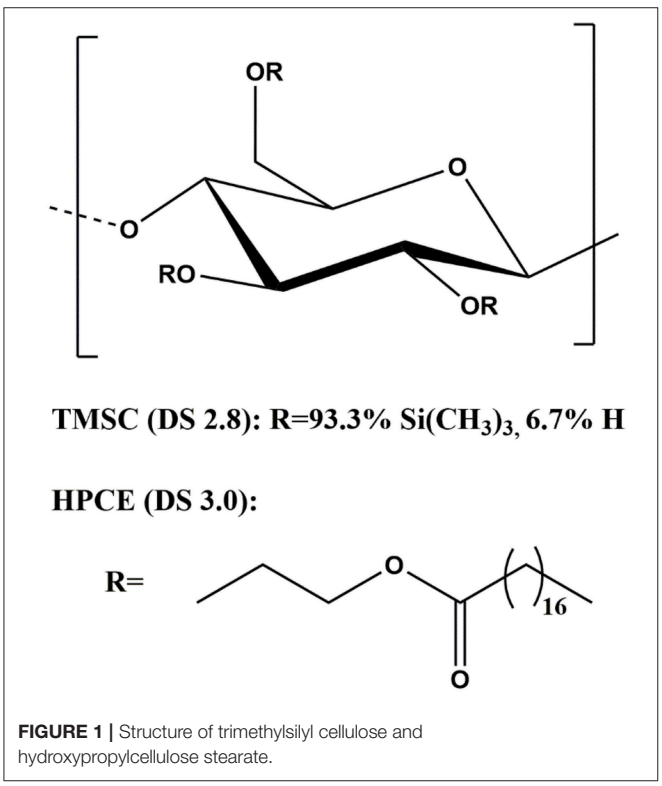

FIGURE 1 | Structure of trimethylsilyl cellulose and hydroxypropylcellulose stearate.

Profilometry

Thickness of the thin films was determined by scratching the films with a scalpel and measuring the profile of a scan length of 1,000 µm and a duration of 3 s using a DETAK 150 Stylus Profiler from Veeco (Bruker, USA) on a hydraulic balanced stone table with a diamond stylus with a radius of 12.5 µm and a force of 3 mg. Three films of each sample were measured at 6 locations before and after regeneration. Film thickness and film roughness was calculated from the resulting profile using Software Vision 64.

Contact Angle (CA) and Surface Free Energy (SFE) Determination

Static contact angle measurements were performed with a Drop Shape Analysis System DSA100 (Krüss GmbH, Germany) with a T1E CCD video camera (25 frames per second) and the DSA1 v 1.90 software. All measurements were performed at least three times on minimum two manufactured films with Milli-Q water and diiodomethane using a droplet size of 3 µL and a dispense rate of 400 µL min^{-1}. Static CAs were calculated with the Young-Laplace equation, and the SFE was determined with the Owen-Wendt-Rabel-Kaelble (OWRK) method. Surface tension of 50.80 and 72.80 mN m^{-1} for diidomethane and water were used, respectively.

Adsorption Experiments

A phosphate buffer containing 8.1 mM disodium phosphate, 1.9 mM sodium phosphate and 100 mM sodium chloride at pH 7.4 was used to carry out the adsorption experiments of BSA on the films. Surface Plasmon Resonance Spectroscopy (SPR) was performed with a MP-SPR Navi 200 from Bionavis Ltd (Finland), using 785 nm laser in both measurement channels. The attached autosampler MP-SPR Navi 210A was set to 20 µl min^{-1} flow rate. The equilibration of the thin films was observed by measuring the spectra with full angular scan (39–78°) and scan speed of 8° s^{-1} at 24.5° and plot the SPR-angle over time. A concentration

of 1.0 mg ml^{-1} of BSA was dissolved in the buffer and exposed to the thin films for 10 min. Adsorbed mass (Γ) was calculated with the de Feijter equation,

$$\Gamma = \frac{\Delta\Theta^* \kappa^* d_p}{dn/dc} \quad (1)$$

using the refractive index increment (dn/dc) 0.182 $cm^3\ g^{-1}$. The $\Delta\Theta$ is the angular response of the surface plasmon resonance. For thin layers (<100 nm), $k \times d_p$ can be considered constant and can be obtained by calibration of the instrument by determination of the decay wavelength l_d. Here it was 1.09×10^{-7} cm/° (at 670 nm) and 1.9×10^{-7} cm/° (at 785 nm) in aqueous systems.

Quartz Crystal Microbalance and Dissipation (QCM-D) instrument (model E4) from Q-Sense (Sweden) was used with gold sensors purchased from QuartzPro (Sweden). The attached peristaltic pump was set to 0.1 ml min^{-1}. Adsorption was performed in the same conditions as the SPR analyses. The data was analyzed using Johannsmann modeling (Johannsmann et al., 1992; Naderi and Claesson, 2006).

Atomic Force Microscopy

Most AFM and all FFM measurements were acquired using an Asylum Research MFP-3D AFM (USA). The instrument is equipped with a closed-loop planar x-y-scanner with a scanning range of 85 μm × 85 μm and a z-range of 15 μm. The tapping mode AFM images were recorded with standard silicon probes (Olympus AC160TS, cantilever spring constant ∼30 N m^{-1}, tip radius ∼10 nm). The measurements were obtained in ambient conditions at 50 ± 8% relative humidity and a temperature of 22 ± 1°C. Topography images of three independent positions were recorded for each sample. All the data was processed in the open-source software Gwyddion (Necas and Klapetek, 2012). For the 5 μm × 5 μm images, a roughness analysis (Teichert, 2002) was performed by calculating the 1D height-height correlation function:

$$C(x) = \langle [z(x_0 + x) - \langle z \rangle][z(x_0 - \langle z \rangle)] \rangle \quad (2)$$

of each scan line and then averaging over all lines. The resulting values were fitted with the function:

$$C(x) = \sigma^2 e^{-\left(\frac{|x|}{\xi}\right)^{2\alpha}} \quad (3)$$

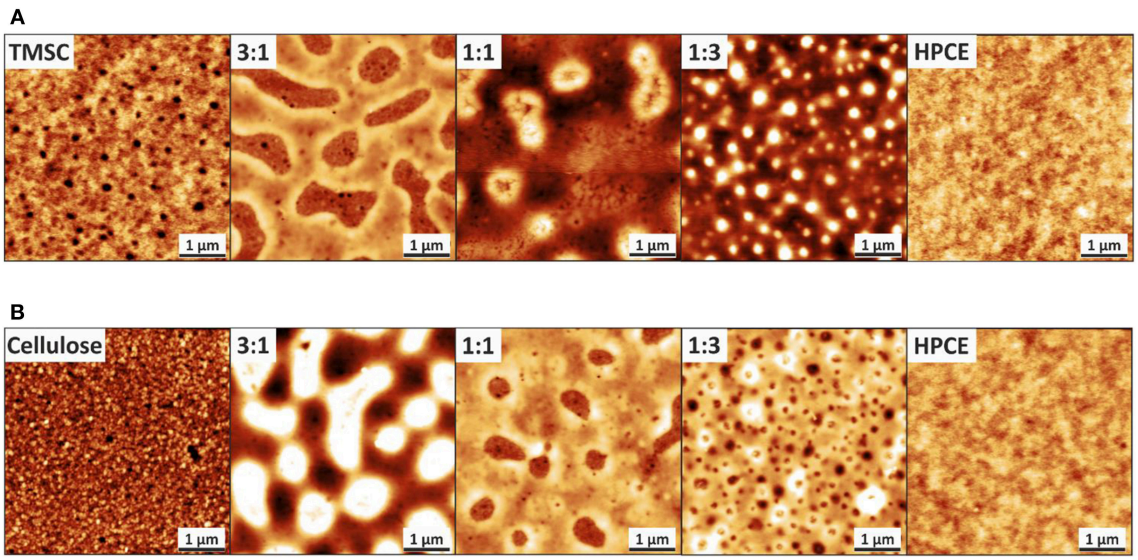

FIGURE 2 | AFM topography images of **(A)** TMSC:HPCE and **(B)** cellulose:HPCE blend films. The z-scale for the neat films is 10 nm and for all the blend films 60 nm. The z-directional height increases with increasing brightness.

TABLE 1 | RMS roughness and lateral correlation length of the roughness of the blend films prior (TMSC:HPCE) and after (cellulose:HPCE) regeneration.

	RMS roughness σ [nm]	Lateral correlation length ξ [nm]		RMS roughness σ [nm]	Lateral correlation length ξ [nm]
TMSC	1.50 ± 0.05	95 ± 5	Cellulose	1.50 ± 0.20	55 ± 10
3:1	7.60 ± 0.30	185 ± 15	3:1	19.80 ± 0.30	310 ± 10
1:1	12.60 ± 0.80	320 ± 20	1:1	8.00 ± 0.40	180 ± 5
1:3	14.15 ± 0.75	145 ± 10	1:3	10.20 ± 0.10	155 ± 5
HPCE	1.10 ± 0.05	120 ± 10	HPCE	1.10 ± 0.10	140 ± 10

The data is obtained from analysis of the 5 μm × 5 μm topography images.

The parameters σ, ξ, and α are used to characterize the surface roughness (Teichert, 2002). The σ denotes the root mean square (RMS) roughness, i.e., the standard deviation of the height values, which is a common measure for the vertical roughness. The lateral correlation length ξ describes the lateral fluctuation of the height values and α is the so-called Hurst parameter or roughness exponent. It determines the shape of C(x) and quantifies the jaggedness of the surface.

For FFM, which is recorded in contact mode, NT-MDT CSG10/Au probes with a tip radius of about 30 nm and a low cantilever spring constant of 0.1 N m^{-1} were employed. Images with frame size of 5 μm × 5 μm were obtained with a constant scan speed of 2.5 μm s^{-1}. A vertical force of about 10 nN was applied during the measurements. For acquisition of an FFM image, standard contact mode AFM scan including the lateral trace and retrace channel were recorded. The raw lateral signals were converted to friction images by subtracting the lateral retrace from the lateral trace signal and dividing it by two for each image (Kalihari et al., 2010; Shen et al., 2014). This eliminates topography artifacts and a possible offset.

The quantitative interpretation in terms of friction coefficient is not straightforward, and literature includes several calibration methods (Klapetek, 2018). Lateral force sensitivity calibration was done here according to the wedge calibration method of Varenberg et al. (2003). Quantitative friction images were obtained by multiplying the resulting friction image data with the lateral force sensitivity using the Gwyddion software.

AFM force spectroscopy measurements to investigate the adhesion properties of the film surfaces were performed with a scan rate of 2 Hz and a force distance of 0.5 μm. For these measurements, HSC60 probes from Team Nanotec (Germany) were used which have a cantilever spring constant of about 50 N/m and a tip radius of 60 nm. Here, 32 × 32 px^2 maps were obtained on 5 μm × 5 μm topography scans.

A Veeco Multimode Quadrax MM AFM (Bruker, USA) in tapping mode using standard silicon probes (NCH-VS1-W, NanoWorld AG) was used for recording film topography after they were rinsed with chloroform.

Surface Morphology and Area Determination

To quantify the observed surface features for the individual blend films, ten individual cross-sections of the features were obtained from the topography images for each film with the Gwyddion software to determine the height and width of the features. The values are given as mean ± standard deviation.

The AFM topography images were used for calculating effective surface fractions of the blend films. These are referred to as "effective surface fraction" or "surface fraction" later in the manuscript. The film component fraction derived from spinning solution is referred to as "volume fraction" or "volume ratio." Masked surfaces were evaluated by the surface area estimate method in Gwyddion, computed by simple triangulation that considers heights and spatial relations in the surface. For this purpose, additional points were added in-between four neighboring points using the mean values of these pixels. Four triangles are formed, and the surface area is approximated by summing their areas. Masking was done by threshold in *z*-value and adjusting with a pen tool. Single noise pixel was removed by grain filtering function. For films that showed a reliable phase contrast in the tapping mode topography analysis, the masks were determined from the phase information.

RESULTS AND DISCUSSION

Spin coated TMSC and HPCE films formed into smooth one-component film morphologies—indicating a uniform film formation—while the blend films containing both derivatives resulted in films with spinodal decomposition and are presented via three composition ratios, 3:1, 1:1, and 1:3 (**Figure 2A**). These TMSC:HPCE blend film surfaces consisted of domains which either formed cavities (TMSC:HPCE 3:1) or protrusions in lower

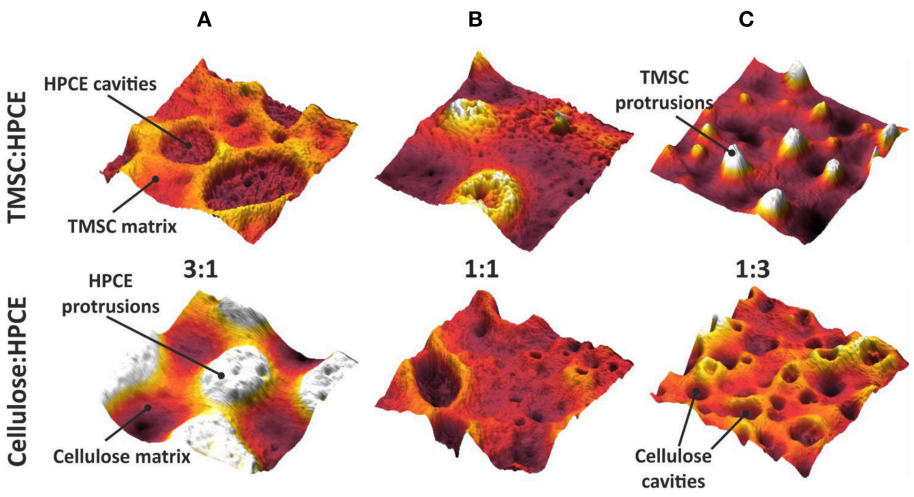

FIGURE 3 | Three-dimensional (2 μm × 2 μm) AFM topography images of the TMSC:HPCE (top row) and cellulose:HPCE (bottom row) blend films. **(A)** 3:1, **(B)** 1:1, and **(C)** 1:3. The z-scale is 60 nm in all cases.

sub-micrometer range. Protrusions with height 35 ± 10 nm and width of 780 ± 130 nm were determined for TMSC:HPCE 1:1 and of height of 55 ± 10 nm and width of 340 ± 50 nm for TMSC:HPCE 1:3. The protrusions increased in height with increasing HPCE content but decreased in lateral size.

The regeneration of TMSC into cellulose is accompanied by the cleavage of the silyl groups and simultaneous formation of hydrogen bonds of the created hydroxyl groups. This led to densification and reduction in film thickness (**Figure S1**), similar to reported elsewhere (Wolfberger et al., 2015), of the regenerated parts and consequently, more complex morphology (**Figure 2B**). HPCE is unaffected by the treatment (compare **Figures 2A,B**). After conversion to cellulose, the blend film cellulose fraction mass was reduced which translated into an inverted morphology compared to the TMSC:HPCE blend films. The cellulose:HPCE 3:1 surface was characterized by protrusions with arbitrary size and a height of 40 ± 10 nm, whereas the cellulose:HPCE 1:1 and 1:3 films contained cavities which decrease in lateral size. The 1:1 sample showed random-shaped surface features with a lateral width of 660 ± 80 nm, but the more spherical-shaped features on the 1:3 blend film surface had a width of only 250 ± 25 nm. An overview of this data is presented in **Table 1**.

The phase assignment was confirmed by treating the cellulose:HPCE blend films with chloroform that removed the HPCE phase. The remaining cellulose matrix was visualized and confirmed that the cellulose was the continuous phase in 3:1 blends, and the discontinuous one in 1:1 and 1:3 films (see **Figure S2A**). The phase assignments were incorporated in three-dimensional AFM topography images (**Figure 3**). The TMSC:HPCE 3:1 blend film consisted of a continuous TMSC matrix with HPCE cavities. Regeneration of the TMSC to cellulose resulted in a shrinkage of the TMSC domains. Therefore, the HPCE domains were protruding from the surface of the cellulose:HPCE blend films. With increasing HPCE amount, the matrix increasingly consisted of HPCE and the TMSC domains formed protrusions, which collapsed during cellulose regeneration (**Figures 3B,C**).

The visualization of the blend film after removal of the HPCE phase of 1:1 film did not only reveal the cellulose left behind in islands (**Figure S2A**). Lateral phase separation is chiefly responsible for the phase separation patterns that were observed upon the spinodal decomposition (**Figure 2**). This can take place independently or simultaneously with vertical separation which results in heterogeneous layer formation in the z-direction (Karim et al., 1998; Heriot and Jones, 2005). Dissolution of the HPCE phase revealed the cellulose skeleton left behind creating roughness beyond the apparent cellulose islands (**Figure S2A**).

The vertical separation and z-directional morphology evidently had an impact on the surface composition of the films meaning that the volume fraction did not necessarily equal to a surface area fraction. We used the AFM analyses to calculate effective surface area taking into consideration the surface roughness. The calculated surface areas were converted into surface fraction so that the TMSC or regenerated cellulose phase area was divided by the total area. The surface area could not be solely determined from the topography analysis (**Figure S2B**) but required phase imaging to reveal additional cellulose domains (**Figure S2C**). These were counted in to the cellulose surface fraction. Neither the TMSC:HPCE (diamonds) nor cellulose:HPCE (circles) surface fraction correlated directly with the volume fraction of the polymer blends used in spin coating (**Figure 4**). The surface fraction decreased upon regeneration in the case of high cellulose dominant blend films and increased with HPCE dominant ones. The differences in surface fraction of cellulose between the 1:3 and 1:1 sample is small (30% vs. 37%), but the resulting microstructures are very different (**Figures 3B,C**, lower row).

The roughness σ of the resulting blend thin films increased by factors of 4 to 20 compared to the neat films (**Table 1**). For the TMSC:HPCE blend films, the 1:3 composition featured the largest σ while after regeneration by HCl vapors, the cellulose:HPCE 3:1 film exhibited largest σ. The lateral correlation lengths ξ were lowest for the pure films. For the blend films, ξ increased by up to a factor of 3. TMSC:HPCE 1:1 and cellulose:HPCE 3:1 showed the highest values.

Derivatization of cellulose with the hydroxypropyl stearyl side chain (**Figure 1**) modifies the hydrophobicity of the molecule and this should reflect to the water contact angle and the surface free energy (SFE) of the films. The water contact angle of the cellulose film was 36.6 ± 0.3 degrees, TMSC film 94.6 ± 0.1 degrees, and that of the HPCE film 77.9 ± 0.5 degrees. The SFE of the blend films increased with increasing cellulose fraction (**Figure S3**) while prior to regeneration SFE was below 30 mJ m^{-2} for all the films. Consequently, the polar contribution decreased with the same trend (**Figure S4**).

Correlation of Friction Coefficient, Adhesion Force, Surface Roughness to Surface Free Energy and Protein Affinity of the Cellulose/HPCE Blend Films

The contact mode FFM images (**Figure 5A**) enclose the distinct differences between the neat and the cellulose/HPCE blend films' friction (indicated by the contrast differences). The average friction coefficients (Klunsner et al., 2010) were lower for the blend films than for the pure films (**Figure 5B**). The same applied for the adhesion forces (**Figure 5C**) where the blends featured lower values (20–50 nN) than the cellulose and HPCE films (65 ± 2 nN, and 104 ± 5 nN, respectively). It should be noted here that friction force data is in good agreement with those reported for cellulose spheres interacting with modified silica surfaces in a similar applied force range (∼5 nN) (Bogdanovic et al., 2001).

Non-specific Protein Deposition—BSA Adsorption

Cellulose in general is not very prone to non-specific protein adsorption. This originates from the highly hydrated, hydrophilic cellulosic material, having hydrogel characteristics. Upon protein deposition, the water that is close to the surface of the cellulose and on the surface of the protein needs to be replaced—a process which is, if there are not any specific contributions—entropically unfavorable. Several approaches have shown that either anionic or cationic coatings on cellulose thin films may alter the adsorption behavior of proteins (Orelma et al., 2011;

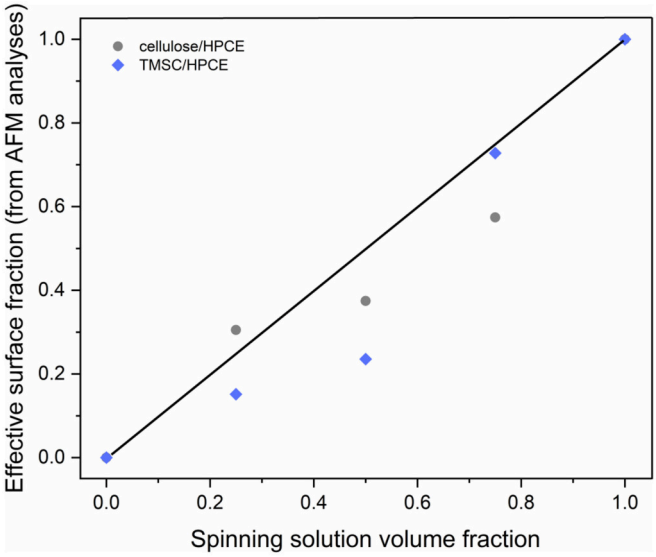

FIGURE 4 | Relationship of the TMSC:HPCE blend spinning solution volume fraction and experimentally determined effective surface fraction of the TMSC:HPCE (diamonds) and cellulose:HPCE films (circles). The black line represents identical volume and surface fraction.

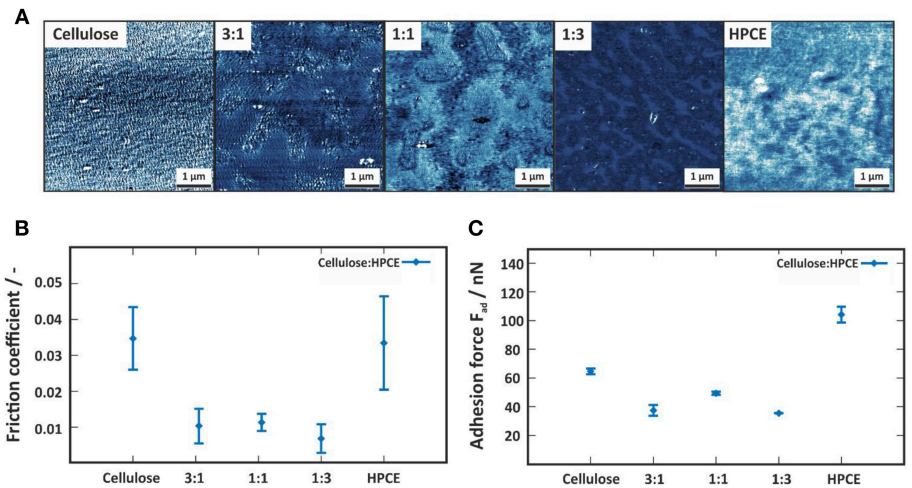

FIGURE 5 | (A) Contact mode friction force images of the cellulose, cellulose:HPCE and HPCE films. The z-scale of all images is 5 mV. **(B)** Friction coefficient and **(C)** adhesion force for the cellulose, cellulose:HPCE and HPCE films.

Mohan et al., 2013, 2014) depending on the employed pH during adsorption and the isoelectric point of the protein. On hydrophobic surfaces, proteins adhere spontaneously in a non-specific fashion and often they (partially) lose their ternary or quaternary structure and denaturate during deposition (Norde and Lyklema, 1991; Sagvolden et al., 1998). One would expect that the incorporation of a hydrophobic component such as HPCE into the cellulose film would trigger non-specific adsorption different from affinity to the cellulose regions. We chose BSA (pH 7.4) as a demonstrator probe for non-specific protein interactions of the blend films and studied the adsorption process using a combination of SPR spectroscopy and QCM-D. The combination of these techniques gives complementing insight into the amount of adsorbed protein. While QCM-D is a gravimetric technique capable of sensing any type of mass (i.e., water, and BSA, Γ^{QCM}) on the surface, SPR spectroscopy allows for determination of dry mass (Γ^{SPR}) by employing the de Feijter equation (1). The difference between Γ^{QCM} and Γ^{SPR} is the amount of water in the film. This amount of water decreased with lowering the cellulose content in the films and reaches its minimum for the 1:3 cellulose:HPCE film (**Figure 6A**). The HPCE film should swell the least, and hence, the major fraction of water can be assumed to be associated with the BSA on the surface. The amount of water in the BSA layer is 65%.

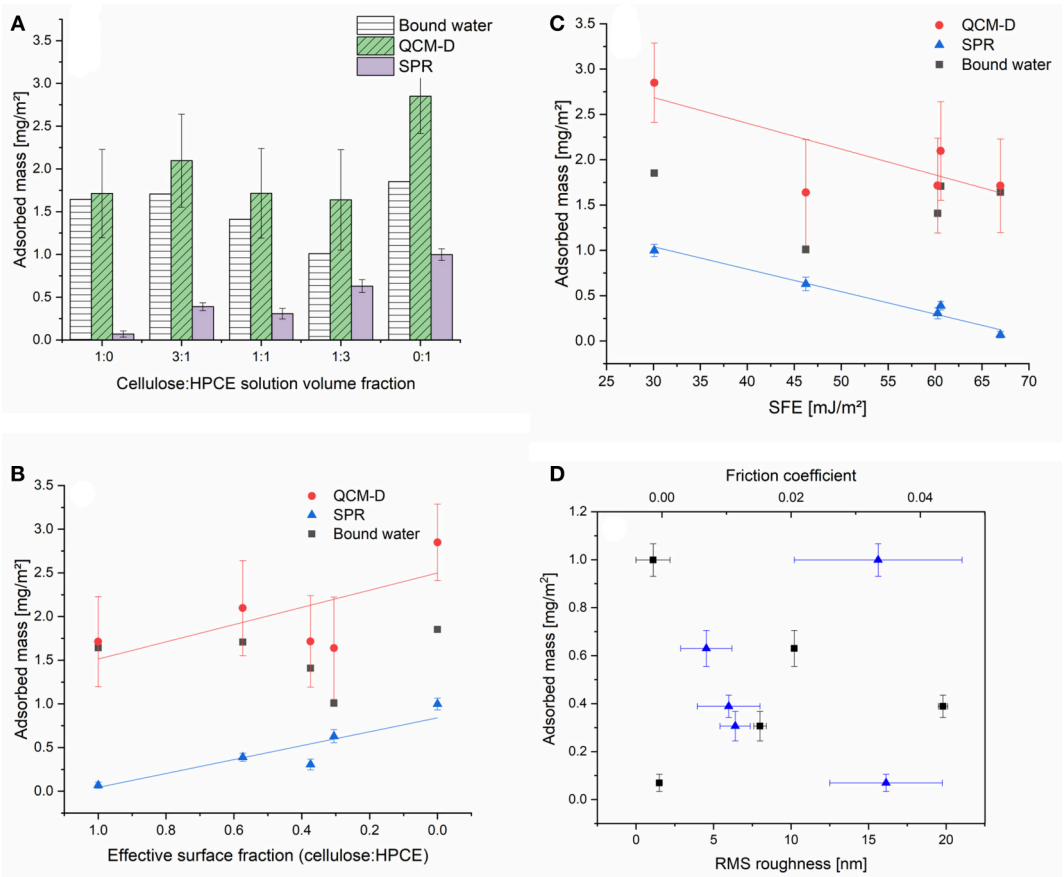

FIGURE 6 | (A) Adsorbed mass (mg m^{-2}) of BSA on the cellulose:HPCE blend films determined by SPR and QCM-D. Adsorbed masses with respect to the **(B)** surface fraction, and **(C)** surface free energy. **(D)** RMS roughness (squares) from the AFM measurements and friction coefficients (triangles) from the FFM analysis contrasted to the adsorbed amount based on SPR analyses.

The HPCE film experiences the highest BSA adsorbed amount (based on SPR) of 1 mg m^{-2}. The other extreme is the neat cellulose film that features low BSA adsorption (Γ^{SPR} 0.1 mg m^{-2}) which is in good agreement with other reports in these conditions (Niegelhell et al., 2017; Weißl et al., 2018). The highly swollen hydrogel character is revealed in the QCM-D data for the pure cellulose film, showing 1.7 mg m^{-2} water in the layer corresponding to 96% of hydration.

The increase in volume fraction of the HPCE led to a linear increase in the amount of adsorbed BSA on the surfaces. Contrasting the SPR adsorbed mass to the effective surface fraction revealed that the 1:1 blend film (volumetric) was an outlier in the adsorption trend and a lower amount of protein was deposited than what would have been expected (**Figure 6B**). Comparing this data to the other few reports on protein adsorption on cellulose based blend films revealed that also for the other systems protein adsorption minima were determined close to the 1:1 volume ratio (Niegelhell et al., 2016, 2017; Strasser et al., 2016). The cellulose:HPCE 3:1 film contains 57% of cellulose based on surface fraction, but still, it shows a higher BSA adsorption (0.39 mg m^{-2}) than the cellulose:HPCE 1:1 film (0.30 mg m^{-2}) with lower cellulose content (37% surface fraction).

The influence of surface free energy, roughness, and friction coefficient on the BSA adsorption is plotted against Γ^{QCM}, Γ^{SPR}, and bound water (**Figures 6C,D**). The SFE has a decisive influence on the BSA adsorption (**Figure 6C**). For the neat cellulose and HPCE films, surface roughness as well as friction coefficient were similar, but the SFE significantly differed. For the blend films however, the correlation between SFE and adsorbed mass was straightforward at first glance: lower surface energy translated to more hydrophobic surface resulting in higher non-specific protein deposition (**Figure 6C**). However, the SFE development did not correlate linearly with the effective surface fraction (**Figure S3**). There is a plateau in the SFE development with surface fraction of 0.37 (1:1) after which the cellulose dominated the SFE. One would expect much lower SFEs due to the actual surface fraction of just 37% of cellulose which would lead to higher non-specific protein adsorption. It is therefore rather the wetting properties of the blend films that are tuned by the morphology and configuration and these further affect the

adsorption. The roughness did not have a direct correlation to the adsorbed mass through the series, and neither did the friction coefficient (**Figure 6D**). Since the adsorbed mass and the SFE exhibited a linear correlation, it is clear that the roughness and friction coefficient correlation with SFE is similar to the adsorbed mass (**Figure S5** vs. **Figure 6D**).

CONCLUSIONS

Friction of cellulose films could be altered by blend composition including a low surface energy derivative. A surface fraction of 37% of cellulose (1:1 volume fraction) exhibited outlier adsorption inhibiting the protein adsorption. Surface energy rather than friction was a decisive factor for protein adsorption on the films. However, the SFE did not follow linearly the component surface area fraction. Wetting and adhesion typically correlate with surface friction. However, this correlation was not verified here to provide a correlation of friction to protein adsorption on the surface. Surface configuration—periodicity of the structure and feature size—might be an underlying factor.

AUTHOR CONTRIBUTIONS

CC was responsible of FFM and some of the AFM measurements, FFM data analysis, area calculations, and contributed in writing of the manuscript. GT was responsible of the SPR and QCM-D measurements, area calculations, and writing. MN and MB contributed with HPCE synthesis and characterization and MH with AFM measurements. CP assisted with QCM-D measurements and corresponding data analysis. SS and CT contributed in data analysis and writing. TN contributed with experimental analyses and writing the manuscript.

FUNDING

TN acknowledges Wallenberg Wood Science Center and Chalmers Area of Advance Materials for funding. The members of the Christian Doppler Laboratory for Fiber Swelling and Paper Performance gratefully acknowledge the financial support of the Austrian Federal Ministry of Economy, Family and Youth and the National Foundation for Research, Technology and Development.

SUPPLEMENTARY MATERIAL

The Supplementary Material for this article can be found online at: https://www.frontiersin.org/articles/10.3389/fchem.2019.00239/full#supplementary-material

REFERENCES

An, Y. H., and Friedman, R. J. (1998). Concise review of mechanisms of bacterial adhesion to biomaterial surfaces. *J. Biomed. Mater. Res.* 43, 338–348.

Bogdanovic, G., Tiberg, F., and Rutland, M. W. (2001). Sliding friction between cellulose and silica surfaces. *Langmuir* 17, 5911–5916. doi: 10.1021/la010330c

Chung, K. K., Schumacher, J. F., Sampson, E. M., Burne, R. A., Antonelli, P. J., and Brennan, A. B. (2007). Impact of engineered surface microtopography on biofilm formation of *Staphylococcus aureus*. *Biointerphases* 2, 89–94. doi: 10.1116/1.2751405

Chyasnavichyus, M., Young, S. L., and Tsukruk, V. V. (2015). Recent advances in micromechanical characterization of polymer, biomaterial, and cell surfaces with atomic force microscopy. *Japan. J. Appl. Phys.* 54:08LA02. doi: 10.7567/JJAP.54.08LA02

Dalnoki-Veress, K., Forrest, J., Stevens, J., and Dutcher, J. (1997). Phase separation morphology of spin-coated polymer blend thin films. *Phys A Stat. Mech. Appl.* 239, 87–94. doi: 10.1016/S0378-4371(96)00471-2

Emerson, J. A., Garabedian, N. T., Moore, A. C., Burris, D. L., Furst, E. M., and Epps, T. H. (2017). Unexpected tribological synergy in polymer blend coatings: leveraging phase separation to isolate domain size effects and reduce friction. *ACS Appl. Mater. Interfaces* 9, 34480–34488. doi: 10.1021/acsami.7b10170

Frisbie, C. D., Rozsnyai, L. F., Noy, A., Wrighton, M. S., and Lieber, C. M. (1994). Functional group imaging by chemical force microscopy. *Science* 265, 2071–2074. doi: 10.1126/science.265.5181.2071

Ganser, C., Niegelhell, K., Czibula, C., Chemelli, A., Teichert, C., Schennach, R., et al. (2016). Topography effects in AFM force mapping experiments on xylan-decorated cellulose thin films. *Holzforschung* 70, 1115–1123. doi: 10.1515/hf-2016-0023

Halls, J. J. M., Walsh, C. A., Greenham, N. C., Marseglia, E. A., Friend, R. H., Moratti, S. C., et al. (1995). Efficient photodiodes from interpenetrating polymer networks. *Nature* 376, 498–500. doi: 10.1038/376498a0

Hammerschmidt, J. A., Moasser, B., Gladfelter, W. L., Haugstad, G., and Jones, R. R. (1996). Polymer viscoelastic properties measured by friction force microscopy. *Macromolecules* 29, 8996–8998. doi: 10.1021/ma9603239

Heriot, S. Y., and Jones, R. A. (2005). An interfacial instability in a transient wetting layer leads to lateral phase separation in thin spin-cast polymer-blend films. *Nat. Mater.* 4, 782–786. doi: 10.1038/nmat1476

Hlawacek, G., Shen, Q., Teichert, C., Lex, A., Trimmel, G., and Kern, W. (2009). Hierarchy of adhesion forces in patterns of photoreactive surface layers. *J. Chem. Phys.* 130:044703. doi: 10.1063/1.3062841

Johannsmann, D., Mathauer, K., Wegner, G., and Knoll, W. (1992). Viscoelastic properties of thin films produced with a quartz-crystal resonator. *Phys. Rev. B* 46, 7808–7815. doi: 10.1103/PhysRevB.46.7808

Kalihari, V., Haugstad, G., and Frisbie, C. D. (2010). Distinguishing elastic shear deformation from friction on the surfaces of molecular crystals. *Phys. Rev. Lett.* 104:086102. doi: 10.1103/PhysRevLett.104.086102

Karim, A., Slawecki, T., Kumar, S., Douglas, J., Satija, S., Han, C., et al. (1998). Phase-separation-induced surface patterns in thin polymer blend films. *Macromolecules* 31, 857–862. doi: 10.1021/ma970687g

Katsikogianni, M., and Missirlis, Y. (2004). Concise review of mechanisms of bacterial adhesion to biomaterials and of techniques used in estimating bacteria-material interactions. *J. Eur. Cell Mater.* 8, 37–57. doi: 10.22203/eCM.v008a05

Klapetek, P. (2018). *Quantitative Data Processing in Scanning Probe Microscopy: SPM Applications for Nanometrology*. Amsterdam: Elsevier.

Klunsner, T., Shen, Q., Hlawacek, G., Teichert, C., Fateh, N., Fontalvo, G. A., et al. (2010). Morphology characterization and friction coefficient determination of sputtered V2O5 films. *Thin Solid Films* 519, 1416–1420. doi: 10.1016/j.tsf.2010.09.040

Kocun, M., Labuda, A., Meinhold, W., Revenko, I., and Proksch, R. (2017). Fast, high resolution, and wide modulus range nanomechanical mapping with bimodal tapping mode. *ACS Nano* 11, 10097–10105. doi: 10.1021/acsnano.7b04530

Kontturi, E., Johansson, L.-S., and Laine, J. (2009). Cellulose decorated cavities on ultrathin films of PMMA. *Soft Matter* 5, 1786–1788. doi: 10.1039/b901059a

Kontturi, E., Nyfors, L., and Laine, J. (2010). Utilizing polymer blends to prepare ultrathin films with diverse cellulose textures. *Macromol. Symp.* 294, 45–50. doi: 10.1002/masy.200900032

Kontturi, E., Thune, P. C., and Niemantsverdriet, J. W. (2003a). Cellulose model surfaces-simplified preparation by spin coating and characterization by X-ray photoelectron spectroscopy, infrared spectroscopy, and atomic force microscopy. *Langmuir* 19, 5735–5741. doi: 10.1021/la0340394

Kontturi, E., Thune, P. C., and Niemantsverdriet, J. W. (2003b). Novel method for preparing cellulose model surfaces by spin coating. *Polymer* 44, 3621–3625. doi: 10.1016/S0032-3861(03)00283-0

Marti, O., Colchero, J., and Mlynek, J. (1990). Combined scanning force and friction microscopy of mica. *J. Nanotechnol.* 1:141. doi: 10.1088/0957-4484/1/2/003

Mate, C. M., Mcclelland, G. M., Erlandsson, R., and Chiang, S. (1987). Atomic-scale friction of a tungsten tip on a graphite surface. *Phys. Rev. Lett.* 59, 1942–1945.

Medronho, B., Romano, A., Miguel, M. G., Stigsson, L., and Lindman, B. (2012). Rationalizing cellulose (in)solubility: reviewing basic physicochemical aspects and role of hydrophobic interactions. *Cellulose* 19, 581–587. doi: 10.1007/s10570-011-9644-6

Meyer, G., and Amer, N. M. (1990). Simultaneous measurement of lateral and normal forces with an optical-beam-deflection atomic force microscope. *J Appl. Phys. Lett.* 57, 2089–2091. doi: 10.1063/1.103950

Mohan, T., Niegelhell, K., Zarth, C. S., Kargl, R., Köstler, S., Ribitsch, V., et al. (2014). Triggering protein adsorption on tailored cationic cellulose surfaces. *Biomacromolecules* 15, 3931–3941. doi: 10.1021/bm500997s

Mohan, T., Ristić, T., Kargl, R., Doliska, A., Köstler, S., Ribitsch, V., et al. (2013). Cationically rendered biopolymer surfaces for high protein affinity support matrices. *Chem. Comm.* 49, 11530–11532. doi: 10.1039/c3cc46414h

Naderi, A., and Claesson, P. M. (2006). Adsorption properties of polyelectrolyte-surfactant complexes on hydrophobic surfaces studied by QCM-D. *Langmuir* 22, 7639–7645. doi: 10.1021/la061118h

Nau, M., Seelinger, D., and Biesalski, M. (2018). Functional surface coatings from tailor-made long-chain hydroxypropyl cellulose ester nanoparticles. *Cellulose* 25, 5769–5780. doi: 10.1007/s10570-018-1981-2

Necas, D., and Klapetek, P. (2012). Gwyddion: an open-source software for SPM data analysis. *Cent. Eur. J. Phys.* 10, 181–188. doi: 10.2478/s11534-011-0096-2

Niegelhell, K., Süßenbacher, M., Jammernegg, K., Ganner, T., Schwendenwein, D., Schwab, H., et al. (2016). Enzymes as biodevelopers for nano- and micropatterned bicomponent biopolymer thin films. *Biomacromolecules* 17, 3743–3749. doi: 10.1021/acs.biomac.6b01263

Niegelhell, K., Süßenbacher, M., Sattelkow, J., Plank, H., Wang, Y., Zhang, K., et al. (2017). How bound and free fatty acids in cellulose films impact nonspecific protein adsorption. *Biomacromolecules* 18, 4224–4231. doi: 10.1021/acs.biomac.7b01260

Norde, W., and Lyklema, J. (1991). Why proteins prefer interfaces. *J. Biomater. Sci. Polymer Edn.* 2, 183–202. doi: 10.1080/09205063.1991.9756659

Nyfors, L., Suchy, M., Laine, J., and Kontturi, E. (2009). Ultrathin cellulose films of tunable nanostructured morphology with a hydrophobic component. *Biomacromolecules* 10, 1276–1281. doi: 10.1021/bm900099e

Orelma, H., Filpponen, I., Johansson, L.-S., Laine, J., and Rojas, O. J. (2011). Modification of cellulose films by adsorption of CMC and chitosan for controlled attachment of biomolecules. *Biomacromolecules* 12, 4311–4318. doi: 10.1021/bm201236a

Orelma, H., Filpponen, I., Johansson, L. S., Osterberg, M., Rojas, O. J., and Laine, J. (2012a). Surface functionalized Nanofibrillar Cellulose (NFC) film as a platform for immunoassays and diagnostics. *Biointerphases* 7:61. doi: 10.1007/s13758-012-0061-7

Orelma, H., Johansson, L. S., Filpponen, I., Rojas, O. J., and Laine, J. (2012b). Generic method for attaching biomolecules via avidin-biotin complexes immobilized on films of regenerated and nanofibrillar cellulose. *Biomacromolecules* 13, 2802–2810. doi: 10.1021/bm300781k

Overney, R. M., Meyer, E., Frommer, J., Brodbeck, D., Luthi, R., Howald, L., et al. (1992). Friction measurements on phase-separated thin-films with a modified atomic force microscope. *Nature* 359, 133–135. doi: 10.1038/359133a0

Overney, R. M., Meyer, E., Frommer, J., Guntherodt, H. J., Fujihira, M., Takano, H., et al. (1994). Force microscopy study of friction and elastic compliance of phase-separated organic thin-films. *Langmuir* 10, 1281–1286. doi: 10.1021/la00016a049

Pelton, R. (2009). Bioactive paper provides a low cost paltform for diagnostics. *Trends Anal. Chem.* 8, 925–942. doi: 10.1016/j.trac.2009.05.005

Sagvolden, G., Giaever, I., and Feder, J. (1998). Characteristic protein adhesion forces on glass and polystyrene substrates by atomic force microscopy. *Langmuir* 14, 5984–5987. doi: 10.1021/la980271b

Schaub, M., Wenz, G., Wegner, G., Stein, A., and Klemm, D. (1993). Ultrathin films of cellulose on silicon wafers. *Adv. Mater.* 5, 919–922. doi: 10.1002/adma.19930051209

Schumacher, J. F., Aldred, N., Callow, M. E., Finlay, J. A., Callow, J. A., Clare, A. S., et al. (2007a). Species-specific engineered antifouling topographies: correlations between the settlement of algal zoospores and barnacle cyprids. *Biofouling* 23, 307–317. doi: 10.1080/08927010701393276

Schumacher, J. F., Carman, M. L., Estes, T. G., Feinberg, A. W., Wilson, L. H., Callow, M. E., et al. (2007b). Engineered antifouling microtopographies–effect of feature size, geometry, and roughness on settlement of zoospores of the green alga Ulva. *Biofouling* 23, 55–62. doi: 10.1080/08927010601136957

Shen, Q., Edler, M., Griesser, T., Knall, A. C., Trimmel, G., Kern, W., et al. (2014). *Ex situ* and *in situ* characterization of patterned photoreactive thin organic surface layers using friction force microscopy. *Scanning* 36, 590–598. doi: 10.1002/sca.21159

Sondhauß, J., Lantz, M., Gotsmann, B., and Schirmeisen, A. (2015). β-relaxation of PMMA: tip size and stress effects in friction force microscopy. *Langmuir* 31, 5398–5405. doi: 10.1021/acs.langmuir.5b00735

Strasser, S., Niegelhell, K., Kaschowitz, M., Markus, S., Kargl, R., Stana-Kleinschek, K., et al. (2016). Exploring nonspecific protein adsorption on lignocellulosic amphiphilic bicomponent films. *Biomacromolecules* 17, 1083–1092. doi: 10.1021/acs.biomac.5b01700

Tamayo, J., and Garcia, R. (1996). Deformation, contact time, and phase contrast in tapping mode scanning force microscopy. *Langmuir* 12, 4430–4435. doi: 10.1021/la960189l

Teichert, C. (2002). Self-organization of nanostructures in semiconductor heteroepitaxy. *Phys. Rep.* 365, 335–432. doi: 10.1016/S0370-1573(02)00009-1

Varenberg, M., Etsion, I., and Halperin, G. (2003). An improved wedge calibration method for lateral force in atomic force microscopy. *Rev. Sci. Instruments* 74, 3362–3367. doi: 10.1063/1.1584082

Weißl, M., Niegelhell, K., Reishofer, D., Zankel, A., Innerlohinger, J., and Spirk, S. (2018). Homogeneous cellulose thin films by regeneration of cellulose xanthate: properties and characterization. *Cellulose* 25, 711–721. doi: 10.1007/s10570-017-1576-3

Wolfberger, A., Petritz, A., Fian, A., Herka, J., Schmidt, V., Stadlober, B., et al. (2015). Photolithographic patterning of cellulose: a versatile dual-tone photoresist for advanced applications. *Cellulose* 22, 717–727. doi: 10.1007/s10570-014-0471-4

Xue, L. J., Zhang, J. L., and Han, Y. C. (2012). Phase separation induced ordered patterns in thin polymer blend films. *Prog. Polym. Sci.* 37, 564–594. doi: 10.1016/j.progpolymsci.2011.09.001

Zhang, Y., Carbonell, R. G., and Rojas, O. J. (2013). Bioactive cellulose nanofibrils for specific human IgG binding. *Biomacromolecules* 14, 4161–4168. doi: 10.1021/bm4007979

Conflict of Interest Statement: The authors declare that the research was conducted in the absence of any commercial or financial relationships that could be construed as a potential conflict of interest.

frontiers in Chemistry

ORIGINAL RESEARCH
published: 22 May 2019
doi: 10.3389/fchem.2019.00370

Natural Shape-Retaining Microcapsules With Shells Made of Chitosan-Coated Colloidal Lignin Particles

*Tao Zou, Mika H. Sipponen and Monika Österberg**

Department of Bioproducts and Biosystems, School of Chemical Engineering, Aalto University, Espoo, Finland

Thin film coating of charged nanoparticles with oppositely charged polymers is an efficient and straightforward way for surface modification, but synthetic polyelectrolytes should be replaced by abundant biopolymers. In this study a thin film of chitosan was adsorbed onto colloidal lignin particles (CLPs) that were then systematically studied for olive oil stabilization with an objective to develop shape-retaining microcapsules that comprised of only renewable biomaterials. Full surface coverage was achieved with merely 5 wt% of chitosan relative to the dry weight of CLPs, reversing their surface charge from negative to positive. Such modification rendered the chitosan-coated particles excellent stabilizers for forming Pickering emulsions with olive oil. The emulsion droplets could be further stabilized by sodium triphosphate that provided ionic intra- and inter-particle cross-linking of the chitosan corona on the CLPs. Following the optimum conditions, the non-cross-linked microcapsules exhibited a strong stability against coalescence and the electrostatically stabilized ones additionally retained their shape upon drying and rewetting. Non-cross-linked microcapsules were used to demonstrate encapsulation and rapid release of ciprofloxacin as a model lipophilic drug in aqueous media. Overall, the combination of antimicrobial chitosan and antioxidative lignin nanoparticles hold unprecedented opportunities as biocompatible and biodegradable materials for controlled drug delivery.

Keywords: lignin nanoparticles, chitosan, thin film coating, Pickering emulsion, microcapsule, drug delivery

OPEN ACCESS

Edited by:
Eero Kontturi,
School of Chemical Technology, Aalto University, Finland

Reviewed by:
Gloria Huerta-Angeles,
Contipro Inc., Czechia
Torbjörn Pettersson,
Royal Institute of Technology, Sweden

****Correspondence:***
Monika Österberg
monika.osterberg@aalto.fi

Specialty section:
This article was submitted to Polymer Chemistry, a section of the journal Frontiers in Chemistry

Received: *21 January 2019*
Accepted: *06 May 2019*
Published: *22 May 2019*

Citation:
Zou T, Sipponen MH and Österberg M (2019) Natural Shape-Retaining Microcapsules With Shells Made of Chitosan-Coated Colloidal Lignin Particles. Front. Chem. 7:370. doi: 10.3389/fchem.2019.00370

INTRODUCTION

Lignin is the second most abundant natural biopolymer and the most abundant aromatic polymer in nature (Ragauskas et al., 2014). Annually over 70 million tons of industrial lignin is produced as a by-product in the pulp/paper industry. However, only 5% of industrial lignin is commercialized as value-added products, such as additives, dispersants, adhesives, or surfactants (Laurichesse and Avérous, 2014). The rest 95% is used as low value energy source or simply treated as waste. The low extent of commercialization of lignin is mainly due to its complex and inhomogeneous structure resulting from different sources and extraction processes (Li et al., 2015). However, recent studies have shown that fabricating spherical micro- or nanoparticles from lignin not only enables the large scale utilization of lignin (Ago et al., 2016; Leskinen et al., 2017a; Ashok et al., 2018; Lintinen et al., 2018), but also improves properties such as surface activity, antioxidative, UV shielding, and antimicrobial activity for potential high-value applications (Beisl et al., 2017).

To name a few examples, colloidal lignin particles (CLPs) have been utilized to entrap hydrophobic drugs for drug delivery purposes in biomedicine (Chen et al., 2016; Dai et al., 2017; Figueiredo et al., 2017; Sipponen et al., 2018b). By introducing CLPs in cellulose nanofilms, Farooq, and co-workers rendered the composite films waterproof, provided antioxidant activity and UV-shielding in addition to the improved mechanical properties (Farooq et al., 2019). Surface-modification of CLPs by adsorption has been demonstrated with synthetic poly(diallyldimethylammonium chloride) (Lievonen et al., 2016), proteins (Leskinen et al., 2017b), and cationic lignin (Sipponen et al., 2017). Such modifications alter the interfacial properties of the particles and broaden the window for possible high-value applications. For instance, cationic CLPs were demonstrated for binding negatively charged enzymes for enhanced catalytic activity in aqueous ester synthesis (Sipponen et al., 2018a).

In addition, micro- and nanoscaled lignin particles have been exploited as surface-active stabilizers for Pickering emulsions (Wei et al., 2012; Yang et al., 2013; Nypelö et al., 2015; Ago et al., 2016; Sipponen et al., 2017). Pickering emulsions are stabilized by solid particles at the oil/water interface (Pickering, 1907). Compared to conventional surfactant-stabilized emulsions, Pickering emulsions are more stable against coalescence, because high energy input is required to remove solid particles from the oil/water interface (Binks, 2002; Rayner et al., 2014; Berton-Carabin and Schroën, 2015). Additionally, some food-grade particles are less toxic than synthetic surfactants (Yang et al., 2017). Therefore, Pickering emulsions can be applied in a wide range of fields including biomedicine, cosmetics, and food (McClements, 2015; Tang et al., 2015; Yang et al., 2017).

To date, lignin-stabilized Pickering emulsions reported in scientific articles are mainly aliphatic or aromatic hydrocarbon oil-based, e.g., kerosene, hexadecane, styrene, and toluene (Wei et al., 2012; Yang et al., 2013; Nypelö et al., 2015; Ago et al., 2016; Sipponen et al., 2017). Such oils are often toxic, which therefore are not suitable for biomedicine, cosmetics, or food. Instead, triglyceride vegetable oils are a better choice, since they do not present any safety issues (Pouton and Porter, 2008). Furthermore, triglycerides are good solvents for many lipophilic drugs and have the ability to increase intestinal wall permeability, which makes them particularly useful for drug delivery (Kalepu et al., 2013). Nevertheless, unmodified CLPs exhibit limited capacity in stabilizing triglyceride-in-water Pickering emulsions, possibly due to insufficient hydrophilicity. Sipponen et al. modified CLPs by adsorption of cationic lignin to form more hydrophilic cationic CLPs (c-CLPs), which exhibited improved capacity for stabilizing olive oil compared to unmodified CLPs (Sipponen et al., 2017). Yet, the formed olive oil-in-water emulsions were not sufficiently stable. Additionally, alike other quaternary ammonium substances (Zhang C. et al., 2015), the cationic lignin grafted with quaternary ammonium groups may be toxic.

Chitosan, on the other hand, has shown good emulsification capacity in stabilizing triglyceride-in-water emulsions whether in the form of molecules (Schulz et al., 1998; Del Blanco et al., 1999; Rodriǵuez et al., 2002) or particles (Mwangi et al., 2016a; Shah et al., 2016; Asfour et al., 2017). Furthermore, chitosan possesses biologically relevant properties such as biocompatibility, biodegradability, bio-adhesion, and antimicrobial activity (Pavinatto et al., 2010; Croisier and Jérôme, 2013; Asfour et al., 2017). As a consequence, chitosan appears to be a plausible material for modifying CLPs to form triglyceride-based Pickering emulsions.

In this work, we systematically studied the modification of CLPs by thin film coating of chitosan and determined the emulsification capacities of the chitosan-coated CLPs (chi-CLPs) for olive oil. We used sodium triphosphate (STP) to ionically cross-link the chi-CLPs locating at the oil-water interface and compared the mechanical properties of the electrostatically stabilized chi-CLP microcapsules to those of non-cross-linked ones. Finally, we demonstrated the ability of the chi-CLP microcapsules in the encapsulation and release of ciprofloxacin at various pH values at 37°C. Overall, this work provides optimum conditions for the preparation of non-coalescent and shape-retaining microcapsules for future applications in controlled drug delivery in the field of biomedicine.

MATERIALS AND METHODS

Materials

Kraft lignin (BioPiva 100) used in this work was isolated from softwood using the LignoBoost® technology at Domtar's Plymouth plant (NC, USA). The kraft lignin was well-characterized in the previous publication (Sipponen et al., 2018a). The number and weight average molecular weights (M_n and M_w) of the kraft lignin are 1,193 and 5,250 g/mol, respectively. The carboxyl groups, aliphatic hydroxyl groups, and total phenolic hydroxyl groups of the kraft lignin are 0.57, 1.89, and 4.05 mmol/g, respectively. Tall oil fatty acid (TOFA) "For2" was a kind gift from Forchem Oyj (Finland). Chitosan (molecular weight 100 to 300 kDa, deacetylation degree ≥90%) and sodium triphosphate (STP) (≥98%) were purchased from Fisher Scientific (Acros organics). Olive oil (highly refined, low acidity), ciprofloxacin (≥98%), poly(styrene) ($\overline{M}_w$: 35,000 g/mol) and acetic acid (glacial, ≥99.8%) were purchased from Sigma-Aldrich. The content of free fatty acid in olive oil was determined to be 1.9 ± 0.2 wt% ($n = 7$) by titration (Sipponen et al., 2017). All purchased chemicals and solvents were used without further purification.

Preparation of Chitosan Solution

1 wt% chitosan solution was prepared by dissolving 1 g of chitosan in 99 g of 0.1 M acetic acid under stirring for 24 h. The dissolution of chitosan in 0.1 M acetic acid resulted in an increase of the pH value from 2.9 to 4.5, which indicated a partial protonation of chitosan (ca. 60 to 70% protonation of the primary amine groups, calculated according to the pKa 4.75 of acetic acid and the deacetylation degree of chitosan).

Preparation of Aqueous Colloidal Lignin Particles

Preparation of 0.2 wt% colloidal lignin particle (CLP) dispersion followed the procedure described in the previous publication (Sipponen et al., 2017) with the modification that in this study

2 g kraft lignin (dry weight) was dissolved in 200 g of acetone-water mixture (mass ratio: 3:1), instead of using THF-water mixture as the solvent. The final aqueous CLP dispersion (0.2 wt%) was obtained with a lignin mass yield of 85%. The particle diameter and zeta potential of the CLPs at native pH 3.9 were determined to be 97 nm (PDI 0.18) and −27 mV, respectively. The preparation of 1 wt% CLP dispersion was similar to that of 0.2 wt% CLP dispersion except that in this case rotary evaporation (40°C under reduced pressure) was used to remove acetone instead of dialysis. 0.5 wt% CLP dispersion was prepared by diluting the 1 wt% CLP dispersion with deionized water. The particle diameter and zeta potential of the CLPs (0.5 and 1 wt%) were 113 nm (PDI 0.19) and −30 mV (at native pH 3.1), respectively.

Preparation of Chitosan-Coated Colloidal Lignin Particles (chi-CLPs)

Chitosan-coated colloidal lignin particles (chi-CLPs) were prepared by adding CLP dispersion (0.2 or 0.5 or 1 wt%) slowly into 1 wt% chitosan solution under vigorous stirring for 30 min. The prepared chi-CLP dispersions were stored over night before use. For 0.2 wt% chi-CLP dispersions, the mass ratio of chitosan to CLP was varied from 0 to 200 mg/g. For 0.5 and 1 wt% chi-CLP dispersions, chi-CLPs were prepared at a fixed mass ratio of 50 mg/g.

Preparation of chi-CLP Stabilized Oil-in-Water Pickering Emulsions

The Pickering emulsions were prepared by ultrasonication (Branson 450 Digital Sonifier with a 3 mm-diameter microtip) under ice bath condition at a fixed volume ratio of 1:1 olive oil to chi-CLP (or CLP) dispersion. More specifically, 60 s with the cycles 10 s on and 5 s off were applied for emulsion formation, the amplitude was set at 10% for a total volume of 2 ml and 40% for 10 ml. These procedures resulted in similar size distributions of oil droplets when the concentration of the chi-CLP (50 mg/g) dispersion was 0.5 or 1 wt%.

Preparation of Ionically Cross-Linked Pickering Emulsions

Pickering emulsion formed with 1 wt% chi-CLP (50 mg/g) dispersion was used for the cross-linking study. The preparation was achieved by adding the emulsion slowly into 6 wt% sodium triphosphate (STP) aqueous solution at the volume ratio of 1:9 (emulsion: STP solution) under vigorous stirring for 30 min.

Preparation of Ciprofloxacin-Loaded Pickering Emulsions

1 wt% chi-CLP (50 mg/g) dispersion was used for forming the emulsion with ciprofloxacin-loaded oil for release study. Ciprofloxacin was firstly dissolved (20 mg/mL) in TOFA followed by dilution with olive oil to 2 mg/mL. The emulsion formation followed the aforementioned procedure.

Ciprofloxacin Release Study

The release study was performed in three different pH buffers, pH 2 (the buffer was prepared by mixing 0.1 M KCl and 0.02 M HCl to obtain a solution at pH 2), pH 5.5 (0.05 M PBS) and pH 7.4 (0.05 M PBS) at 37°C. For each sample, 1.2 mL ciprofloxacin-loaded emulsion (50% oil phase) was injected into 60 ml of buffer solution. The aliquots were taken at various time intervals and filtered through a 0.2 μm syringe filter to separate the oil droplets and/or lignin particles. The concentration of ciprofloxacin in the buffer was calculated from the absorbance values at 277 nm, after correcting with the absorbance resulting from minor dissolution of lignin in the absence of ciprofloxacin, according to the calibration curve shown in **Figure S1**. The average of four ciprofloxacin-loaded samples and two reference samples were used in the analysis and reporting of data.

Particle Diameter and Zeta Potential Analysis

Particle diameters and zeta potentials of CLPs and chi-CLPs were analyzed using a Zetasizer Nano ZS90 instrument (Malvern Instruments Ltd., U.K.). A dip cell probe was utilized for the determination of the zeta potential. CLP, chi-CLP dispersions and chitosan solution were diluted accordingly with deionized water or pH 4.5 acetic acid prior to measurement. Mean values of three replicates of the particle diameter (Z-average, intensity mean) and zeta potential were used in the analysis and reporting of data.

Droplet Diameter and Uniformity of Emulsion Analysis

The droplet diameter of the emulsion was determined by static light scattering (Mastersizer 2000, Malvern, UK). The emulsions were diluted with deionized water to reach the laser obscuration of 6 to 12% prior to starting the measurement. The refractive index (RI) of olive oil and water used in the calculations were 1.47 and 1.33, respectively. Mean droplet diameter was calculated over volume data (d_{43}, De Brouckere Mean Diameter). Uniformity of the droplets was calculated according to Equation (1)

$$Uniformity = \frac{\sum X_i |d(v,\ 0.5) - d_i|}{d(v,\ 0.5) \sum X_i} \quad (1)$$

where $d(v,\ 0.5)$ is the median diameter in the volume-based distribution, d_i is the diameter in class i and X_i is the corresponding volume fraction in %. Mean values of six replicates of mean droplet diameter (d_{43}) and uniformity were used in the analysis and reporting of data.

Microscopy Observation

Confocal Microscopy

The emulsions stabilized by 1 wt% chi-CLP (50 mg/g) were imaged with the confocal laser scanning microscope (Leica DMRXE, Germany). Emulsions were diluted 50 times with deionized water or with 6 wt% STP aqueous solution followed by staining the oil with Nile red (1 mg/mL in ethanol) (ca. 50 μl of Nile red in 1 ml emulsion) prior to measurement. For each sample, a drop (5 μl) of the Nile red-stained emulsion was placed on the glass slide for imaging at the wavelength of 488 nm, using a 10× air objective and a 63× oil immersion objective.

Optical Microscopy

A Leica Zeiss (DM750) optical microscope was used for observing the emulsions without staining.

Environmental-SEM

A Zeiss Environmental Scanning Electron Microscope (EVO HD15) was used for observing the surface morphology of the oil droplets. The emulsion capsule that was stabilized with 1 wt% chi-CLP (50 mg/g) and cross-linked with STP was selected for the observation. A drop (5 μl) of the diluted emulsion (500 times with 6 wt% STP aqueous solution) was cooled at −20°C in a Peltier cooling element in order to freeze the oil and sublimate the water. During the observation, the temperature was kept at −20°C and the pressure of the SEM chamber was set at 50 Pa, images were captured with an EPSE detector.

AFM

The AFM analysis was carried out with a MultiMode eight atomic force microscope equipped with a NanoScope V controller (Bruker Corporation, U.S.A.). The images for CLPs were obtained in tapping mode under ambient air condition with NCHV-A tapping mode probes (Bruker). The images for oil droplets (stabilized by chi-CLP and cross-linked with STP) were obtained in ScanAsyst mode under ambient air condition with SCANASYST-AIR probes (Bruker). Samples were prepared by dropping 5 μl of the diluted dispersion or emulsion on the mica surfaces and drying under ambient conditions. Nanoscope analysis 1.5 software was used for image analysis.

QCM-D

The lignin substrates for QCM-D studies were prepared as described by Salas et al. (2013) except that the lignin used in this study was kraft lignin. In brief, lignin was spin-coated onto gold-coated QCM crystals (Q-Sense, Sweden) that had been pre-coated with poly(styrene). Adsorption of chitosan on the thin films were carried out using QCM-D E4 (Q-Sense, Sweden) in continuous flow mode. Chitosan was firstly dissolved (1 wt%) in 0.1 M acetic acid and then diluted with pH 4.5 acetic acid to 100 μg/mL. During the measurements, the lignin films were firstly rinsed with pH 4.5 acetic acid buffer at the flow rate of 0.1 mL/min until a plateau baseline (Δf_5) was reached, followed by replacing the acetic acid buffer with the diluted chitosan solution. The temperature was controlled at 25°C throughout the experiments. The mass of chitosan adsorbed on the lignin surface was related to the change of resonance frequency Δf according to the Sauerbrey equation (Sauerbrey, 1959):

$$\Delta m = -\mathrm{C}\Delta \mathrm{f}/\mathrm{n} \quad (2)$$

where Δm is the change of mass, Δf is the change of resonance frequency determined by the device, C is a constant (0.177 mg m^{-2} Hz^{-1}) that describes the sensitivity of the device to changes in mass, n is the overtone number ($n = 1$ represents the fundamental frequency at 4.95 MHz). The energy dissipation due to adsorption is indicated by the dissipation factor D (Rodahl and Kasemo, 1996), which is defined as:

$$D = \frac{E_{dis}}{2\pi E_{st}} \quad (3)$$

where E_{dis} is the dissipated energy and E_{st} is the stored energy during one oscillation cycle. The dissipation change is defined as, $\Delta D = D–D_0$, where D_0 denotes the initial dissipation prior to adsorption. In this work, the average values (Δf_5 and ΔD_5) of two replicate samples were used in the analysis and reporting of data.

RESULTS AND DISCUSSION

The overarching objective of this work was to establish a reliable approach for chitosan-coated CLPs, and application of the modified particles in stabilization of olive oil-in-water Pickering emulsion capsules. A general scheme of this work is shown in **Figure 1**. The CLPs were prepared by rapid anti-solvent nanoprecipitation method, followed by either dialysis or evaporation to remove the acetone that was used as solvent. In contrast to the more commonly used THF (Lievonen et al., 2016), acetone can be easily removed by evaporation, as acetone has no azeotrope with water (Smallwood, 2012). The obtained CLPs were modified with thin film coating of chitosan by physical adsorption and systematically studied for the stabilization of Pickering emulsions. Selected emulsion capsules were further stabilized by non-covalent cross-linking. Encapsulation of a model drug into the oil phase and its release from the non-cross-linked capsules was finally demonstrated in aqueous media. The first important step was to optimize the chitosan coating and emulsion formation processes, which are discussed more in detail below.

Determining the Minimum Needed Chitosan Coating on CLPs

The CLPs purified by dialysis (0.2 wt%) were used for assessing the effect of mass ratio of chitosan to CLP on the particle properties. It was determined by DLS that pure CLPs had the average particle diameter of 97 nm (PDI 0.18) and zeta potential of −27 mV (at native pH 3.9). When 10 mg/g chitosan to CLP was added into the CLP dispersion, the dispersion showed strong aggregation and sedimentation, indicating neutralization of CLPs by chitosan (**Figure 2A**). When 20 mg/g chitosan to CLP was added, the zeta potential of CLP was reversed from negative (−27 mV) to positive (17.6 mV), showing overcompensation of the surface charge by chitosan. The overcompensation can be explained as follows. Firstly, chitosan could easily adsorb onto the surfaces of CLPs, which was mainly driven by the large entropy gain of the released counterions from both CLPs and chitosan (Kronberg et al., 2014). Secondly, once adsorbed, columbic attraction, hydrogen bonding and van der Waals forces were the attraction forces between chitosan and CLP. The adsorption also caused conformational entropy loss of chitosan, yet this was much smaller relative to the entropy gain of the released counterions. On the basis of adsorption, the overcompensation could happen as the absolute charge density of chitosan (apparent zeta potential +54.4 mV) (**Figure S2**) was higher than that of CLPs (−27 mV). However, at the mass ratio 20 mg/g chitosan to CLP, the amount of chitosan was not sufficiently high to cover all the surfaces of CLPs, which was indicated by the broad

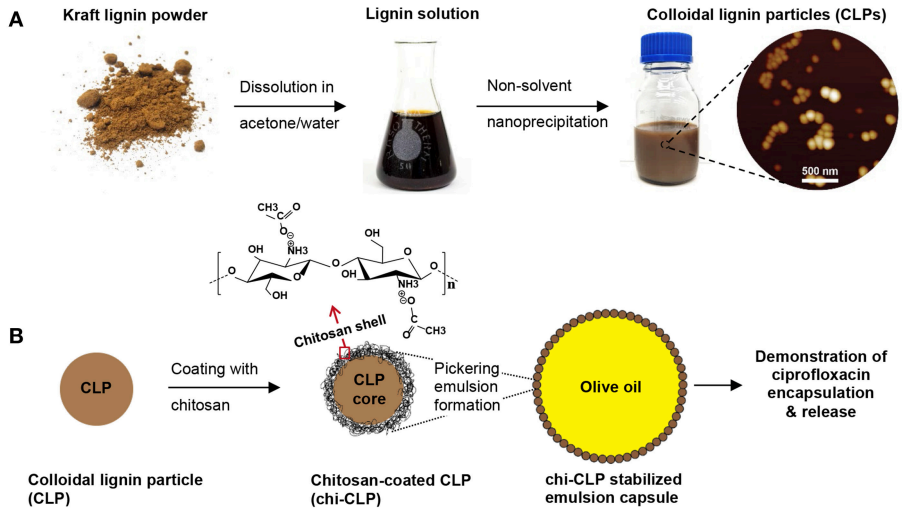

FIGURE 1 | General scheme of this work. **(A)** Preparation of colloidal lignin particles (CLPs). **(B)** Coating of CLPs with chitosan for forming Pickering emulsion with olive oil, and demonstration of the emulsion capsules for drug delivery. Note: not drawn to scale.

particle diameter distribution and not high enough positive surface charge of chi-CLP20 (**Figure S3**).

At the mass ratio of 35 mg/g chitosan to CLP, the chi-CLP35 exhibited a higher surface charge density (24.6 mV) than that of chi-CLP20 (17.6 mV), and the resulting particle diameter distribution of chi-CLP35 (PDI 0.25) was also much narrower than that of chi-CLP20 (PDI 0.43) (**Figure 2B** and **Figure S3**). Those values indicated that, at 35 mg/g, the CLPs were efficiently covered by chitosan, and thus the chi-CLP dispersion became stable. Higher mass ratios of chitosan to CLP resulted in similar particle diameter distributions (**Figure S3**) compared to that obtained at 35 mg/g, but a slight increase in the particle diameter as well as zeta potential was observed (**Figure 2B**). Such observation resulted from the presence of excess chitosan in the aqueous phase. With excess chitosan relative to the CLP surfaces, large chitosan molecules were more prone to adsorb than the smaller ones due to lower solubility/stability of large chitosan molecules in solution. This phenomenon has been described in detail elsewhere (Fu and Santore, 1998; Terada et al., 2004; Kronberg et al., 2014). The adsorption of chitosan to lignin surface was also studied by using QCM-D. It was shown in **Figure 2C** that, the adsorption of chitosan on lignin film was rather slow, probably due to the low negative charge of lignin. Comparing to CLPs that formed via self-assembly, lignin film that was prepared by spin-coating probably had a lower density of charged groups oriented toward the aqueous phase. In addition, the low value of sensed mass Δm and negligible change in dissipation factor ΔD detected by QCM-D indicated that the adsorbed chitosan layer on lignin surface was very thin (Rodahl and Kasemo, 1996; Naderi and Claesson, 2006).

The excess of chitosan in the aqueous phase was indicated by DLS measurement. As shown in **Figure 2D**, the increase of chitosan/CLP mass ratio from 75 to 200 mg/g resulted in a stronger dependency of the particle diameter as the function of chi-CLP concentration. The particle diameter of chi-CLP75 increased slightly with increased concentration, yet it increased significantly more in the case of chi-CLP200. Such phenomena can be explained by the increased viscosity of the aqueous media in the presence of excess chitosan. The more excess chitosan in the aqueous phase, the larger the overestimation of particle diameter determined by DLS. The swelling/deswelling of chi-CLPs could be neglected in this case, as the dispersions were diluted with pH 4.5 acetic acid and thus the pH and ionic strength remained constant throughout the experiments. As another evidence, the zeta potential remained essentially unchanged as a function of chi-CLP concentration (**Figure 2E**). The unchanged zeta potential also indicated that no detectable desorption of chitosan occurred upon dilution.

Effect of Chitosan to CLP Mass Ratio on Emulsion Formation

Olive oil-based Pickering emulsions were formed using 0.2 wt% chi-CLP dispersions, in which the mass ratio of chitosan to CLP varied from 0 to 200 mg/g. The volume ratio of olive oil to chi-CLP dispersion was fixed at 1:1. The emulsions were formed by ultrasonication and hand-shaking. It was found that, the mass ratio of chitosan to CLP had a strong effect on the properties of the emulsions that formed by ultrasonication. At low mass ratio of chitosan to CLP ($\leq$20 mg/g), the formed emulsions were poor that showed broad biphasic diameter distributions of the oil droplets (**Figure 3B** and **Figure S4**). However, with a higher mass ratio of chitosan to CLP at 35 mg/g, a strong increase of the fraction of small oil droplets with diameter between ca. 10 to 100 μm and reduction in droplets between 100 to 1,000 μm occurred (**Figure S4**). Effectively, optical microscopic images showed that oil droplets from around 10 to 100 μm dominated the diameter distribution (**Figure 3B**). This transition happened in accordance with the partial to efficient coverage of CLPs by chitosan from 20 to 35 mg/g mass ratios. We can therefore conclude that a sufficient coverage of CLPs by chitosan is essential

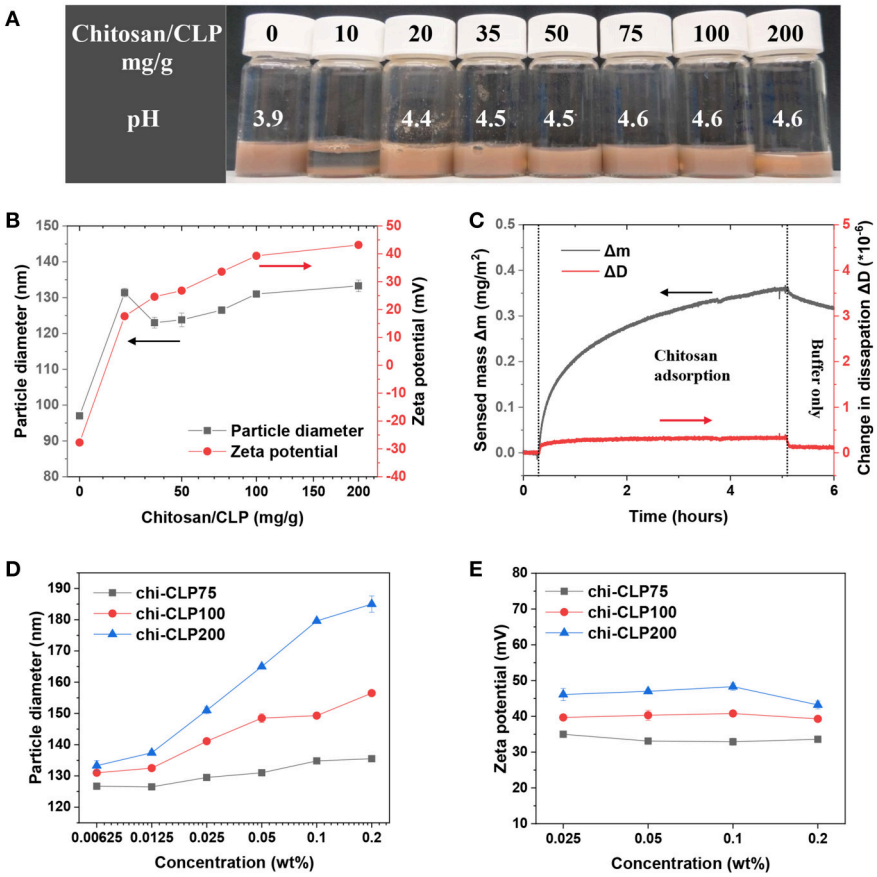

FIGURE 2 | Characterization of coating of CLPs with chitosan. **(A)** Photograph of the chi-CLP dispersions (0.2 wt%, with chitosan-to-CLP mass ratio varying from 0 to 200 mg/g) after storage for 2 h. **(B)** Particle diameter and zeta potential of chi-CLPs plotted against the mass ratio of chitosan to CLP. **(C)** QCM-D analysis of adsorbed mass of chitosan on lignin surface. **(D)** Particle diameter of chi-CLP75, chi-CLP100, and chi-CLP200 plotted against the chi-CLP concentration, chi-CLP dispersions were diluted with pH 4.5 aqueous acetic acid. **(E)** Zeta potential of chi-CLP75, chi-CLP100, and chi-CLP200 plotted against chi-CLP concentration, chi-CLP dispersions were diluted with pH 4.5 aqueous acetic acid. The error bars in **(B,D,E)** denote the standard deviations of three replicates. Note: chi-CLP10 was not measurable by DLS due to strong aggregation and sedimentation.

for stabilization of olive oil in water. This finding correlates well with the limited emulsification capacity of regular anionic CLPs (Sipponen et al., 2017) and good emulsification capacity of cationic chitosan for triglycerides (Schulz et al., 1998; Del Blanco et al., 1999; Rodríguez et al., 2002). When the mass ratio of chitosan to CLP was increased to 50 mg/g, the distribution of the droplets became nearly monophasic, the droplets mainly distributed between 10 to 100 μm and the "macro" droplets from 100 to 1,000 μm vanished (**Figure S4A**). Such transition can be explained from two aspects. On the one hand, the cationic charge density along with the hydrophilicity (Zhang S. et al., 2015) of the chi-CLPs increased with higher chitosan-to-CLP coating ratio, which enhanced the attraction of chi-CLP to olive oil that contained 2 wt% of negatively charged oleic acids. On the other hand, the excess chitosan in the aqueous phase was likely involved in forming the emulsion with chi-CLP and thus reduced the coalescence of the oil droplets. The involvement of chitosan in the emulsion formation was also indicated by the fact that the average diameter of oil droplets decreased slightly further with more excess chitosan from chi-CLP50 to chi-CLP200 (**Figures 3B,C**). The mean droplet diameter nearly plateaued at ∼25 μm, which is considerably smaller size than reported for triglyceride-in-water Pickering emulsions stabilized with chitosan particles alone or as mixtures with STP (Mwangi et al., 2016a; Shah et al., 2016).

Comparison of the amounts of chi-CLPs required to obtain stable emulsions to those in the literature reveals that the emulsifier-to-oil ratios obtained in the present work are significantly lower. The stable emulsions in **Figure 3A** contained chi-CLPs at the coating ratio of 100 mg/g and at 0.2 wt% concentration that equals 0.2 wt% emulsifier relative to olive oil. Previously, 0.5 wt% of cationic lignin-coated CLPs were used in incomplete stabilization of olive oil/water emulsion (Sipponen et al., 2017), while the values for aggregated chitosan particles range from 0.3 wt% (oleic acid-in-water) (Asfour et al., 2017) to 1.2 wt% (medium chain triglycerides-in-water) (Mwangi et al., 2016b). We expect that the lower ratio of chi-CLPs that suffices for emulsion

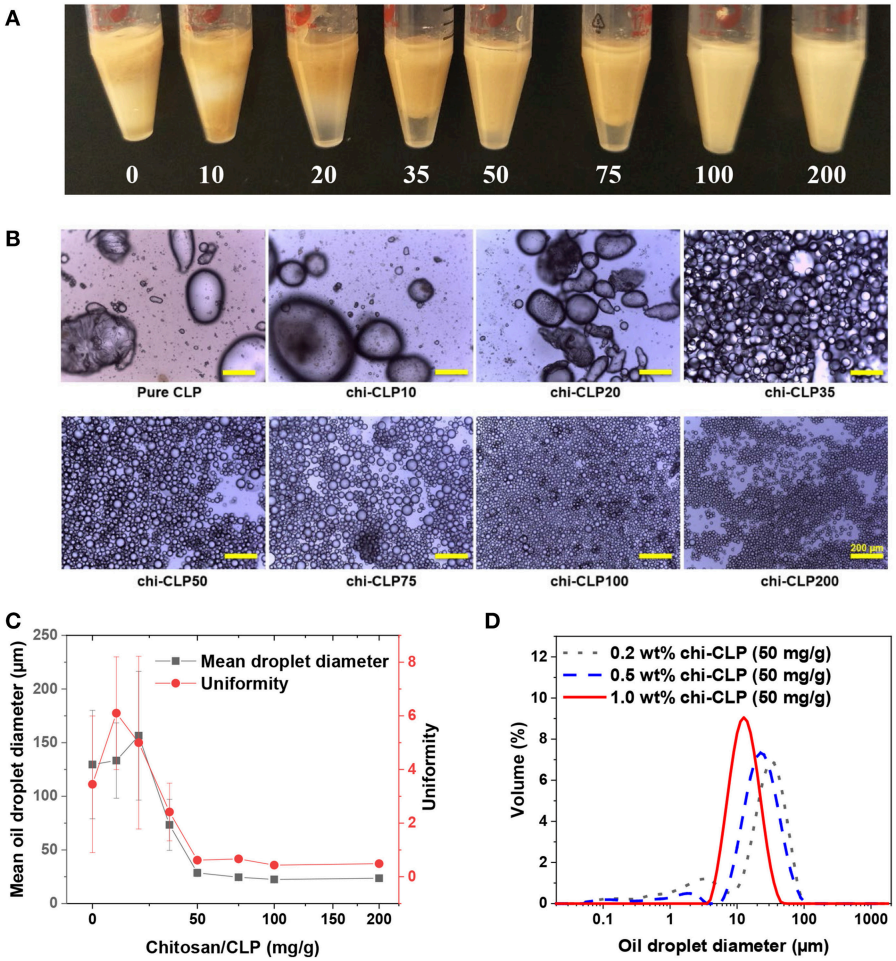

FIGURE 3 | Effect of chitosan to CLP mass ratio and chi-CLP concentration on the properties of olive oil-in-water (volume ratio 1:1) Pickering emulsions (formed by ultrasonication). **(A)** Photograph of the Pickering emulsions stabilized by 0.2 wt% chi-CLPs (0 to 200 mg/g). **(B)** Optical microscopic images of the Pickering emulsions stabilized by 0.2 wt% chi-CLPs (0 to 200 mg/g) (Scale bars: 200 μm). **(C)** Mean oil droplet diameter (d_{43}) and uniformity (according to Equation 1) plotted against the mass ratio of chitosan to CLP from 0 to 200 mg/g (0.2 wt%). The error bars denote standard deviations of six replicates. **(D)** Diameter distribution of the oil droplets stabilized by 0.2, 0.5, and 1 wt% chi-CLPs at a fixed mass ratio of 50 mg/g chitosan to CLP. Note: photograph, optical microscopic images and diameter measurements were done 24 h after emulsion formation.

stabilization in the present work stems from the large surface area and efficient assembly of the colloidal particles at the oil/water interface.

Interestingly, when comparing the emulsions that formed by hand-shaking. Even chi-CLP10 succeeded in forming the emulsion with olive oil, while pure CLP failed to do so. Additionally, optical microscopic images showed that all the emulsions showed broad droplet diameter distributions ranging from a few to hundreds micrometers regardless of chitosan to CLP mass ratio (**Figure S5**). This is reasonable, because the energy input generated by manual shaking is much lower and inhomogeneous compared to that of ultrasonication. As a consequence, hand-shaking could not produce small and uniform emulsion droplets even with the presence of excess chitosan.

Effect of chi-CLP Concentration on Emulsion Formation

Aforementioned results showed that the minimum coating ratio at which the emulsions became nearly monophasic was 50 mg/g chitosan to CLP. Therefore, this mass ratio was fixed for studying the effect of chi-CLP concentration on the emulsion properties. Three different concentrations of chi-CLP dispersions (0.2, 0.5, and 1 wt% chi-CLP) were used to form emulsions with olive oil (volume ratio 1:1) by ultrasonication. As anticipated, higher concentration of chi-CLP dispersion resulted in emulsions with smaller mean droplet diameter and better uniformity (**Figure 3D**). This phenomenon can be understood from the perspective of diffusive and adsorptive kinetics of the chi-CLPs. At higher concentration of the chi-CLP dispersion, a shorter diffusion time of the particles to the oil/water interfaces and a faster adsorption occurs due to shorter diffusion distances.

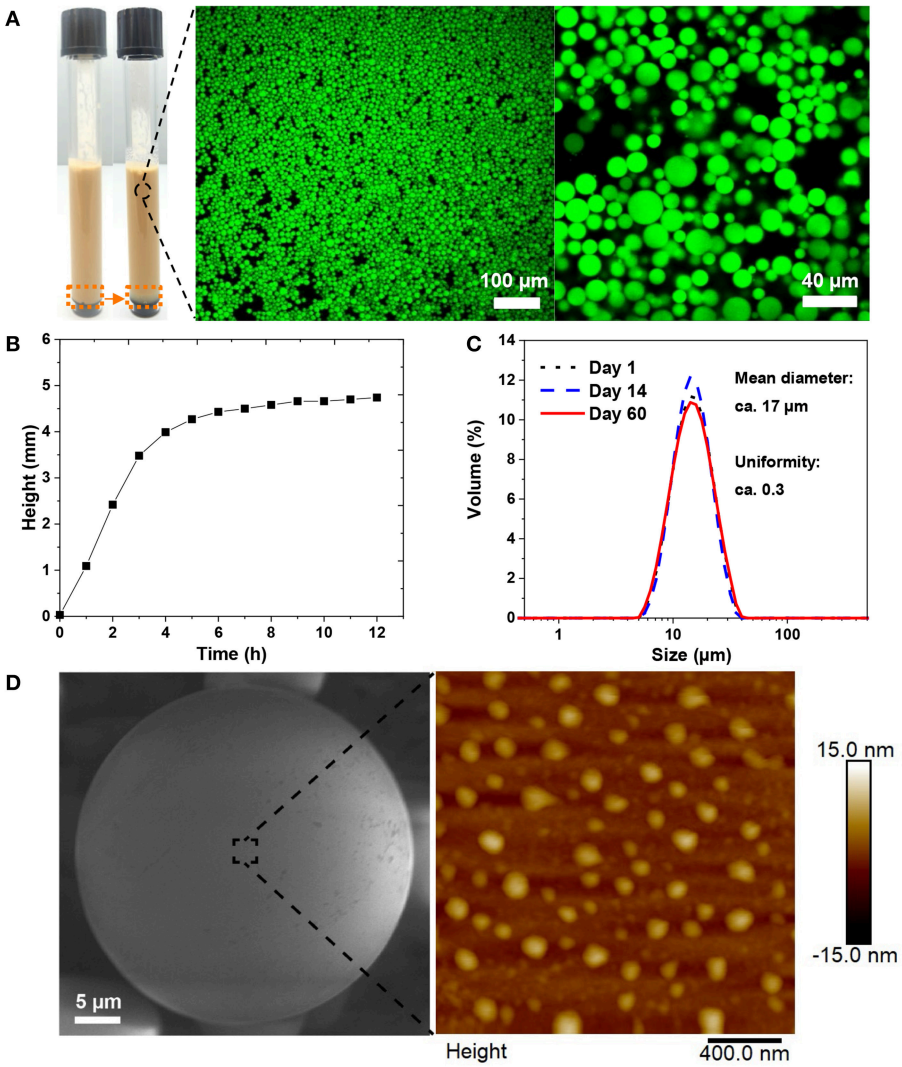

FIGURE 4 | Stability and surface morphology of the emulsion stabilized by 1 wt% chi-CLP (50 mg/g). **(A)** Photograph of the emulsion (before and after creaming) and the corresponding confocal microscopic images of the emulsion (oil was stained by Nile red). **(B)** Creaming behavior of the emulsion, measured with Turbiscan (height was chosen at the backscattered intensity 0.5 (**Figure S9**) and rescaled by starting from 0, corresponding to the height change marked by orange dash boxes in **A**). **(C)** Diameter distributions of the oil droplets on day 1, day 14, and day 60 from emulsion formation. **(D)** Surface morphology of a single oil droplet covered by STP cross-linked chi-CLPs, imaged with E-SEM (left, oil was solidified at −20°C) and AFM (right, measured at ambient conditions).

As a consequence, the oil droplets were more efficiently and rapidly covered by the chi-CLPs during the transient mixture of oil and water caused by ultrasonication, which therefore resulted in less coalescence of the oil droplets during formation. Finally, an emulsion with smaller and more uniform droplets was obtained. At the highest concentration (1 wt%) of chi-CLP dispersion, the formed emulsion showed the smallest mean droplet diameter of ca. Seventeen micrometer with the most uniform diameter distribution (**Figures 3D**, **4A**). Such uniformity value of ca. 0.3 outperforms the uniformity of 0.5 reported for palm oil/water Pickering emulsion stabilized by aggregated chitosan particles (Mwangi et al., 2016a). As another comparison, chitosan molecule alone could not result in such uniform droplets with olive oil, even at the concentration of 1 wt% (**Figure S6**). Furthermore, long term observation (over 6 months) found that the emulsions stabilized by chitosan molecules were much less stable than those stabilized by chi-CLPs (**Figure S7**). Additionally, calculated from the data in **Figure 4A**, the emulsion stability index (volume ratio of the emulsion layer to the total volume) was nearly one, which is obviously much higher than that obtained with cationic colloidal lignin particles (Sipponen et al., 2017).

Stability and Surface Morphology of the Emulsion

The emulsion stabilized by 1 wt% chi-CLP (50 mg/g) was selected for further stability test. In general, the emulsion exhibited a strong stability against coalescence, where the droplet

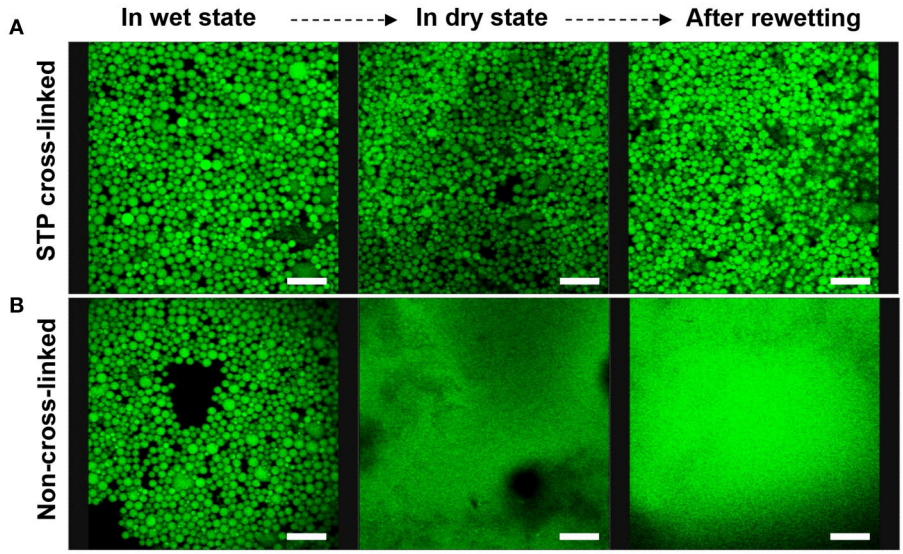

FIGURE 5 | Confocal microscopic images of sodium triphosphate (STP) cross-linked and non-cross-linked olive oil-in-water (volume ratio 1:1) Pickering emulsions stabilized by 1 wt% chi-CLP (50 mg/g) (Scale bars: 80 μm). **(A)** STP cross-linked emulsion in wet state (oil droplets in water), in dry state (water evaporated at room temperature), and after rewetting with deionized water. **(B)** Non-cross-linked emulsion in wet state, dry state and after rewetting as the reference.

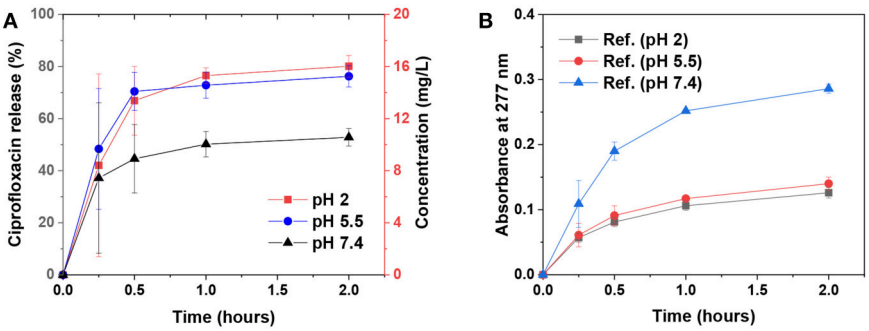

FIGURE 6 | Ciprofloxacin release from the emulsion capsules [stabilized by 1 wt% chi-CLP (50 mg/g)] to the buffer solutions at various pH values. **(A)** Ciprofloxacin release kinetics at pH 2, 5.5, and 7.4 at 37°C, mean values ± standard deviations of four replicate samples are shown. **(B)** Absorbance of the reference samples (without ciprofloxacin) at 277 nm measured under same conditions as the ciprofloxacin-loaded samples, mean values ± absolute deviations of two replicates are shown.

diameter distribution of the emulsion did not change over 2 months (**Figure 4C**). Such strong stability resulted from the high energy requirement for the desorption of chi-CLPs from oil/water interface and the positive charge of the chi-CLPs that providing electrostatic stabilization (Binks and Clint, 2002; Rayner et al., 2014). In addition, the relative high viscosity (**Figure 4B**) also contributed to the high stability of the emulsion. As a consequence, the emulsion could be utilized for drug storage purposes, since many drugs are degradable when exposed to oxygen and UV light, which can be inhibited by the antioxidative, and UV shielding properties of the lignin nanoparticles (Farooq et al., 2019).

The surface morphology of the capsule was rather smooth when observed under environmental SEM (**Figure 4D**, left). A closer observation by AFM showed that the particles were partly embedded in the oil droplets (**Figure 4D**, right). SEM also showed that a longer exposure of the frozen droplet to the electron beam could expose the embedded chi-CLPs from the surface of the oil droplet (**Figure S8**). Such observations indicated that the chi-CLPs had a strong affinity to the oil.

Ionic Cross-Linking of the Emulsion Capsules for Enhanced Mechanical Performance

The emulsion stabilized by 1 wt% chi-CLP (50 mg/g) was selected for the ionic cross-linking study. Instead of covalent cross-linking of chi-CLPs, ionic cross-linking is reversible, and can be done easily at ambient conditions. In this work, sodium triphosphate (STP) was used because it has low toxicity (Human

and Environmental Risk Assessment, CAS: 7758-29-4)[1] and has been used successfully in cross-linking chitosan (Mwangi et al., 2016a; Shah et al., 2016; Larbi-Bouamrane et al., 2017). The ionic cross-linking of chi-CLP by STP followed similar mechanism as the CLP coating by chitosan. Briefly, the replacement of the monovalent counterions of chitosan by trivalent triphosphate resulted in a large entropy gain. After cross-linking of the emulsion capsules, the mechanical stability of the oil droplets increased significantly. The oil could still be retained in the chi-CLP capsules even after drying and rewetting, indicating that the corona of the capsules was very strong (**Figure 5A**). In comparison, the non-cross-linked emulsion capsules easily broke down after drying and released the oil (**Figure 5B**). Similar observation was confirmed by optical microscopy, which showed that the cross-linked emulsion capsules retained their round shape after drying, yet the non-cross-linked ones were broken up to irregular shapes (**Figure S10**). With the exception of organic/inorganic capsules prepared by emulsion polymerization (Zhang et al., 2010; Wang et al., 2012), essentially all of the prior works have visualized shell rupture of Pickering capsules upon drying (van Rijn et al., 2011; Sipponen et al., 2017). In addition to their enhanced stability, the rewettable emulsion capsules prepared in the current work enable changing the aqueous phase or forced diffusion of oleophilic substances into the capsules by water evaporation. Besides, compared to the covalent epoxy cross-linking of lignin capsules demonstrated by Tortora et al. (2014), our approach is reversible. The ionic cross-linkers are released into aqueous phase upon dilution by water due to the deprotonation of the protonated primary amine groups (pK_a 6.5), which is beneficial for dissembling of the capsules that serve as drug carriers.

Ciprofloxacin Release From the Emulsion Capsules at Various PH Values

The biocompatibility of various types of lignins is currently under intense investigation. Recent studies have indicated that kraft lignin and alkali lignin are not antiproliferative and instead mostly biocompatible (Tortora et al., 2014; Dai et al., 2017; Figueiredo et al., 2017). We selected ciprofloxacin as a model drug for the release demonstration by the emulsion capsule which was stabilized by 1 wt% chi-CLP (50 mg/g). Ciprofloxacin is an antibiotic drug (Zeiler and Grohe, 1986) that has potential synergic effect with chi-CLPs that likely possess antimicrobial activities (Croisier and Jérôme, 2013; Beisl et al., 2017). The drug release experiment was conducted under simulated physiological conditions, i.e., at pH 2, 5.5, and 7.4 at 37°C. As shown in **Figure 6A**, the release rate of ciprofloxacin from the capsule to the buffer was rather fast regardless of the pH. The leveling-off concentration was lower at pH 7.4 compared to that of pH 2 and 5.5, mainly because lower aqueous solubility of the drug at higher pH (Maurer et al., 1998). The fast release was related to the small diameter of the droplets, which were well-dispersed in the buffer at the initial stage. Additionally, the chi-CLP coating of the oil droplets allowed rapid diffusion and leakage of the drug from inter-particle pores. Apart from that, the reference samples (without ciprofloxacin) showed that the emulsion capsules were much more stable at acid pH compared to pH 7.4, where the absorbance at 277 nm indicated partial dissolution of CLPs (**Figure 6B**). From this perspective, the microcapsules can be beneficial for an intestinal drug delivery, since the dissolution of CLPs at higher pH can result in a larger porosity of the capsules and thus faster drug release.

[1]*Human and Environmental Risk Assessment, CAS: 7758-29-4.* Available online at: https://www.heraproject.com/files/13-f-04-%20hera%20stpp%20full%20web%20wd.pdf (accessed December 21, 2018).

CONCLUSION

In this study, the important parameters for the preparation of colloidally stable chitosan-coated CLPs and their application for emulsion stabilization were studied. We found that the thin film coating of CLPs by chitosan significantly improved their emulsification capacity for olive oil. In addition, the uniformity of the emulsion droplets could be further improved at a higher concentration of chitosan-coated CLP (chi-CLP) dispersion. The obtained Pickering emulsions exhibited strong stability against coalescence, and the droplet diameter distribution remained almost unchanged for over 2 months. The positively charged chi-CLP layer locating at the oil/water interface could be electrostatically cross-linked by sodium triphosphate, which resulted in enhanced mechanical stability of the emulsion capsules. Such microcapsule with the shell that mainly comprised of CLPs are beneficial for instance for drug storage purposes, since CLPs possess antioxidative and UV-shielding properties. On the other hand, the cationic net charge of the microcapsules due to chitosan is also interesting with respect to bioadhesion and drug delivery into cells. Ongoing work in our laboratory is focused on closer investigation of these interactions of colloidal lignin particles with living cells.

AUTHOR CONTRIBUTIONS

TZ designed and carried out the experiments under the guidance of MS. The results were analyzed by TZ with input from MS and MÖ. The manuscript was drafted by TZ with contributions from all of the authors.

ACKNOWLEDGMENTS

This work made use of Aalto University Bioeconomy Facilities. The authors acknowledge Dr. Jani Seitsonen, Dr. Juan José Valle Delgado, Dr. Siqi Huan, and Dr. Long Bai for technical assistance. TZ acknowledges funding from the Novo Nordisk Foundation (SUSCELL project, Reference Number: NNF17OC0027658). MS and MÖ acknowledge Academy of Finland for funding (Grants 296547 and 278279, respectively).

SUPPLEMENTARY MATERIAL

The Supplementary Material for this article can be found online at: https://www.frontiersin.org/articles/10.3389/fchem.2019.00370/full#supplementary-material

REFERENCES

Ago, M., Huan, S., Borghei, M., Raula, J., Kauppinen, E. I., and Rojas, O. J. (2016). High-throughput synthesis of lignin particles (∼30 nm to ∼2 μm) via aerosol flow reactor: size fractionation and utilization in Pickering emulsions. *ACS Appl. Mater. Interfaces* 8, 23302–23310. doi: 10.1021/acsami.6b07900

Asfour, M. H., Elmotasem, H., Mostafa, D. M., and Salama, A. A. A. (2017). Chitosan based Pickering emulsion as a promising approach for topical application of rutin in a solubilized form intended for wound healing: *in vitro* and *in vivo* study. *Int. J. Pharm.* 534, 325–338. doi: 10.1016/j.ijpharm.2017.10.044

Ashok, R. P. B., Oinas, P., Lintinen, K., Sarwar, G., Kostiainen, M. A., and Österberg, M. (2018). Techno-economic assessment for the large-scale production of colloidal lignin particles. *Green Chem.* 20, 4911–4919. doi: 10.1039/C8GC02805B

Beisl, S., Friedl, A., and Miltner, A. (2017). Lignin from micro- to nanosize: applications. *Int. J. Mol. Sci.* 18:2367. doi: 10.3390/ijms18112367

Berton-Carabin, C. C., and Schroën, K. (2015). Pickering emulsions for food applications: background, trends, and challenges. *Annu. Rev. Food Sci. Technol.* 6, 263–297. doi: 10.1146/annurev-food-081114-110822

Binks, B. P. (2002). Particles as surfactants—similarities and differences. *Curr. Opin. Colloid Interface Sci.* 7, 21–41. doi: 10.1016/S1359-0294(02)00008-0

Binks, B. P., and Clint, J. H. (2002). Solid wettability from surface energy components: relevance to Pickering emulsions. *Langmuir* 18, 1270–1273. doi: 10.1021/la011420k

Chen, N., Dempere, L. A., and Tong, Z. (2016). Synthesis of pH-responsive lignin-based nanocapsules for controlled release of hydrophobic molecules. *ACS Sustain. Chem. Eng.* 4, 5204–5211. doi: 10.1021/acssuschemeng.6b01209.

Croisier, F., and Jérôme, C. (2013). Chitosan-based biomaterials for tissue engineering. *Eur. Polym. J.* 49, 780–792. doi: 10.1016/j.eurpolymj.2012.12.009

Dai, L., Liu, R., Hu, L.-Q., Zou, Z.-F., and Si, C.-L. (2017). Lignin nanoparticle as a novel green carrier for the efficient delivery of resveratrol. *ACS Sustain. Chem. Eng.* 5, 8241–8249. doi: 10.1021/acssuschemeng.7b01903

Del Blanco, L. F., Rodriguez, M. S., Schulz, P. C., and Agulló, E. (1999). Influence of the deacetylation degree on chitosan emulsification properties. *Colloid Polym Sci.* 277, 1087–1092. doi: 10.1007/s003960050495

Farooq, M., Zou, T., Riviere, G., Sipponen, M. H., and Österberg, M. (2019). Strong, ductile, and waterproof cellulose nanofibril composite films with colloidal lignin particles. *Biomacromolecules* 20, 693–704. doi: 10.1021/acs.biomac.8b01364

Figueiredo, P., Lintinen, K., Kiriazis, A., Hynninen, V., Liu, Z., Bauleth-Ramos, T., et al. (2017). *In vitro* evaluation of biodegradable lignin-based nanoparticles for drug delivery and enhanced antiproliferation effect in cancer cells. *Biomaterials* 121, 97–108. doi: 10.1016/j.biomaterials.2016.12.034

Fu, Z., and Santore, M. M. (1998). Kinetics of competitive adsorption of PEO chains with different molecular weights. *Macromolecules* 31, 7014–7022. doi: 10.1021/ma980042w

Kalepu, S., Manthina, M., and Padavala, V. (2013). Oral lipid-based drug delivery systems—an overview. *Acta Pharm. Sin. B* 3, 361–372. doi: 10.1016/j.apsb.2013.10.001

Kronberg, B., Holmberg, K., and Lindman, B. (2014). *Surface Chemistry of Surfactants and Polymers*. Chichester, UK: John Wiley & Sons.

Larbi-Bouamrane, O., Bal, Y., Aliouche,1, D., Cote, G., and Chagnes, A. (2017). Preparation and characterization of cross-linked chitosan microcapsules for controlled delivery of oxytetracycline. *Indian J. Pharm. Sci.* 78, 715–724. doi: 10.4172/pharmaceutical-sciences.1000175

Laurichesse, S., and Avérous, L. (2014). Chemical modification of lignins: towards biobased polymers. *Prog. Polym. Sci.* 39, 1266–1290. doi: 10.1016/j.progpolymsci.2013.11.004

Leskinen, T., Smyth, M., Xiao, Y., Lintinen, K., Mattinen, M.-L., Kostiainen, M. A., et al. (2017a). Scaling up production of colloidal lignin particles. *Nordic Pulp Paper Res. J.* 32, 586–596. doi: 10.3183/NPPRJ-2017-32-04-p586-596

Leskinen, T., Witos, J., Valle-Delgado, J. J., Lintinen, K., Kostiainen, M., Wiedmer, S. K., et al. (2017b). Adsorption of proteins on colloidal lignin particles for advanced biomaterials. *Biomacromolecules* 18, 2767–2776. doi: 10.1021/acs.biomac.7b00676

Li, C., Zhao, X., Wang, A., Huber, G. W., and Zhang, T. (2015). Catalytic transformation of lignin for the production of chemicals and fuels. *Chem. Rev.* 115, 11559–11624. doi: 10.1021/acs.chemrev.5b00155

Lievonen, M., Valle-Delgado, J. J., Mattinen, M.-L., Hult, E.-L., Lintinen, K., Kostiainen, M. A., et al. (2016). A simple process for lignin nanoparticle preparation. *Green Chem.* 18, 1416–1422. doi: 10.1039/C5GC01436K

Lintinen, K., Xiao, Y., Ashok, R. B., Leskinen, T., Sakarinen, E., Sipponen, M., et al. (2018). Closed cycle production of concentrated and dry redispersible colloidal lignin particles with a three solvent polarity exchange method. *Green Chem.* 20, 843–850. doi: 10.1039/C7GC03465B

Maurer, N., Wong, K. F., Hope, M. J., and Cullis, P. R. (1998). Anomalous solubility behavior of the antibiotic ciprofloxacin encapsulated in liposomes: a 1H-NMR study. *Biochim. Biophys. Acta Biomembr.* 1374, 9–20. doi: 10.1016/S0005-2736(98)00125-4

McClements, D. J. (2015). *Food Emulsions : Principles, Practices, and Techniques*, 3rd Edn. Boca Raton, FL: CRC Press. doi: 10.1201/b18868

Mwangi, W. W., Ho, K.-W., Ooi, C.-W., Tey, B.-T., and Chan, E.-S. (2016a). Facile method for forming ionically cross-linked chitosan microcapsules from Pickering emulsion templates. *Food Hydrocolloids* 55, 26–33. doi: 10.1016/j.foodhyd.2015.10.022

Mwangi, W. W., Ho, K.-W., Tey, B.-T., and Chan, E.-S. (2016b). Effects of environmental factors on the physical stability of Pickering-emulsions stabilized by chitosan particles. *Food Hydrocolloids* 60, 543–550. doi: 10.1016/j.foodhyd.2016.04.023

Naderi, A., and Claesson, P. M. (2006). Adsorption properties of polyelectrolyte–surfactant complexes on hydrophobic surfaces studied by QCM-D. *Langmuir* 22, 7639–7645. doi: 10.1021/la061118h

Nypelö, T. E., Carrillo, C. A., and Rojas, O. J. (2015). Lignin supracolloids synthesized from (W/O) microemulsions: use in the interfacial stabilization of Pickering systems and organic carriers for silver metal. *Soft Matter* 11, 2046–2054. doi: 10.1039/C4SM02851A

Pavinatto, F. J., Caseli, L., and Oliveira, O. N. (2010). Chitosan in Nanostructured Thin Films. *Biomacromolecules* 11, 1897–1908. doi: 10.1021/bm1004838.

Pickering, S. U. (1907). CXCVI.—Emulsions. *J. Chem. Soc. Trans.* 91, 2001–2021. doi: 10.1039/CT9079102001

Pouton, C. W., and Porter, C. J. H. (2008). Formulation of lipid-based delivery systems for oral administration: materials, methods and strategies. *Adv. Drug Deliv. Rev.* 60, 625–637. doi: 10.1016/j.addr.2007.10.010

Ragauskas, A. J., Beckham, G. T., Biddy, M. J., Chandra, R., Chen, F., Davis, M. F., et al. (2014). Lignin valorization: improving lignin processing in the biorefinery. *Science* 344:1246843. doi: 10.1126/science.1246843

Rayner, M., Marku, D., Eriksson, M., Sjöö, M., Dejmek, P., and Wahlgren, M. (2014). Biomass-based particles for the formulation of Pickering type emulsions in food and topical applications. *Colloids Surf. A* 458, 48–62. doi: 10.1016/j.colsurfa.2014.03.053

Rodahl, M., and Kasemo, B. (1996). Frequency and dissipation-factor responses to localized liquid deposits on a QCM electrode. *Sens. Actuat. B Chem.* 37, 111–116. doi: 10.1016/S0925-4005(97)80077-9

Rodríguez, M. S., Albertengo, L. A., and Agulló, E. (2002). Emulsification capacity of chitosan. *Carbohydr. Polym.* 48, 271–276. doi: 10.1016/S0144-8617(01)00258-2

Salas, C., Rojas, O. J., Lucia, L. A., Hubbe, M. A., and Genzer, J. (2013). On the surface interactions of proteins with lignin. *ACS Appl. Mater. Interfaces* 5, 199–206. doi: 10.1021/am3024788

Sauerbrey, G. (1959). The use of quarts oscillators for weighing thin layers and for microweighing. *Z. Phys.* 155, 206–222.

Schulz, P. C., Rodríguez, M. S., Del Blanco, L. F., Pistonesi, M., and Agulló, E. (1998). Emulsification properties of chitosan. *Colloid Polym. Sci.* 276, 1159–1165. doi: 10.1007/s003960050359

Shah, B. R., Li, Y., Jin, W., An, Y., He, L., Li, Z., et al. (2016). Preparation and optimization of Pickering emulsion stabilized by chitosan-tripolyphosphate nanoparticles for curcumin encapsulation. *Food Hydrocolloids* 52, 369–377. doi: 10.1016/j.foodhyd.2015.07.015

Sipponen, M. H., Farooq, M., Koivisto, J., Pellis, A., Seitsonen, J., and Österberg, M. (2018a). Spatially confined lignin nanospheres for biocatalytic ester synthesis in aqueous media. *Nat. Commun.* 9:2300. doi: 10.1038/s41467-018-04715-6

Sipponen, M. H., Lange, H., Ago, M., and Crestini, C. (2018b). Understanding lignin aggregation processes. A case study: budesonide entrapment and stimuli

controlled release from lignin nanoparticles. *ACS Sustain. Chem. Eng.* 6, 9342–9351. doi: 10.1021/acssuschemeng.8b01652

Sipponen, M. H., Smyth, M., Leskinen, T., Johansson, L.-S., and Österberg, M. (2017). All-lignin approach to prepare cationic colloidal lignin particles: stabilization of durable Pickering emulsions. *Green Chem.* 19, 5831–5840. doi: 10.1039/C7GC02900D

Smallwood, I. (2012). *Handbook of Organic Solvent Properties*. Oxford, UK: Butterworth-Heinemann.

Tang, J., Quinlan, P. J., and Tam, K. C. (2015). Stimuli-responsive Pickering emulsions: recent advances and potential applications. *Soft Matter* 11, 3512–3529. doi: 10.1039/C5SM00247H

Terada, E., Samoshina, Y., Nylander, T., and Lindman, B. (2004). Adsorption of cationic cellulose derivatives/anionic surfactant complexes onto solid surfaces. *I. Silica Surf. Langmuir* 20, 1753–1762. doi: 10.1021/la035626s

Tortora, M., Cavalieri, F., Mosesso, P., Ciaffardini, F., Melone, F., and Crestini, C. (2014). Ultrasound driven assembly of lignin into microcapsules for storage and delivery of hydrophobic molecules. *Biomacromolecules* 15, 1634–1643. doi: 10.1021/bm500015j

van Rijn, P., Mougin, N. C., Franke, D., Park, H., and Böker, A. (2011). Pickering emulsion templated soft capsules by self-assembling cross-linkable ferritin– polymer conjugates. *Chem. Commun.* 47, 8376–8378. doi: 10.1039/C1CC12005K

Wang, X., Zhou, W., Cao, J., Liu, W., and Zhu, S. (2012). Preparation of core–shell CaCO3 capsules via Pickering emulsion templates. *J. Colloid Interface Sci.* 372, 24–31. doi: 10.1016/j.jcis.2012.01.018

Wei, Z., Yang, Y., Yang, R., and Wang, C. (2012). Alkaline lignin extracted from furfural residues for pH-responsive Pickering emulsions and their recyclable polymerization. *Green Chem.* 14, 3230–3236. doi: 10.1039/C2GC36278C

Yang, Y., Fang, Z., Chen, X., Zhang, W., Xie, Y., Chen, Y., et al. (2017). An overview of Pickering emulsions: solid-particle materials, classification, morphology, and applications. *Front. Pharmacol.* 8:287. doi: 10.3389/fphar.2017.00287

Yang, Y., Wei, Z., Wang, C., and Tong, Z. (2013). Lignin -based Pickering HIPEs for macroporous foams and their enhanced adsorption of copper(ii) ions. *Chem. Commun.* 49, 7144–7146. doi: 10.1039/C3CC42270D

Zeiler, H.-J., and Grohe, K. (1986). "The *in vitro* and *in vivo* activity of ciprofloxacin," in *Ciprofloxacin: Microbiology—Pharmacokinetics—Clinical Experience Current Topics in Infectious Diseases and Clinical Microbiology*, eds H. C. Neu and D. S. Reeves (Wiesbaden: Vieweg+Teubner Verlag), 14–18. doi: 10.1007/978-3-663-01930-5_3

Zhang, C., Cui, F., Zeng, G., Jiang, M., Yang, Z., Yu, Z., et al. (2015). Quaternary ammonium compounds (QACs): a review on occurrence, fate and toxicity in the environment. *Sci. Total Environ.* 518–519, 352–362. doi: 10.1016/j.scitotenv.2015.03.007

Zhang, K., Wu, W., Guo, K., Chen, J., and Zhang, P. (2010). Synthesis of Temperature-responsive Poly(N-isopropyl acrylamide)/Poly(methyl methacrylate)/Silica Hybrid capsules from inverse Pickering emulsion polymerization and their application in controlled drug release. *Langmuir* 26, 7971–7980. doi: 10.1021/la904841m

Zhang, S., Zhou, Y., and Yang, C. (2015). Pickering emulsions stabilized by the complex of polystyrene particles and chitosan. *Colloids Surf. A Physicochem. Eng. Aspects* 482, 338–344. doi: 10.1016/j.colsurfa.2015.06.029

Conflict of Interest Statement: The authors declare that the research was conducted in the absence of any commercial or financial relationships that could be construed as a potential conflict of interest.

The handling editor declared a shared affiliation, though no other collaboration, with TZ, MS, MÖ at time of review.

frontiers in Chemistry

ORIGINAL RESEARCH
published: 24 May 2019
doi: 10.3389/fchem.2019.00367

Spatially Resolved Crosslinking of Hydroxypropyl Cellulose Esters for the Generation of Functional Surface-Attached Organogels

*Maximilian Nau, Simon Trosien, David Seelinger, Anna K. Boehm and Markus Biesalski**

Laboratory of Macromolecular Chemistry and Paper Chemistry, Ernst-Berl Institute of Chemistry, Technische Universität Darmstadt, Darmstadt, Germany

Chemistry, geometric shape and swelling behavior are the key parameters that determine any successful use of man-made polymeric networks (gels). While understanding of the swelling behavior of both water-swellable hydrogels and organogels that swell in organic solvents can be considered well-advanced with respect to fossil fuel-based polymer networks, the understanding, in particular, of wood-derived polymers in such a network architecture is still lacking. In this work, we focus on organogels derived from hydroxypropyl cellulose (HPC) ester. The latter polymer was functionalized with saturated and unsaturated fatty acids, respectively. Due to their tailored chemical constitution, we demonstrated that such polysaccharide can be crosslinked and simultaneously surface-bound by using a photo-induced radical reaction using a photo-initiator. Based on the choice of fatty acid used in the design of the HPC ester, and by controlling the degree of substitution (DS) obtained during the esterification of the polysaccharide, modular manipulation of the physical properties (e.g., polarity) of the resulting gel is possible. Depending on the initiator employed, different wavelengths of light, from UV to visible, can be utilized for the crosslinking reaction, which facilitates the deployment of a range of light sources and different lithographic methods. Additionally, we showed that altering of the illumination time allows to tailor the netpoint density, and thus, the degree of linear deformation in equilibrium and the swelling kinetics. Finally, we performed a proof-of-principle experiment to demonstrate the application of our material for the generation of spatially resolved polymer patches to enrich organic molecules from a solution within a microfluidic channel.

Keywords: hydroxypropyl cellulose, surface modification, organo gels, surface patterning, photo-crosslinking

OPEN ACCESS

Edited by:
Eero Kontturi,
School of Chemical Technology, Aalto University, Finland

Reviewed by:
Bruno Jean,
UPR5301 Centre de Recherches sur les Macromolecules Végétales (CERMAV), France
Tamilselvan Mohan,
University of Maribor, Slovenia

****Correspondence:***
Markus Biesalski
biesalski@tu-darmstadt.de

Specialty section:
This article was submitted to Polymer Chemistry, a section of the journal Frontiers in Chemistry

Received: *18 January 2019*
Accepted: *03 May 2019*
Published: *24 May 2019*

Citation:
Nau M, Trosien S, Seelinger D, Boehm AK and Biesalski M (2019) Spatially Resolved Crosslinking of Hydroxypropyl Cellulose Esters for the Generation of Functional Surface-Attached Organogels. Front. Chem. 7:367. doi: 10.3389/fchem.2019.00367

INTRODUCTION

Swellable polymer networks have been extensively studied in recent decades, with subsequent development for use in a wide range of applications (Osada and Gong, 1998). In addition to hydrogels (networks that swell in water), which gained considerable attention during the last decades, because of their great potential in medicinal applications [e.g., tissue engineering (Annabi et al., 2014), drug delivery, and point-of-care diagnostics] (Rivest et al., 2007; van Tomme et al., 2008; Jagur-Grodzinski, 2009), organogels, which swell in organic solvents (Suzuki and Hanabusa, 2010), are highly interesting and offer promising perspectives in areas such as drug delivery

(Vintiloiu and Leroux, 2008; Esposito et al., 2018), food applications (Marangoni, 2012; Chaves et al., 2018), cosmetics (Kirilov et al., 2014), separation, and purification processes (Venkatesan and Sarles, 2016; Lai et al., 2018; Prati et al., 2018), as well as analytics (Hinze et al., 1996; Mukhopadhyay et al., 2006; Xue et al., 2015). In general, the three-dimensional network structure of a polymer gel can be stabilized by various molecular interactions, in which the individual molecules are connected to each other by secondary forces [such as arene-arene interactions (Ajayaghosh and Praveen, 2007), halogen (Meazza et al., 2013), van der Waals forces, hydrogen bonds, and combinations thereof (Sangeetha and Maitra, 2005; George and Weiss, 2006; Hirst et al., 2008; Datta and Bhattacharya, 2015)] or covalent chemical bonds (Segarra-Maset et al., 2013; García et al., 2014). While adjusting the structure and the properties of gels is not trivial, when they are based on small molecules that are non-covalently connected, the design of covalently bound gels is considered more modular since various functionalities can be easily introduced, e.g., by the co-polymerization of functional groups or by the control of crosslinking density through the adjustment of potential crosslinking moieties in the gel constituting molecules. Furthermore, the use of covalently linked molecules implies highly stable materials whose macroscopic shapes are easily controllable when network formation is triggered by an external stimulus, e.g., by light (Hennink and van Nostrum, 2002). To create such a polymer network photochemically, one possibility is the reaction of double bonds in a radical reaction, e.g., by using a photo-initiator systems, such as camphor quinone/tertiary amine systems (Jakubiak et al., 2003), borates (Toba et al., 1997), or benzophenone derivatives (Merlin et al., 1980).

A variety of materials have been studied for the synthesis of such gels; among these, bio-based polymers such as cellulose and cellulose derivatives have been popular (Larsson et al., 2017; Wang and Zhang, 2018). Cellulose is a highly interesting compound because it provides a large number of valuable benefits: For example, as the most abundant polymer on earth, cellulose is highly available in bulk and originates from well-developed wood-disintegration processes (Klemm et al., 2005). However, because of the low solubility of unmodified cellulose in common organic solvents (i.e., alcohols, THF, chloroform, etc.), the controlled modification of the polysaccharide is highly challenging. Typically, harsh reaction conditions are necessary for heterogeneous functionalization, and the controlled partial substitution of the biomolecule is not trivial (Klemm et al., 2005). Therefore, various solvent systems have been established to improve a specific cellulose reaction, but all of these systems entail a range of challenges (e.g., toxicity, complex workup procedures, or limited scope of the chemical reactions; Heinze and Koschella, 2005). Due to this complexity, many scientists use cellulose derivatives rather than unmodified cellulose. Presently, a variety of cellulose-derived polymers are commercially available as bulk material. One important example is hydroxypropyl cellulose (HPC), which is readily available because of its industrial use in coatings and food applications (Wüstenberg, 2014). Like native cellulose, HPC provides 3 hydroxy groups per anhydroglucose unit (AGU) and exhibits a significantly higher solubility in many common organic solvents compared to the unmodified polysaccharide. Due to this property, further modification is technologically simplified, and the molecule can be, for example, esterified with various carboxylic acids in a one-step reaction while retaining good control of the degree of substitution (DS; Nau et al., 2018). Therefore, the polysaccharide can be easily equipped with various functions, such as fluorescence labels (e.g., pyrene; Winnik et al., 1987), that can be used as macro initiators for further polymerization (Ostmark et al., 2007), and control of the film formation properties and optical properties, amongst others, is possible (Bhadani and Gray, 1983). To use HPC as a base material for functional polymer gels, different approaches have been described in the literature. Gehrke et al. chemically crosslinked HPC by treatment with divinyl sulfone and analyzed the resulting microstructure and swelling characteristics (Harsh and Gehrke, 1991; Kabra et al., 1998). Other strategies that achieved covalent network formation of HPC include reaction with methacrylic anhydride (Hoo et al., 2013), *p*-formaldehyde (Suto, 1989), dialdehydes (Suto and Yoshinaka, 1993), and isocyanates (Suto et al., 1992), the formation of disulfide bonds (Tan et al., 2011), and gamma ray or electron beam irradiation (Wach et al., 2002). With respect to the light-induced formation of swellable HPC polymer gels, very few reports have been published to date. Bhadani and Gray esterified HPC with acryloyl chloride followed by photo-crosslinking already to stabilize the mesophase structure of a cholesteric film (Bhadani and Gray, 1984). The polymer was effectively crosslinked, and the structure was stable over a broad range of temperatures, but the mechanical properties of the resulting films were not optimal. An elegant approach was very recently described by Teramoto et al. (Yano et al., 2018). In their work, HPC was first esterified with cinnamoyl chloride, which can be crosslinked by illumination with UV light. The degree of crosslinking can be controlled either by adjusting the DS or by modulating the irradiation time. However, UV light (280 nm) is required for the crosslinking reaction, and relatively high DS values (1.3–3) are necessary for efficient network formation, which dramatically limits the flexibility of the system. Therefore, it is highly desirable to develop an alternative method that is more modular regarding polarity and light source.

In the present manuscript, we report a different approach for the photo-induced chemical crosslinking of HPC as films on solid model-surfaces using radical initiators. The approach is highly efficient and versatile with respect to the light source and thus allows for spatially resolved network formation in well-defined areas by using a commercially available 405 nm laser diode combined with an x/y movement system. In contrast to lithographic methods based on the use of photomasks (Böhm et al., 2013; Kargl et al., 2013), this method provides more versatile and faster approach tosurface patterning with less instrumental effort. In the first step, we functionalized HPC in a controlled fashion with unsaturated fatty acids, which can be crosslinked by using a photo-induced radical reaction. Via subsequent co-esterification steps, various functionalities can be introduced, yielding different and tailored functions of this polysaccharide. During the crosslinking process, *in situ* attachment of the polymer network to a model surface exposing

allyl groups is possible. Consequently, we investigated the influence of the illumination time on network formation. For this purpose, the swelling process of the surface-bound gels was monitored via time-resolved confocal fluorescence microscopy. Finally, a microfluidic device was developed as a simple demonstration, in which a surface-attached functional HPC gel was used for the local upconcentration of organic model analytes, giving an interesting prospect for further research into low-instrumented sensing and/or purification devices.

MATERIALS AND METHODS

In this section, the most relevant results of the polymer synthesis are shown. For the clarity of the manuscript, further details for the syntheses and preparation procedures, a complete list of all solvents and reagents (including suppliers and purities), detailed information of all instruments and measurement methods, and details on reference experiments (bulk swelling) are shown in the **Supplementary Material**.

Polymer Synthesis

To synthesize the photo-crosslinkable polymers, we first dissolved HPC in THF (tetrahydrofuran) and then brought it to reaction with fatty acid chlorides. To generate a hydrophobic polymer, HPC was treated with stearoyl chloride (6 equiv.) and 10-undecenoyl chloride (1 equiv.) in a one-pot synthesis to afford a mixed HPC ester **1**. Details of the synthesis can be found in the **Supplementary Material**. The reaction led to degrees of substitution of 2.75 for stearoyl and 0.25 for undecenoyl moieties (DS were determined by NMR, see the **Supplementary Material**; **Figure 1**). In addition to this non-polar mixed ester, we synthesized a polar, hydrophilic polymer via the same method, which after cross-linking yielded a hydrogel rather than an organogel. To this end, we treated HPC with small amounts (0.5 equiv.) of 10 undecenoyl chloride so that hydrophilic reference ester **2** was obtained in quantitative yield, exhibiting a DS of 0.3 (**Figure 1**). Finally, the chemical structure of each polymer was characterized according to our recently published work (for details see **Supplementary Material**).

Note that stearoyl esters of cellulose are capable to form complexes with proteins such as bovine serum albumin (Niegelhell et al., 2017). For this reason, the formation of stearoyl esters, and tailored networks thereof is of particular interest.

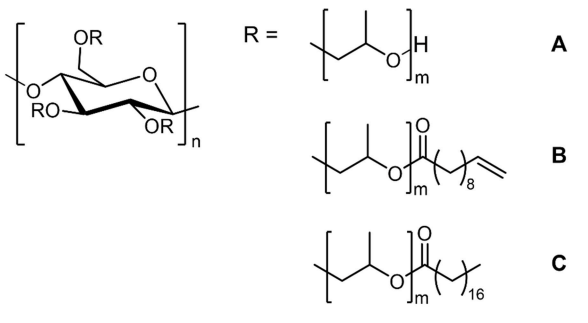

Groups per AGU:

HPC ester	A	B	C
1	-	0.25	2.75
2	2.70	0.30	-

FIGURE 1 | Synthesis of HPC esters **1** and **2**: Hydrophobic ester **1** exhibits 0.25 undecenoyl (B) and 2.75 stearoyl groups (C) per AGU, and hydrophilic ester **2** is esterified by 0.30 undecenoyl groups (B) per AGU, whereas 2.70 OH groups per AGU remain unmodified (A).

RESULTS AND DISCUSSION

Spatially Resolved Crosslinking and *in situ* Surface Attachment

Next, we were interested in designing organogels by attaching polymer **1** to the surface of a planar solid substrate in a spatially controlled fashion using a photo-initiator. Benzophenone derivatives, amongst others, are capable of generating radicals by illumination. These well-established photo-initiators provide various highly beneficial properties for the crosslinking of many systems: The activation and radical formation of benzophenone (BP) itself can be accomplished at relatively high wavelengths when compared to similar compounds (the upper absorption maximum of BP is located at $\lambda = 340$ nm; Allen et al., 1990). Consequently, it is not necessary to use high-energy light, which would otherwise be likely to damage sensitive molecules (Riga et al., 2017). Furthermore, radical formation with BP is a reversible process, implying high efficiency as an initiator (Dorman and Prestwich, 1994). If BP is functionalised with electron-donating or electron-withdrawing groups, the activation wavelength can be shifted, which allows the use of a broad range of light sources (Allen et al., 1990). To form the spatially controlled network of **1**, we decided to use a commercial laser diode ($\lambda = 405$ nm) as the light source because it is readily available and inexpensive. In addition, 405 nm light can be produced by light emitting diodes (LEDs), which opens the opportunity for the high-efficiency implementation of this method in a larger scale setting, in contrast to the use of mercury vapor lamps to generate UV radiation. Therefore, Michler's ketone [4,4′-bis(diethylamino)-benzophenone, DEABP] was found to be the most suitable initiator (see the **Supplementary Material**). To cross-link the reactive groups within the polysaccharide with functional groups on the solid substrate, appropriate pre-functionalization of the planar surface was carried out. We treated a glass slide with a mixture of allyltriethoxysilane (All-TES) and tetraethyl orthosilicate (TEOS; Ratio 15:85) by the method of Andrieu-Brunsen and co-workers (Krohm et al., 2016). Extensive characterization of this surface was reported in the literature (Krohm et al., 2016). Thus, a stable and homogeneous surface providing allyl functionalities was obtained. Note, allyl groups of All-TES are predestined for radical reactions and thus enable the polymer to be attached to the surface by a radical reaction pathway (Burkhard, 1950).

A DEABP-containing polymer solution in chloroform was solvent-casted onto the allyl-modified glass slide followed by

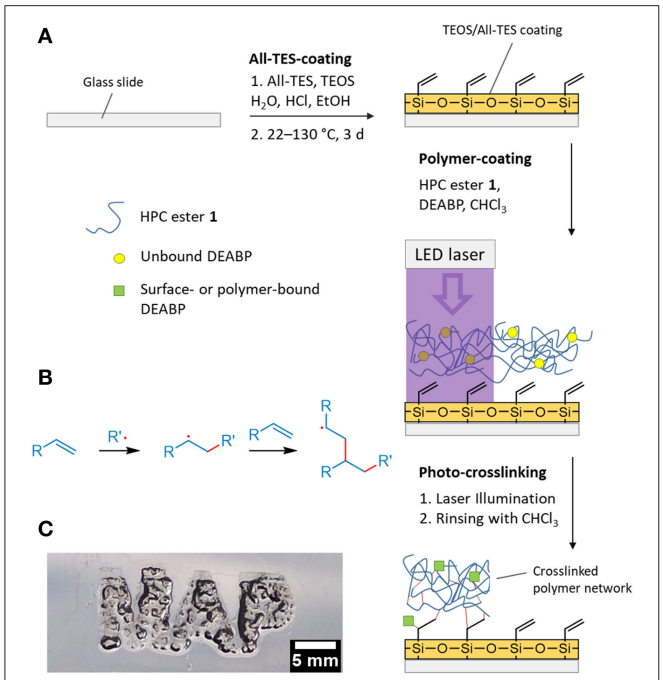

FIGURE 2 | (A) Schematic of the production of surface-bound polymer network 1 crosslinked via laser treatment; **(B)** reaction scheme of the radical reaction between generated polymer radicals and double bonds of the polymer or the All-TES surface; **(C)** photograph of the surface-attached polymer network swollen in $CHCl_3$. The illumination time used to generate the network was 20 ms with a 405 nm laser diode.

air drying and treatment with short pulses of laser light (laser-diode, 1,000 mW, 100 µm spot dia., $\lambda = 405$ nm). The actual spatial resolution of this setup is currently limited by said spot diameter. A scheme of this process is shown in **Figure 2A**. By installing the laser in a computer numerically controlled (CNC) x/y movement system (see **Supplementary Material**), the production of polymer networks with well-defined geometries was easily accomplished (resolution: 350 DPI, limited by the control system; see **Figure 2B**). Finally, any unbound polymer was removed by rinsing with $CHCl_3$, yielding a surface-bound swellable polymer network in well-defined regions (see **Figure 2**).

Next, we examined the influence of the illumination time on the generation of the polymer network by laser light. To this end, the pulse-lengths during illumination were altered between 5 and 40 ms, and the swelling behavior of the spatially confined and surface-attached polymer networks was characterized by analyzing the linear deformation parameter α (one-dimensional relative swelling degree: the thickness of the swollen polymer film divided by the thickness of the dry polymer film) in equilibrium swelling. While α refers to the linear deformation in general we introduce α_m to as an additional parameter to denote α in equilibrium state. Therefore, the film thicknesses were determined by confocal laser scanning microscopy (CLSM; for details of the analysis see the **Supplementary Material**, for still frames captured at different times see **Figure 3A**). Note that DEABP itself is non-fluorescent when excited at a wavelength of 488 nm (the wavelength used in the CLSM measurements, see below) but becomes fluorescent after the crosslinking reaction due to alteration of the electronic structure of the molecule. The use of CLSM not only allows a static determination of the film thickness in equilibrium swelling but also enables dynamic monitoring of the swelling process (resolution: 460 ms; **Figure 3B**). For the comparison of the different samples, the parameter α is always referenced to their respective dry film thickness. By illuminating the deposited polymer film with laser light for 5 ms per spot, sufficient network points can be generated to form a surface-bound polymer network. If the illumination time is increased to approximately 30 ms, the degree of equilibrium linear deformation α_m of the polymer network exponentially decreases from $\alpha_{m,5ms} = 5.8$ to $\alpha_{m,30ms} = 2.2$, to a value that is in good agreement with the theoretical value of a quantitatively crosslinked polymer network in bulk (for details of the calculation of this particular value, see **Supplementary Material**; **Figure 3C**, square symbols). If the illumination time is further increased to 40 ms, the polymer network detaches from the surface. The latter phenomenon may be caused by decreased network flexibility, which leads to high mechanical forces and cohesive failure during swelling.

Because of their differences in chemical network structure, the individual samples show distinctly different swelling kinetics: If the netpoint density n is low, the diffusion of the solvent molecules to the substrate near the polymer layers is essentially unhindered by diffusion through the gel. Thus, the swelling behavior appears to follow first-order kinetics, as discussed for a similar system in the literature (**Figure 3B**, black line; Schott, 2006). If the netpoint density is increased, then the local viscosity increases, and the swelling kinetics becomes a product of the actual thermodynamically controlled swelling and diffusion processes, leading to a more complex behavior that may no longer be described by simple first-order kinetics (**Figure 3B**, purple line; Schott, 2006).

To learn more about the network structure from the swelling behavior, the netpoint density n of the surface-attached polymer gel can be estimated by using the Flory-Rhener equation. Because swelling is hindered by surface linkages, only one-dimensional swelling can occur. Consequently, to determine n, the linear deformation α_m may be considered instead of using the volumetric degree of swelling q_m (Toomey et al., 2004). Rühe and co-workers demonstrated that with surface-attached polymer networks, q_m scales as $\alpha_m^{9/5}$ and not as α_m^3, as could be expected, because the surface-attached networks can only swell in one direction, i.e., away from the surface (Toomey et al., 2004). Finally, the Flory-Rhener equation can be transformed into equation 1 for the determination of the netpoint density of our polymer (for further details, see **Supplementary Material**).

$$n = \frac{-\left[\ln\left(1-\frac{1}{\alpha_m^{9/5}}\right)+\frac{1}{\alpha_m^{9/5}}+\chi\left(\frac{1}{\alpha_m^{9/5}}\right)^2\right]}{V_1\left(\sqrt[3]{\frac{1}{\alpha_m^{9/5}}}-\frac{1}{2\alpha_m^{9/5}}\right)} \quad (1)$$

In equation 1, V_1 represents the molar volume of the solvent (i.e., 80.66 cm^3/mol for chloroform), and χ is the characteristic Flory-Huggins polymer-solvent interaction parameter. In our

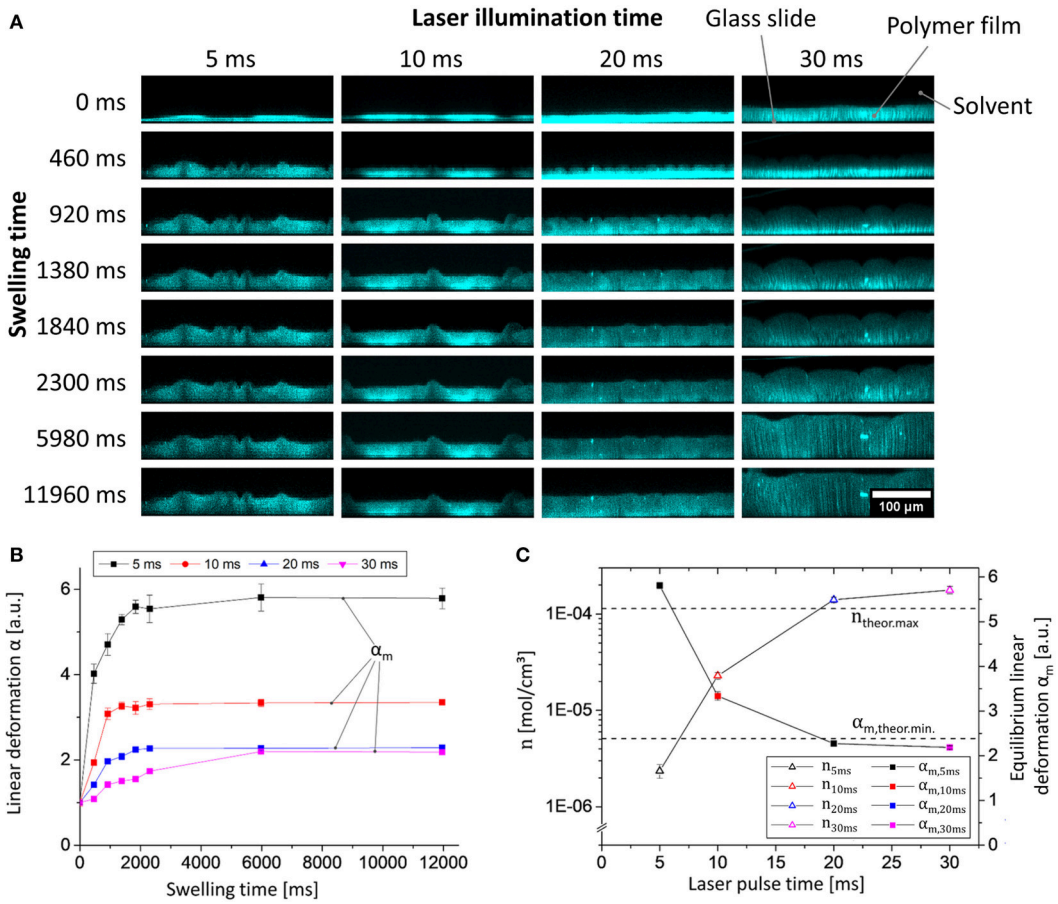

FIGURE 3 | Data from experiments of the swelling of polymer **1** in chloroform photo-crosslinked by different laser illumination times (5, 10, 20, and 30 ms) measured via CLSM: **(A)** Still images of the dynamic x/z CLSM measurements (the microscopic morphology (i.e., non-flat) structure is the result of the spotwise laser illumination); **(B)** plot of linear deformation α vs. swelling time; **(C)** plot of linear deformation in equilibrium α_m vs. laser pulse time (blue plot); netpoint density calculated by equation 1 vs. laser pulse time (black plot) (theoretical maximum/minimum values are visualized as straight horizontal dashed lines).

case here, this parameter was estimated to be $\chi = 0.48$ for 1 in chloroform at 22°C, according to incremental calculations by the method of Hoy (as shown in the **Supplementary Material**; van Krevelen and te Nijenhuis, 2009). As calculated from equation 1, the netpoint density of the polymer gel increases from $n_{5ms} = 2.4 \times 10^{-6}$ mol/cm^3 to $n_{30ms} = 1.8 \times 10^{-4}$ mol/cm^3 (**Figure 3C**, triangular symbols). Note that the latter apparently corresponds to the calculated maximum of n ($n_{theor.max} = 1.1 \times 10^{-4}$ mol/cm^3, determined from the number of crosslinkable double bonds, see **Supplementary Material**) if the numerous approximations within the Flory-Rhener theory and Hoy's incremental calculation are taken into account (Valentín et al., 2008). Based on these findings, we are able to tailor the netpoint density to desired values simply by modifying the crosslinking parameters, without alteration of the polymer itself. This result demonstrates the versatility of our surface-attached cellulose-derived polymer network.

Application in a Microfluidic Channel

Because the prepared organogels can be attached to solid substrates, we were also interested in using the gels in a microfluidic demonstration device for the separation of an organic model pollutant from an aqueous solution. For this proof of principle a polymer patch, either made from polymer **1** or **2** was generated within a microfluidic channel comprising two glass slides held together by double-sided adhesive tape and with a capillary gap of 100 µm (**Figure 4A**). As a model substance for organic molecules ("pollutants") in water, a saturated aqueous solution of pyrene was transported through the channel via capillary flow, and the gray values at different channel areas were determined during the experiment (**Figure 4B**; **Supplementary Material**). Note that the use of pyrene at the same time serves as a sensor due to its intrinsic fluorescence. If the solution comes into contact with the patch of crosslinked polymer **1**, pyrene accumulates within the patch to a very large extent, and the gray value (i.e., fluorescence) of the polymer patch increases as a result. Consequently, the mean gray value in the same area before the solution has passed through the patch is significantly higher than the value afterwards (**Figure 4B**), demonstrating the absorption and upconcentration of the pyrene in the patch. Note that pyrene did not accumulate in the channels that were composed of hydrophilic network patches of polymer **2**,

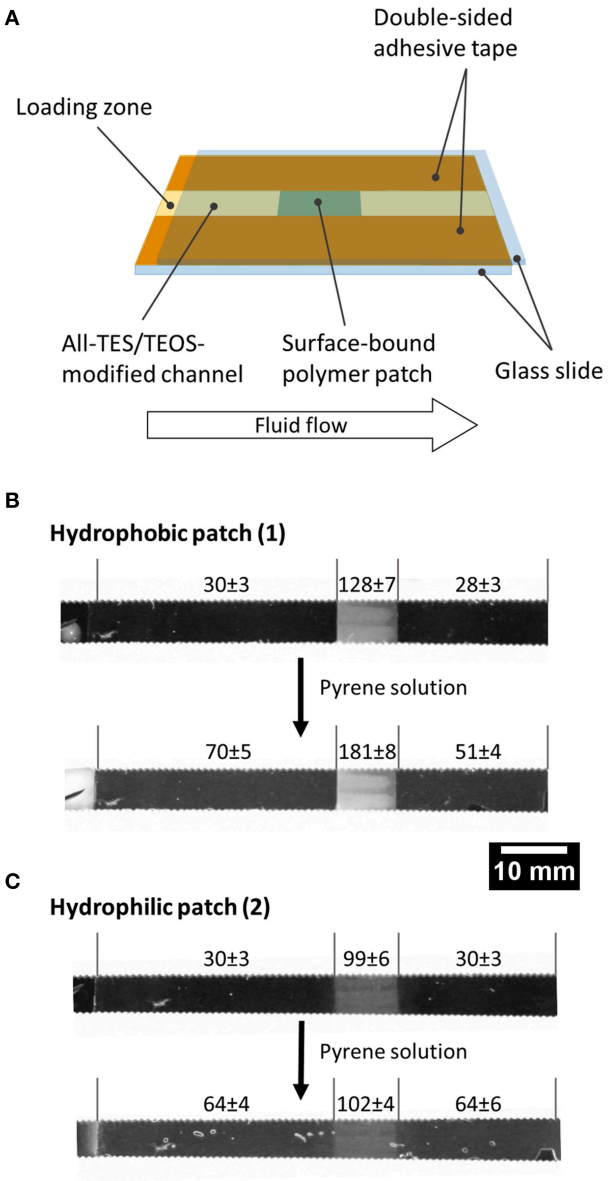

FIGURE 4 | Microfluidic proof-of-principle device. A network of polymer **1** was generated within a microfluidic channel and used to collect pyrene from an aqueous pyrene solution: **(A)** scheme of the setup, **(B,C)** gray values of the channel before and after transport of the solution.

because hydrophobic interactions are intrinsically prevented due to missing hydrophobic side chains as compared to the network composed of polymer **1** (see **Figure 4C**). Although the results reported here are qualitative, nonetheless, this simple experiment demonstrates that the surface-attached organogel is capable of upconcentrating non-polar organic molecules from solution.

CONCLUSION

In conclusion, we developed a novel and versatile method to efficiently photo-crosslink hydroxypropyl cellulose derivatives for the generation of swellable polymer networks with a focus on organogels. The method is highly versatile and allows for the synthesis of organogels by esterification of the cellulose biomolecule with different fatty acids. By using DEABP as a photo-initiator, network formation can be induced by illumination with a conventional 405 nm laser [equipped with a computer numerically controlled (CNC) x/y movement system]. As a result, spatially resolved crosslinking of the polymer via laser illumination is possible. The swelling behavior (degree of swelling) and, thus, the netpoint density (estimated by the Flory-Rhener equilibrium swelling theory) of the surface-linked network, was determined via confocal fluorescence microscopy, yielding results that matched the theoretical estimation. This method allows the dynamic monitoring of the swelling process and, hence, the determination of the swelling kinetics. As a result, gels providing low netpoint densities swell through first-order kinetics, whereas the swelling of networks with higher crosslinking degrees follows a more complex mechanism. Finally, as a proof of principle, we generated a microfluidic channel based on a hydrophobic polymer network patch; our channel is able to concentrate an organic model dye within the patch, as opposed to a reference channel that is incorporating a hydrophilic polymer network patch. This is a promising starting point to increase the sensitivity of analytical devices, by locally increasing the analyte concentration. Via specific adjustment of the netpoint density, the control of the swelling behavior, and therefore, the flow speed and the dye-gel interaction, will be investigated in future trials.

AUTHOR CONTRIBUTIONS

All authors listed, have made substantial, direct, and intellectual contribution to the work. MN, DS, and AB performed all experiments. MN, MB, and ST analyzed the data, reviewed the literature, and wrote the manuscript. MB coordinated the complete project. All authors discussed and reviewed the results and approved the manuscript.

FUNDING

We gratefully acknowledge the financial support by the German Research Foundation (DFG) within the Collaborative Research Centre 1194 Interaction of Transport and Wetting Processes, Project A05.

ACKNOWLEDGMENTS

We thank Tobias Meckel for discussion and help concerning microscopy.

SUPPLEMENTARY MATERIAL

The Supplementary Material for this article can be found online at: https://www.frontiersin.org/articles/10.3389/fchem.2019.00367/full#supplementary-material

REFERENCES

Ajayaghosh, A., and Praveen, V. K. (2007). Pi-organogels of self-assembled p-phenylenevinylenes: Soft materials with distinct size, shape, and functions. *Account. Chem. Res.* 40, 644–656. doi: 10.1021/ar7000364

Allen, N. S., Lam, E., Kotecha, J. L., Green, W. A., Timms, A., Navaratnam, S., et al. (1990). Photochemistry of novel 4-alkylamino benzophenone initiators: a conventional laser flash photolysis and mass spectrometry study. *J. Photochem. Photobiol. A* 54, 367–388. doi: 10.1016/1010-6030(90)85009-L

Annabi, N., Tamayol, A., Uquillas, J. A., Akbari, M., Bertassoni, L. E., Cha, C., et al. (2014). 25th anniversary article: rational design and applications of hydrogels in regenerative medicine. *Adv. Mater.* 26, 85–124. doi: 10.1002/adma.201303233

Bhadani, S. N., and Gray, D. G. (1983). Cellulose-based liquid crystalline polymers; esters of (Hydroxypropyl) cellulose. *Mol. Cryst. Liq. Cryst.* 99, 29–38. doi: 10.1080/00268948308072026

Bhadani, S. N., and Gray, D. G. (1984). Crosslinked cholesteric network from the acrylic acid ester of (Hydroxypropyl)cellulose. *Mol. Cryst. Liq. Cryst.* 102, 255–260. doi: 10.1080/01406568408070536

Böhm, A., Gattermayer, M., Trieb, C., Schabel, S., Fiedler, D., Miletzky, F., et al. (2013). Photo-attaching functional polymers to cellulose fibers for the design of chemically modified paper. *Cellulose* 20, 467–483. doi: 10.1007/s10570-012-9798-x

Burkhard, C. A. (1950). The reaction of mercaptans with alkenyl silanes. *J. Am. Chem. Soc.* 72, 1078–1080. doi: 10.1021/ja01159a007

Chaves, K. F., Barrera-Arellano, D., and Ribeiro, A. P. B. (2018). Potential application of lipid organogels for food industry. *Food Res. Inter.* 105, 863–872. doi: 10.1016/j.foodres.2017.12.020

Datta, S., and Bhattacharya, S. (2015). Multifarious facets of sugar-derived molecular gels: Molecular features, mechanisms of self-assembly and emerging applications. *Chem. Soc. Rev.* 44, 5596–5637. doi: 10.1039/c5cs00093a

Dorman, G., and Prestwich, G. D. (1994). Benzophenone photophores in biochemistry. *Biochemistry* 33, 5661–5673. doi: 10.1021/bi00185a001

Esposito, C. L., Kirilov, P., and Roullin, V. G. (2018). Organogels, promising drug delivery systems: An update of state-of-the-art and recent applications. *J. Control. Release* 271, 1–20. doi: 10.1016/j.jconrel.2017.12.019

García, J. M., Jones, G. O., Virwani, K., McCloskey, B. D., Boday, D. J., ter Huurne, G. M., et al. (2014). Recyclable, strong thermosets and organogels via paraformaldehyde condensation with diamines. *Science* 344, 732–736. doi: 10.1126/science.1251484

George, M., and Weiss, R. G. (2006). Molecular organogels. Soft matter comprised of low-molecular-mass organic gelators and organic liquids. *Account. Chem. Res.* 39, 489–497. doi: 10.1021/ar0500923

Harsh, D. C., and Gehrke, S. H. (1991). Controlling the swelling characteristics of temperature-sensitive cellulose ether hydrogels. *J. Control. Release* 17, 175–185. doi: 10.1016/0168-3659(91)90057-K

Heinze, T., and Koschella, A. (2005). Solvents applied in the field of cellulose chemistry - a mini review. *Polim. Cienc. Tecnol.* 15, 84–90. doi: 10.1590/S0104-14282005000200005

Hennink, W. E., and van Nostrum, C. F. (2002). Novel crosslinking methods to design hydrogels. *Adv. Drug Deliv. Rev.* 54, 13–36. doi: 10.1016/S0169-409X(01)00240-X

Hinze, W. L., Uemasu, I., Dai, F., and Braun, J. M. (1996). Analytical and related applications of organogels. *Curr. Opin. Coll. Interface Sci.* 1, 502–513. doi: 10.1016/S1359-0294(96)80119-1

Hirst, A. R., Escuder, B., Miravet, J. F., and Smith, D. K. (2008). High-tech applications of self-assembling supramolecular nanostructured gel-phase materials: From regenerative medicine to electronic devices. *Angew. Chem.* 47, 8002–8018. doi: 10.1002/anie.200800022

Hoo, S. P., Loh, Q. L., Yue, Z., Fu, J., Tan, T. T. Y., Choong, C., et al. (2013). Preparation of a soft and interconnected macroporous hydroxypropyl cellulose methacrylate scaffold for adipose tissue engineering. *J. Mater. Chem. B* 1, 3107–3117. doi: 10.1039/c3tb00446e

Jagur-Grodzinski, J. (2009). Polymeric gels and hydrogels for biomedical and pharmaceutical applications. *Polym. Adv. Technol.* 21, 27–47. doi: 10.1002/pat.1504

Jakubiak, J., Allonas, X., Fouassier, J. P., Sionkowska, A., Andrzejewska, E., Linden, L. Å., et al. (2003). Camphorquinone–amines photoinitating systems for the initiation of free radical polymerization. *Polymer* 44, 5219–5226. doi: 10.1016/S0032-3861(03)00568-8

Kabra, B. G., Gehrke, S. H., and Spontak, R. J. (1998). Microporous, responsive hydroxypropyl cellulose Gels. 1. Synthesis and microstructure. *Macromolecules* 31, 2166–2173. doi: 10.1021/ma970418q

Kargl, R., Mohan, T., Köstler, S., Spirk, S., Doliška, A., Stana-Kleinschek, K., et al. (2013). Functional patterning of biopolymer thin films using enzymes and lithographic methods. *Adv. Funct. Mater.* 23, 308–315. doi: 10.1002/adfm.201200607

Kirilov, P., Rum, S., Gilbert, E., Roussel, L., Salmon, D., Abdayem, R., et al. (2014). Aqueous dispersions of organogel nanoparticles - potential systems for cosmetic and dermo-cosmetic applications. *Int. J. Cosm. Sci.* 36, 336–346. doi: 10.1111/ics.12131

Klemm, D., Heublein, B., Fink, H.-P., and Bohn, A. (2005). Cellulose: fascinating biopolymer and sustainable raw material. *Angew. Chem.* 44, 3358–3393. doi: 10.1002/anie.200460587

Krohm, F., Kind, J., Savka, R., Alcaraz Janßen, M., Herold, D., Plenio, H., et al. (2016). Photochromic spiropyran- and spirooxazine-homopolymers in mesoporous thin films by surface initiated ROMP. *J. Mater. Chem. C* 4, 4067–4076. doi: 10.1039/C5TC04054J

Lai, H. Y., Leon, A., d., Pangilinan, K., and Advincula, R. (2018). Superoleophilic and under-oil superhydrophobic organogel coatings for oil and water separation. *Progr. Org. Coat.* 115, 122–129. doi: 10.1016/j.porgcoat.2017.11.001

Larsson, M., Johnsson, A., Gårdebjer, S., Bordes, R., and Larsson, A. (2017). Swelling and mass transport properties of nanocellulose-HPMC composite films. *Mater. Des.* 122, 414–421. doi: 10.1016/j.matdes.2017.03.011

Marangoni, A. G. (2012). Organogels: an alternative edible oil-structuring method. *J. Am. Oil Chem. Soc.* 89, 749–780. doi: 10.1007/s11746-012-2049-3

Meazza, L., Foster, J. A., Fucke, K., Metrangolo, P., Resnati, G., and Steed, J. W. (2013). Halogen-bonding-triggered supramolecular gel formation. *Nat. Chem.* 5, 42–47. doi: 10.1038/nchem.1496

Merlin, A., Lougnot, D.-J., and Fouassier, J.-P. (1980). Laser spectroscopy of substituted benzophenone used as photo-initiators of vinyl polymerization. *Polymer Bull.* 2, 847–853. doi: 10.1007/BF00255514

Mukhopadhyay, P., Iwashita, Y., Shirakawa, M., Kawano, S.-I., Fujita, N., and Shinkai, S. (2006). Spontaneous colorimetric sensing of the positional isomers of dihydroxynaphthalene in a 1D organogel matrix. *Angew. Chem.* 45, 1592–1595. doi: 10.1002/anie.200503158

Nau, M., Seelinger, D., and Biesalski, M. (2018). Functional surface coatings from tailor-made long-chain hydroxypropyl cellulose ester nanoparticles. *Cellulose* 134:44949. doi: 10.1007/s10570-018-1981-2

Niegelhell, K., Süßenbacher, M., Sattelkow, J., Plank, H., Wang, Y., Zhang, K., et al. (2017). How bound and free fatty acids in cellulose films impact nonspecific protein adsorption. *Biomacromolecules* 18, 4224–4231. doi: 10.1021/acs.biomac.7b01260

Osada, Y., and Gong, J.-P. (1998). Soft and wet materials: polymer gels. *Adv. Mater.* 10, 827–837.

Ostmark, E., Harrisson, S., Wooley, K. L., and Malmström, E. E. (2007). Comb polymers prepared by ATRP from hydroxypropyl cellulose. *Biomacromolecules* 8, 1138–1148. doi: 10.1021/bm061043w

Prati, S., Volpi, F., Fontana, R., Galletti, P., Giorgini, L., Mazzeo, R., et al. (2018). Sustainability in art conservation: a novel bio-based organogel for the cleaning of water sensitive works of art. *Pure Appl. Chem.* 90, 239–251. doi: 10.1515/pac-2017-0507

Riga, E., Saar, J., Erath, R., Hechenbichler, M., and Lienkamp, K. (2017). On the Limits of benzophenone as cross-linker for surface-attached polymer hydrogels. *Polymers* 9:686. doi: 10.3390/polym9120686

Rivest, C., Morrison, D. W. G., Ni, B., Rubin, J., Yadav, V., Mahdavi, A., et al. (2007). Microscale hydrogels for medicine and biology: synthesis, characteristics and applications. *J. Mech. Mater. Struct.* 2, 1103–1119. doi: 10.2140/jomms.2007.2.1103

Sangeetha, N. M., and Maitra, U. (2005). Supramolecular gels: functions and uses. *Chem. Soc. Rev.* 34, 821–836. doi: 10.1039/b417081b

Schott, H. (2006). Swelling kinetics of polymers. *J. Macromol. Sci. Part B* 31, 1–9. doi: 10.1080/00222349208215453

Segarra-Maset, M. D., Nebot, V. J., Miravet, J. F., and Escuder, B. (2013). Control of molecular gelation by chemical stimuli. *Chem. Soc. Rev.* 42, 7086–7098. doi: 10.1039/c2cs35436e

Suto, S. (1989). Crosslinked hydroxypropyl cellulose solid films cast from liquid crystalline solutions. *J. Appl. Polym. Sci.* 37, 2781–2784. doi: 10.1002/app.1989.070370927

Suto, S., Tashiro, H., and Karasawa, M. (1992). Preparation and mechanical properties of chemically cross-linked hydroxypropyl cellulose solid films retaining cholesteric liquid crystalline order. *J. Appl. Polym. Sci.* 45, 1569–1585. doi: 10.1002/app.1992.070450908

Suto, S., and Yoshinaka, M. (1993). Chemical cross-linking of cholesteric liquid-crystalline hydroxypropyl cellulose with dialdehydes. *J. Mater. Sci.* 28, 4644–4650. doi: 10.1007/BF00414253

Suzuki, M., and Hanabusa, K. (2010). Polymer organogelators that make supramolecular organogels through physical cross-linking and self-assembly. *Chem. Soc. Rev.* 39, 455–463. doi: 10.1039/b910604a

Tan, J., Kang, H., Liu, R., Wang, D., Jin, X., Li, Q., et al. (2011). Dual-stimuli sensitive nanogels fabricated by self-association of thiolated hydroxypropyl cellulose. *Polym. Chem.* 2, 672–678. doi: 10.1039/C0PY 00348D

Toba, Y., Yasuike, M., and Usui, Y. (1997). The 'onium butyltriphenylborates as novel donor-acceptor initiators for free radical photopolymerization. *Chem. Commun.* 1997, 675–676. doi: 10.1039/A700579B

Toomey, R., Freidank, D., and Rühe, J. (2004). Swelling behavior of thin, surface-attached polymer networks. *Macromolecules* 37, 882–887. doi: 10.1021/ma034737v

Valentín, J. L., Carretero-González, J., Mora-Barrantes, I., Chassé, W., and Saalwächter, K. (2008). Uncertainties in the determination of cross-link density by equilibrium swelling experiments in natural rubber. *Macromolecules* 41, 4717–4729. doi: 10.1021/ma8005087

van Krevelen, D. W., and te Nijenhuis, K. (2009). *Properties of Polymers*. Amsterdam: Elsevier.

van Tomme, S. R., Storm, G., and Hennink, W. E. (2008). *In situ* gelling hydrogels for pharmaceutical and biomedical applications. *Int. J. Pharmac.* 355, 1–18. doi: 10.1016/j.ijpharm.2008.01.057

Venkatesan, G. A., and Sarles, S. A. (2016). Droplet immobilization within a polymeric organogel improves lipid bilayer durability and portability. *Lab Chip* 16, 2116–2125. doi: 10.1039/c6lc00391e

Vintiloiu, A., and Leroux, J.-C. (2008). Organogels and their use in drug delivery–a review. *J. Control. Release* 125, 179–192. doi: 10.1016/j.jconrel.2007.09.014

Wach, R. A., Mitomo, H., Yoshii, F., and Kume, T. (2002). Hydrogel of radiation-induced cross-linked hydroxypropylcellulose. *Macromol. Mater. Eng.* 287, 285–295. doi: 10.1002/1439-2054(20020401)287:4<285:AID-MAME285>3.0.CO;2-3

Wang, J., and Zhang, K. (2018). Modular adjustment of swelling behaviors of surface-modified solvent-responsive polymeric nanoparticles based on cellulose 10-undecenoyl ester. *J. Phys. Chem. C* 122, 7474–7483. doi: 10.1021/acs.jpcc.7b11521

Winnik, F. M., Winnik, M. A., Tazuke, S., and Ober, C. K. (1987). Synthesis and characterization of pyrene-labeled hydroxypropyl cellulose and its fluorescence in solution. *Macromolecules* 20, 38–44. doi: 10.1021/ma00167a008

Wüstenberg, T. (2014). *Cellulose and Cellulose Derivatives in the Food Industry: Fundamentals and Applications*. New York, NY: Wiley-VCH.

Xue, P., Yao, B., Wang, P., Gong, P., Zhang, Z., and Lu, R. (2015). Strong fluorescent smart organogel as a dual sensing material for volatile acid and organic amine vapors. *Chemistry* 21, 17508–17515. doi: 10.1002/chem.201502401

Yano, S., Iwase, T., Teramoto, N., Shimasaki, T., and Shibata, M. (2018). Synthesis, thermal properties and cell-compatibility of photocrosslinked cinnamoyl-modified hydroxypropyl cellulose. *Carbohyd. Polymers* 184, 418–426. doi: 10.1016/j.carbpol.2017.12.087

Conflict of Interest Statement: The authors declare that the research was conducted in the absence of any commercial or financial relationships that could be construed as a potential conflict of interest.

frontiers in Chemistry

ORIGINAL RESEARCH
published: 17 July 2019
doi: 10.3389/fchem.2019.00507

Hybrid Gibbsite Nanoplatelet/Cellulose Nanocrystal Multilayered Coatings for Oxygen Barrier Improvement

*Maud Chemin[1,2], Laurent Heux[1], David Guérin[2], Laura Crowther-Alwyn[2] and Bruno Jean[1]**

[1] Univ. Grenoble Alpes, CNRS, CERMAV, Grenoble, France, [2] Centre Technique du Papier, Functional Products and Surfaces, Grenoble, France

We have investigated the ability of multilayered hybrid thin films of cellulose nanocrystals (CNCs) and gibbsite nanoplatelets (GNPs) to be built by the layer-by-layer (LbL) technique onto substrates selected for packaging applications, and to improve the oxygen barrier properties. Using complementary structural characterization techniques, namely atomic force microscopy, ellipsometry, and spectral reflectance, we show that when deposited onto model silicon substrates these hybrid films were homogenous and of reduced porosity, and were comprised of alternately deposited monolayers of GNPs and CNCs. The successful deposition of such homogeneous and dense hybrid thin films onto various types of flexible substrates showing different chemical compositions, hydrophilicity, and surface morphology, ranging from cardboard to smart paper, polyethylene (PE) films, and PE-coated cardboard was also confirmed by scanning electron microscopy observations. In view of the diversity of these substrates we could confirm the remarkable robustness of such a deposition process, likely due to (i) the adaptability of the LbL assembling technique and (ii) the strong electrostatic and hydrogen bonding interactions between GNPs and CNCs. The measurement of the oxygen transmission rate (OTR) at 23°C and 50% RH showed that the oxygen barrier properties of the bare substrates could be significantly improved (e.g., 75% decrease of the OTR) after the deposition of such thin (<100 nm) multilayered hybrid films. This lowered permeability was tentatively attributed to the highly tortuous morphology of the coating, acting to impede the gas diffusion. These partially biosourced very thin films stand as good candidates for using as coatings showing high oxygen barrier performance.

Keywords: oxygen barrier, layer-by-layer (LbL), thin films, gibbsite nanoplatelets, cellulose nanocrystals

OPEN ACCESS

Edited by:
Eero Kontturi,
Aalto University, Finland

Reviewed by:
Jian Yu,
Institute of Chemistry (CAS), China
Marino Lavorgna,
Institute for Polymers Composites and Biomaterials (CNR), Italy
Per Larsson,
Royal Institute of Technology, Sweden

***Correspondence:**
Bruno Jean
bruno.jean@cermav.cnrs.fr

Specialty section:
This article was submitted to Polymer Chemistry, a section of the journal Frontiers in Chemistry

Received: *15 February 2019*
Accepted: *02 July 2019*
Published: *17 July 2019*

Citation:
Chemin M, Heux L, Guérin D, Crowther-Alwyn L and Jean B (2019) Hybrid Gibbsite Nanoplatelet/Cellulose Nanocrystal Multilayered Coatings for Oxygen Barrier Improvement. Front. Chem. 7:507. doi: 10.3389/fchem.2019.00507

INTRODUCTION

Food packaging is a constantly growing market, which is however still mainly based on the use of non-renewable and non-biodegradable petroleum-derived species. To overcome this situation, which causes considerable environmental issues, a world-wide research effort is undertaken to develop eco-friendly packaging materials containing building blocks of renewable origin.

In this context, as summarized in numerous recent reviews, nanocelluloses have emerged as a promising class of bio-based colloids, able to fulfill the requirements for the production of thin films and coatings, adapted to packaging applications, in particular exhibiting high oxygen barrier, optical transparency and mechanical resistance (Azeredo et al., 2017; Ferrer et al., 2017; Hubbe et al., 2017; Thomas et al., 2018; Qin et al., 2019). Nanocelluloses comprise both (i) the slender flexible nanofibrils (CNFs) extracted following a mechanical disintegration of cellulose fibers coupled with enzymatic and/or chemical treatments and (ii) the shorter rigid cellulose nanocrystals (CNCs) usually derived from partial sulfuric acid hydrolysis of any cellulose source (Klemm et al., 2011, 2018; Moon et al., 2011). Both CNFs and CNCs, which are endowed with a rather low density and strong mechanical properties, are now commercialized in large quantities. While the flexible nature of the CNFs makes them highly appropriate for film formation, a high degree of nanofibrillation is needed if one wants to obtain a low porosity and low permeability of these so-called nanopapers. However, such requirements are not always met by industrial products, which may contain high fractions of microfibers. To the opposite, CNCs often yield brittle films when casted, but thanks to their tunable cellulose-source-dependent aspect ratio and true homogeneous nanometric size (typically a few hundreds of nm in length and 3–30 nm in cross-section), they can be used as major ingredients to prepare thin functional surface coatings deposited onto cellulosic or non-cellulosic substrates (Li et al., 2013).

As far as the deposition method is concerned, the layer-by-layer (LbL) assembly technique first introduced by Iler and then developed by the Decher group stands out as a highly convenient technique to build nanostructured multilayered thin films associating two species, providing that they exhibit mutual attractive interactions (Iler, 1966; Decher et al., 1992; Decher and Schlenoff, 2012). Initially introduced by Iler with colloids, the method then focused on polyelectrolytes with opposite charges, and has now been expanded to a wide variety of building blocks. In particular, it was shown that CNCs and bio- or synthetic polymers could be assembled using the LbL technique in multilayered thin films with a very high degree of structural control, which cannot be reached with other deposition techniques (Martin and Jean, 2014). In a recent work, we have replaced the polymer component by positively charged inorganic gibbsite nanoplatelets (GNPs) to form innovative hybrid all-nanoparticles (GNPs/CNCs) thin films (Martin et al., 2017). The choice of GNPs, which show structural similarities with clay nanoparticles (e.g., montmorillonite or vermiculite), was based on their property to impede the diffusion and permeation of gas molecules, as shown in numerous studies (Priolo et al., 2010, 2012, 2015; Wu et al., 2012; Rhim et al., 2013; Song et al., 2016; Qin et al., 2019). In the work by Martin et al., a structural investigation based on the use of atomic force microscopy (AFM) and neutron reflectivity showed that the growth and density of GNPs/CNCs films could be tuned over a wide range during their preparation by varying the ionic strength of the CNCs suspension and the film drying protocol (Martin et al., 2017). Specifically, by building the films under aqueous conditions with no added salt in the suspensions and drying the films at the end of the process yielded very thick porous slabs. On the other hand, drying the film after each layer deposition and adding 10 mM of monovalent salt in the CNCs suspension led to the production of thin, dense and well-stratified multilayered films.

The present study addresses the possibility to use our established protocol for such multilayered architecture as an efficient coating to improve the oxygen barrier properties of different cellulosic and non-cellulosic substrates possessing different chemical compositions, hydrophilicity, mechanical properties, and surface morphology. We first describe the building of GNPs/CNCs films onto model silicon substrates (inherently covered by a thin silicon oxide layer) using the LbL assembly technique, characterizing the films by AFM, ellipsometry and light reflectance. Then, the ability of such hybrid thin films to be deposited on various substrates was investigated and the resulting structures were characterized by scanning electron microscopy. The effect of the deposition of GNPs/CNCs multilayered films on the oxygen transmission rate was finally investigated to probe the ability of these thin partially biosourced coatings for improving oxygen barrier properties.

EXPERIMENTAL SECTION

Materials

Chemicals

Cotton linters were provided by Buckeye Cellulose Corporation and used as the cellulose source for CNCs without any further purification. Polyethyleneimine (PEI, $Mw \approx 25{,}000$), poly(allylamine hydrochloride) (PAH, $Mw \approx 50{,}000$), and poly(sodium 4-styrene sulfonate) (PSS, $Mw \approx 70{,}000$) were purchased from Sigma-Aldrich and used at 2, 4, and 4 g/L, respectively. Aluminum isopropoxide (>98%, $M = 204.25$ g/mol) and aluminum sec-butoxide (>98%, $M = 246.33$ g/mol) were purchased from TCI and used without any further purification. NaCl, HCl 37% and H_2SO_4 96% were purchased from Prolabo, Fisher Scientific, and Acros Organics, respectively. Ethanol and chloroform were purchased from Biosolve. Demineralized water was systematically used.

Substrates

Four different flexible substrates of interest were used for film deposition: an uncoated kraft cardboard of 225 g/m² produced by StoraEnso (CKB Nude™), a polyethylene-coated cardboard produced by StoraEnso (Cupforma Natura 2PE) and composed of a base board of 232 g/m² coated on both sides with polyethylene (PE, 12 and 15 g/m² on topside and reverse side, respectively), a low density virgin PE substrate of 92.5 g/m² from RAJA (sheath 30B) and a smart paper of 190 g/m² from Felix Schoeller (pe:smart paper type 1). This last substrate was composed of a raw paper coated on both sides with resin and with a hydrophilic primer layer on topside. It was developed in the framework of the European project Autonomous Printed Paper Products for functional Labels and Electronics (A3Ple). Additionally, one-side polished <001> silicon wafers (Sil'tronix ST) were used as model solid substrates.

Cellulose Nanocrystals (CNCs)

Cellulose nanocrystals were prepared from the sulfuric acid hydrolysis of cotton linters as initially reported by Revol et al.

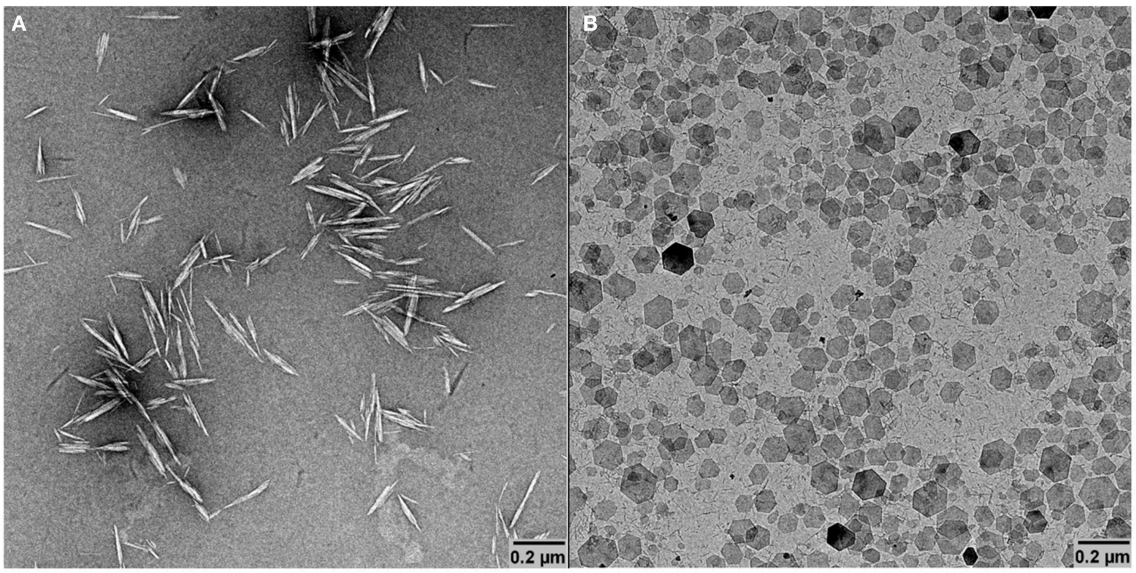

FIGURE 1 | TEM micrographs of CNCs **(A)** and GNPs **(B)**.

(1992). Briefly, the cotton linters were treated with 64 wt.% sulfuric acid for 30 min at 60°C, cooled by ice addition and washed by four centrifugation/redispersion cycles. The resulting suspension was dialyzed against deionized water until the conductivity of the dialysis bath reached the conductivity of deionized water and sonicated twice for 3 min with a Branson model 450 sonifier at 30% amplitude. After these treatments, the suspension was filtered through 8 µm and then 1 µm cellulose nitrate membranes (Sartorius). The resulting 2.3 wt.% CNC suspension was concentrated by ultrafiltration using 10,000 kDa ultrafiltration membranes from Millipore to 3.9 wt.% and 10 mM of NaCl was added to the CNCs suspension, which was used for multilayered film build up. To avoid any microbial spoilage, about 1 mL chloroform per liter was added to the suspensions, which were stored at 4°C.

Gibbsite Nanoplatelets (GNPs)

Gibbsite nanoplatelets were obtained by a hydrothermal treatment of 0.08 M aluminum isopropoxide and 0.08 M aluminum sec-butoxide in 0.09 M hydrochloric acid (Wijnhoven et al., 2005). After a 10 day dissolution step, the suspension was heated for 72 h at 84°C in an oven (to limit the growth of boehmite nanorods at higher temperature) and then dialyzed against deionized water. The resulting 0.8 wt.% suspension was concentrated by ultrafiltration using 10,000 kDa ultrafiltration membranes (Millipore) to 4.8 wt.%. The pH of the GNPs suspension was set at 5.9 using hydrochloric acid (0.1 M). To avoid any bacterial contamination, some chloroform was added to the suspension, which was stored at 4°C.

Layer-by-Layer Assembly

The Si wafers solid substrates were cleaned with ethanol, followed by rinsing with water. Prior to hybrid film deposition using the LbL assembly process, all substrates, i.e., solid model or flexible, were subjected to a plasma cleaning treatment (PELCO easiGlow™, 0.39 mbar, 15 mA, 25 s) to get rid of organic contaminants and possibly confer negative charges to the surface. Before the deposition of the first GNPs layer, a multilayered "primer" composed of a PEI/PSS/PAH/PSS polyelectrolyte stack was laid on the substrate by sequential dipping into the corresponding solution for 20 min for PEI and 15 min for PSS and PAH, with intermediate rinsing steps of 5 min in water. Hybrid thin films were then assembled using a dipping LbL process as illustrated in **Figure 2**. The negatively charged substrate was first immersed in the positively-charged GNPs suspension for 5 min, then the substrate was rinsed for 5 min with distilled water and the substrate was immersed in the negatively charged CNCs suspension for an identical time and finally rinsed for 5 min. The rinsing steps are required to remove loosely bound nanoparticles and ensure that only strongly interacting particles are adsorbed. This cycle was repeated to reach the desired number of deposited bilayers, *n*, where a bilayer is defined as a layer of GNPs plus a layer of CNCs. Samples were dried using gentle air blowing after each dipping/rinsing step, i.e., after each layer deposition.

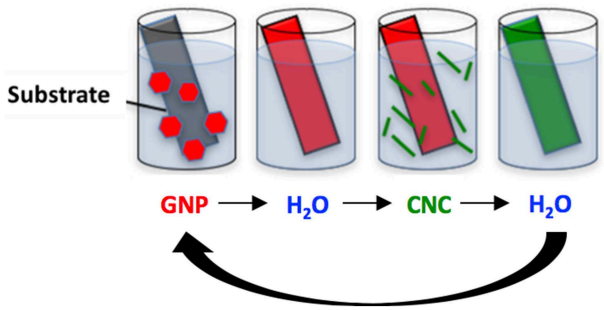

FIGURE 2 | Schematic representation of the layer by layer assembly process.

For solid silicon model substrates, samples with three different numbers of bilayers, $n = 4$, 7, and 11, have been prepared. For flexible substrates that were used to evaluate the potential of the film as an oxygen barrier coating, samples with $n = 1$, 4, 7, and 7.5 were prepared. $n = 7.5$ corresponds to the samples with $n = 7$ plus an additional layer of GNPs only. For these samples, each experiment was realized in triplicate to allow three oxygen permeability measurements.

The notation $(GNPs/CNCs)_n$ designates a multilayered film containing n number of deposited (GNPs/CNCs) bilayers. The polyelectrolyte primer layer was omitted in the notation for clarity.

Methods

Zeta Potential

The zeta potential of CNCs and GNPs was measured from 0.1 wt.% suspensions by electrophoresis coupled with laser Doppler velocimetry using a Malvern NanoZS instrument. Samples were measured in 10 mM NaCl. Data were averaged over three measurements, each of them comprising 10 sub-runs.

Transmission Electron Microscopy

Drops of *ca.* 0.001 wt.% GNPs or CNCs suspensions were deposited onto glow-discharged carbon-coated TEM grids. After 2 min, the liquid in excess was wicked away with a filter paper and, for CNCs only, prior to drying, a drop of 2% uranyl acetate was deposited on the specimen. After 2 min, the stain in excess was blotted off and the remaining thin liquid film was allowed to dry. The specimens were observed using a Philips CM200 electron microscope operated at 80 kV. The images were recorded with a TVIPS F216 TemCam camera (2,040 × 2,040 pixels).

Atomic Force Microscopy

AFM height images were recorded at randomly selected surface positions in peak force mode using a Dimension Icon instrument (Bruker, Santa Barbara, CA). The cantilevers Scanassist-Air (Bruker, Santa Barbara, CA) used were triangular and had a force contact of 0.4 N/m and a resonance frequency of 70 kHz at tip scan rates of 1 Hz. AFM images were processed using the flattening function of the Gwyddion software, and the RMS roughness was calculated on $5 \times 5\ \mu m^2$ images.

Scanning Electron Microscopy

Prior to observations, samples were coated with 2–3 nm Au/Pd using a Baltec MED 020 apparatus. Secondary electron images of the specimens were recorded with a FEI Quanta 250 scanning electron microscope (SEM) equipped with a field emission gun and operated at 2 kV.

To obtain images of cross-sections, samples were prepared as follows. A piece of the sample (about 0.3 by 0.6 cm^2) was placed between two pieces of polystyrene so as to sandwich the flexible sample and prevent deformation. This assembly was then placed in a sample holder, which was introduced in the cryo-ultramicrotome (Leica UC6 instrument) tank cooled at −110°C. The cooled samples were cut to obtain sharp cross-sections and brought back to room temperature by blowing with compressed air to avoid condensation of water on the surface.

Ellipsometry

Ellipsometric measurements were performed using an imaging ellipsometer EP3-SE (Nanofilm Technology GmbH, Germany). Experiments were performed *ex situ* under air conditions at a wavelength ranging from 379 to 809 nm (Xenon lamp was used as light source) at three different angles of incidence: 65, 70, and 75°. The instrument was used in total internal reflection mode and both the intensity and the phase changes of the reflected light were monitored and converted into two ellipsometric angles Ψ and Δ. The data were acquired and evaluated using the EP3View V235 Software (Nanofilm, Germany). Optical modeling was performed using the EP4Model 1.0.1 software (Nanofilm, Germany). All thicknesses were measured at only one spot of the sample with four nulling zones, leading to 0.1–0.5 nm and 0.006 accuracy for respectively the thickness and the refractive index.

The fit model used was composed of four layers: silicon substrate, a SiO_2 layer of 1 nm, a primer layer, and a transparent $(GNPs/CNCs)_n$ film as a Cauchy layer without extinction ($k = 0$) with a refractive index n_{film} calculated as:

$$n_{film}(\lambda) = A + \frac{B}{\lambda^2} \quad (1)$$

Least-square fitting of the experimental data with adequate optical models allowed us to determine the refractive index as well as the thickness of the film layer. Then, according to the effective medium approximation model (Xie et al., 2006), the particle volume fraction could be calculated as:

$$\Phi(\text{nanoparticles}) = \frac{A(\text{film}) - 1}{A(\text{nanoparticles}) - 1} \quad (2)$$

Note that this equation is only valid for $k = 0$. Moreover, $A_{nanoparticles}$ was chosen equal to 1.56 corresponding to GNPs and CNCs.

Before measurements on GNP/CNC coated samples, the thickness of the primer layer was measured in exactly the same condition with A(primer) = 1.435 and B(primer) = 0 corresponding to the average refractive index of each polymer composing the primer layer. The primer layer thickness was then calculated to be equal to 6.6 nm.

Spectral Reflectance

SR measurements were performed using a F20 Thin-Film Analyzer (Filmetrics, USA). Experiments were performed at a wavelength ranging from 190 to 1,100 nm. The data were acquired and evaluated by the FILMeasure software, using standard SiO_2 layer on silicon substrate. The Filmetrics technique allowed determining the thin-film thicknesses by measuring the light that is reflected perpendicular to the film surface over a wide range of wavelengths. It then analyses these data by comparing it to a series of calculated reflectance spectra with an accuracy of 2 nm. All thicknesses given are an average value of 10 measurements performed at different spots on each sample. The thickness deviation was measured as 0.3, 2.4, 0.6, and 1.1 nm for $n = 0$, 4, 7, and 11, respectively.

Oxygen Transmission Rate Measurement

The OTR was measured according to the Centre Technique du Papier (CTP) internal method, adapted from ASTM F2714-08—Oxygen Headspace Analysis of Packages Using Fluorescent Decay. The measurements were performed with a fiber optic oxygen transmitter (Fibox 4 from PreSens Precision Sensing GmbH, Germany). The oxygen sensor in the optical window of the upper chamber was read out via a polymer optical fiber, which is connected to an oxygen transmitter. The upper chamber was flushed with oxygen free medium (nitrogen, 23°C, 0% relative humidity) while the lower chamber was flushed with a medium of known oxygen concentration, here conditioned air at 23°C and 50% relative humidity. The tested material was fixed between these chambers. The specific exchange area was fixed at 7.07 cm^2 using an aluminum mask (tape 1456 from 3M). The oxygen transmission rate of the tested material was calculated from the increase in oxygen concentration over time in the upper chamber, in volume of oxygen per area, gas pressure and time ($cm^3/m^2 \cdot d \cdot bar$). The experiments were carried out once on each coated substrate giving an averaged value over three measurements.

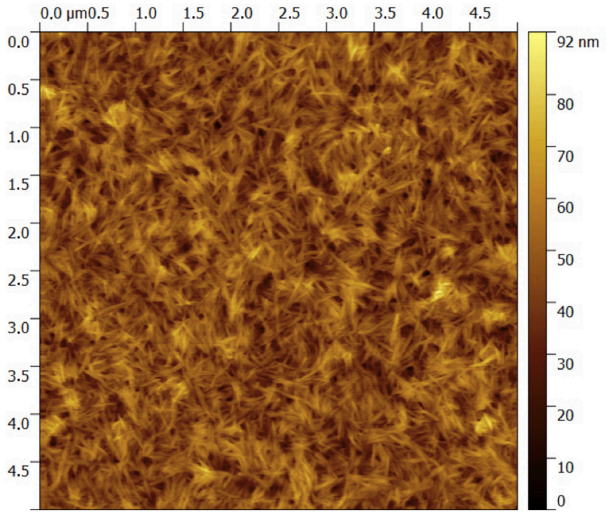

FIGURE 3 | 5 × 5 μm^2 AFM topography image of a $(GNPs/CNCs)_4$ multilayered film deposited on a Si wafer.

RESULTS AND DISCUSSION

Nanoparticles Characterization

The basic structural and charge properties of the two types of nanoparticles used to build the hybrid CNCs/GNPs thin films were first characterized. As shown in **Figure 1A**, the produced cotton CNCs are rod-like particles with a length between 100 and 300 nm and a width between 10 and 30 nm, each particle being a fascicle of a few parallel elementary subunits, in line with literature reports (Elazzouzi-Hafraoui et al., 2008). AFM and small angle neutron scattering results from the literature further show that the height of cotton CNCs is ∼6 nm (Elazzouzi-Hafraoui et al., 2008; Cherhal et al., 2015; Martin et al., 2017). The TEM micrograph in **Figure 1B** shows that GNPs appear as hexagonal platelets of 105 nm average diameter. In our previous work, the height of these platelets, ∼ 4 nm, was extracted from a statistical analysis of AFM topography images (Martin et al., 2017). Zeta potential measurements indicated that CNCs were negatively charged with a value of -40 ± 2 mV and that GNPs were positively charged with a value of $+52 \pm 3$ mV. In addition, conductometric titration of CNCs suspensions gave a charge content of about 260 mmol kg^{-1}, which corresponds to a sulfur content of 0.69% and a charge density of 0.5 e^-/nm^2, assuming all charges stem from sulfate groups. According to the literature, the surface charge density of GNPs is 5 $+/nm^2$ (Wierenga et al., 1998). Note that the pH of the CNCs suspension was 2.2, ensuring CNCs to be negatively charged. Ester-sulfate groups resulting from the sulfuric hydrolysis are indeed in their acidic form under these conditions. For GNPs, the pH is a sensitive parameter: Below pH 4 the GNPs dissolve in water; between pH 4 and pH 7 the GNPs are positively charged but above pH 7, the particle edges become negatively charged and gelation may occur (Wierenga et al., 1998). Accordingly, to ensure that both types of particles exhibit opposite charges, the pH of the GNPs suspension was adjusted to 5.9.

Building Hybrid Films on Model Substrate

GNPs/CNCs multilayers were first assembled on silicon wafers as smooth and solid model substrate using the LbL assembly process, as illustrated in **Figure 2**. The structural properties of the resulting films were investigated by AFM, ellipsometry and spectral reflectance. AFM topography images performed on $(GNPs/CNCs)_4$, $(GNPs/CNCs)_7$, and $(GNPs/CNCs)_{11}$ films show surfaces densely covered by CNCs (**Figure 3**). As shown in our previous work, this observation confirms that the used LbL process conditions led to the formation of homogeneous films. Strikingly, no underlying platelets can be distinguished, suggesting that the interactions between the two types of particles are particularly effective to allow a full coverage of a GNPs layer by a CNCs layer. In fact, the interaction between CNCs and GNPs is strong enough to allow for a short dipping time between the layer deposition: this time could be reduced to 5 min, as opposed to 15 min in our previous study. In **Figure 3**, the CNCs appear randomly oriented and their RMS rugosity was calculated equal to 8.2 ± 1.1 nm. As shown in **Supplementary Figure 1**, the GNPs-terminated films showed a very good coverage of the underlying CNCs layer by the subsequent GNPs deposition.

The thickness of the films determined by ellipsometry and spectral reflectance is plotted in **Figure 4** as a function of the number of deposited bilayers. The thickness increases linearly with *n*, irrespective of the technique used, showing a successful film growth. The thickness increment per bilayer is equal to 13 nm. Knowing that the thicknesses of nanoparticles are around 4 and 7 nm for GNPs and CNCs, respectively, one can conclude that each deposition corresponds to a single layer of each nanoparticle type. Moreover, the measured thicknesses are in total agreement with our previous work, where the film thicknesses were measured using AFM and neutron reflectivity (Martin et al., 2017). In addition, ellipsometry measurements allowed us to calculate the particle volume fraction Φ in the films

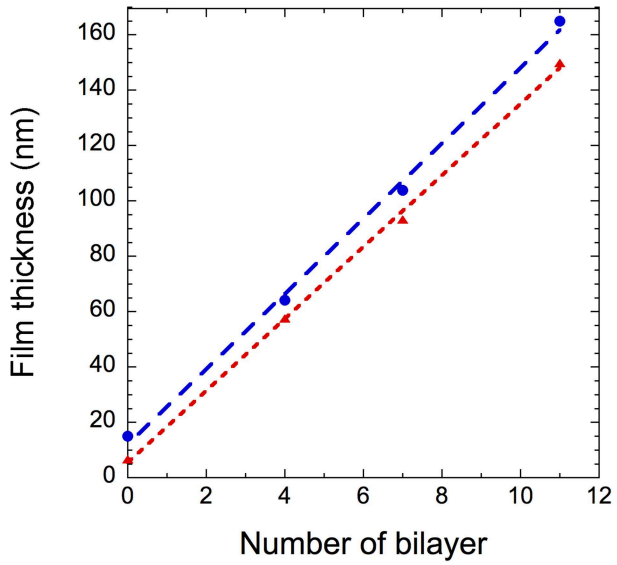

FIGURE 4 | $(GNPs/CNCs)_n$ film thickness as a function of the number of bilayers deposited on a Si wafer using spectral reflectance (●) and ellipsometry (▲). Dashed lines are linear fits to the data.

TABLE 1 | Thickness, refractive index, and particle volume fraction of $(GNP/CNC)_n$ determined by ellipsometry.

Number of bilayers	Thickness (nm)	Refractive index (A)	Refractive index (B)	$\Phi_{nanoparticles}$
4	57.6	1.481	6,917	0.83
7	93.2	1.512	6,712	0.90
11	149.9	1.492	9,932	0.86

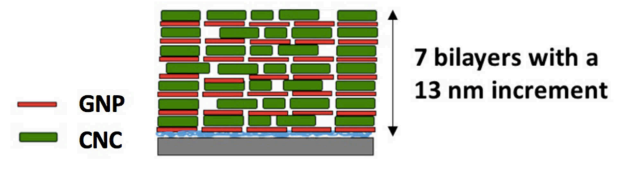

FIGURE 5 | Schematic representation of the likely structure of a $(GNPs/CNCs)_7$ hybrid film.

from their refractive index (Equation 2). **Table 1** summarizes the values of refractive index and corresponding particle volume fraction for $n = 4$, 7, and 11. Φ is close to 0.85 for all n values, showing that the films are very dense. Note that in our previous work a Φ value of nearly 0.8 was deduced from neutron reflectivity (Martin et al., 2017). This comparison therefore allows us to validate the present ellipsometry data. The linear growth together with the constant particle volume fraction suggest that the hybrid films built on model Si wafers exhibit the same internal structure irrespective of the thickness: they consist of repeated dense bilayers, leading to smooth films of low porosity and likely stratified as schematized in **Figure 5**.

Growth and Structure of the Films on Various Substrates

The aforementioned results demonstrate our ability to build dense hybrid all-nanoparticle GNPs/CNCs multilayered films on Si wafer. In the next step, we have investigated the possibility to build these films on various substrates, i.e., kraft cardboard, PE-coated cardboard, PE-LD film, and smart paper, exhibiting different chemical compositions, hydrophilicity, mechanical properties, flexibility and surface roughness.

The same LbL process was used on these four substrates and SEM imaging was performed to observe the surface of the deposited film. SEM micrographs of the substrates before and after the deposition of a $(GNPs/CNCs)_4$ film for kraft cardboard, PE-coated cardboard, smart paper and PE-LD film are shown in **Figures 6–8** and **Supplementary Figure 2**, respectively. A successful deposition is observed on all studied substrates. The observations are similar to those with the Si wafers, showing very dense and homogeneous films with a complete coverage of GNPs by CNCs. Since the $(GNPs/CNCs)_n$ films were very thin (<200 nm), the surface topography of the raw substrate was preserved. Identical dense CNCs top layers were obtained for hydrophobic (PE-coated cardboard and PE-LD films) as well as for hydrophilic (kraft cardboard and smart paper) substrates, smooth (PE-coated cardboard, PE-LD films and smart paper), rough (kraft cardboard) surfaces and very flexible (PE-LD films and smart paper) together with more rigid (kraft cardboard and PE-coated cardboard) samples. These results confirm the exceptional robustness of the deposition and building process, which is due not only to the versatility of the LbL assembly technique but also to the strong interactions between CNCs and GNPs that even allow using relatively short dipping times.

In addition, as shown in **Supplementary Figures 3**, **4**, GNPs-terminated coatings on PE-LD and kraft cardboard substrates exhibit a fairly regular and dense paving of the surface by the inorganic platelets, which is in line with the observations on model substrates. The inherent higher roughness of the commercial substrates therefore does not seem to impede the propensity of GNPs to densely cover the underlying CNCs and to lay flat on the surface.

The attempts to obtain sharp cross-sections of the films proved difficult, possibly due to the mismatch in composition and mechanical properties between the substrate and coating. Nevertheless, exploitable images could be recorded for $(GNPs/CNCs)_4$ films onto kraft cardboard and PE-LD and $(GNPs/CNCs)_7$ films onto PE-coated cardboard and smart paper substrates (**Supplementary Figures 5–7** and **Figure 9**, respectively). These images first showed void-free contact between the coating and the external surface of the different substrates, irrespective of their roughness or hydrophilic or hydrophobic character. In addition, it could be observed in each case that in the direction perpendicular to the film surface, homogeneous and dense (GNPs/CNCs) coatings were deposited. The thickness of the coating is constant along the cross-section and follows in a smooth and continuous manner the morphology of the underlying substrate. Quantitatively, as shown in **Supplementary Figure 8**, the thickness values that were measured are in close agreement with the values obtained

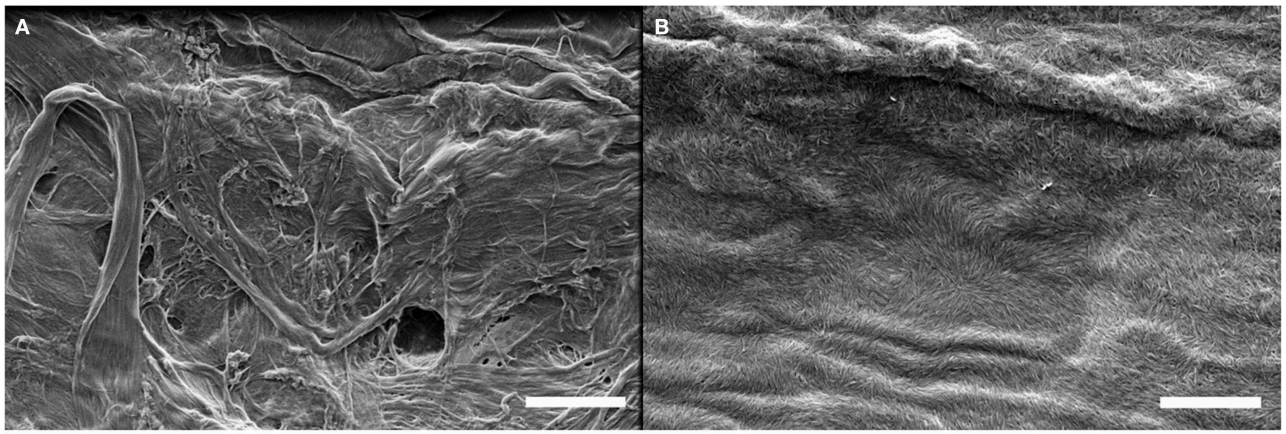

FIGURE 6 | SEM images of the kraft cardboard substrate before **(A)** and after **(B)** deposition of a $(GNPs/CNCs)_4$ multilayered film. Scale bar: 2 μm.

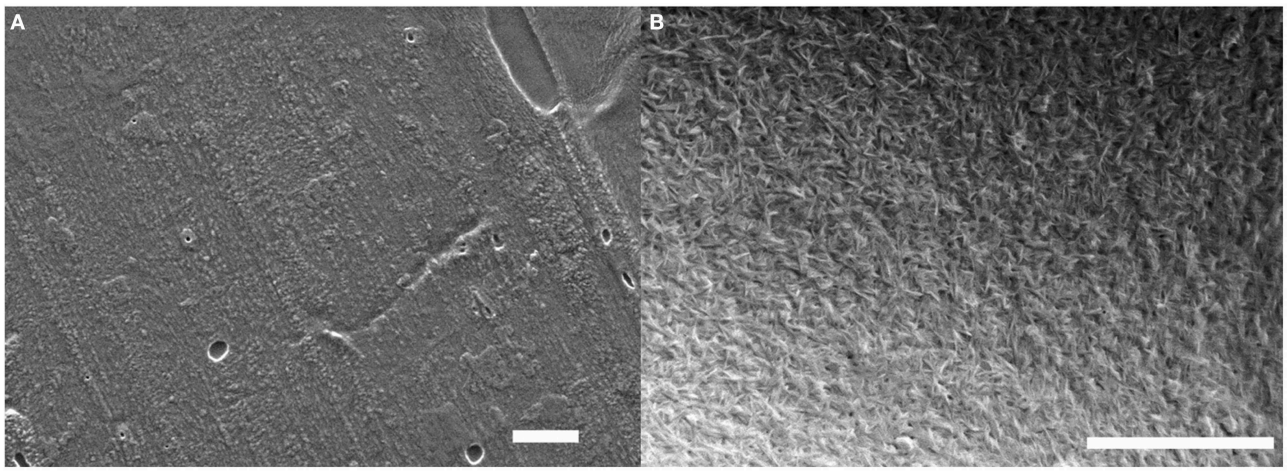

FIGURE 7 | SEM images of the PE-coated cardboard substrate before **(A)** and after **(B)** deposition of a $(GNPs/CNCs)_4$ multilayered film. Scale bar: 2 μm.

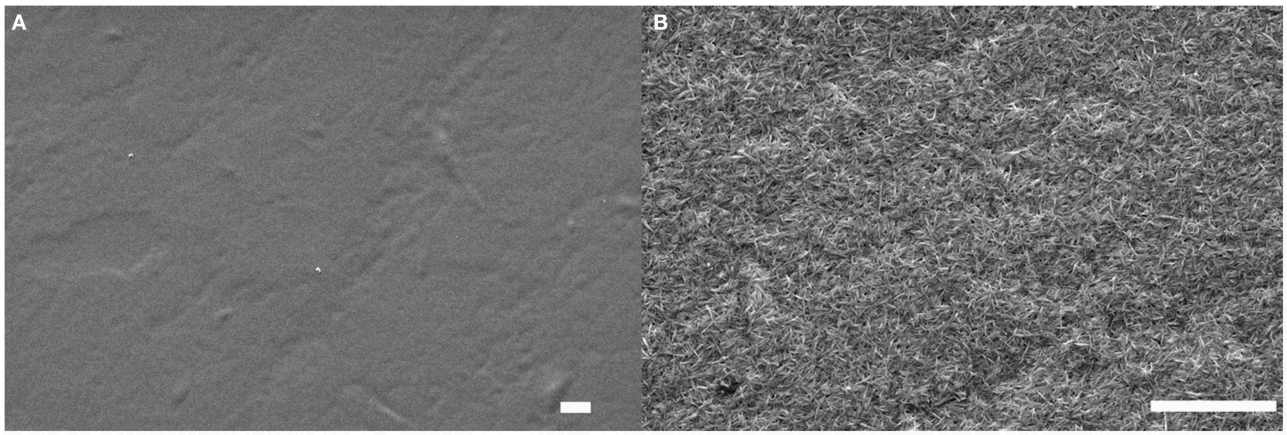

FIGURE 8 | SEM images of the smart paper substrate before **(A)** and after **(B)** deposition of a $(GNPs/CNCs)_4$ multilayered film. Scale bar: 2 μm.

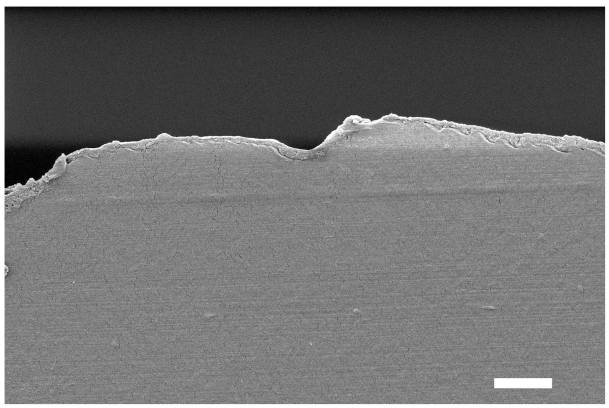

FIGURE 9 | Cross-section SEM image of the smart paper substrate after deposition of a $(GNPs/CNCs)_7$ multilayered film. Scale bar: 2 μm.

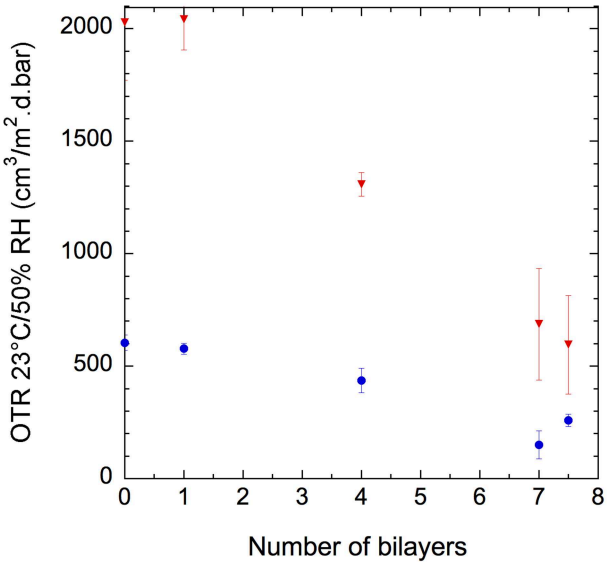

FIGURE 10 | Oxygen transmission rate of $(GNPs/CNCs)_n$-coated PE-coated cardboard (▾) and smart paper (●) substrates as a function of the number of deposited bilayers, *n*, at 23°C and 50% RH.

on model Si surfaces, suggesting a similar film architecture (i.e., a coating composed of superimposed nanoparticle-monolayers) and indicating a linear thickness increase of the coating on the commercial substrate with the number of deposited layers.

Oxygen Barrier Properties

In **Figure 10**, we present the effect on the oxygen barrier properties of the deposition of $(GNPs/CNCs)_n$ thin films onto PE-coated cardboard and smart paper substrates as a function of bilayers number. It must be noted that measurements were performed with a fiber optic oxygen transmitter (at 23°C using conditioned air at 21% oxygen and 50%RH as test gas, and dry nitrogen as carrier gas. Results indicate that for both substrates, the deposition of one bilayer does not show any positive or negative effect on oxygen transmission. Nevertheless, with four bilayers a positive effect started to occur. Indeed, for smart paper and PE-coated cardboard, the OTR value, respectively dropped down by 20% and 36%, after the deposition of $(GNPs/CNCs)_4$ thin films when compared to the bare substrates. Interestingly, this positive effect is intensified with 7 bilayers, since a $(GNPs/CNCs)_7$ film depositions on smart paper allows for a 75% OTR decrease and a 59% OTR decrease with PE-coated board, which corresponds to a significant improvement of the oxygen barrier properties. The absolute values of 150 and 600 $cm^3/m^2 \cdot d \cdot bar$ for smart paper and PE-coated board can be compared with classical samples showing a medium-oxygen barrier: in PET-coated cardboard, a typical value would be 100–150 $cm^3/m^2 \cdot d \cdot bar$ at 23°C, 50%RH for a coating of 22 g/m^2 PET (CTP internal data, 2016).

Based on the theory of permeability in the case of two separate laminate layers and using the OTR values measured for the pristine and coated substrates as well as the LbL film thickness measured on the model surfaces (but shown to be in close agreement with the one on the commercial substrates), the permeability of the LbL films was calculated and summarized in **Supplementary Table 1** (Crank, 1979). Surprisingly, a dependence of the permeability on the number of bilayers was obtained. It is assumed that the stratified LbL coating only composed of nanoparticles cannot be identified with a homogeneous layer with an inherent, thickness-independent, permeability as is the case for pure polymer layers. The particularly low value of the thickness of the films might also account for this result. However, when considering the $1 \leq n \leq 7$ range, a close to linear improvement of the OTR was obtained.

The permeability of a membrane, such as that of a nanocomposite film is the product of the diffusion coefficient and the solubility. In our case, the coating can be considered as a nanocomposite comprising two types of fillers in a matrix of air. According to the Nielsen model, the presence of the impenetrable GNPs and CNCs results in a longer, more tortuous path for gas molecules to go through, with the result of increasing their diffusion and reducing the overall permeability. This tortuous effect depends not only on the aspect ratio and volume fraction of the fillers but also on the location and orientation of the nanoparticles. It can be expected that the higher the volume fraction, aspect ratio and order parameter, the lower the permeability. In the case of pure CNCs coatings, the permeability data could be fitted using the Bharadwaj model, evidencing the effect of anisotropy on the gas barrier properties (Bharadwaj, 2001; Chowdhury et al., 2019). For the present system, extra complexity arises from the presence of two types of nanoparticles, each one having its own aspect ratio, volume fraction and order parameter, which results in a doubled number of parameters, some of them being unknown. For instance, the total volume fraction was estimated but the individual volume fraction for each type of particle is not known and thus this extra complexity renders almost impossible the fitting of the results to the available models. However, qualitative interpretations of the data can be proposed, given the similarities in the thickness of the coatings deposited onto model or commercial substrates. It can therefore

be assumed that a film architecture independent from the substrate was achieved. Accordingly, the very high density (low porosity) of the all-nanoparticle films measured by ellipsometry and neutron reflectivity on model surfaces is most probably conserved in the case of the commercial substrates, which will lead to a high tortuosity and limited oxygen diffusion, even though films of limited thickness (<100 nm) were deposited. Additionally, the measured small thickness increment per bilayer and the SEM observations suggest that both GNPs and CNCs lay flat with their long axis perpendicular to the diffusion direction, which will also maximize the aspect ratio effect on the limitation of oxygen transfer. The observed OTR variations with the number of bilayers can tentatively be attributed to an increase of the tortuous path with the thickness of the film that results in a decrease of the oxygen permeability.

In order to check if the upper layer had any effect on OTR, the deposition of 7.5 bilayers—allowing the upper layer to consist of GNPs—was investigated but no difference with $n = 7$ was observed (**Figure 10**). This result confirms that the film tortuosity—correlated to particle shapes and film structure—and film thickness are the key parameters governing the oxygen barrier properties at this relative humidity.

CONCLUSION

In this study, the ability of thin hybrid multilayered films to be deposited onto various substrates of interest for packaging applications with the goal of enhancing their oxygen barrier properties has been investigated. Structural investigation techniques show that homogeneous films composed of alternating monolayers of CNCs and GNPs nanoplatelets can be built onto the surface of smooth and rigid model substrates. These films, which are of particularly high density, exhibit a thickness that varies linearly with the number of deposited bilayers. Interestingly, these hybrid coatings can also be constructed onto flexible substrates regardless of their hydrophilicity, composition and surface topography. Such versatility arises from the conjunction of the use of the LbL assembly technique and from the intrinsic properties of the two types of nanoparticles used, which were previously shown to strongly interact through electrostatic attractions and hydrogen bonding. OTR measurements demonstrate that these partially bio-sourced all-nanoparticles hybrid thin films improved the oxygen barrier properties when deposited onto flexible paper substrates with up to 75% decrease in the oxygen permeability. This work thus provides an initial perspective for the potential of LbL formed films consisting only of nanoparticles, such as gibbsite nanoplatelets and cellulose nanocrystals, to improve the oxygen barrier properties of flexible paper-based substrates. The adaptability of the process to a wide variety of supports and the very limited thickness needed for substantial barrier properties enhancement implying very small amounts of materials, are strong assets for possible industrial applications.

DATA AVAILABILITY

All datasets generated for this study are included in the manuscript and/or the **Supplementary Files**.

AUTHOR CONTRIBUTIONS

MC completed the experimental work and analyses. MC, BJ, and LC-A designed the experimental plan and conducted project development. MC and BJ prepared the manuscript and all authors read, revised, and approved the submitted version. BJ, LC-A, DG, and LH conceived the project and contributed to data analysis and manuscript composition.

FUNDING

Financial support from Institut Carnot PolyNat (ANR N° 16-CARN-025-01).

ACKNOWLEDGMENTS

The authors acknowledge experimental support from Nanobio-ICMG FR 2607 and thank Christine Lancelon-Pin (CERMAV, Grenoble) for the electron microscopy images, Hugues Bonnet (DPM, Grenoble) for technical assistance on ellipsometry, and Geneviève Cortot (CTP, Grenoble) for helping with OTR measurements. BJ thanks M. Chanzy and H. Chanzy for suggestions during the writing of this manuscript.

SUPPLEMENTARY MATERIAL

The Supplementary Material for this article can be found online at: https://www.frontiersin.org/articles/10.3389/fchem.2019.00507/full#supplementary-material

REFERENCES

Azeredo, H. M. C., Rosa, M. F., and Mattoso, L. H. C. (2017). Nanocellulose in bio-based food packaging applications. *Industr. Crops Product.* 97, 664–671. doi: 10.1016/j.indcrop.2016.03.013

Bharadwaj, R. K. (2001). Modeling the barrier properties of polymer-layered silicate nanocomposites. *Macromolecules* 34, 9189–9192. doi: 10.1021/ma010780b

Cherhal, F., Cousin, F., and Capron, I. (2015). Influence of charge density and ionic strength on the aggregation process of cellulose nanocrystals in aqueous suspension, as revealed by small-angle neutron scattering. *Langmuir* 31, 5596–5602. doi: 10.1021/acs.langmuir.5b00851

Chowdhury, R. A., Nuruddin, M., Clarkson, C., Montes, F., Howarter, J., and Youngblood, J. P. (2019). Cellulose Nanocrystal (CNC) coatings with controlled anisotropy as high-performance gas barrier films. *ACS Appl. Mater. Interfaces* 11, 1376–1383. doi: 10.1021/acsami.8b16897

Crank, J. (1979). *The Mathematics of Diffusion, 2nd Edn.* Oxford, UK: Oxford University Press.

Decher, G., Hong, J. D., and Schmitt, J. (1992). Buildup of ultrathin multilayer films by a self-assembly process: III. Consecutively alternating adsorption of

anionic and cationic polyelectrolytes on charged surfaces. *Thin Solid Films* 210, 831–835. doi: 10.1016/0040-6090(92)90417-A

Decher, G., and Schlenoff, J. B. (eds.). (2012). *Multilayer Thin Films: Sequential Assembly of Nanocomposite Materials, 2nd Edn.* Weinheim: Wiley-VCH.

Elazzouzi-Hafraoui, S., Nishiyama, Y., Putaux, J.-L., Heux, L., Dubreuil, F., and Rochas, C. (2008). The shape and size distribution of crystalline nanoparticles prepared by acid hydrolysis of native cellulose. *Biomacromolecules* 9, 57–65. doi: 10.1021/bm700769p

Ferrer, A., Pal, L., and Hubbe, M. (2017). Nanocellulose in packaging: advances in barrier layer technologies. *Industr. Crops Product.* 95, 574–582. doi: 10.1016/j.indcrop.2016.11.012

Hubbe, M. A., Ferrer, A., Tyagi, P., Yin, Y., Salas, C., Pal, L., et al. (2017). Nanocellulose in thin films, coatings, and plies for packaging applications: a review. *Bio Resour.* 12, 2143–2233.

Iler, R. K. (1966). Multilayers of colloidal particles. *J. Coll. Interface Sci.* 21, 569–594. doi: 10.1016/0095-8522(66)90018-3

Klemm, D., Cranston, E. D., Fischer, D., Gama, M., Kedzior, S. A., Kralisch, D., et al. (2018). Nanocellulose as a natural source for groundbreaking applications in materials science: today's state. *Mater. Today* 21, 720–748. doi: 10.1016/j.mattod.2018.02.001

Klemm, D., Kramer, F., Moritz, S., Lindstrom, T., Ankerfors, M., Gray, D., et al. (2011). Nanocelluloses: a new family of nature-based materials. *Angew. Chem. Int. Edn.* 50, 5438–5466. doi: 10.1002/anie.201001273

Li, F., Biagioni, P., Bollani, M., Maccagnan, A., and Piergiovanni, L. (2013). Multi-functional coating of cellulose nanocrystals for flexible packaging applications. *Cellulose* 20, 2491–2504. doi: 10.1007/s10570-013-0015-3

Martin, C., Barker, R., Watkins, E. B., Dubreuil, F., Cranston, E. D., Heux, L., et al. (2017). Structural variations in hybrid all-nanoparticle gibbsite nanoplatelet/cellulose nanocrystal multilayered films. *Langmuir* 33, 7896–7907. doi: 10.1021/acs.langmuir.7b02352

Martin, C., and Jean, B. (2014). Nanocellulose/polymer multilayered thin films: tunable architectures towards tailored physical properties. *Nordic Pulp Paper Res. J.* 29, 19–30. doi: 10.3183/NPPRJ-2014-29-01-p019-030

Moon, R. J., Martini, A., Nairn, J., Simonsen, J., and Youngblood, J. (2011). Cellulose nanomaterials review: structure, properties and nanocomposites. *Chem. Soc. Rev.* 40, 3941–3994. doi: 10.1039/c0cs00108b

Priolo, M. A., Gamboa, D., and Grunlan, J. C. (2010). Transparent clay–polymer nano brick wall assemblies with tailorable oxygen barrier. *ACS Appl. Mater. Interfaces* 2, 312–320. doi: 10.1021/am900820k

Priolo, M. A., Holder, K. M., Greenlee, S. M., and Grunlan, J. C. (2012). Transparency, gas barrier, and moisture resistance of large-aspect-ratio vermiculite nanobrick wall thin films. *ACS Appl. Mater. Interfaces* 4, 5529–5533. doi: 10.1021/am3014289

Priolo, M. A., Holder, K. M., Guin, T., and Grunlan, J. (2015). Recent advances in gas barrier thin films via layer-by-layer assembly of polymers and platelets. *Macromol. Rapid Commun.* 36, 866–79. doi: 10.1002/marc.201500055

Qin, S., Pour, M. G., Lazar, S., Köklükaya, O., Gerringer, J., Song, Y., et al. (2019). Super gas barrier and fire resistance of nanoplatelet/nanofibril multilayer thin films. *Adv. Mat. Interfaces* 6:1801424. doi: 10.1002/admi.201801424

Revol, J. F., Bradford, H., Giasson, J., Marchessault, R. H., and Gray, D. G. (1992). Helicoidal self-ordering of cellulose microfibrils in aqueous suspension. *Int. J. Biol. Macromolecules* 14, 170–172. doi: 10.1016/s0141-8130(05)80008-x

Rhim, J.-W., Park, H.-M., and Ha, C.-S. (2013). Bio-nanocomposites for food packaging applications. *Progr. Polym. Sci.* 38, 1629–1652. doi: 10.1016/j.progpolymsci.2013.05.008

Song, Y., Hagen, D. A., Qin, S., Holder, K. M., Falke, K., and Grunlan, J. C. (2016). Edge charge neutralization of clay for improved oxygen gas barrier in multilayer nanobrick wall thin films. *ACS Appl. Mater. Interfaces* 8, 34784–34790. doi: 10.1021/acsami.6b12937

Thomas, B., Raj, M. C., Athira, K. B., Rubiyah, M. H., Joy, J., Moores, A., et al. (2018). Nanocellulose, a versatile green platform: from biosources to materials and their applications. *Chem. Rev.* 118, 11575–11625. doi: 10.1021/acs.chemrev.7b00627

Wierenga, A. M., Lenstra, T. A. J., and Philipse, A. P. (1998). Aqueous dispersions of colloidal gibbsite platelets: synthesis, characterisation and intrinsic viscosity measurements. *Coll Surfaces A* 134, 359–371. doi: 10.1016/s0927-7757(97)00224-0

Wijnhoven, J. E. G. J., van't Zand, D. D., van der Beek, D., and Lekkerkerker, H. N. W. (2005). Sedimentation and phase transitions of colloidal gibbsite platelets. *Langmuir* 21, 10422–10427. doi: 10.1021/la0513860

Wu, C.-N., Saito, T., Fujisawa, S., Fukuzumi, H., and Isogai, A. (2012). Ultrastrong and high gas-barrier nanocellulose/clay-layered composites. *Biomacromolecules* 13, 1927–1932. doi: 10.1021/bm300465d

Xie, H., Wei, J., and Zhang, X. (2006). Characterisation of sol-gel thin films by spectroscopic ellipsometry. *J. Phys. Conf. Series* 28, 95–99. doi: 10.1088/1742-6596/28/1/020

Conflict of Interest Statement: The authors declare that the research was conducted in the absence of any commercial or financial relationships that could be construed as a potential conflict of interest.

frontiers in Chemistry

REVIEW
published: 17 July 2019
doi: 10.3389/fchem.2019.00488

Ultrathin Films of Cellulose: A Materials Perspective

Eero Kontturi[1]* *and Stefan Spirk*[2]*

[1] Department of Bioproducts and Biosystems, School of Chemical Engineering, Aalto University, Espoo, Finland, [2] Institute of Paper, Pulp and Fiber Technology, Graz University of Technology, Graz, Austria

A literature review on ultrathin films of cellulose is presented. The review focuses on different deposition methods of the films—all the way from simple monocomponent films to more elaborate multicomponent structures—and the use of the film structures in the vast realm of materials science. The common approach of utilizing cellulose thin films as experimental models is therefore omitted. The reader will find that modern usage of cellulose thin films constitutes an exciting emerging area within materials science and it goes far beyond the traditional usage of the films as model systems.

Keywords: cellulose derivatives, cellulose solvents, nanocellulose, spin coating, sensors

OPEN ACCESS

Edited by:
Giuseppe Mensitieri,
University of Naples Federico II, Italy

Reviewed by:
Artur J. M. Valente,
University of Coimbra, Portugal
Jian Yu,
Institute of Chemistry (CAS), China
Luigi Torre,
University of Perugia, Italy

***Correspondence:**
Eero Kontturi
eero.kontturi@aalto.fi
Stefan Spirk
stefan.spirk@tugraz.at

Specialty section:
This article was submitted to Polymer Chemistry, a section of the journal Frontiers in Chemistry

Received: *25 March 2019*
Accepted: *25 June 2019*
Published: *17 July 2019*

Citation:
Kontturi E and Spirk S (2019) Ultrathin Films of Cellulose: A Materials Perspective. Front. Chem. 7:488. doi: 10.3389/fchem.2019.00488

INTRODUCTION

Ultrathin films (thickness <100 nm) represent an important category of modern materials. Constant advances in deposition techniques as well as in micro and nanoscale patterning have significantly contributed in developing the functionality of thin films. Particularly in materials technology, ultrathin films play a major role in products like solar cells, sensors, and displays. It is obvious that the present research prospects reach far and wide.

Cellulose—the polysaccharide that is responsible for the structural scaffold of all plant fibers (Rosenau et al., 2018)—has a somewhat different history from many other materials concerning ultrathin films. Much of the research activity has been focused on utilizing thin films as experimental models, that is, as so-called model films (Kontturi et al., 2006). In this realm, cellulose thin films have been applied to study, for example, adsorption phenomena and water interactions with cellulosic materials—something that is difficult to directly deduce from morphologically and chemically heterogeneous natural fibers. Aside the modeling approach, the use of ultrathin cellulose films has recently expanded to materials applications, with proposed usage as biosensors and thermoelectric materials among others.

The aim of this literature study is to review the development with ultrathin films of cellulose for materials purposes roughly during the past decade. An exhaustive review (Kontturi et al., 2006) exists by one of the authors (EK) but, published in 2006, it is already grossly outdated. Moreover, the 2006 review focused nearly exclusively on the use of the films as model films chiefly because the aspect of materials applications was underdeveloped at the time. For this reason, we have here concentrated on different structures with cellulose ultrathin films and how one can utilize them as materials. In particular, a thorough account of different casting and post-treatment methods is given because of their importance precisely in the realm of materials science. Patterned structures, submonolayers, textures, and blends have emerged as an important part of the topic. We emphasize that the use of ultrathin cellulose films as model surfaces has been almost totally omitted in this review. This is not to undermine the significance of model films. The research on physico-chemical interactions with cellulose films has grown into a field with hundreds of literature accounts and the incorporation of those references would simply blow this review out of

its proportions and overshadow the impact on materials science which stands as the objective here. In other words, the modeling approach warrants a review on its own. A good review already exists on surface forces in lignocellulosic systems (Österberg and Valle-Delgado, 2017) but a comprehensive review on all aspects of experimental modeling with ultrathin cellulose films is still missing.

The review is split in two sections. First, an account is given on various ways to deposit the cellulose films together with the background information and obvious challenges that are specific to cellulose. The second part is devoted to applications of ultrathin cellulose films in materials science. Some notions of most important references of the pre-2006 research are given, but the main focus is set on the research published after that, thus resulting in a markedly updated view on what one can achieve with cellulose films. We foresee that the review is not only useful for the cellulose specialist but that researchers from diverse fields can benefit and get ideas from its generic narrative.

FILM DEPOSITION

Cellulose is the trivial name for poly(β– 1 →4-D-glucopyranose), consisting exclusively of linearly arranged anhydroglucose units (**Figure 1**). It is the structural component of all green plants. In fact, all biosynthesized cellulose occurs in the form of semi-crystalline microfibrils, long nanoscopic threads that form the structural scaffold of plant fibers (**Figure 1**; Nishiyama, 2009). The structural role of cellulose is the basis of its high strength and stiffness: individual microfibrils have been estimated to bear the tensile strength of ca. 2–6 GPa (Saito et al., 2013), and modulus at around 100 GPa (Eichhorn, 2012). Furthermore, plant fibers aim at longevity and durability and therefore, cellulose as its main structural component is relatively inert and stubbornly insoluble.

The sparse solubility of cellulose (Medronho et al., 2012) is an issue with thin film preparation. While the deposition of ultrathin inorganic films are dominated by vapor deposition techniques, thin films from soft materials are usually prepared by solution-based techniques. With ultrathin cellulose films, two deposition methods have dominated over others: spin coating and Langmuir-Blodgett (LB) or Langmuir-Schaefer (LS) deposition. In spin coating, high speed spinning of the solution on a substrate results in solvent removal and subsequently a solid film with a high degree of reproducibility (Norrman et al., 2005). In Langmuir-Blodgett deposition (Ariga et al., 2013), a solution of the to-be-coated substance is first deposited on a surface of an immiscible liquid (usually water), and the solvent is allowed to evaporate. In the second step, a monolayer of the floating substance on the liquid subphase is formed physically by a means of barriers (so-called Langmuir film) and finally, a solid substrate is dipped through the monolayer, resulting in ideally a monomolecular film on the substrate. The thickness of the film can be tuned by the number of dips, each contributing ideally to a rise of one monolayer in thickness. With both techniques, the intrinsic insolubility of cellulose poses problems which can be overcome or circumvented in three different fashions: (i) direct use of cellulose solvents, (ii) use of dissolving derivatives that can be regenerated to cellulose after film deposition, and (iii) use of colloidal dispersions of nanosized cellulose. The following passages will elaborate on each of these approaches.

Film Deposition Directly From a Cellulose Solution

The prospect of applying a direct cellulose solvent for film deposition is attractive but it is far from an unproblematic approach. Aside from a class of relatively new solvents called ionic liquids, virtually all cellulose solvents are bicomponent or tricomponent systems involving a component that is solid at room temperature. These include mixtures of dimethylacetamide (DMAc) with LiCl (Dawsey and Mccormick, 1990), urea with aqueous NaOH (Cai and Zhang, 2005), or N-methylmorpholine-N-oxide (NMMO) with water (Rosenau et al., 2001). Obviously, if cellulose is cast from such solution into a solid film, the solid component from the solvent will also prevail in the film and it has to be removed by rinsing after the deposition.

Nearly all modern accounts with direct cellulose solvents utilize spin coating as the deposition technique (Generally, cellulose solvents are miscible in water and traditional LB-deposition with an aqueous subphase cannot therefore be used). Probably the most popular solvent has been NMMO/water or NMMO/DMSO which was introduced by the Wågberg group already in the early 2000s (Gunnars et al., 2002; Fält et al., 2004) while DMAc/LiCl as a casting solvent has also received some attention (Eriksson et al., 2005; Sczech and Riegler, 2006). A comprehensive survey by Aulin et al. (2009) on the crystallinity and morphology of different cellulose films revealed that the films spin coated from NMMO/water bore a semicrystalline structure with cellulose II, i.e., the order that arises from regenerated cellulose. The films spun from DMAc/LiCl, on the other hand, were almost completely amorphous. The films from both NMMO/water and DMAc/LiCl exhibited a fair degree of roughness, possibly due to the tracks left by the solid component after its removal (**Figures 2a,b**). Interestingly, the phase contrast image of the film deposited from NMMO/water shows clearly a fibrillar structure in contrast to the predominantly amorphous morphology of the film casted from DMAc/LiCl.

NMMO/water was also the solvent of choice when end-functionalized cellulose molecules were used for deposition (Yokota et al., 2007a). The idea was to attach a sulfur containing moiety (thiosemicarbazide) to the reducing end of dissolved cellulose molecules and subsequently expose the solution to a gold surface. The covalent bond, formed between sulfur and gold, aligned the cellulose chains parallel with each other, imposing a native cellulose I crystalline form, as analyzed by electron diffraction. Besides a recent account on thermally induced sol-gel transition from a DMAc/LiCl solvent (Wan et al., 2017), the end-tethering method is still the only form of regeneration that has led to cellulose I crystallites from solution. It is also a heavy indication of parallel alignment of cellulose I as opposed to

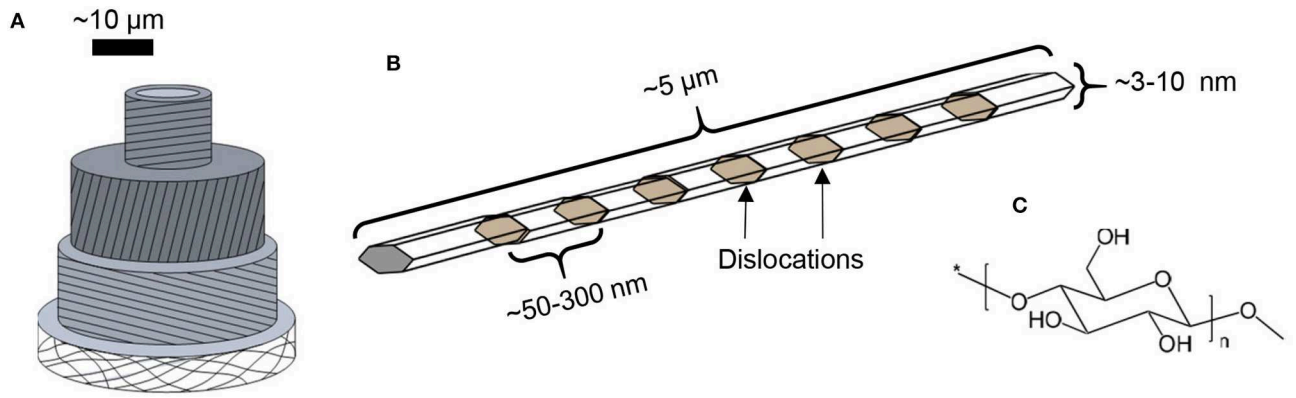

FIGURE 1 | Schematic representations of **(A)** plant cell, **(B)** semi-crystalline cellulose microfibril, and **(C)** cellulose molecule.

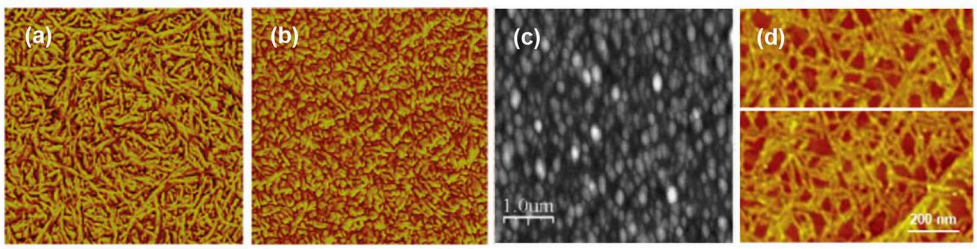

FIGURE 2 | AFM images of cellulose films spin coated from a solution of **(a)** NMMO/water, 1 × 1 μm^2 scan (Reproduced from Aulin et al., 2009 with permission from American Chemical Society), **(b)** DMAc/LiCl, 1 × 1 μm^2 (Reproduced from Aulin et al., 2009 with permission from American Chemical Society) and **(c)** thiourea/NaOH/water, 5 × 5 μm^2 scan (Reproduced from Yan et al., 2008 with permission from John Wiley & Sons, 2008); **(d)** individual cellulose molecules cast from a CED solution, 1 × 1 μm^2 scan (copyright Elsevier 2007) (Yokota et al., 2007b).

anti-parallel alignment of cellulose II—a topic that has aroused substantial controversy over the years (Langan et al., 2001; Dinand et al., 2002; Kim et al., 2006).

Curiously, urea/NaOH/water, one of the new and relatively popular solvents for cellulose, has not been exploited in thin film deposition. However, its more obscure variant thiourea/NaOH/water has been used for spin coating cellulose with relatively similar morphology to previously published films from other direct solvents (**Figure 2c**; Yan et al., 2008). Ionic liquids are also a popular new class of cellulose solvents and one of them, namely 1-ethyl-3-methylimidazolium acetate (EMIMAc) diluted with DMSO, was used for thin film deposition by Kargl et al. (2015a). Films of thickness from submonolayer regime to hundreds of nanometers were reported.

A notable offshoot from the films deposited directly from a cellulose solution is the contribution by Yokota et al. (2007b) to cast submonolayers of single cellulose molecules (**Figure 2d**). The individualized single molecules were deposited by adsorption from a dilute cupriethylenediamine (CED) solution and subsequent evaporation of the solvent. Single molecular submonolayers have not been explored further with cellulose despite the undisputed popularity of the approach since the late 1990s in polymer science (Sheiko and Möller, 2001).

Film Deposition via a Dissolving Cellulose Derivative

Monocomponent Cellulose Films

When utilizing a derivative as an aid to cast ultrathin films of cellulose, there is a single compound that dominates the research scene: trimethylsilyl cellulose (TMSC). Depending on its degree of substitution (DS), TMSC dissolves in many common organic solvents (Demeter et al., 2003). The TMSC solution can be effortlessly utilized in both LB deposition and spin coating and, once the film is cast, it can be hydrolyzed to cellulose by exposing it to fumes of aqueous HCl solution, as shown in the pioneering effort by Schaub et al. (1993) (**Figure 3A**). HCl vapor is able to fully hydrolyze the TMSC to cellulose without interfering much with the film morphology—something that would occur if the film was to be immersed in liquid HCl instead (Schaub et al., 1993). As a result, spin coated TMSC-based cellulose films (**Figure 3B**; Kontturi et al., 2003a,b) are much smoother than what can be achieved from direct deposition from a solvent (**Figure 2**). The LB deposited films from TMSC (**Figure 3C**; Holmberg et al., 1997) are highly smooth in any case due to the deposition technique.

The crystallinity of the TMSC-based cellulose films depends on the deposition technique. When LB deposition is used, the films turn out crystalline with the cellulose II polymorph (Aulin

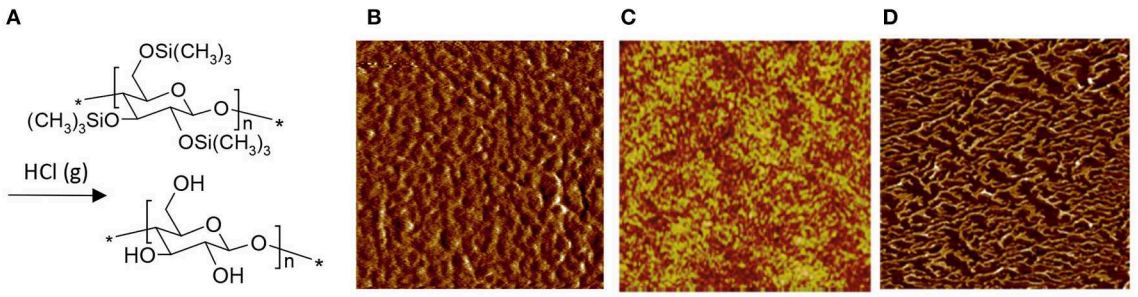

FIGURE 3 | (A) Reaction scheme of TMSC conversion to cellulose with HCl vapor; AFM images of **(B)** spin coated cellulose film, regenerated from TMSC (Reproduced from Kontturi et al., 2003a with permission from American Chemical Society), **(C)** Langmuir-Schaefer deposited cellulose film, regenerated from TMSC (Reproduced from Aulin et al., 2009 with permission from American Chemical Society) and **(D)** Langmuir-Schaefer deposited cellulose monolayer on hydrophobized silica, regenerated from TMSC (Reproduced from Niinivaara and Kontturi, 2014 with permission from Royal Society of Chemistry). All images are 1 × 1 μm^2 scans.

et al., 2009). With spin coating, on the other hand, the films are close to amorphous (Kontturi et al., 2011). Unlike many grades of bulk amorphous cellulose, the material in the TMSC-based ultrathin films does not start to crystallize when exposed to water (Kontturi et al., 2011).

The hydrolysis reaction from TMSC to cellulose in the 2D confinement of the supported ultrathin film received more attention in subsequent studies in the early 2010s. It was quantitatively shown that the thickness of spin coated TMSC contracted by about 60% upon hydrolysis, presumably due to the removal of bulky TMS groups and the onset of hydrogen bonding, largely prevented in TMSC but prevalent in cellulose (Kontturi and Lankinen, 2010). Simultaneously the density of the film, as monitored by x-ray reflectivity (XRR), increased from ∼1 to ∼1.5 g cm^{-3} which is close to the reported value for amorphous cellulose in bulk (Kontturi and Lankinen, 2010). Furthermore, an *in situ* quartz crystal microbalance (QCM) study (Mohan et al., 2012b) on the TMSC film hydrolysis showed similar results although the hydrolysis appeared to follow a two-phase kinetics contrary to the one-phase first order kinetics suggested by *ex situ* XRR. Another contemporaneous *in situ* study by total internal reflection (TIR) Raman spectroscopy also favored the two phase kinetic model (Woods et al., 2011). The possible reason behind the discrepancy between XRR and QCM/Raman data may lie in the scarcity of the measurement points in the XRR study. Meanwhile, small angle x-ray scattering (SAXS) measurements showed that substantial rearrangements occur in the cellulose film if the hydrolysis is continued further (up to 60 min) (Ehmann et al., 2015b). This was hypothetically ascribed to a greater mobility of shorter cellulose chains which are being formed by hydrolytic cleavage as a side reaction to the TMS group removal by acid vapor.

TMSC has also been used to prepare submonolayers films of cellulose, i.e., films where the amount of cellulose is so low that it does not exhibit full coverage over the substrate. When spin coated, the submonolayers appear as nanosized patches made of ca. 20–30 individual cellulose chains (Kontturi et al., 2005a). After LS deposition, on the other hand, the submonolayer morphology depends on the substrate used. In case of a hydrophobic, low surface energy substrate, the TMSC and subsequent cellulose submonolayers contract into fractals because of the entropic strive (**Figure 3D**; Niinivaara and Kontturi, 2014).

In the modern literature dominated by TMSC, another cellulose derivative to be used for cellulose thin film preparation is cellulose xanthate (CX) which is widely used for manufacturing viscose fibers and films and therefore a large scale commodity. Thin films were prepared by spin coating CX on silicon and gold substrates followed by regeneration using HCl vapor (Weißl et al., 2018). In contrast to TMSC, side products are not exclusively volatile but must be removed by a rinsing step using water. The obtained films are smooth and exhibit similar properties as the films derived from TMSC (e.g., with BSA adsorption).

Multicomponent Films

Because of the good solubility of TMSC in common solvents, it has been applied to prepare mixed or blended films with other polymers. Ultrathin films from polymer blends is a field that developed significantly during the late 1990s and early 2000s when atomic force microscopy (AFM) became a ubiquitous commodity in research laboratories worldwide (Xue et al., 2012). The idea behind polymer blend films is simple: when two immiscible polymers, dissolved in a common solvent, are cast onto an ultrathin film, phase separation occurs. The emerging phase separation patterns depend on the interactions between the polymers, their solubility in the relevant solvent, molecular weight, surface free energy, and the interactions between the polymers and the substrate. By simply spin coating two polymers from a common solvent, it is possible to create a large palette of textures as ultrathin films. The approach has been used, among others, to prepare anti-reflection coatings from polystyrene (PS)/poly(methyl methacrylate) (PMMA) blends (Walheim et al., 1999).

With cellulose-containing materials, TMSC/PS films, subsequently hydrolyzed to cellulose/PS films, were the first ones to be introduced (**Figure 4A**; Kontturi et al., 2005b). Later on, TMSC/PS morphology was utilized to tune the hydrophobic/hydrophilic proportion on an ultrathin cellulose film (Nyfors et al., 2009) and to immobilize gold nanoparticles on cellulose films with high spatial precision (Taajamaa et al.,

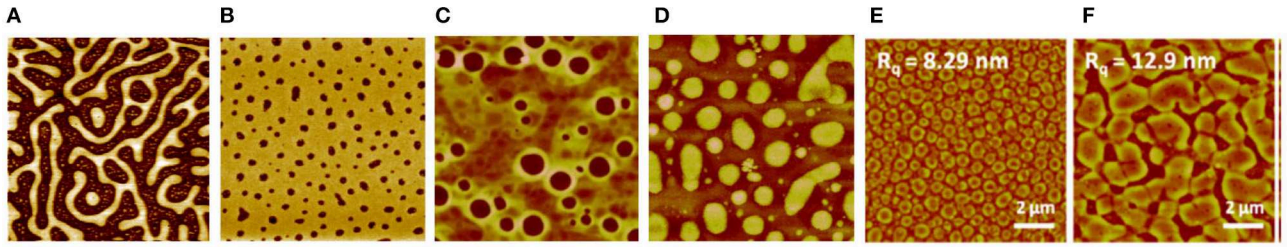

FIGURE 4 | AFM images of blend films of cellulose, regenerated from TMSC with other polymers at following ratios: **(A)** TMSC/PS 2:1, 20 × 20 μm^2 scan as in reference (Reproduced from Kontturi et al., 2005b with permission from American Chemical Society); **(B)** TMSC/PMMA 1:7, 5 × 5 μm^2 scan (Reproduced from Kontturi et al., 2009 with permission from Royal Society of Chemistry); **(C)** TMSC/CTA 1:2, 5 × 5 μm^2 scan (Reproduced from Taajamaa et al., 2011 with permission from Royal Society of Chemistry); **(D)** same film as in **(C)** but CTA has been removed with a selective solvent, 5 × 5 μm^2 scan (Reproduced from Taajamaa et al., 2011 with permission from Royal Society of Chemistry); **(E)** TMSC/CSE 3:1, 10 × 10 μm^2 scan (Reproduced from Niegelhell et al., 2017 with permission from American Chemical Society); **(F)** TMSC/CSE 1:1, 10 × 10 μm^2 scan (Reproduced from Niegelhell et al., 2017 with permission from American Chemical Society).

2013). Moreover, cellulose/PMMA films were introduced in the form of continuous PMMA layers with nano-sized cavities that bore disk-like cellulose at the bottom (Kontturi et al., 2009). The size of these cellulose-decorated cavities could be tuned by the original TMSC/PMMA ratio between 10–150 nm and the depth between 1–10 nm (**Figure 4B**).

TMSC was also used with cellulose acetate, to prepare ultrathin films of two distinct cellulose derivatives (Taajamaa et al., 2011). The resulting morphologies were peculiar with pores emerging that were exclusively in the cellulose acetate phase (**Figure 4C**). As usual, TMSC could be readily hydrolyzed to cellulose with HCl vapor but also cellulose acetate was hydrolyzed to cellulose with the use of ammonia vapor from aqueous NH_4OH. After hydrolysis of one component, the other unhydrolyzed component could be removed by a selective solvent, leading to ultrathin cellulose films with unique morphological features (**Figure 4D**). Later on, the approach from 2D ultrathin films of TMSC/cellulose acetate was transferred to 3D morphologies of non-woven electrospun fiber networks (Taajamaa et al., 2012). Another study on two cellulose derivatives consisted of ultrathin films from TMSC and cellulose stearoyl ester (CSE) (Niegelhell et al., 2017). Either pillars or continuous networks of cellulose with CSE could be tailored according to the TMSC/CSE ratios (**Figures 4E,F**).

The initial concept of blend cellulose films was developed further with the introduction of cellulose/lignin ultrathin films, first by Rojas et al. (Hoeger et al., 2012) and later by the Spirk group (Strasser et al., 2016). Lignin, a non-linear macromolecule consisting of phenylpropyl units, is the second important macromolecule in landplants (Feofilova and Mysyakina, 2016). In their early effort, Hoeger et al. used TMSC with acetylated lignin to cast ultrathin films by spin coating and subsequently hydrolyzing them to cellulose/lignin films (Hoeger et al., 2012). In a later study, Strasser et al. utilized lignin palmitate with TMSC, followed by HCl hydrolysis which transformed TMSC into cellulose but left lignin palmitate intact (Strasser et al., 2016). In addition, cellulose/lignin palmitate blend films exhibited an unexpected behavior when exposed to bovine serum albumin (BSA) (Strasser et al., 2016). The lignin palmitate acted as a sacrificial layer which was emulsified when in contact with BSA solutions, as observed by quartz crystal microbalance with dissipation monitoring (QCM-D). These results were supported by AFM images showing that the LP domains shrank in width and height after BSA exposure. A similar mechanism was observed for cellulose—stearic acid (SA) blends (Niegelhell et al., 2017). In such materials, the stearic acid underwent self-organization and enriched on the surface after spin coating and subsequent regeneration. Similar as for the cellulose-LP blends, the SA was removed upon exposing it to BSA, as shown by surface plasmon resonance (SPR) spectroscopy.

Concerning blend films incorporating TMSC, it is customary practice to optionally dissolve the other component after TMSC has been hydrolyzed to cellulose (Kontturi et al., 2005b). This is a routine found already in the seminal papers on polymer blend thin films, such as PS/PMMA (Walheim et al., 1997). With cellulose, however, a selective solvent for the other component is exceptionally easy to find because of the inherent insolubility of cellulose. Another way to approach selective removal of the other component is by specific enzymes. In this vein, Niegelhell et al. spin coated blend films from TMSC and poly(3-hydroxybutyrate) (PHB) and exposed them either to cellulose degrading cellulase enzymes or PHB degrading PHB-depolymerase (Niegelhell et al., 2016). The initial morphologies in TMSC/PHB blend films had TMSC forming protruding circular domains that shrank after their hydrolysis to cellulose (**Figure 5**).

Patterned Films via Lithography

Ordered, geometrically regular patterns on ultrathin films are mainly achieved by lithographic techniques. The first report on micropatterned cellulose thin films was reported by Tanaka et al. (2004). They used hard UV lasers to decompose a cellulose film, thereby leaving pads of cellulose with a size of ∼40 to 60 microns. The major idea of the patterning was to deposit cell membranes (i.e., human erythrocyte membranes) on the patterned cellulose thin films and to study the function of proteins in their native environment (**Figure 6**). Further they used the microtemplates to deposit microsomes from rabbit muscles. Both membrane patterns were stable for a period of over 1 week.

Another approach to induce patterns on cellulose is soft lithography in combination with enzymes (Kargl et al., 2013).

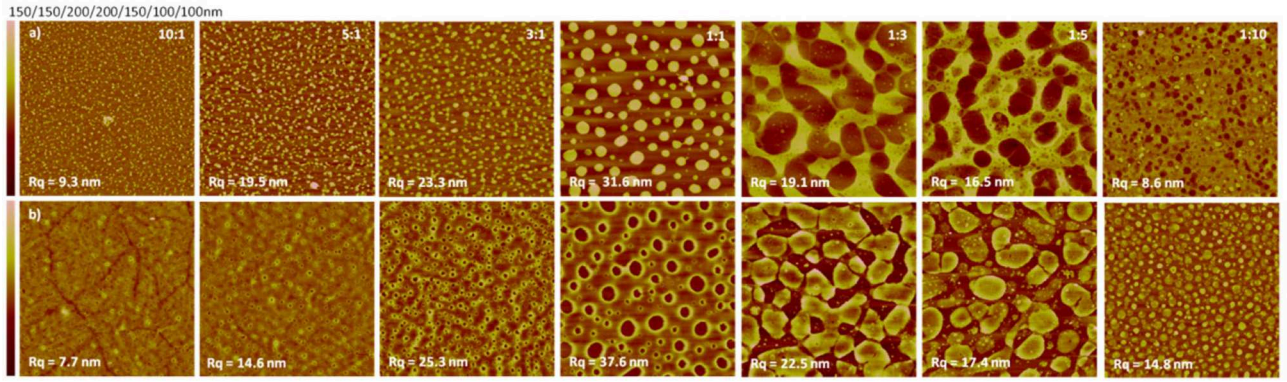

FIGURE 5 | AFM images (size 10 × 10 μm^2) of enzymatic degradation of PHB/cellulose thin films with PHB-depolymerase **(a)** or cellulase **(b)** (Reproduced from Niegelhell et al., 2016 with permission from American Chemical Society).

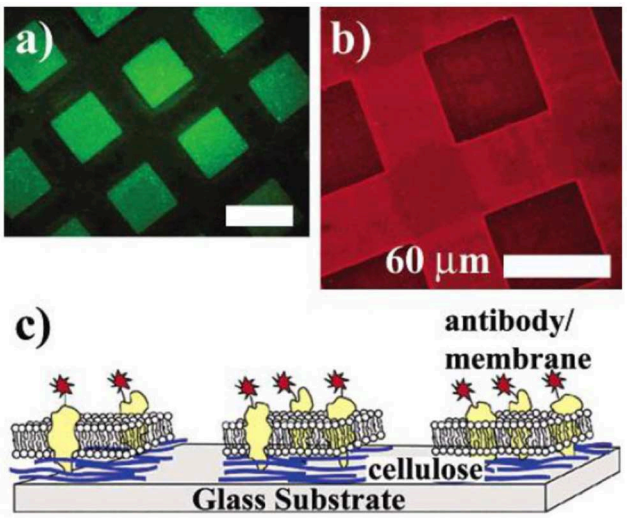

FIGURE 6 | (a) Fluorescence image of cellulose micropatterns exposed to a solution of bovine serum albumin labeled with fluorescein isothiocyanate (FITC-BSA) after removing the photomask. FITC-BSA adsorbs only onto the ablated area (bare glass substrate). **(b)** Human erythrocyte membranes spread on cellulose microtemplates (without BSA treatment). After incubation, the cytoplasmic domain of Band 3 is identified with a monoclonal and a TRITC-labeled polyclonal antibody (inside label). **(c)** Orientation of the erythrocyte membrane after spreading. Erythrocyte ghosts selectively adhere and rupture only on the cellulose micropatterns, exposing their cytoplasmic side (Reproduced from Tanaka et al., 2004 with permission from American Chemical Society).

This approach exploits the bioavailability of cellulose to enzymes capable of digesting it, i.e., cellulases. The approach works by protecting the cellulose by a micropatterned stamp. The accessible channels are filled with cellulase solution and the cellulose is digested. In such a way, cellulose micropatterns with feature sizes below 10 microns could be created. While this approach is elegant, it is quite laborious, setting a need for simpler routes.

One major step forward in patterning cellulose films was the use of masks protecting parts of the TMSC films during exposure to HCl. That way, regeneration occurs only in the accessible parts while the protected areas remain unaffected (Spirk et al., 2010). This procedure works on nearly any substrate although exact preparation procedures must be altered (e.g., use of 2-butanon as component in solvents) in order to deposit the TMSC onto specific polymer slides because standard solvents used for deposition may dissolve the substrate. These macroscopically structured slides were then used for a variety of applications (see section Applications Based on Surface Modification of Ultrathin Cellulose Films).

While these approaches are highly reproducible and useful for the generation of large cellulose patterns, they have inherent limitations due to the size of the mask features that could be employed during HCl exposure. Therefore, concepts from polymer science were transferred to cellulose film patterning by using photo acid generators (PAG) (Wolfberger et al., 2014). PAGs are photolabile compounds, which decompose under illumination to generate acids. The main idea behind them is to induce a solubility change during the UV exposure which could be induced in principle by crosslinking, addition of functionalities or cleavage of functional groups. In the case of TMSC, the silyl groups are cleaved off in the illuminated areas, resulting in cellulose (**Figure 7**). The manufacturing of the resist works by addition of PAGs to the TMSC precursor, followed by spin coating the components and exposure to UV light under application of masks. Already after exposure, a clear step height difference is visible indicating that TMSC has been converted to cellulose. A following development step using the solvent used for preparation (to remove TMSC) yields micro and sub-microstructured cellulose thin films (**Figure 8**). Alternatively, the film can also be developed using enzymes (to remove the cellulose) and subsequent treatment with UV light leads to a positive type resist. Actually, this was the first cellulose based photoresist (see section Applications Based on the Internal Structure of Ultrathin Cellulose Films) (Wolfberger et al., 2015).

The feature size of the structures was further reduced to the real nanometer regime by a focused ion beam (Ganner et al., 2016). Usually, electron beams harm biopolymers rather fast to create carbon. Ganner et al. demonstrated that conversion to

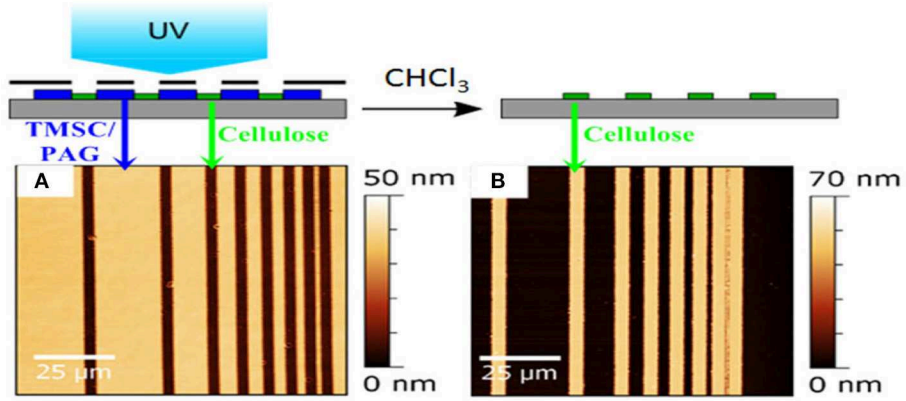

FIGURE 7 | AFM images of TMSC ultrathin films using a photolithographic mask after irradiation **(A)** and rinsing **(B)**. The smallest structure has a size of ca. 1 micron and wavelengths below 365 nm have been excluded by an emissive filter to prevent degradation of cellulose during the illumination step. [Reproduced from Wolfberger et al., 2014 under the terms of the Creative Commons Attribution (CC-BY) license].

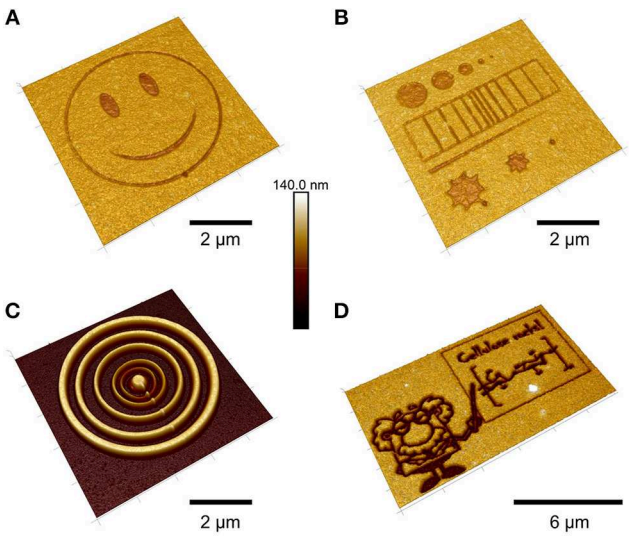

FIGURE 8 | AFM height images of TMSC films treated with an electron beam **(A,B,D)** and subsequent development with toluene **(C)** [Reproduced from Ganner et al., 2016 under the terms of the Creative Commons Attribution (CC-BY) license].

carbon can be overcome by exposing the films to the right dose, to merely induce regeneration of TMSC to cellulose. The influence of the dose was monitored by the enzymatic degradation of the structures and confirmed by ATR IR spectroscopy. Feature sizes down to 70 nm were created by this method.

Film Deposition From Colloidal Nanocellulose Dispersions

With colloidal dispersions for cellulose film deposition, the idea is to circumvent the difficult solubility issue by omitting dissolution altogether. Here, it is important to use nanosized cellulose dispersions to retain the ultrathin status for the films. For example, microcrystalline cellulose consists of fiber fragment particles generally in the size range of tens of microns, which render them far too large for ultrathin film deposition (thickness <100 nm).

Nanosized cellulose—by and large—comes in two main types: cellulose nanocrystals (CNCs) and cellulose nanofibers (CNFs) (Klemm et al., 2011; Kontturi et al., 2018). Although technology for CNC isolation has existed since the mid-twentieth century (Rånby, 1951) and for CNF isolation since the early 1980s (Turbak et al., 1983), the real upsurge of nanocellulose research started after mid-2000s when research on renewables was ready to belatedly step into the nanotechnology bandwagon (Klemm et al., 2011; Kontturi et al., 2018). Contrary to most synthetic nanoparticles, both nanocellulose sorts are prepared by a top-down approach. CNFs are essentially isolated microfibrils obtained by disintegration of a delignified fiber cell wall (Abdul Khalil et al., 2014; Nechyporchuk et al., 2016). CNCs are, to simplify, cut CNFs that are attained via acid hydrolysis which breaks the semicrystalline microfibril into more or less individual crystallites by selective hydrolysis of the disordered segments in the microfibrils (**Figure 1**; Trache et al., 2017). It must be noted that CNCs are not isolated via CNFs but they can be acquired directly through hydrolysis of fibers.

Ultrathin Films of CNCs

CNCs are typically prepared by hydrolysis with concentrated sulfuric acid. The acid not only selectively cleaves the disordered segments in cellulose microfibrils: it also introduces sulfate half-esters on the CNC surface (Dong et al., 1998). The charged sulfate groups play an important role in stabilizing aqueous CNC suspensions with electrostatic repulsion. Even at relatively high concentrations, CNC suspensions are fluid dispersions, although slow separation into isotropic and liquid crystal phases can be found above a certain critical concentration (∼10 wt.%) (Lagerwall et al., 2014).

The first account of ultrathin CNC films dates back to 2003 where Edgar and Gray applied spin coating to obtain smooth films that were stabilized with a mild heat treatment (Edgar

and Gray, 2003). The treatment possibly removes water from between the CNCs, thus preventing re-dispersion when exposed to water. The phenomenon is possibly similar to hornification which is usually interpreted as a drying (and heat) induced irreversible aggregation of cellulose microfibrils in the fiber cell wall (Fernandes Diniz et al., 2004; Pönni et al., 2012). It is important to note that the mild heat treatment does not influence the sulfate groups on the surface of CNCs, as shown by Notley et al. who observed a large electrostatic component when probing the surface forces of CNC films (Notley et al., 2006). In any case, the method of spin coating and subsequent mild heat treatment has been used for preparing stable ultrathin films of CNCs ever since (**Figure 9A**).

Electrostatics brought in by the sulfated CNC surfaces are also helpful when controlling submonolayer deposition of CNCs. Anionic CNCs disperse neatly on a cationic TiO_2 surface (**Figure 9B**; Kontturi et al., 2007), which has been later utilized when observing dimensions of individualized CNCs by AFM (Kontturi and Vuorinen, 2009). On anionic substrates, such as mica or silica, the CNCs tend to agglomerate in submonolayers, not enabling discerning of the individual CNCs.

Layer-by-layer (LbL) deposition is another means of film casting able to utilize charge on the CNC surface. Alternating layers of sulfated CNCs and cationic polyallylamine were introduced by Cranston and Gray (2006). Soon afterward, Podsiadlo et al. introduced LbL films of CNCs and polyethyleneimine which exhibited antireflective properties due to the suitable pore size distribution within the network of exceptionally long, tunicate-based CNCs (Podsiadlo et al., 2007). Since then, LbL films incorporating CNCs have emerged at regular intervals (Jean et al., 2008, 2009; Cerclier et al., 2010; Moreau et al., 2012; Olivier et al., 2012; Dammak et al., 2013; Olszewska et al., 2013; Azzam et al., 2014, 2015, 2017; Gill et al., 2017; Martin et al., 2017; Mauroy et al., 2018).

An account of all-cellulose films was presented by Niinivaara et al. (2016) who spin coated TMSC on a spin coated CNC layer and regenerated the TMSC to cellulose. Instead of appearing as two discrete layers, the TMSC was able to penetrate into the CNC network, forming a unique structure where CNCs were embedded in amorphous cellulose. The uptake of water vapor for these films exhibited an anomalous trend which did not follow the amorphous/crystalline ratio of amorphous cellulose and CNCs.

Besides spin coating, the accounts on alternative deposition techniques for CNC thin films are scattered. LB or LS deposition is not feasible for colloidal nanocellulose under the general setup of an aqueous subphase because nanocellulose dispersions themselves are virtually always dispersed in water. However, the Rojas group has reported LS films of CNCs by utilizing a cationic surfactant, dioctadecyldimethylammonium bromide (DODA) which easily forms a monolayer on water and complexes with CNCs that have been dispersed in the subphase (Habibi et al., 2010). Smooth ultrathin films with controlled thickness could be achieved from CNCs obtained from different sources, namely sisal, ramie, and cotton. The work was based on preliminary results on the same system, published few years earlier (Habibi et al., 2007).

Because nanosized cellulose is nearly always anisotropic, either rods (CNCs) or threads (CNFs), its orientation has been a pressing question, especially when used in composites as reinforcing materials. Orientation of CNCs in an ultrathin film would make a good precedent for orienting nanocellulose in larger matrices. In this vein, Hoeger et al. (2011) investigated orienting CNCs by a means of convective assembly—a method that has been highly successful in creating ordered layers of a variety of nanoparticles. It is based on capillary forces that work their way through the receding meniscus upon evaporation of a solvent. By the aid of a withdrawal plate to facilitate the movement of the meniscus, CNC films with >50% orientation could be formed. The technique was developed further by coupling convective assembly with electric field assisted shear assembly (Csoka et al., 2011).

Ultrathin Films of CNFs

Although CNFs as materials were introduced in the early 1980s (Turbak et al., 1983), it was not until 2006–2007 when their popularity surged due to several novel entries on preparation via mechanical disintegration with suitable pretreatments (Abe et al., 2007; Henriksson et al., 2007; Pääkkö et al., 2007) and an influential chemical pretreatment called TEMPO-mediated oxidation (Saito et al., 2006, 2007). The latter

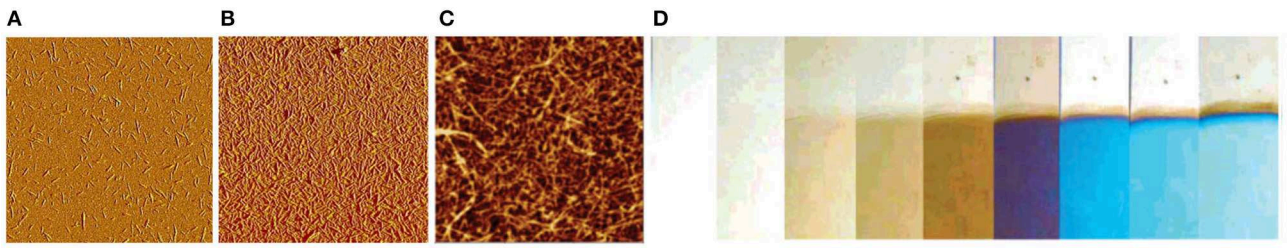

FIGURE 9 | (A) AFM image of spin coated submonolayer of CNCs on TiO_2, 5 × 5 μm^2 scan (Reproduced from Kontturi et al., 2007 with permission from American Chemical Society); **(B)** AFM image of spin coated layer of CNCs with full coverage, 5 × 5 μm^2 scan (Reproduced from Kontturi et al., 2007 with permission from American Chemical Society); **(C)** AFM image of LbL deposited CNF film, 1.5 × 1.5 μm^2 scan (Reproduced from Wågberg et al., 2008 with permission from American Chemical Society); **(D)** photograph of LbL deposited CNF films of different thickness values, resulting in colored structures through optical interference (Reproduced from Wågberg et al., 2008 with permission from American Chemical Society).

involves hypochlorite oxidation of cellulose catalyzed by 2,2,6,6-tetramethylpiperidine-1-oxyl radical (TEMPO) which is capable of selectively oxidizing the primary alcohol in the C6 position in cellulose This results in carboxylated cellulose microfibrils which can be effortlessly be individualized into CNFs because of electrostatic repulsion. Therefore, TEMPO-oxidized CNFs possess a high anionic charge density but indeed all CNF grades are at least mildly anionic due to the presence of hemicelluloses (mainly xylan) and oxidized structures on the microfibrils (Tenhunen et al., 2014; Tanaka et al., 2016).

The seminal problem with ultrathin film deposition concerning CNFs is their susceptibility to gel formation even at very low (∼1 wt.%) concentrations (Fall et al., 2011). Gels are obviously not generally suitable for thin film deposition that are based on fluid suspensions or solutions. For example, the thickness control with spin coating does not work if one is not free to increase the suspension concentration of CNFs due to gelling. Even acquiring a film with full coverage from the dilute fluid suspensions is not straightforward. In the first successful account, Ahola et al. had to use 3-aminopropyltrimethoxysilane (APTS) as a high charge density cationic anchor for CNF films with full coverage (Ahola et al., 2008). Later on, the community has settled to use an adsorbed layer of PEI to anchor the CNFs (**Figure 9C**). Concerning submonolayer structures, Werner et al. created submonolayers by adsorbing CNFs on circular domains of printed cationic polyelectrolytes (Werner et al., 2008).

When slightly thicker films of CNFs in the ultrathin regime are in demand, LbL deposition with cationic polyelectrolytes is an option, although the films cannot be considered to consist of pure CNF. The Wågberg group has been particularly active with investigating LbL systems involving CNFs. In a fundamental contribution (Wågberg et al., 2008), CNFs with added anionic charge by carboxymethylation were deposited with either PEI, PAH, or poly(diallyldimethylammonium chloride) (PDADMAC). The thickness of the resulting LbL films with CNFs depended not only on the choice of polyelectrolyte but it could be controlled by electrolyte addition which affected the coiling of the polyelectrolyte during LbL. The different thickness values led naturally to varying degrees of optical interference, i.e., color formation within the films (**Figure 9D**). The build-up of CNF/PEI films was thoroughly investigated in a follow-up publication (Aulin et al., 2008). Continuation to the work was published in a paper on all-CNF films, resulting from an LbL deposition from anionic and cationically modified CNFs (Aulin et al., 2010). Moreover, copolymers of N-isopropylacrylamide and cationic (3-acrylamidopropyl)trimethylammonium chloride were utilized for a thermoresponsive LbL film with CNFs (Utsel et al., 2010).

Unicomponent CNF films with a thickness control over a wider range—without layer-by-layer approach—are feasible with electrophoretic deposition (EPD), as demonstrated for highly charged TEMPO-oxidized CNFs by Wilson et al. (2018). The work was partially based on an earlier study where EPD was used to prepare thick films of CNCs (Chen et al., 2014). Otherwise, TEMPO-oxidized CNFs have not been popular with thin films simply because of their instability after the deposition: TEMPO-CNFs tend to re-disperse because of their high charge density and tricks like heat treatment—which works well with CNCs of lower charge density—are not able to prevent the re-dispersion. Therefore, ultrathin films of TEMPO-CNFs have been reported mainly in such cases that have not involved liquid exposure after the film deposition, for example, when checking the film response to water vapor (Hakalahti et al., 2017). These films have been deposited by spin coating.

MATERIALS APPLICATIONS OF ULTRATHIN CELLULOSE FILMS

Unlike the vast influence imparted by nanocellulose on materials science (Kontturi et al., 2018), ultrathin cellulose films have been far less popular in materials applications. The flurry of activity during the present decade, however, indicates that ultrathin films in materials can be considered an emerging trend. The majority of accounts are based on, in one way or another, enhanced biomolecule immobilization on the film surfaces, focusing mainly on proteins and DNA. This is generally achieved by surface modification of cellulose films via covalent or non-covalent (chiefly adsorption) means. The other option is to utilize the internal structure of the films for, e.g., membranes or optoelectronics. The reader will notice that most of these applied accounts only hint toward genuine application and that the field is not as mature as that of film deposition elaborated in section Film Deposition.

Applications Based on Surface Modification of Ultrathin Cellulose Films

The use of cellulose thin films as a support or active layer in materials development was originally driven from the biosensor perspective. Biosensors rely on specific interactions between a receptor and an acceptor. Such specific interactions are characteristic for biological systems and cover a wide range of biomolecules. Particularly protein-protein interactions have been in the focus of research activities on cellulosic surfaces. The main reason why cellulose is an excellent material for biosensor surfaces is its rather low non-specific interaction with proteins, while chemical modification (e.g., carboxylation, carbodiimide chemistry) can be easily accomplished. The low non-specific protein adsorption on cellulosic surfaces originates from the high degree of solvation of the cellulose molecules inside the thin film structures, thereby impeding the deposition of proteins having a large amount of water inside their structure as well. In order to realize a non-specific cellulose-protein interaction, water needs to be removed from the system, which is entropically unfavorable. In order to test surfaces toward non-specific protein adsorption, BSA is often used as a probe. It is well known that on neat cellulose thin films (e.g., from TMSC or CX), the amount of deposited BSA is very low under various conditions (Taajamaa et al., 2013; Weißl et al., 2018). Even close to the isoelectric point of BSA (4.8), where solubility is at its lowest due to a zero net charge of BSA, hardly any BSA adsorbs on a cellulose surface. However, the interaction

of BSA with the cellulose surface can be increased if charged moieties, e.g., chitosan, cationic cellulose (Mohan et al., 2013b, 2014), cationic starch (Kontturi et al., 2008; Niegelhell et al., 2018), or carboxymethyl cellulose are introduced on the films. While the attachment of cationic polymers is irreversible due to electrostatic and entropic interactions, the irreversible deposition of carboxymethyl cellulose onto cellulose is far more intriguing, since a negatively charged polymer irreversibly adsorbs on a (slightly) negatively charged cellulose film. It has been shown that for related cases such as xyloglucans, energy is gained by conformational similarity between the cellulose and the xyloglucan chains. Therefore, it has been speculated that the same applies as the driving force for carboxymethyl cellulose (CMC) deposition on cellulosic substrates (Kargl et al., 2012).

Since the charge of proteins depends on their pK_a value, they can be electrostatically deposited just by adjustment of the pH value. The group of Rojas showed in a benchmark study how physisorption of CMC and chitosan having different degrees of substitution affect the interaction of BSA and human immunoglobulin G (hIgG) with cellulose (Orelma et al., 2011). The idea was to use the charges of CMC and chitosan to tune the protein adsorption onto the surfaces, which was followed using a wide range of experimental techniques such as SPR and QCM-D. As expected, the highest amount of protein was determined close to the isoelectric points of the proteins (Orelma et al., 2011). Later, this concept was extended to cationic cellulose and trimethyl chitosans, where also the water content of the adsorbed protein layer was investigated by combination of QCM-D and SPR measurements (Mohan et al., 2013a, 2014). In the latter studies, different types of fluorescent labeled BSAs were additionally used to quantify the amount of deposited protein via fluorescent microscopy, showing a dynamic range of the modified cellulose film sensor probes from several μmol/L to some pmol/L. The rendering of the surfaces was accomplished via microspotting which enabled the automated fabrication of protein coated sensor slides on polymer substrates. The irreversible deposition of CMC on cellulose thin films was further used in other studies to anchor biomolecules onto the surfaces. Carboxylic groups on a surface enable the use of carbodiimide chemistry on cellulosic surfaces, which nowadays mostly involve the additional use of *N*-hydroxysuccinimide (NHS) esters to form a more stable intermediate with higher efficiencies in binding, particularly with NH_2-rich molecules. One of the first attempts to exploit these concepts on regenerated cellulose thin films was carried out by Orelma et al. who chemically immobilized avidin on the surfaces using 1-ethyl-3-[3-dimethylaminopropyl]-carbodiimide (EDC) combined with NHS, i.e., so-called EDC/NHS chemistry (Orelma et al., 2012a). Avidin has a highly selective interaction with biotin (often referred to as vitamin B7). Therefore, biotinylation of different types of proteins has been a widely employed strategy to render surfaces with different types of proteins in a highly selective manner. The authors also showed that the immobilization of avidin as well as its coupling with biotinylated BSA and hemoglobin can be performed in high yields and proposed these films as generic substrates for antibody detection (**Figure 10**; Orelma et al., 2012b). Other examples that included the use of EDC/NHS chemistry to achieve binding of biologically active materials were related to blood specific applications. One of such applications involves the use of anticoagulant coatings for materials that come in direct contact with blood, i.e., catheters, blood tubings, and stents. In such applications, the blood coagulation needs to be prevented or at least delayed, which is usually realized by deposition of negatively charged polymers such as heparin or other sulfated polysaccharides. The Spirk group showed that cellulose thin films can be used as substrate for such an application. By deposition of CMC, followed by EDC/NHS chemistry or, alternatively, rendering the surfaces with PEI, simultaneous antimicrobial and anticoagulant silver and gold nanoparticles can be irreversibly deposited on such surfaces (Breitwieser et al., 2013; Ehmann et al., 2015a). The resulting functionalized surfaces showed significant prolongation of coagulation of blood serum compared to pure cellulose thin films.

Concerning patterned cellulose layers created by masking and selective regeneration (see **Figures 6**–**8**), microspotting was used to deposit a further layer on top (e.g., CMC or cationic polysaccharides) in order to alter the surface for biomolecule immobilization. In the case of CMC, EDC/NHS chemistry was applied to anchor an ss-DNA strand (Kargl et al., 2013). These pads were then exposed to a complementary fluorescent labeled DNA strand, demonstrating high selectivity and affinity. The developed DNA sensor provided sensitivity down to 80 nmol/L of DNA (Kargl et al., 2013). The same authors later translated this technology into microarrays using the same approach, including optimization protocols (e.g., presence of ions or type of CMC) to improve the performance of the sensors (**Figure 11**; Kargl et al., 2015b). In a similar manner, protein sensor probes have been created by microspotting as already mentioned above (Mohan et al., 2013a, 2014) and functional conjugates using aminofluorescein as model compounds for proteins have been reported (Mohan et al., 2012a).

Blend films, such as those shown in **Figures 4**, **5**, have been utilized with the aim to generate anti-biofouling surfaces with low non-specific protein adsorption. These films include PHB/cellulose, cellulose/cellulose stearate, and cellulose/cellulose hydroxypropylstearate blends (Niegelhell et al., 2016, 2017). For all films, there was a minimum in the BSA adsorption close to ratios of 1:1 and 1:3. In the case of PHB, hardly any BSA was adsorbing which led to speculations whether wetting effects of the films may cause this behavior. In such case, the one polymer is coating the other polymer via capillary forces, thereby forming a very thin layer on top of the whole film. Although there are some indications, force friction microscopy investigations did not reveal a clear correlation to support these speculations, at least for the cellulose/cellulose hydroxypropylstearate blend films. However, the blend films with the lowest surface free energy were also those with the lowest BSA deposition on the surface, i.e., the surface free energy of the blend film involving cellulose and a hydrophobic component was higher than that of pure cellulose. It is evident that such a difference must be caused by roughness effects whereas it seems that the surface configuration—periodicity of the structure and feature size—might be an underlying factor.

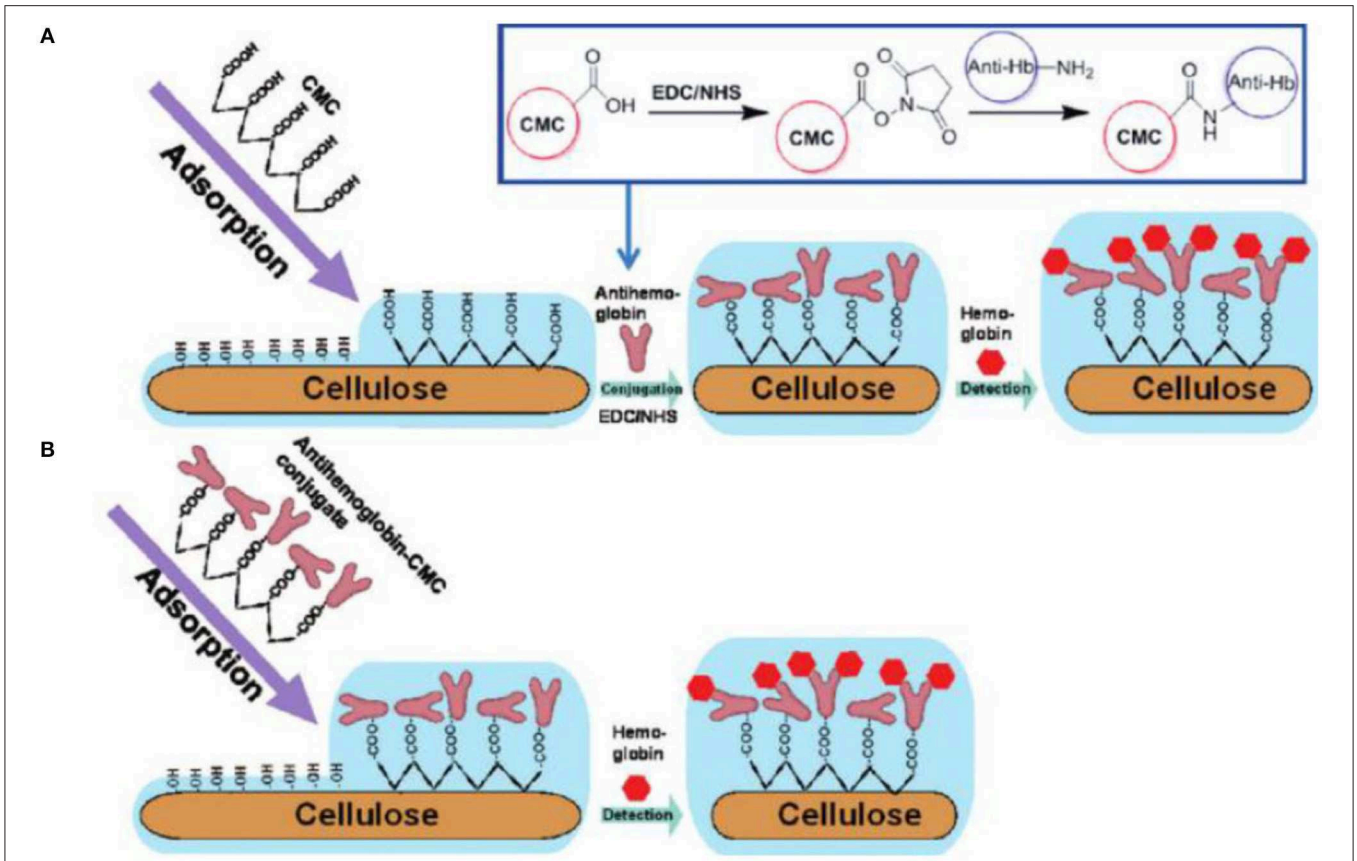

FIGURE 10 | Preparation of Immunochemical Hemoglobin Assay on the Cellulose Surface. **(A)** Carboxymethyl cellulose (CMC) is irreversibly adsorbed on cellulose and then antibodies are covalently conjugated on CMC-modified cellulose and **(B)** antibodies are pre-conjugated with CMC and then the pre-conjugated conjugate is irreversibly adsorbed on cellulose (Reproduced from Orelma et al., 2012b with permission from American Chemical Society).

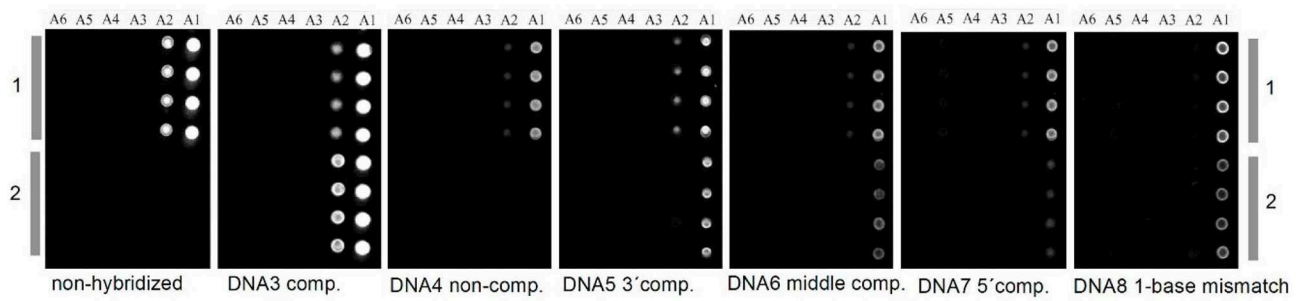

FIGURE 11 | Carboxymethyl cellulose decorated cellulose thin films in DNA microarrays before and after hybridization (copyright Elsevier 2015) (Kargl et al., 2015b).

The group of Garnier studied the adsorption of various proteins on deuterated cellulose films (Su et al., 2016; Raghuwanshi et al., 2017a,b). In that case, deuteration was performed by supplying cellulose producing bacteria with deuterated nutrients (i.e., deuterated glucose) followed by trimethylsilylation and processing as for non-deuterated samples. Deuteration is accompanied by enabling better contrast in neutron scattering, thereby allowing for very precise layer thickness determination of the adsorbed layer. Horse radish peroxidase (HPR) as an important representative of peroxidases was investigated. HRP is an important protein since, like avidin, it is often used in biochemical assays in order to label proteins and to detect antibodies. In a similar manner, immunoglobulin G (IgG) antibodies were visualized by neutron reflectivity and compared to results from other techniques, such as QCM-D. The background of these studies was to evaluate the amount of

IgG in respect to blood typing assays that were later reported on paper substrates.

Other methodologies to modify cellulose thin films by direct reaction on the surface have been recently introduced by the Stana-Kleinschek group. They showed that lysine moieties can be easily introduced on ready-made cellulose thin films by activation with N,N′-carbonyldiimidazole and subsequent aminolysis with lysine to yield a cellulose lysine carbamate film. In a similar manner, fuorates, and their aminated counterparts have been prepared (Elschner et al., 2016, 2018). These modifications have been developed to tune protein affinity to the surfaces, which was indicated by QCM-D.

In principle, a direct application of cellulose thin films is their use as a substrate for supported lipid bilayers (SLB) (Tanaka and Sackmann, 2005). SLBs serve as model systems for cell membranes to better understand membrane functions (e.g., transport, adhesion, signal transduction; Tanaka et al., 2001, 2004; Goennenwein et al., 2003). However, their manufacturing must consider several properties of the substrate they are deposited on. The support for the SLBs must be compatible to proteins and cells and should not induce denaturation of any component. Further, it should be amphiphilic (i.e., hydrophilic and hydrophobic) while being chemically stable toward the SLBs. Cellulose thin films fulfill these prerequisites, since their rather high degree of swelling leads to rather low non-specific interaction with biomolecules.

Applications Based on the Internal Structure of Ultrathin Cellulose Films

This part of the review consists of accounts where the actual structure of the cellulose film has been utilized as a material—as opposed to the attempts that make use of the film surface, or modified surface, in the previous section. It is a more scattered collection of literature entries, resulting in a more inconsistent and uneven narrative.

As already mentioned, the micropatterned films created with the aid of PAGs were utilized as photoresists (see **Figure 6**; Wolfberger et al., 2014, 2015). A negative type resist with a thickness of 32 nm was shown to be efficient as dielectric gate material in thin film transistors. Performance indicators showed that gate leak currents as well as the impedance of the films feature excellent values.

Another contribution by the Spirk group focused on cellulose—PHB films (as in **Figure 5**) which were used to create bioorthogonally degradable films to realize so called bioresists (Niegelhell et al., 2016). These studies were further accompanied by fast scan AFM imaging providing videos of the enzymes (PHB depolymerase and cellulases) in real time. Additionally, the results were corroborated by SPR spectroscopy. Feature sizes between nano and micrometer size can be obtained depending on the ratio of the two polymers in the films.

The internal addition of precursors or functional molecules allows for further applications of cellulose based thin films. Here, the solubility of TMSC in organic solvents is exploited which allows for addition of either drugs, nanoparticle precursors, or even nanoparticles. For instance Maver and coworkers showed that cellulose thin films, doped with diclofenac, exhibit a similar release profile as with fiber treated samples (Maver et al., 2015). Since drug release studies on fibers are very laborious and time consuming, the use of cellulose thin films was proposed as a viable alternative to these tests. Furthermore, Parra et al. incorporated hydroxygallium phthalocyanine into the cellulose structure. That way, they could come up with a gas sensor capable to detect 0.1 ppm of oxygen which was better than just immobilizing the phtalocyanine alone (Parra et al., 2007). A different system was introduced as a humidity sensor probe, obtained by using a ternary system composed of alternating layers of cellulose, polyvinyl alcohol and poly(N-vinylcarbazole). Seven trilayers of these polymers formed a photonic crystal which showed a response toward alterations in humidity levels (Manfredi et al., 2016).

Carrying on with the theme of incorporating components into the films, a variety of nanoparticles has been deposited on or in cellulose thin films. One strategy to create nanoparticle rendered thin films is to add a precursor to the TMSC solution, deposited by spin coating on a surface and either converted to the nanoparticle before or after regeneration of the TMSC to cellulose. Bismuth based nanoparticles have recently gained attention due to their potential use as new contrast agents for magnetic resonance imaging (Gösweiner et al., 2018). Such nanoparticles can be created from labile bismuth compounds such as $BiPh_3$, and from bismuth xanthates that are added to TMSC before processing. While $BiPh_3$ can be degraded by UV light to elemental Bi nanoparticles in the low nanometer range (Breitwieser et al., 2015), the xanthates are converted to the bismuth sulfides via the Chugaev reaction (80 nm length, 25 nm width) (Reishofer et al., 2017a). This procedure works also for other metal sulfides and in a similar way $CuInS_2$ nanoparticles (diameters of few nm) have been created in a TMSC matrix. This was exploited in optoelectronic devices (a nanocrystal thin film solar cell) with good performance and a photocurrent efficiency of ca. 1% (Reishofer et al., 2017b). The xanthates can be also deposited as an individual layer in the surface of the cellulose films. This was accomplished on cellulose thin films from cellulose xanthate where alternating multilayers of cellulose and $CuInS_2$ with adjustable thickness were created. Upon exposure to UV light, the $CuInS_2$ layers generated photocurrents (**Figure 12**; Weißl et al., 2019). In another attempt with inorganic materials, Nissinen and coworkers studied the formation of calcium sulfates in/on cellulose thin films spin coated from NMMO in an industrial context. They pretreated the cellulose thin films with Ca^{2+} ions and exposed the films to concentrated solutions of Bassanite (calcium sulfate hemihydrate). They observed that depending on the activation procedure the rate of crystallization can be controlled (Nissinen et al., 2013, 2014). In a recent report, cellulose thin films were decorated with different nanodots [silicon-dots (SiDs), carbon-dots (CDs)] or nitrogen-doped carbon dots (N-CDs). The authors propose the use of these nanodots in biomedical applications due to their non-toxicity compared to other frequently used materials (Cuevas et al., 2019).

A multilayered structure with TEMPO-CNFs and ZnO was achieved by consecutive adsorption of CNFs and atomic layer

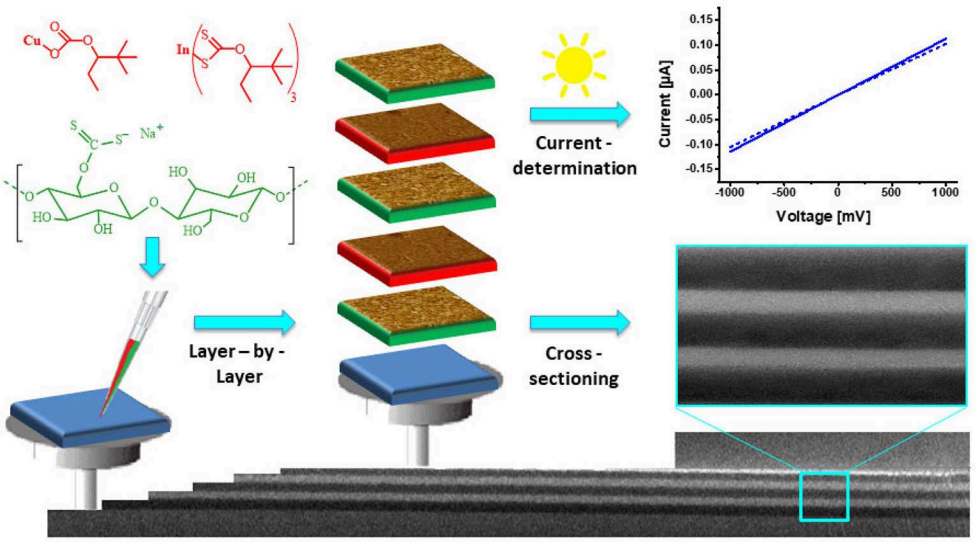

FIGURE 12 | Schematic illustration of the preparation of cellulose/$CuInS_2$ multilayer films and their characterization using cross-sectional SEM (Reproduced from Weißl et al., 2019 with permission from Elsevier).

deposition (ALD) of ZnO (Jin et al., 2017). These hybrid films were envisaged as thermoelectric materials because the thermal conductivity of the films could be controlled with the insulating cellulose layers in between the ZnO layers.

On a different note, the Peinemann group published a series of papers on thin film membranes based on cellulose thin films (Puspasari et al., 2016, 2018a,b,c). They used either crosslinking (e.g., by glutaraldehyde) or blending with other materials (e.g., PEI or siloxanes) to achieve certain material characteristics, including zero salt rejection, enhanced dehumidification performance, more size and charge selectivity to mention but a few.

Future Outlook on Applications With Ultrathin Cellulose Films

Overall, utilizing the inherent structure of cellulose within the thin films for materials applications is an approach still in its infancy. There are no commercial applications at present but the current scientific literature gives indications as to where some of the business-related interests may lie in the near future. For example, clear proof-of-concept exists of functioning photoresists from cellulose and its derivatives. Cellulose based photoresist overcome several issues of conventional photoresists. For the preparation of photoresists, environmentally harmful and often toxic solvents such as chlorobenzene are used while the photoresist materials consist of persistent polymers that contribute to plastic pollution. Instead, biodegradable cellulose derivatives proposed so far for phototresists can be processed from ecosolvents such as ethyl acetate. European legislation will further push the replacement of conventional, non-biodegradable, non-renewable synthetic polymers by biobased greener solutions in the next decade and this will certainly affect photoresists as well. Still, further developments are required to commercialize the technology into products, involving adhesion on various substrates, efficiency, durability and resistance in harsh environments for instance.

Similar issues abound with membrane technology: organic solvents are generally required for preparation of the present commercial membranes and this could be omitted particularly if water-based nanocellulose dispersions are used for membrane manufacture. Ultimately, however, the performance of cellulose thin films will dictate their pliability in relevant applications. Concern about the dimensional stability of cellulose films under water and humidity, for example, is one of the factors that could limit its usage.

However, the specific response of cellulose to water and humidity may be seen as an advantageous issue from materials perspective. Recent work on fundamental understanding of the cellulose-water interactions within ultrathin films underline this relationship (Kontturi et al., 2013; Niinivaara et al., 2015, 2016; Tammelin et al., 2015; Reid et al., 2016; Hakalahti et al., 2017). Indeed, the native functions of cellulose may be utilized for specific functionalities in the future. Humidity sensors or various actuators based on humidity would be obvious examples for potential applications. There is, however, room also for more sophisticated functional materials based on water/humidity response of cellulose in thin films in the realm of, e.g., smart material solutions.

Biomedical applications of cellulose based thin films have been shown to have a huge potential as well. Here, several proof of concepts from various groups do exist that propose the detection of biomolecules such as DNA and proteins. Proteins seem to have the largest potential for commercialization in the field of enzyme immobilization and antibody detection. Antibody detection is a crucial point when it comes to blood typing and it was already shown

that IgG can be effectively detected on such films. Here the combination of patterned cellulose thin films for in combination with microfluidics could be an opportunity to develop new products.

CONCLUSION

This review has shown how the focus on cellulose films has recently shifted to another direction. Ultrathin films of cellulose were previously perceived mainly as tools for experimental modeling, by applying them as model films to probe and interpret fundamental physico-chemical phenomena occurring with cellulose-based materials. Although the modeling aspect is still important, utilization of these films in materials applications has become an equally important activity. This aspect is still in its infancy, but we see a significant potential in the approach where the functional features of cellulose in its native environment could be utilized for its applications within ultrathin films.

AUTHOR CONTRIBUTIONS

EK wrote the Introduction and Conclusions as well as the section on Film Deposition. SS was largely responsive for the section on Materials Applications.

FUNDING

EK acknowledges Academy of Finland (grant no. 303452) for funding. SS acknowledges the Christian Doppler Laboratory for Fiber Swelling and Paper Performance for financial support of the Austrian Federal Ministry of Economy, Family and Youth, and the National Foundation for Research, Technology and Development.

ACKNOWLEDGMENTS

EK is also grateful for the support by the FinnCERES Materials Bioeconomy Ecosystem.

REFERENCES

Abdul Khalil, H. P. S., Davoudpour, Y., Islam, M. N., Mustapha, A., Sudesh, K., Dungani, R., et al. (2014). Production and modification of nanofibrillated cellulose using various mechanical processes: a review. *Carbohydr. Polym.* 99, 649–665. doi: 10.1016/j.carbpol.2013.08.069

Abe, K., Iwamoto, S., and Yano, H. (2007). Obtaining cellulose nanofibers with a uniform width of 15 nm from wood. *Biomacromolecules* 8, 3276–3278. doi: 10.1021/bm700624p

Ahola, S., Salmi, J., Johansson, L. S., Laine, J., and Österberg, M. (2008). Model films from native cellulose nanofibrils. preparation, swelling, and surface interactions. *Biomacromolecules* 9, 1273–1282. doi: 10.1021/bm701317k

Ariga, K., Yamauchi, Y., Mori, T., and Hill, J. P. (2013). 25th anniversary article: what can be done with the Langmuir-Blodgett method? Recent developments and its critical role in materials. *Science* 25, 6477–6512. doi: 10.1002/adma.201302283

Aulin, C., Ahola, S., Josefsson, P., Nishino, T., Hirose, Y., Osterberg, M., et al. (2009). Nanoscale cellulose films with different crystallinities and mesostructures–their surface properties and interaction with water. *Langmuir* 25, 7675–7685. doi: 10.1021/la900323n

Aulin, C., Johansson, E., Wågberg, L., and Lindström, T. (2010). Self-organized films from cellulose I nanofibrils using the Layer-by-Layer technique. *Biomacromolecules* 11, 872–882. doi: 10.1021/bm100075e

Aulin, C., Varga, I., Claesson, P. M., Wågberg, L., and Lindström, T. (2008). Buildup of polyelectrolyte multilayers of polyethyleneimine and microfibrillated cellulose studied by *in situ* dual-polarization interferometry and quartz crystal microbalance with dissipation. *Langmuir* 24, 2509–2518. doi: 10.1021/la7032884

Azzam, F., Chaunier, L., Moreau, C., Lourdin, D., Bertoncini, P., and Cathala, B. (2017). Relationship between Young's modulus and film architecture in cellulose nanofibril-based multilayered thin films. *Langmuir* 33, 4138–4145. doi: 10.1021/acs.langmuir.7b00049

Azzam, F., Moreau, C., Cousin, F., Menelle, A., Bizot, H., and Cathala, B. (2014). Cellulose nanofibril-based multilayered thin films: effect of ionic strength on porosity, swelling, and optical properties. *Langmuir* 30, 8091–8100. doi: 10.1021/la501408r

Azzam, F., Moreau, C., Cousin, F., Menelle, A., Bizot, H., and Cathala, B. (2015). Reversible modification of structure and properties of cellulose nanofibril-based multilayered thin films induced by postassembly acid treatment. *Langmuir* 31, 2800–2807. doi: 10.1021/acs.langmuir.5b00211

Breitwieser, D., Kriechbaum, M., Ehmann, H. M. A., Monkowius, U., Coseri, S., Sacarescu, L., et al. (2015). Photoreductive generation of amorphous bismuth nanoparticles using polysaccharides – Bismuth–cellulose nanocomposites. *Carbohydr. Polym.* 116, 261–266. doi: 10.1016/j.carbpol.2014.06.017

Breitwieser, D., Spirk, S., Fasl, H., Ehmann, H. M. A., Chemelli, A., Reichel, V. E., et al. (2013). Design of simultaneous antimicrobial and anticoagulant surfaces based on nanoparticles and polysaccharides. *J. Mat. Chem. B* 1, 2022–2030. doi: 10.1039/c3tb00272a

Cai, J., and Zhang, L. (2005). Rapid dissolution of cellulose in LiOH/Urea and NaOH/Urea aqueous solutions. *Macromol. Biosci.* 5, 539–548. doi: 10.1002/mabi.200400222

Cerclier, C., Cousin, F., Bizot, H., Moreau, C., and Cathala, B. (2010). Elaboration of spin-coated cellulose-xyloglucan multilayered thin films. *Langmuir* 26, 17248–17255. doi: 10.1021/la102614b

Chen, Q., De Larraya, U. P., Garmendia, N., Lasheras-Zubiate, M., Cordero-Arias, L., Virtanen, S., et al. (2014). Electrophoretic deposition of cellulose nanocrystals (CNs) and CNs/alginate nanocomposite coatings and free standing membranes. *Colloids Surf. B Biointerfaces* 118, 41–48. doi: 10.1016/j.colsurfb.2014.03.022

Cranston, E. D., and Gray, D. G. (2006). Morphological and optical characterization of polyelectrolyte multilayers incorporating nanocrystalline cellulose. *Biomacromolecules* 7, 2522–2530. doi: 10.1021/bm0602886

Csoka, L., Hoeger, I. C., Peralta, P., Peszlen, I., and Rojas, O. J. (2011). Dielectrophoresis of cellulose nanocrystals and alignment in ultrathin films by electric field-assisted shear assembly. *J. Colloid Interface Sci.* 363, 206–212. doi: 10.1016/j.jcis.2011.07.045

Cuevas, A., Campos, B. B., Romero, R., Algarra, M., Vazquez, M. I., and Benavente, J. (2019). Eco-friendly modification of a regenerated cellulose based film by silicon, carbon and N-doped carbon quantum dots. *Carbohydr. Polym.* 206, 238–244. doi: 10.1016/j.carbpol.2018.10.074

Dammak, A., Moreau, C., Beury, N., Schwikal, K., Winter Heiko, T., Bonnin, E., et al. (2013). Elaboration of multilayered thin films based on cellulose nanocrystals and cationic xylans: application to xylanase activity detection. *Holzforschung* 67, 579–586. doi: 10.1515/hf-2012-0176

Dawsey, T. R., and Mccormick, C. L. (1990). The lithium chloride/dimethylacetamide solvent for cellulose: a literature review. *J. Macro. Sci. Part C* 30, 405–440. doi: 10.1080/07366579008050914

Demeter, J., Mormann, W., Schmidt, J., and Burchard, W. (2003). Solution behavior of trimethylsilyl cellulose of different degrees of substitution, studied by static and dynamic light scattering. *Macromolecules* 36, 5297–5303. doi: 10.1021/ma0300286

Dinand, E., Vignon, M., Chanzy, H., and Heux, L. (2002). Mercerization of primary wall cellulose and its implication for the conversion of cellulose I→ cellulose II. *Cellulose* 9, 7–18. doi: 10.1023/A:1015877021688

Dong, X. M., Revol, J.-F., and Gray, D. G. (1998). Effect of microcrystallite preparation conditions on the formation of colloid crystals of cellulose. *Cellulose* 5, 19–32. doi: 10.1023/A:1009260511939

Edgar, C. D., and Gray, D. G. (2003). Smooth model cellulose I surfaces from nanocrystal suspensions. *Cellulose* 10, 299–306. doi: 10.1023/A:1027333928715

Ehmann, H. M. A., Breitwieser, D., Winter, S., Gspan, C., Koraimann, G., Maver, U., et al. (2015a). Gold nanoparticles in the engineering of antibacterial and anticoagulant surfaces. *Carbohydr. Polym.* 117, 34–42. doi: 10.1016/j.carbpol.2014.08.116

Ehmann, H. M. A., Werzer, O., Pachmajer, S., Mohan, T., Amenitsch, H., Resel, R., et al. (2015b). Surface-sensitive approach to interpreting supramolecular rearrangements in cellulose by synchrotron grazing incidence small-angle X-ray scattering. *ACS Macro Lett.* 4, 713–716. doi: 10.1021/acsmacrolett.5b00306

Eichhorn, S. J. (2012). Stiff as a board: perspectives on the crystalline modulus of cellulose. *ACS Macro Lett.* 1, 1237–1239. doi: 10.1021/mz300420k

Elschner, T., Bracic, M., Mohan, T., Kargl, R., and Stana Kleinschek, K. (2018). Modification of cellulose thin films with lysine moieties: a promising approach to achieve antifouling performance. *Cellulose* 25, 537–547. doi: 10.1007/s10570-017-1538-9

Elschner, T., Reishofer, D., Kargl, R., Griesser, T., Heinze, T., and Kleinschek, K. S. (2016). Reactive cellulose-based thin films - a concept for multifunctional polysaccharide surfaces. *RSC Adv.* 6, 72378–72385. doi: 10.1039/C6RA14227C

Eriksson, J., Malmsten, M., Tiberg, F., Callisen, T. H., Damhus, T., and Johansen, K. S. (2005). Model cellulose films exposed to H. insolens glucoside hydrolase family 45 endo-cellulase—the effect of the carbohydrate-binding module. *J. Colloid Interface Sci.* 285, 94–99. doi: 10.1016/j.jcis.2004.10.042

Fall, A. B., Lindström, S. B., Sundman, O., Ödberg, L., and Wågberg, L. (2011). Colloidal stability of aqueous nanofibrillated cellulose dispersions. *Langmuir* 27, 11332–11338. doi: 10.1021/la201947x

Fält, S., Wågberg, L., Vesterlind, E. L., and Larsson, P. T. (2004). Model films of cellulose II – improved preparation method and characterization of the cellulose film. *Cellulose* 11, 151–162. doi: 10.1023/B:CELL.0000025403.23775.75

Feofilova, E. P., and Mysyakina, I. S. (2016). Lignin: Chemical structure, biodegradation, and practical application (a review). *Appl. Biochem. Microbiol.* 52, 573–581. doi: 10.1134/S0003683816060053

Fernandes Diniz, J. M. B., Gil, M. H., and Castro, J. A. A. M. (2004). Hornification—its origin and interpretation in wood pulps. *Wood Sci. Technol.* 37, 489–494. doi: 10.1007/s00226-003-0216-2

Ganner, T., Sattelkow, J., Rumpf, B., Eibinger, M., Reishofer, D., Winkler, R., et al. (2016). Direct-write fabrication of cellulose nano-structures via focused electron beam induced nanosynthesis. *Sci. Rep.* 6:32451. doi: 10.1038/srep32451

Gill, U., Sutherland, T., Himbert, S., Zhu, Y., Rheinstädter, M. C., Cranston, E. D., et al. (2017). Beyond buckling: humidity-independent measurement of the mechanical properties of green nanobiocomposite films. *Nanoscale* 9, 7781–7790. doi: 10.1039/C7NR00251C

Goennenwein, S., Tanaka, M., Hu, B., Moroder, L., and Sackmann, E. (2003). Functional incorporation of integrins into solid supported membranes on ultrathin films of cellulose: impact on adhesion. *Biophys. J.* 85, 646–655. doi: 10.1016/S0006-3495(03)74508-1

Gösweiner, C., Lantto, P., Fischer, R., Sampl, C., Umut, E., Westlund, P.-O., et al. (2018). Tuning nuclear quadrupole resonance: a novel approach for the design of frequency-selective MRI contrast agents. *Phys. Rev. X* 8:021076. doi: 10.1103/PhysRevX.8.021076

Gunnars, S., Wågberg, L., and Cohen Stuart, M. A. (2002). Model films of cellulose: I. Method development and initial results. *Cellulose* 9, 239–249. doi: 10.1023/A:1021196914398

Habibi, Y., Foulon, L., Aguié-Béghin, V., Molinari, M., and Douillard, R. (2007). Langmuir–Blodgett films of cellulose nanocrystals: preparation and characterization. *J. Colloid Interface Sci.* 316, 388–397. doi: 10.1016/j.jcis.2007.08.041

Habibi, Y., Hoeger, I., Kelley, S. S., and Rojas, O. J. (2010). Development of Langmuir–Schaeffer cellulose nanocrystal monolayers and their interfacial behaviors. *Langmuir* 26, 990–1001. doi: 10.1021/la902444x

Hakalahti, M., Faustini, M., Boissière, C., Kontturi, E., and Tammelin, T. (2017). Interfacial mechanisms of water vapor sorption into cellulose nanofibril films as revealed by quantitative models. *Biomacromolecules* 18, 2951–2958. doi: 10.1021/acs.biomac.7b00890

Henriksson, M., Henriksson, G., Berglund, L. A., and Lindström, T. (2007). An environmentally friendly method for enzyme-assisted preparation of microfibrillated cellulose (MFC) nanofibers. *Eur. Polym. J.* 43, 3434–3441. doi: 10.1016/j.eurpolymj.2007.05.038

Hoeger, I., Rojas, O. J., Efimenko, K., Velev, O. D., and Kelley, S. S. (2011). Ultrathin film coatings of aligned cellulose nanocrystals from a convective-shear assembly system and their surface mechanical properties. *Soft Matter* 7, 1957–1967. doi: 10.1039/c0sm01113d

Hoeger, I. C., Filpponen, I., Martin-Sampedro, R., Johansson, L.-S., Österberg, M., Laine, J., et al. (2012). Bicomponent lignocellulose thin films to study the role of surface lignin in cellulolytic reactions. *Biomacromolecules* 13, 3228–3240. doi: 10.1021/bm301001q

Holmberg, M., Berg, J., Stemme, S., Ödberg, L., Rasmusson, J., and Claesson, P. (1997). Surface force studies of Langmuir–Blodgett cellulose films. *J. Colloid Interface Sci.* 186, 369–381. doi: 10.1006/jcis.1996.4657

Jean, B., Dubreuil, F., Heux, L., and Cousin, F. (2008). Structural details of cellulose nanocrystals/polyelectrolytes multilayers probed by neutron reflectivity and AFM. *Langmuir* 24, 3452–3458. doi: 10.1021/la703045f

Jean, B., Heux, L., Dubreuil, F., Chambat, G., and Cousin, F. (2009). Non-Electrostatic building of biomimetic cellulose–xyloglucan multilayers. *Langmuir* 25, 3920–3923. doi: 10.1021/la802801q

Jin, H., Marin, G., Giri, A., Tynell, T., Gestranius, M., Wilson, B. P., et al. (2017). Strongly reduced thermal conductivity in hybrid ZnO/nanocellulose thin films. *J. Mater. Sci.* 52, 6093–6099. doi: 10.1007/s10853-017-0848-5

Kargl, R., Mohan, T., Bračič, M., Kulterer, M., Doliška, A., Stana-Kleinschek, K., et al. (2012). Adsorption of carboxymethyl cellulose on polymer surfaces: evidence of a specific interaction with cellulose. *Langmuir* 28, 11440–11447. doi: 10.1021/la302110a

Kargl, R., Mohan, T., Koestler, S., Spirk, S., Doliska, A., Stana-Kleinschek, K., et al. (2013). Functional patterning of biopolymer thin films using enzymes and lithographic methods. *Adv. Funct. Mater.* 23, 308–315. doi: 10.1002/adfm.201200607

Kargl, R., Mohan, T., Ribitsch, V., Saake, B., Puls, J., and Stana-Kleinschek, K. (2015a). Cellulose thin films from ionic liquid solutions. *Nordic Pulp Pap. Res. J.* 30, 6–13. doi: 10.3183/npprj-2015-30-01-p006-013

Kargl, R., Vorraber, V., Ribitsch, V., Kostler, S., Stana-Kleinschek, K., and Mohan, T. (2015b). Selective immobilization and detection of DNA on biopolymer supports for the design of microarrays. *Biosens. Bioelectron.* 68, 437–441. doi: 10.1016/j.bios.2015.01.038

Kim, N.-H., Imai, T., Wada, M., and Sugiyama, J. (2006). Molecular directionality in cellulose polymorphs. *Biomacromolecules* 7, 274–280. doi: 10.1021/bm0506391

Klemm, D., Kramer, F., Moritz, S., Lindstrom, T., Ankerfors, M., Gray, D., et al. (2011). Nanocelluloses: a new family of nature-based materials. *Angew. Chem. Int. Ed Engl.* 50, 5438–5466. doi: 10.1002/anie.201001273

Kontturi, E., Johansson, L.-S., Kontturi, K. S., Ahonen, P., Thüne, P. C., and Laine, J. (2007). Cellulose nanocrystal submonolayers by spin coating. *Langmuir* 23, 9674–9680. doi: 10.1021/la701262x

Kontturi, E., Johansson, L.-S., and Laine, J. (2009). Cellulose decorated cavities on ultrathin films of PMMA. *Soft Matter* 5, 1786–1788. doi: 10.1039/b901059a

Kontturi, E., Laaksonen, P., Linder, M. B., Nonappa, Groschel, A. H., Rojas, O. J., and Ikkala, O. (2018). Advanced materials through assembly of nanocelluloses. *Adv. Mater. Weinheim.* 30:e1703779. doi: 10.1002/adma.201703779

Kontturi, E., and Lankinen, A. (2010). Following the kinetics of a chemical reaction in ultrathin supported polymer films by reliable mass density determination with X-ray reflectivity. *J. Am. Chem. Soc.* 132, 3678–3679. doi: 10.1021/ja100669w

Kontturi, E., Suchy, M., Penttilä, P., Jean, B., Pirkkalainen, K., Torkkeli, M., et al. (2011). Amorphous characteristics of an ultrathin cellulose film. *Biomacromolecules* 12, 770–777. doi: 10.1021/bm101382q

Kontturi, E., Tammelin, T., and Osterberg, M. (2006). Cellulose–model films and the fundamental approach. *Chem. Soc. Rev.* 35, 1287–1304. doi: 10.1039/B601872F

Kontturi, E., Thüne, P. C., Alexeev, A., and Niemantsverdriet, J. W. (2005a). Introducing open films of nanosized cellulose—atomic force microscopy and quantification of morphology. *Polymer* 46, 3307–3317. doi: 10.1016/j.polymer.2005.02.087

Kontturi, E., Thüne, P. C., and Niemantsverdriet, J. W. (2003a). Cellulose model surfacessimplified preparation by spin coating and characterization by X-ray photoelectron spectroscopy, infrared spectroscopy, and atomic force microscopy. *Langmuir* 19, 5735–5741. doi: 10.1021/la03 40394

Kontturi, E., Thüne, P. C., and Niemantsverdriet, J. W. (2003b). Novel method for preparing cellulose model surfaces by spin coating. *Polymer* 44, 3621–3625. doi: 10.1016/S0032-3861(03)00283-0

Kontturi, E., Thüne, P. C., and Niemantsverdriet, J. W. (2005b). Trimethylsilylcellulose/polystyrene blends as a means to construct cellulose domains on cellulose. *Macromolecules* 38, 10712–10720. doi: 10.1021/ma0504419

Kontturi, E., and Vuorinen, T. (2009). Indirect evidence of supramolecular changes within cellulose microfibrils of chemical pulp fibers upon drying. *Cellulose* 16, 65–74. doi: 10.1007/s10570-008-9235-3

Kontturi, K. S., Kontturi, E., and Laine, J. (2013). Specific water uptake of thin films from nanofibrillar cellulose. *J. Mater. Chem. A* 1, 13655–13663. doi: 10.1039/c3ta12998e

Kontturi, K. S., Tammelin, T., Johansson, L.-S., and Stenius, P. (2008). Adsorption of cationic starch on cellulose studied by QCM-D. *Langmuir* 24, 4743–4749. doi: 10.1021/la703604j

Lagerwall, J. P. F., Schütz, C., Salajkova, M., Noh, J., Hyun Park, J., Scalia, G., et al. (2014). Cellulose nanocrystal-based materials: from liquid crystal self-assembly and glass formation to multifunctional thin films. *Npg Asia Mater.* 6:e80. doi: 10.1038/am.2013.69

Langan, P., Nishiyama, Y., and Chanzy, H. (2001). X-ray structure of mercerized cellulose II at 1 Å resolution. *Biomacromolecules* 2, 410–416. doi: 10.1021/bm005612q

Manfredi, G., Mayrhofer, C., Kothleitner, G., Schennach, R., and Comoretto, D. (2016). Cellulose ternary photonic crystal created by solution processing. *Cellulose* 23, 2853–2862. doi: 10.1007/s10570-016-1031-x

Martin, C., Barker, R., Watkins, E. B., Dubreuil, F., Cranston, E. D., Heux, L., et al. (2017). Structural variations in hybrid all-nanoparticle gibbsite nanoplatelet/cellulose nanocrystal multilayered films. *Langmuir* 33, 7896–7907. doi: 10.1021/acs.langmuir.7b02352

Mauroy, C., Levard, C., Moreau, C., Vidal, V., Rose, J., and Cathala, B. (2018). Elaboration of cellulose nanocrystal/ge-imogolite nanotube multilayered thin films. *Langmuir* 34, 3386–3394. doi: 10.1021/acs.langmuir.8b00091

Maver, T., Maver, U., Mostegel, F., Griesser, T., Spirk, S., Smrke, D. M., et al. (2015). Cellulose based thin films as a platform for drug release studies to mimick wound dressing materials. *Cellulose* 22, 749–761. doi: 10.1007/s10570-014-0515-9

Medronho, B., Romano, A., Miguel, M. G., Stigsson, L., and Lindman, B. (2012). Rationalizing cellulose (in)solubility: reviewing basic physicochemical aspects and role of hydrophobic interactions. *Cellulose* 19, 581–587. doi: 10.1007/s10570-011-9644-6

Mohan, T., Kargl, R., Kostler, S., Doliska, A., Findenig, G., Ribitsch, V., et al. (2012a). Functional polysaccharide conjugates for the preparation of microarrays. *ACS Appl. Mater. Interfaces* 4, 2743–2751. doi: 10.1021/am300375m

Mohan, T., Niegelhell, K., Zarth, C. S. P., Kargl, R., Köstler, S., Ribitsch, V., et al. (2014). Triggering protein adsorption on tailored cationic cellulose surfaces. *Biomacromolecules* 15, 3931–3941. doi: 10.1021/bm500997s

Mohan, T., Ristic, T., Kargl, R., Doliska, A., Köstler, S., Ribitsch, V., et al. (2013a). Cationically rendered biopolymer surfaces for high protein affinity support matrices. *Chem. Comm.* 49, 11530–11532. doi: 10.1039/c3cc46414h

Mohan, T., Spirk, S., Kargl, R., Doliška, A., Ehmann, H. M. A., Köstler, S., et al. (2012b). Watching cellulose grow – Kinetic investigations on cellulose thin film formation at the gas–solid interface using a quartz crystal microbalance with dissipation (QCM-D). *Colloids Surf. A* 400, 67–72. doi: 10.1016/j.colsurfa.2012.02.053

Mohan, T., Zarth, C., Doliska, A., Kargl, R., Grießer, T., Spirk, S., et al. (2013b). Interactions of a cationic cellulose derivative with an ultrathin cellulose support. *Carbohydr. Polym.* 92, 1046–1053. doi: 10.1016/j.carbpol.2012.10.026

Moreau, C., Beury, N., Delorme, N., and Cathala, B. (2012). Tuning the architecture of cellulose nanocrystal–poly(allylamine hydrochloride) multilayered thin films: influence of dipping parameters. *Langmuir* 28, 10425–10436. doi: 10.1021/la301293r

Nechyporchuk, O., Belgacem, M. N., and Bras, J. (2016). Production of cellulose nanofibrils: a review of recent advances. *Ind. Crops Prod.* 93, 2–25. doi: 10.1016/j.indcrop.2016.02.016

Niegelhell, K., Chemelli, A., Hobisch, J., Griesser, T., Reiter, H., Hirn, U., et al. (2018). Interaction of industrially relevant cationic starches with cellulose. *Carbohydr. Polym.* 179, 290–296. doi: 10.1016/j.carbpol.2017.10.003

Niegelhell, K., Süßenbacher, M., Jammernegg, K., Ganner, T., Schwendenwein, D., Schwab, H., et al. (2016). Enzymes as biodevelopers for nano- and micropatterned bicomponent biopolymer thin films. *Biomacromolecules* 17, 3743–3749. doi: 10.1021/acs.biomac.6b01263

Niegelhell, K., Süßenbacher, M., Sattelkow, J., Plank, H., Wang, Y., Zhang, K., et al. (2017). How bound and free fatty acids in cellulose films impact nonspecific protein adsorption. *Biomacromolecules* 18, 4224–4231. doi: 10.1021/acs.biomac.7b01260

Niinivaara, E., Faustini, M., Tammelin, T., and Kontturi, E. (2015). Water vapor uptake of ultrathin films of biologically derived nanocrystals: quantitative assessment with quartz crystal microbalance and spectroscopic ellipsometry. *Langmuir* 31, 12170–12176. doi: 10.1021/acs.langmuir.5b01763

Niinivaara, E., Faustini, M., Tammelin, T., and Kontturi, E. (2016). Mimicking the humidity response of the plant cell wall by using two-dimensional systems: the critical role of amorphous and crystalline polysaccharides. *Langmuir* 32, 2032–2040. doi: 10.1021/acs.langmuir.5b04264

Niinivaara, E., and Kontturi, E. (2014). 2D dendritic fractal patterns from an amphiphilic polysaccharide. *Soft Matter* 10, 1801–1805. doi: 10.1039/c3sm52946k

Nishiyama, Y. (2009). Structure and properties of the cellulose microfibril. *J. Wood Sci.* 55, 241–249. doi: 10.1007/s10086-009-1029-1

Nissinen, T., Li, M., Brielles, N., and Mann, S. (2013). Calcium sulfate hemihydrate-mediated crystallization of gypsum on Ca^{2+}-activated cellulose thin films. *CrystEngComm* 15, 3793–3798. doi: 10.1039/C2CE26814K

Nissinen, T., Li, M., Davis, S. A., and Mann, S. (2014). *In situ* precipitation of amorphous and crystalline calcium sulphates in cellulose thin films. *CrystEngComm* 16, 3843–3847. doi: 10.1039/C4CE00228H

Norrman, K., Ghanbari-Siahkali, A., and Larsen, N. B. (2005). 6 Studies of spin-coated polymer films. *Ann. Rep. Sect.* 101, 174–201. doi: 10.1039/b408857n

Notley, S. M., Eriksson, M., Wågberg, L., Beck, S., and Gray, D. G. (2006). Surface forces measurements of spin-coated cellulose thin films with different crystallinity. *Langmuir* 22, 3154–3160. doi: 10.1021/la052886w

Nyfors, L., Suchy, M., Laine, J., and Kontturi, E. (2009). Ultrathin cellulose films of tunable nanostructured morphology with a hydrophobic component. *Biomacromolecules* 10, 1276–1281. doi: 10.1021/bm900099e

Olivier, C., Moreau, C., Bertoncini, P., Bizot, H., Chauvet, O., and Cathala, B. (2012). Cellulose nanocrystal-assisted dispersion of luminescent single-walled carbon nanotubes for Layer-by-Layer assembled hybrid thin films. *Langmuir* 28, 12463–12471. doi: 10.1021/la302077a

Olszewska, A. M., Kontturi, E., Laine, J., and Österberg, M. (2013). All-cellulose multilayers: long nanofibrils assembled with short nanocrystals. *Cellulose* 20, 1777–1789. doi: 10.1007/s10570-013-9949-8

Orelma, H., Filpponen, I., Johansson, L.-S., Laine, J., and Rojas, O. J. (2011). Modification of cellulose films by adsorption of cmc and chitosan for controlled attachment of biomolecules. *Biomacromolecules* 12, 4311–4318. doi: 10.1021/bm201236a

Orelma, H., Johansson, L.-S., Filpponen, I., Rojas, O. J., and Laine, J. (2012a). Generic method for attaching biomolecules via avidin-biotin complexes immobilized on films of regenerated and nanofibrillar cellulose. *Biomacromolecules* 13, 2802–2810. doi: 10.1021/bm300781k

Orelma, H., Teerinen, T., Johansson, L.-S., Holappa, S., and Laine, J. (2012b). CMC-modified cellulose biointerface for antibody conjugation. *Biomacromolecules* 13, 1051–1058. doi: 10.1021/bm201771m

Österberg, M., and Valle-Delgado, J. J. (2017). Surface forces in lignocellulosic systems. *Curr. Opin. Colloid Interface Sci.* 27, 33–42. doi: 10.1016/j.cocis.2016.09.005

Pääkkö, M., Ankerfors, M., Kosonen, H., Nykänen, A., Ahola, S., Österberg, M., et al. (2007). Enzymatic hydrolysis combined with mechanical shearing and high-pressure homogenization for nanoscale cellulose fibrils and strong gels. *Biomacromolecules* 8, 1934–1941. doi: 10.1021/bm061215p

Parra, V., Vilar, M. R., Battaglini, N., Ferraria, A. M., Botelho Do Rego, A. M., Boufi, S., et al. (2007). New hybrid films based on cellulose and hydroxygallium

phthalocyanine. Synergetic effects in the structure and properties. *Langmuir* 23, 3712–3722. doi: 10.1021/la063114i

Podsiadlo, P., Sui, L., Elkasabi, Y., Burgardt, P., Lee, J., Miryala, A., et al. (2007). Layer-by-Layer assembled films of cellulose nanowires with antireflective properties. *Langmuir* 23, 7901–7906. doi: 10.1021/la700772a

Pönni, R., Vuorinen, T., and Kontturi, E. (2012). Proposed nano-scale coalescence of cellulose in chemical pulp fibers during technical treatments. *BioResources* 7, 6077–6108. doi: 10.15376/biores.7.4.6077-6108

Puspasari, T., Akhtar, F. H., Ogieglo, W., Alharbi, O., and Peinemann, K.-V. (2018a). High dehumidification performance of amorphous cellulose composite membranes prepared from trimethylsilyl cellulose. *J. Mater. Chem. A* 6, 9271–9279. doi: 10.1039/C8TA00350E

Puspasari, T., Chakrabarty, T., Genduso, G., and Peinemann, K.-V. (2018b). Unique cellulose/polydimethylsiloxane blends as an advanced hybrid material for organic solvent nanofiltration and pervaporation membranes. *J. Mater. Chem. A* 6, 13685–13695. doi: 10.1039/C8TA02697A

Puspasari, T., Huang, T., Sutisna, B., and Peinemann, K.-V. (2018c). Cellulose-polyethyleneimine blend membranes with anomalous nanofiltration performance. *J. Membr. Sci.* 564, 97–105. doi: 10.1016/j.memsci.2018.07.002

Puspasari, T., Yu, H., and Peinemann, K.-V. (2016). Charge- and size-selective molecular separation using ultrathin cellulose membranes. *ChemSusChem* 9, 2908–2911. doi: 10.1002/cssc.201600791

Rånby, B. G. (1951). Fibrous macromolecular systems. Cellulose and muscle. The colloidal properties of cellulose micelles. *Discuss. Faraday Soc.* 11, 158–164. doi: 10.1039/DF9511100158

Raghuwanshi, V. S., Su, J., Garvey, C. J., Holt, S. A., Holden, P. J., Batchelor, W. J., et al. (2017a). Visualization and quantification of IgG antibody adsorbed at the cellulose-liquid interface. *Biomacromolecules* 18, 2439–2445. doi: 10.1021/acs.biomac.7b00593

Raghuwanshi, V. S., Su, J., Garvey, C. J., Holt, S. A., Raverty, W., Tabor, R. F., et al. (2017b). Bio-deuterated cellulose thin films for enhanced contrast in neutron reflectometry. *Cellulose* 24, 11–20. doi: 10.1007/s10570-016-1108-6

Reid, M. S., Villalobos, M., and Cranston, E. D. (2016). Cellulose nanocrystal interactions probed by thin film swelling to predict dispersibility. *Nanoscale* 8, 12247–12257. doi: 10.1039/C6NR01737A

Reishofer, D., Ehmann, H. M., Amenitsch, H., Gspan, C., Fischer, R., Plank, H., et al. (2017a). On the formation of Bi2S3-cellulose nanocomposite films from bismuth xanthates and trimethylsilyl-cellulose. *Carbohydr. Polym.* 164, 294–300. doi: 10.1016/j.carbpol.2017.02.008

Reishofer, D., Rath, T., Ehmann, H. M., Gspan, C., Dunst, S., Amenitsch, H., et al. (2017b). Biobased Cellulosic–CuInS2 nanocomposites for optoelectronic applications. *ACS Sust. Chem. Eng.* 5, 3115–3122. doi: 10.1021/acssuschemeng.6b02871

Rosenau, T., Potthast, A., and Hell, J. (2018). *Cellulose science and Technology Chemistry, Analysis, and Applications.* Hoboken, NJ: Wiley. doi: 10.1002/9781119217619

Rosenau, T., Potthast, A., Sixta, H., and Kosma, P. (2001). The chemistry of side reactions and byproduct formation in the system NMMO/cellulose (Lyocell process). *Prog. Polym. Sci.* 26, 1763–1837. doi: 10.1016/S0079-6700(01)00023-5

Saito, T., Kimura, S., Nishiyama, Y., and Isogai, A. (2007). Cellulose nanofibers prepared by TEMPO-mediated oxidation of native cellulose. *Biomacromolecules* 8, 2485–2491. doi: 10.1021/bm0703970

Saito, T., Kuramae, R., Wohlert, J., Berglund, L. A., and Isogai, A. (2013). An ultrastrong nanofibrillar biomaterial: the strength of single cellulose nanofibrils revealed via sonication-induced fragmentation. *Biomacromolecules* 14, 248–253. doi: 10.1021/bm301674e

Saito, T., Nishiyama, Y., Putaux, J.-L., Vignon, M., and Isogai, A. (2006). Homogeneous suspensions of individualized microfibrils from TEMPO-catalyzed oxidation of native cellulose. *Biomacromolecules* 7, 1687–1691. doi: 10.1021/bm060154s

Schaub, M., Wenz, G., Wegner, G., Stein, A., and Klemm, D. (1993). Ultrathin films of cellulose on silicon wafers. *Adv. Mat.* 5, 919–922. doi: 10.1002/adma.19930051209

Sczech, R., and Riegler, H. (2006). Molecularly smooth cellulose surfaces for adhesion studies. *J. Colloid Interface Sci.* 301, 376–385. doi: 10.1016/j.jcis.2006.05.021

Sheiko, S. S., and Möller, M. (2001). Visualization of macromolecules a first step to manipulation and controlled response. *Chem. Rev.* 101, 4099–4124. doi: 10.1021/cr990129v

Spirk, S., Ehmann, H. M., Kargl, R., Hurkes, N., Reischl, M., Novak, J., et al. (2010). Surface modifications using a water-stable silanetriol in neutral aqueous media. *ACS Appl. Mater. Interfaces.* 2, 2956–2962. doi: 10.1021/am100644r

Strasser, S., Niegelhell, K., Kaschowitz, M., Markus, S., Kargl, R., Stana-Kleinschek, K., et al. (2016). Exploring nonspecific protein adsorption on lignocellulosic amphiphilic bicomponent films. *Biomacromolecules* 17, 1083–1092. doi: 10.1021/acs.biomac.5b01700

Su, J., Raghuwanshi, V. S., Raverty, W., Garvey, C. J., Holden, P. J., Gillon, M., et al. (2016). Smooth deuterated cellulose films for the visualisation of adsorbed bio-macromolecules. *Sci. Rep.* 6:36119. doi: 10.1038/srep36119

Taajamaa, L., Kontturi, E., Laine, J., and Rojas, O. J. (2012). Bicomponent fibre mats with adhesive ultra-hydrophobicity tailored with cellulose derivatives. *J. Mater. Chem.* 22, 12072–12082. doi: 10.1039/c2jm30572k

Taajamaa, L., Rojas, O. J., Laine, J., and Kontturi, E. (2011). Phase-specific pore growth in ultrathin bicomponent films from cellulose-based polysaccharides. *Soft Matter* 7, 10386–10394. doi: 10.1039/c1sm06020a

Taajamaa, L., Rojas, O. J., Laine, J., Yliniemi, K., and Kontturi, E. (2013). Protein-assisted 2D assembly of gold nanoparticles on a polysaccharide surface. *Chem. Commun.* 49, 1318–1320. doi: 10.1039/c2cc37288f

Tammelin, T., Abburi, R., Gestranius, M., Laine, C., Setälä, H., and Österberg, M. (2015). Correlation between cellulose thin film supramolecular structures and interactions with water. *Soft Matter* 11, 4273–4282. doi: 10.1039/C5SM00374A

Tanaka, M., Kaufmann, S., Nissen, J., and Hochrein, M. (2001). Orientation selective immobilization of human erythrocyte membranes on ultrathin cellulose films. *Phys. Chem. Chem. Phys.* 3, 4091–4095. doi: 10.1039/b105007a

Tanaka, M., and Sackmann, E. (2005). Polymer-supported membranes as models of the cell surface. *Nature* 437, 656–663. doi: 10.1038/nature04164

Tanaka, M., Wong, A. P., Rehfeldt, F., Tutus, M., and Kaufmann, S. (2004). Selective deposition of native cell membranes on biocompatible micropatterns. *J. Am. Chem. Soc.* 126, 3257–3260. doi: 10.1021/ja038981d

Tanaka, R., Saito, T., Hänninen, T., Ono, Y., Hakalahti, M., Tammelin, T., et al. (2016). Viscoelastic Properties of Core–Shell-Structured, Hemicellulose-Rich Nanofibrillated cellulose in dispersion and wet-film states. *Biomacromolecules* 17, 2104–2111. doi: 10.1021/acs.biomac.6b00316

Tenhunen, T.-M., Peresin, M. S., Penttilä, P. A., Pere, J., Serimaa, R., and Tammelin, T. (2014). Significance of xylan on the stability and water interactions of cellulosic nanofibrils. *React. Funct. Polym.* 85, 157–166. doi: 10.1016/j.reactfunctpolym.2014.08.011

Trache, D., Hussin, M. H., Haafiz, M. K. M., and Thakur, V. K. (2017). Recent progress in cellulose nanocrystals: sources and production. *Nanoscale* 9, 1763–1786. doi: 10.1039/C6NR09494E

Turbak, A. F. S., Snyder, F. W., Sandberg, K. R. (1983). Microfibrillated cellulose, a new cellulose product: properties, uses, and commercial potential. *J. Appl. Polym. Sci. Appl. Polym. Sympos.* 37, 815–827.

Utsel, S., Malmström, E. E., Carlmark, A., and Wågberg, L. (2010). Thermoresponsive nanocomposites from multilayers of nanofibrillated cellulose and specially designed N-isopropylacrylamide based polymers. *Soft Matter* 6, 342–352. doi: 10.1039/B910481J

Wågberg, L., Decher, G., Norgren, M., Lindström, T., Ankerfors, M., and Axnäs, K. (2008). The build-up of polyelectrolyte multilayers of microfibrillated cellulose and cationic polyelectrolytes. *Langmuir* 24, 784–795. doi: 10.1021/la702481v

Walheim, S., Böltau, M., Mlynek, J., Krausch, G., and Steiner, U. (1997). Structure formation via polymer demixing in spin-cast films. *Macromolecules* 30, 4995–5003. doi: 10.1021/ma9619288

Walheim, S., Schäffer, E., Mlynek, J., and Steiner, U. (1999). Nanophase-separated polymer films as high-performance antireflection coatings. *Science* 283, 520. doi: 10.1126/science.283.5401.520

Wan, Y., An, F., Zhou, P., Li, Y., Liu, Y., Lu, C., et al. (2017). Regenerated cellulose I from LiCl·DMAc solution. *Chem. Commun.* 53, 3595–3597. doi: 10.1039/C7CC00450H

Weißl, M., Niegelhell, K., Reishofer, D., Zankel, A., Innerlohinger, J., and Spirk, S. (2018). Homogeneous cellulose thin films by regeneration of cellulose xanthate: properties and characterization. *Cellulose* 25, 711–721. doi: 10.1007/s10570-017-1576-3

Weißl, M., Rath, T., Sattelkow, J., Plank, H., Eyley, S., Thielemans, W., et al. (2019). Multi-layered nanoscale cellulose/CuInS2 sandwich type thin films. *Carbohydr. Polym.* 203, 219–227. doi: 10.1016/j.carbpol.2018.09.063

Werner, O., Persson, L., Nolte, M., Fery, A., and Wågberg, L. (2008). Patterning of surfaces with nanosized cellulosic fibrils using microcontact printing and a lift-off technique. *Soft Matter* 4, 1158–1160. doi: 10.1039/b715914e

Wilson, B. P., Yliniemi, K., Gestranius, M., Hakalahti, M., Putkonen, M., Lundström, M., et al. (2018). Structural distinction due to deposition method in ultrathin films of cellulose nanofibres. *Cellulose* 25, 1715–1724. doi: 10.1007/s10570-018-1665-y

Wolfberger, A., Kargl, R., Griesser, T., and Spirk, S. (2014). Photoregeneration of trimethylsilyl cellulose as a tool for microstructuring ultrathin cellulose supports. *Molecules* 19, 16266–16273. doi: 10.3390/molecules191016266

Wolfberger, A., Petritz, A., Fian, A., Herka, J., Schmidt, V., Stadlober, B., et al. (2015). Photolithographic patterning of cellulose: a versatile dual-tone photoresist for advanced applications. *Cellulose* 22, 717–727. doi: 10.1007/s10570-014-0471-4

Woods, D. A., Petkov, J., and Bain, C. D. (2011). Surfactant adsorption by total internal reflection Raman spectroscopy. Part III: adsorption onto cellulose. *Colloids Surf. A* 391, 10–18. doi: 10.1016/j.colsurfa.2011.07.027

Xue, L., Zhang, J., and Han, Y. (2012). Phase separation induced ordered patterns in thin polymer blend films. *Prog. Polym. Sci.* 37, 564–594. doi: 10.1016/j.progpolymsci.2011.09.001

Yan, L., Wang, Y., and Chen, J. (2008). Fabrication of a model cellulose surface from straw with an aqueous sodium hydroxide/thiourea solution. *J. Appl. Polym. Sci.* 110, 1330–1335. doi: 10.1002/app.28562

Yokota, S., Kitaoka, T., Sugiyama, J., and Wariishi, H. (2007a). Cellulose I nanolayers designed by self-assembly of its thiosemicarbazone on a gold substrate. *Adv. Mat.* 19, 3368–3370. doi: 10.1002/adma.200602761

Yokota, S., Ueno, T., Kitaoka, T., and Wariishi, H. (2007b). Molecular imaging of single cellulose chains aligned on a highly oriented pyrolytic graphite surface. *Carbohydr. Res.* 342, 2593–2598. doi: 10.1016/j.carres.2007.08.018

Conflict of Interest Statement: The authors declare that the research was conducted in the absence of any commercial or financial relationships that could be construed as a potential conflict of interest.

frontiers in Chemistry

ORIGINAL RESEARCH
published: 18 July 2019
doi: 10.3389/fchem.2019.00515

Aqueous Dispersions of Esterified Lignin Particles for Hydrophobic Coatings

*Qi Hua, Li-Yang Liu, Muzaffer A Karaaslan and Scott Renneckar**

Department of Wood Science, The University of British Columbia, Vancouver, BC, Canada

An aqueous biopolymer dispersion coating system was synthesized utilizing softwood kraft lignin and a long chain organic acid. The chemical treatment of lignin was a two-step procedure, which first consisted of hydroxyethylation of the phenolic groups on lignin utilizing ethylene carbonate and an alkaline catalyst. This first step resulted in the lignin containing more than 80% aliphatic hydroxyl functionality (^{1}H NMR). Following this step, oleic acid was reacted with hydoxyethyl lignin in order to form ester derivatives. With nearly a total reduction in absorbance in the hydroxyl stretching region, FT-IR analysis showed the majority of the hydroxyl groups was esterified forming an ethyl oleate derivative. Semi-quantitative ^{13}C NMR analysis of the lignin revealed 88% substitution of the lignin hydroxyl groups. This derivative was soluble in organic solvent such as toluene and tetrahydrofuran. Solutions of lignin derivatives were slowly precipitated through dialysis, resulting in a stable dispersion of lignin microparticles in distilled water. The 1–2 μm average diameter size of the precipitated particles was found with dynamic light scattering of the suspensions. Spray and spin coating were used to apply the lignin derivative dispersion to different surfaces. For both coating methods, the lignin-based particles enhanced the hydrophobicity of all the substrates tested, resulting in increased water contact angles for glass, kraft pulp sheets and solid wood. Benign reagents involved in the coating synthesis utilized natural compounds that are known to repel water in nature. Combined with the avoidance of volatile organic solvents during application, this process provided a low environmental footprint solution for synthesis of hydrophobic coatings.

Keywords: hydrophobic materials, lignin, coating, organic acid, sustainable, microparticles, wax, nature-inspired

OPEN ACCESS

Edited by:
Eero Kontturi,
Aalto University, Finland

Reviewed by:
Gloria Huerta-Angeles,
Contipro Inc., Czechia
Jian Yu,
Institute of Chemistry (CAS), China

****Correspondence:***
Scott Renneckar
scott.renneckar@ubc.ca

Specialty section:
This article was submitted to Polymer Chemistry, a section of the journal Frontiers in Chemistry

Received: *20 April 2019*
Accepted: *04 July 2019*
Published: *18 July 2019*

Citation:
Hua Q, Liu L-Y, Karaaslan MA and Renneckar S (2019) Aqueous Dispersions of Esterified Lignin Particles for Hydrophobic Coatings. Front. Chem. 7:515. doi: 10.3389/fchem.2019.00515

INTRODUCTION

Wood-based products are an important class of materials in modern society with the ability to contribute to a more sustainable world (Mohanty et al., 2002). Wood based renewable materials can span from the nanoscale (Jiang and Hsieh, 2014; Foster et al., 2018; Jiang et al., 2018), to modify properties, to macroscale structures that perform even better than many metal alloys. Further, new building codes provide greater opportunities for wood-based materials in tall wooden structures with designs toward wooden skyscrapers (Mohammad et al., 2018). While wood structures provide more design opportunities, perceptions that surround longevity of wooden structures, such as fire, pests, and decay, limit further consideration of wood in many applications (Marney and Russell, 2007).

Timbers can biodegrade in high-moisture environments, under ambient conditions if the cell wall is saturated with water; moisture above this fiber saturation point of the cell wall enables mold and decay fungi to attack the structure of the cell wall, depolymerizing the polysaccharides into simple sugars (Eriksson et al., 2012). For wood materials, loss of mass by just a few percent caused by decay fungi, significantly impacts the toughness of wood (Gordobil et al., 2017; Mohanty et al., 2018). Hence, durability impacts the overall performance and moisture exposure can occur in service or during handling and storage at the construction site.

In nature, trees with protection from external factors can survive hundreds of years. In trees, phloem tissue serves as protection from fungi spores and bacteria; a significant fraction of this phloem composition is suberin, a polymeric compound that is a combination of aromatic and aliphatic structure (Franke and Schreiber, 2007). On external surfaces such as leaves, a variety of long chain aliphatic organic compounds in epicuticular waxes imparts hydrophobicity to its surfaces. Highly structured waxes with microscale structures and nanoscale textures can create superhydrophobicity on the leaves of plants (Hu and Deng, 2010). Hence, the use of aliphatic carbon chains is a simple approach to make highly hydrophobic materials. Recently, this method was recreated utilizing cellulose derivatives to produce hydrophobic coating materials (Geissler et al., 2013). Geissler and co-workers developed superhydrophobic coating materials from stearic esterified micro-cellulose particles. Results showed that the micro-/nano scale particle geometries could significantly improve the hydrophobicity of the surface and develop self-cleaning properties, mimicking the lotus leaf.

In addition to nature inspired approaches to limit water absorption and improve water resistance of wood-based materials, chemical methods can directly block hydroxyl groups within the cell wall. Chemical treatment by acetylation or other hydrophobizing agents improves the water resistance of wood materials, but a large amount of reagents is necessary during this process (Lv et al., 2018), and the samples typically require some type of pressurized reactor. These treatments are appropriate for wood-based materials in direct exterior exposure. However, in most cases, a short-term storage needs or temporary protection during construction requires a low-cost treatment solution for lumber or composite panels.

For coatings, renewable materials utilizing biopolymers, such as lignin, were previously explored. Hult et al. determined that esterified lignin showed improved water-proofing for paper board (Hult et al., 2013). Lignin derivatives have also been used to coat wood surfaces to improve hydrophobicity as exhibited with reduced wettability measurements (Gordobil et al., 2017). For these samples, the esterification process was shown to increase the hydrophobic nature of lignin. Halogenated or anhydride compounds were adopted in this process with either partial and full conversion of lignin into its esterified form (Salanti et al., 2016). These methods were performed under standardized conditions requiring solvent, which increases the environmental factor or "E-factor"; the E-factor is a metric that quantifies the amount of product to the amount of waste generated (Sheldon, 2007). The methods of lignin esterification leading to hydrophobization, typically reported in the literature utilized halogenated or anhydride compounds that potentially cause negative environmental issues. For these cases, the green chemistry principle of the use of renewable feedstocks may be offset by creation of waste and toxic byproducts (Gillet et al., 2017). Further, hydrophobic coating applications usually require toxic or highly volatile solvents such as chloroform or acetone for the application of these hydrophobized bio-based coatings (Urushihara and Nishino, 2005). These coatings release volatile organic compounds from the solvent during application, which potentially will cause health hazards with repeated exposure (Clark et al., 2015). In order to avoid these problems, direct esterification was developed by Liu et al using benign and low-cost organic acid as solvent and reagent to efficiently modify the aliphatic OH groups in lignin with carbon length 3∼18 (Liu et al., 2019).

Working from this approach, softwood kraft lignin (extracted from LignoForce system) (Kouisni et al., 2012) was modified utilizing a two-step direct esterification to obtain an ethyl oleate lignin. Specifically, the lignin was modified by ethylene carbonate to obtain lignin only containing aliphatic hydroxyl groups (Liu et al., 2018). Then oleic acid was utilized as both solvent and reagent to realize the direct esterification of hydroxyethyl lignin derivative. This technique created both an aromatic and aliphatic carbon component that is a simplified model of suberin material, found in bark, for the protection of wood. The obtained esterified lignin was then prepared as aqueous micro-lignin particles via dialysis to use as a hydrophobic thin coating for wood-based materials.

MATERIALS AND METHODS

Material and Chemical Reagents

Softwood kraft lignin (SKL)AQQ7 Amallin A^{TM} was donated by West Fraser Corp. (Hinton, Canada). The original SKL had 40% moisture content and was slightly acidic (pH = 2, 15% solid lignin in water). These lignins were then thoroughly washed with distilled water until to a neutral pH was attained and dried by lyophilization before the modification and characterization.

Ethylene carbonate (EC, Alfar Aser), sulfuric acid (Thermal Fischer), oleic acid (Sigma Aldrich), tetrahydrofuran (HPLC grade, Sigma Aldrich) were used, as received. Deuterium reagents including chloroform-D were purchased from Cambridge Isotope Laboratories, Int. Dimethyl sulfoxide-d_6 and toluene -d_8 were obtained from Sigma Aldrich. Anhydrous pyridine was prepared by adding molecular sieves in the Pyridine (Sigma Aldrich, 99.8%).

Preparation of Hydroxyethyl Lignin (HELignin)

Twenty grams of dried lignin powder was load into a 500 ml round bottom flask. Based on a molar ratio to the aromatic hydroxyl group (ArOH, 3.6 mmol/g) in lignin, 64 g ethylene carbonate (10 ArOH) and 2.4 g Na_2CO_3 (0.1 ArOH) were added. The flask was covered with a rubber septum held in place by wire. After purging nitrogen gas to remove air, the reaction proceeded in an oil bath under 120°C for 2.5 h. At the end of

the reaction, the solution was poured slowly into 400 ml pH=2 aqueous sulfuric acid with continuous stirring to precipitate modified lignin. The mixture was then filtered by 0.45 μm PVTF membrane, followed by washing with another 400 ml distilled water until neutral pH and dried by freeze dryer (Liu et al., 2018).

Esterification of HELignin

The direct esterification (catalyst-free esterification) was adopted to obtain esterified lignin following our previous procedure (Liu et al., 2018, 2019). Specifically, 3 g hydroxyethyl lignin was mixed with 30 ml oleic acid in a round bottom flask, which was heated under 180°C (oil bath) for 24 h. After cooling down, the samples were mixed with filter aids (Celite 545, Sigma Aldrich) and washed by 300 ml aqueous ethanol (75% v/v). The mixture was then filtered by 0.20 μm PVTF filter membranes. The lignin-based ester was then washed with 75% aqueous ethanol twice and distilled water twice. THF was used to dissolve the ester product, separating it from solid filter agent by filtration across Whatman No.1 filter paper. THF was added to the remaining solid part and filtered. This step was repeated until the solid filter aid became white, to ensure all the ester product was dissolved by THF. Air dried lignin derivatives from THF were washed with ethanol and distilled water sequentially. The remaining esterified sample was freeze dried (Liu et al., 2019). The above esterification procedures were repeated with acid catalyzed reaction with 1% sulfuric acid (wt) included during the reaction. All reaction conditions and isolation procedures remained the same.

Characterization of Lignin

Nuclear Magnetic Resonance Analysis

^{31}P NMR analysis was used for the characterization of hydroxyl groups in lignin. Specifically, the solvent used to dissolve lignin samples was prepared prior, by mixing chloroform-D and pyridine in a ratio of 1: 1.6. Twenty milligram lignin samples were added into 400 μL of above solvent and then vortexed thoroughly until all solids were fully dissolved. Then the other compounds were added including 100 μL of internal standard (9.6 mg N-hydroxy-5-norbornene-2,3-dicarboximide in 1 ml above solvent), 40 μL of relaxation reagent (5.6 mg chromium (III) acetylacetonate in 1 ml above solvent), and 50 μL phosphorous reagents (2-chloro-4,4,5,5-tetramethyl-1,3,2-dioxaphospholane) (Argyropoulos, 1995; Pu et al., 2011).

^{13}C NMR semi-quantitively analyzed the major aromatic groups, functional groups, and chemical linkages in lignin. Due to the different solubility of resulting lignin, deuterium dimethyl sulfoxide (DMSO-d6) was used to dissolve lignin and HELignin, and toluene-d8 was used for oleate HELignin. Specifically, 150–160 mg lignin samples were dissolved into 450 μL corresponding solvent, following with the addition of 60 μL relaxation reagent (50 mg/ml chromium (III) acetylacetonate in DMSO-d_6 or toluene-d_8) and 15 mg internal standard (1,3,5 trioxane) were added (Balakshin et al., 2016).

All above lignin solutions were transferred into 5 mm NMR tubes and tested by Bruker Avance 300 MHz equipped with a BBO probe at 25°C. Applied parameters for ^{13}C NMR: scan number 20 000, relaxation delay 2 s, acquisition time 1.4 s, and pulse length 8.5 μs; ^{31}P NMR: scan number 800, relaxation delay 5 s, pulse length 6 μs, and acquisition time 1.4 s.

FT-IR Analysis

Sample pellets for transmission FTIR were prepared by mixing 2–3 mg lignin with 200 mg of dried potassium bromide. After thoroughly mixing and compression, the lignin pellets were analyzed using the Perkin Elmer Infrared Spectroscopy (MA, United States). Spectra were collected with a resolution of 4 cm^{-1} and averaged over 32 scans.

Gel Permission Chromatography (GPC)

Five milligram acetylated lignin, acetylated HELignin, or oleate HELignin were dissolved into 1 ml tetrahydrofuran (THF), respectively. The acetylation procedure followed our previous study (Liu et al., 2018). The lignin solutions were stabilized for 48 h before the analysis. Lignin solution was analyzed utilizing Agilent 1100 GPC equipped with three columns including Styragel HR1, HR3, HR4 (Waters Corp.) and analyzed by differential refractive index detector (dRI, Wyatt Corp.) at temperature 35°C. THF was used as eluent at a flow rate 0.7 ml/min. The data was collected utilizing Astra 6.0 and analyzed by conventional calibration methods. The standard polystyrene with different molecular weight was used as standard curve (Lange et al., 2016).

Differential Scanning Calorimetry (DSC)

Seven milligrams of lignin was accurately weighed and sealed in aluminum pans. TA Q1000 (Thermal Analysis Corp.) machine was adopted to analyze the sample under nitrogen gas environment. An annealing procedure was run in advance: room temperature to 105°C with rate of 10°C/min. Samples then were cooled down to −50°C with rate of −5°C/min and then heated to 150°C with rate of 10°C/min, again. The glass transition temperature was analyzed based on the third cycle (Cui et al., 2013).

The Preparation of Lignin Micro-/Nano-Particle Solution

Four hundred milligram lignin and oleate HElignin were dissolved in 20 ml THF, respectively. The solutions were then transferred into dialysis tubing (cellulose membrane, Sigma-Aldrich) and placed into 1,500 ml distilled water for 7 days under slow stirring (**Figure S1**); the distilled water was changed every 24 h. The final concentration for the coating solution was 20 mg/ml (Zhao et al., 2016).

Dynamic Light Scattering (DLS)

After analyzing the distilled water as background, 1.5 ml aqueous lignin-particle solution was diluted by 600 ml of distilled water and stirred at 1,500 rpm for dynamic light scattering analysis. The data was collected and analyzed by Mastersizer 2000. Each sample was run in duplicate.

Spray and Spin Coating

Three types of surfaces were selected for coating analysis: glass, kraft pulp sheets, and wood (yellow poplar). The glass slides were

cleaned by sonication for 30 min to remove all contamination and the surfaces were dried with nitrogen gas. Lignin particle solution was added into an air brush reservoir for spray coating at a distance 25 cm. The Laurell WS 650 Spin Coater was used for spin coating at room temperature. The coated materials were dried under ambient condition in fume hood overnight. To build the coating, this process was repeated 10 times for both spin coating and spray coating.

Contact Angle Analysis

Five microliter distilled water droplets were dispensed on different types of treated surfaces from a height of 2 mm. The contact angle was recorded using a highspeed camera. The initial contact angle was measured and analyzed by Drop Shape Analyzer (DSA) 1.9 software.

Micromorphology Analysis

Scanning electron microscopy (SEM) images were obtained using Hitachi S-2600 Variable Pressure SEM (Tokyo, Japan) at10 kV. A drop of aqueous lignin particle solution was applied to the surface of aluminum film and dried in the fume hood overnight. Untreated and spin coated paper board were also prepared. Before the measurement, a layer from palatium/gold of 10 nm was coated on the surfaces of the samples.

Atom force microscopy images were taken with the Multimode AFM Nanoscope-III (Veeco Instruments, Santa Barbara, USA) using the ScanAsyst TM tapping mode. Four hundred microliter lignin micro particle solution was dropped on freshly cleaved mica, spin coated, and left in a fume hood overnight. AFM images were captured using RTESPA, Veeco Inst. With a silicon cantilever, scan rate of 0.383 Hz and a scan size of 20 × 20 μm (Cho et al., 2017).

RESULTS AND DISCUSSION

A Two-Step Route Toward Esterified Lignin

Softwood kraft lignin (SKL) contains different types of hydroxyl groups, which were reported to have different reactivity for esterification (Thielemans and Wool, 2005). Our previous research showed that the direct esterification, using organic acids as solvent and reagent, could successfully modify the aliphatic OH groups (Liu et al., 2019). Therefore, the hydroxyethylation with ethylene carbonate as both solvent and reagent was used to convert the aromatic OH groups into aliphatic OH groups (**Scheme 1**), to improve the relative reactivity of lignin toward organic acids (Liu et al., 2018). **Figure S2** showed that the starting SKL has aliphatic OH (AlOH, peak 2, 150–145 ppm), aromatic OH (ArOH, peak 3, 144–136 ppm), and carboxylic acid groups (COOH, peak 4, 136–133 ppm) prior to the modification. After the hydroxyethylation, the ArOH and COOH groups were reduced from the spectrum, which signified that these compounds were modified. The exact values of each type of OH groups before and after the hydroxyethylation were reported in **Table 1**. For the hydroxyethylated lignin, the amount of AlOH increased from 2.07 mmol/g to 4.27 mmol/g, while the amount of total OH group decreased from 6.45 mmol/g to 5.03 mmol/g. The significant reduction of the ArOH (0.69 mmol/g) indicated that HELignin had a more uniform chemical structure with more than 80% of the ArOH converted into AlOH groups.

To achieve a lignin sample with hydrophobic characteristics, oleic acid was used to modify the aliphatic OH groups in lignin. Oleic acid was reported as a major component in plant oils potentially serving as abundant resource for making renewable materials (Zuo et al., 2011; Zhang et al., 2017). In order to obtain esterified lignin, high temperature reactions were required to promote the esterification process and providing enough hydrogen ions. To make a comparison, the Fischer esterification process which used 1% H_2SO_4 (98% conc.) as catalysts was also performed at the same temperature and reaction time. Based on ^{13}C NMR spectrum, the degree of substitute (DS) for these two types of esterification routes was calculated based on the change of AlOH groups (*peak cluster 1*: 61.5–58 ppm, **Scheme 1**, **Figures 1A,B**), which was formed during the hydroxyethylation (Balakshin et al., 2016). After the esterification, the *peak cluster 1* disappeared, and the shielding of additional ester group formed a new peak region (*peak cluster 2*: 65–61.5 ppm, **scheme 1**). The degree of substitution (DS) for the esterification reaction was analyzed utilizing these peak structures: DS = peak 2/(peak 1+peak 2). The DS for the esterification with and without 1% H_2SO_4 were 89 and 88%, respectively (**Table 2**). Noteworthy, the peak 2 in **Figure 1D** (with H_2SO_4) had different peak shapes with *peak cluster 1* in **Figure 1B** and *peak cluster 2* in **Figure 1C**. This indicated that the addition of H_2SO_4 may have caused side reactions including the degradation of linkages or further condensation of lignin.

After the hydroxyethyl reaction, FT-IR spectrum showed that modified lignin had slight changes on Aryl-Alkyl ether bond and carbonyl groups (C = O, 1,800–1,600 cm^{-1}) (**Figure 2**). Overall, there were few changes on the HELignin, as the hydroxyethyl reaction only selectively modified the aromatic OH groups without causing obvious side reactions. Confirming this change,

TABLE 1 | Characterization of original lignin and hydroxyethyl lignin (HELignin); For ^{13}C NMR, the aromatic carbon region (160–100 ppm) was set as 100 Ar.

	AlOH (mmol/g)	ArOH (mmol/g)	COOH (mmol/g)	Total OH (mmol/g)	G /100Ar	MeO /100Ar	DC /100Ar	M_w kDa	M_n kDa	PDI	T_g (°C)
Lignin	2.07	3.87	0.56	6.49	80	83	50	6.184	1.366	4.53	165.1
HELignin	4.27	0.69	0.07	5.03	78	78	61	8.468	1.258	6.73	120.1

** aliphatic OH groups (AlOH), aromatic OH groups (ArOH), carboxylic acid groups (COOH), guaiacyl units (G), methoxy content (MeO), degree of condensation (DC), degree of substitution (DS), average molecular weight (M_w), Mn number average molecular weight (M_n), polydispersity index (PDI), glass transition temperature (T_g).*

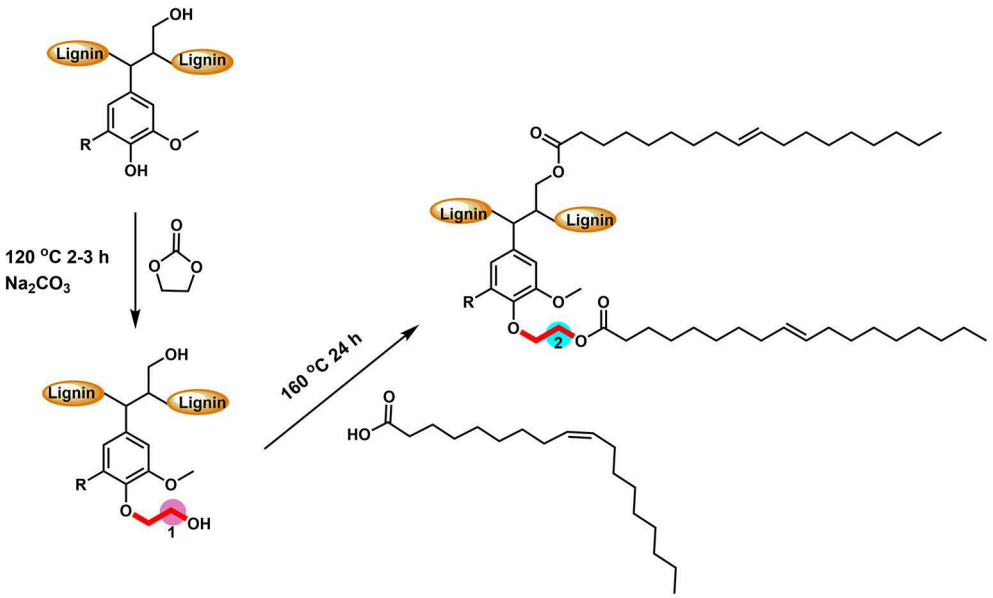

SCHEME 1 | The reactive scheme of two-step esterification for the preparation of oleate hydroxyethyl lignin.

^{1}H NMR spectrum showed the formation of hydroxyethyl group (3.8–4.5 ppm, **Figure S4**) in resulting HELignin

FT-IR analysis is a powerful method in revealing a change in hydroxyl stretching associated with these hydrophilic functional groups. In the spectrum there was evidence of the efficiency of our direct esterification (catalyst-free esterification) toward the hydroxyl groups in HELignin, as illustrated by a clear reduction of hydroxyl group (O-H stretching, 3,650–3,200 cm^{-1}) absorbance. Further, there was evidence of the alkyl chains (C-H, 3,200–2,800 cm^{-1}) and carbonyl linkages (COOR, 1,800–1,700 cm^{-1}) (**Figure 2**). Proton NMR was also used to confirm modification. The attached alkyl chains in HELignin could be found in the upfield (1–2 ppm) of ^{1}H NMR spectrum of oleate HELignin (**Figure S4c**). Overall, the hydrophilic hydroxyl groups in lignin were converted to hydrophobic alkyl chains. The obtained lignin-based ester derivative after the two step process, had a waxy chemical structure, which was used as a precursor for hydrophobic coating materials.

Molecular Weight Analysis of Esterified HELignin

The molecular weight was analyzed with gel permission chromatography (GPC) as shown in **Figure 3**. In agreement with our previous research on other lignin sourced materials, the HELignin had a slightly larger molecule weight (M_w) and wider polydispersity index (PDI) (**Figure 3**). In addition to the hydroxyethyl groups on lignin, an increase in the degree of condensation was found arising from heating lignin in an alkaline environment. Based on the ^{13}C NMR analysis, the degree of condensation increased from 50 (per 100 Ar) to 61 (per 100 Ar) during the hydroxyethyl reaction (**Table 1**). The degree of condensation was calculated based on the equation DC=200+G-ArH (**Figure S3**) (Balakshin et al., 2016).

TABLE 2 | Degree of substitution (DS), molecular weight, and glass transition temperature (T_g) of oleate lignin without and with 1% acid.

	DS %	M_w/ kDa	M_n/ kDa	PDI	T_g (°C)
Oleate HELignin	88	7.53	2.927	2.58	8.1
Oleate HELignin (1% acid)	89	7.096	0.815	8.71	2.7

After the direct esterification, GPC analysis revealed that oleate HELignin with added acid catalyst had a much wider distribution of molecular weight and the traces had multiple peaks due to side reactions such as the condensation or degradation of ether bonds (**Figure S5**). As such, the lignin was not further considered for formulation of the hydrophobic coating. The esterified lignin via direct esterification without acid catalyst had a GPC trace revealing a more uniform molecular weight distribution than the other types of lignin (**Table 2**). However, the reduction of molecular weight for this lignin may be an artifact of the washing procedure to prepare materials for analysis.

Thermal Properties of Esterified HELignin

The thermal properties of lignin before and after modification were also analyzed utilizing differential scanning calorimetry (DSC). The glass transition temperatures (T_g) were detected based on the heat flow baseline shift after the third cycle in a heat-cool-heat program. By derivatizing the sample, the T_g was reduced from 165.1°C (SKL) to 120.1°C (HELignin). This

reduction was larger than previously reported hydroxyethylated lignin sample that had first undergone acetone fractionation (Liu et al., 2018). The HELignin contained a higher amount of hydroxyethyl groups, which potentially would provide additional bulking to the lignin structure, reducing the T_g further. The ethyl-oleate derivative had a significant change of T_g before and after the reaction; reducing the T_g from 120.1°C down to 8.1°C or 2.7°C (1% H_2SO_4 as catalyst) (**Table 2**). This result occurred because the esterification reaction had significantly reduced the amount of aliphatic OH groups (more than 4 out of 5 hydroxyl groups were modified with the long carbon chains), which directly weakened the intra and intermolecular bonding network and caused an increase in free volume. Hence, the alkyl chains created bulky side-groups that enhanced the inner plasticization of the lignin derivative. The change on the T_g of esterified lignin was similar with previous report that using halogenated compounds to obtain a series of lignin with different carbon chain lengths. The T_g of esterified lignin was reduced with increasing carbon chain length and the degree of substitution (Koivu et al., 2016).

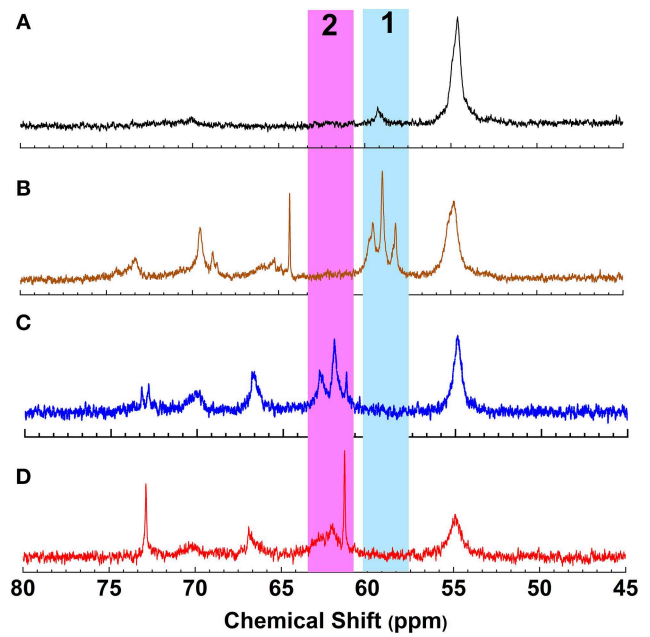

FIGURE 1 | ^{13}C NMR spectrum of **(A)** Lignin, **(B)** Hydroxyethyl lignin (HELignin), **(C)** oleate HELignin, and **(D)** oleate HELignin with 1% H_2SO_4.

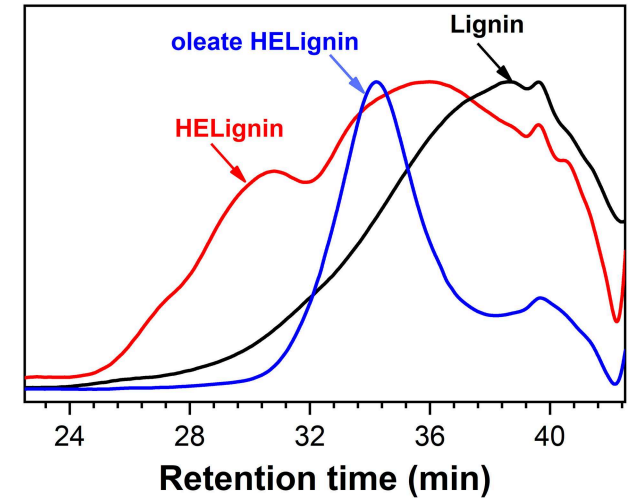

FIGURE 3 | Gel permission chromatography traces of Lignin, Hydroxyethyl lignin (HELignin), and oleate HELignin.

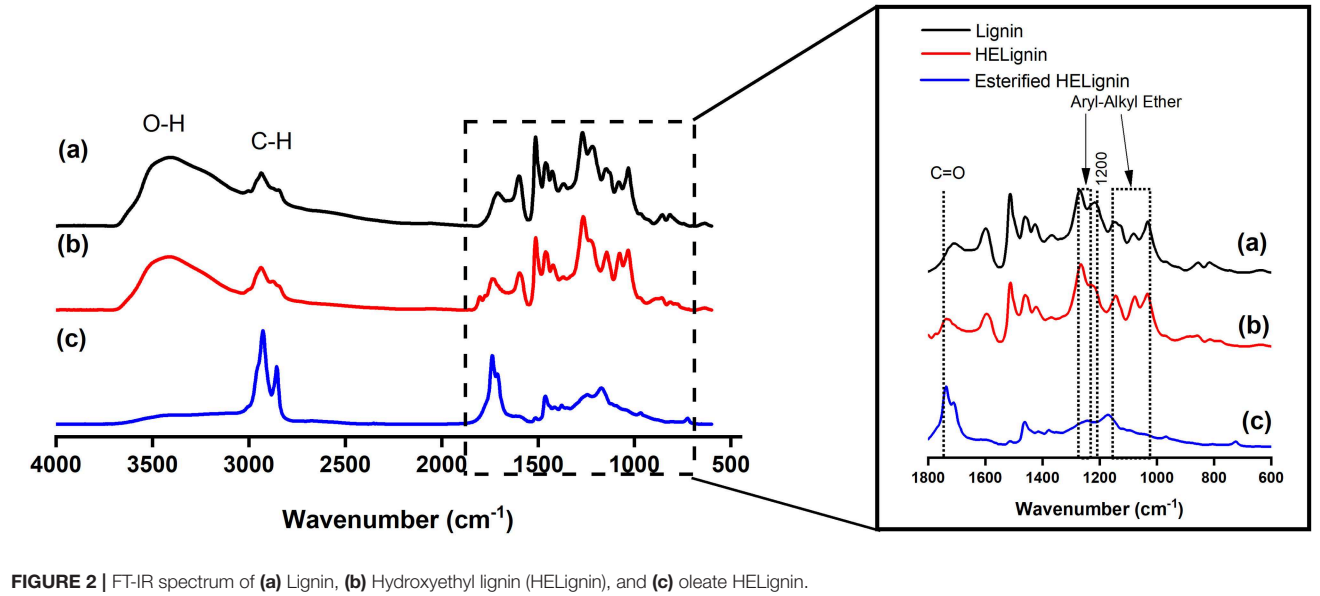

FIGURE 2 | FT-IR spectrum of **(a)** Lignin, **(b)** Hydroxyethyl lignin (HELignin), and **(c)** oleate HELignin.

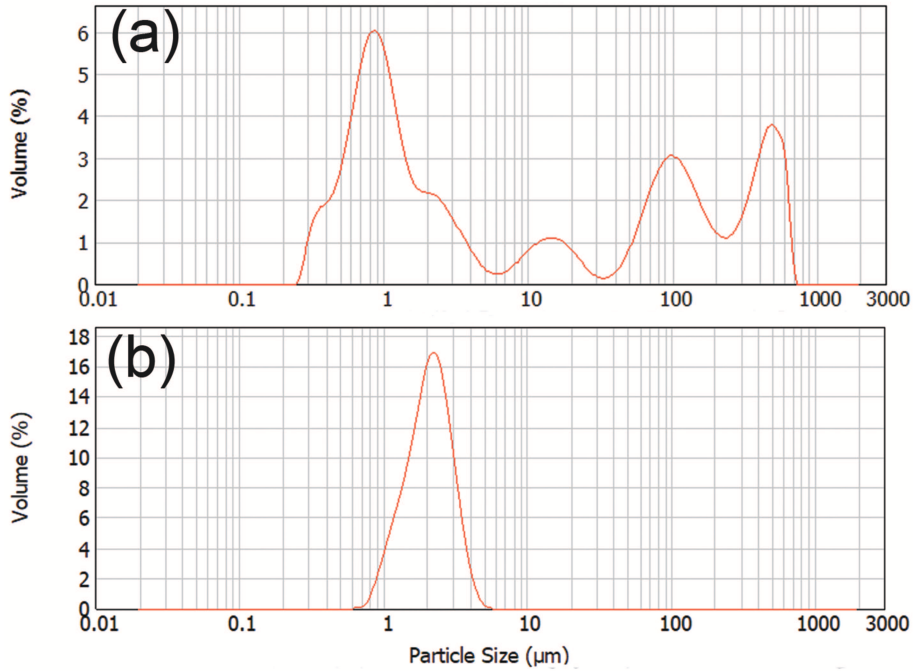

FIGURE 4 | The particle size distribution of **(a)** Lignin, **(b)** oleate HELignin.

Aqueous Lignin Particle Solution

Dynamic light scattering was used to characterize the particle size of the dispersion after controlled precipitation. **Figure 4** showed the distribution of particle sizes of SKL and the oleate HELignin derivative. The particle size for SKL had a large distribution in a range from 200 nm up to the maximum detectable range. This large range of particle sizes may be related to the swelling of the lignin via the available hydroxyl groups. The lignin formed large particles and were precipitated after extended storage. Conversely, the esterified lignin particle solution formed a steady dispersion with a particle size centered at 2 μm. The dispersion was stable for more than 1 week without precipitation.

Contact Angle Analysis

The target application of this lignin-based material was to serve as a sprayable water-based renewable material coating for forest-based products, which is critical in construction and packaging (Gordobil et al., 2017). To illustrate the change in surface behavior, the wettability of the modified surface was investigated using a static contact angle test. Bleached kraft pulp sheet stock, wood, and glass were selected as the test substrates to investigate the hydrophobicity of the coatings consisting of the lignin-oleate microparticles. The oleate esterified HELignin suspension was sprayed onto the various surfaces utilizing an airbrush. Multiple coating cycles were used to form a uniform layer. However, uniformity was difficult to achieve on the non-porous surface. The spin coating was adopted to form a uniform layer on the surface of target materials.

Figure 5 showed that the coating suspensions would increase the hydrophobicity for all three types of material surfaces for both spray and spin coating. The lignin ester deposited on the glass slides had a contact angle 110° (spray) and 95° (spin), while uncoated samples had an angle of 39°. The aqueous lignin particle solution was applied to two common wood-based products which included a solid wood block of yellow poplar and a kraft pulp sheet. For the solid wood, the contact angle increased from 68 to 147° (spray) and 137° (spin) after

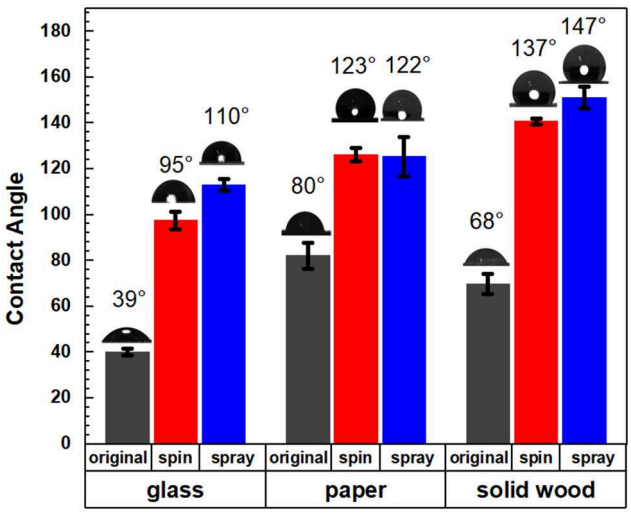

FIGURE 5 | Contact angles of original and coated glass, paper, and solid wood with spin and spray coating methods.

coating with the lignin derivative. This value is more than 20 and 10° greater than previous reported values for organosolv hydrophobized lignin esters on poplar (Gordobil et al., 2017). For the pulp sheet, the contact angle increased significantly from 80° to 122°(spray) and 123°(spin). The supporting video showed that the water droplets disappeared in 10 s for uncoated pulp, while the water droplets on the coated materials were stable after more than 2 min (**Videos S1**, **S2**). Further, the initial contact angles of the lignin oleate ester coated handsheet were similar to reported values for coated filter paper or coated commercial paper board with suberin-like lignin ester derivatives (Antonsson et al., 2008) or tall oil lignin ester derivatives (Hult et al., 2013), respectively. In these cases, the process required dissolution of the lignin derivative into acetone and application to the substrate with an organic solvent. In contrast, spraying or spinning from an aqueous suspension avoids potential VOCs during the application process.

Research into lignin-based particles (Abbati de Assis et al., 2018) is of growing interest from emulsions (Ago et al., 2016) to surfaces (Cusola et al., 2018). This research offers a novel route to tune the chemistry of the lignin particles in a very simple method of direct esterification.

Micromorphology Analysis of Aqueous Lignin Coating

The morphology of coated surfaces was analyzed by scanning electron microscopy (SEM) and atomic force microscopy (AFM); the roughness of surfaces contributes to the hydrophobic properties of waxy coating materials. **Figure 6b** showed that the coated surface of pulp boards had a more "uniform" surface than uncoated pulp board (**Figure 6a**) because the merging of these lignin particles would form a film (**Figure 6c**) to cover the surface. The AFM showed similar morphology (**Figure S6**), as particles merged into clusters, seen as linkages amongst droplet islands. This phenomenon resulted from the fact that the samples were stored at room temperature and the coating material has a low glass transition temperature ($T_g = 8.1°C$). At room temperature, the coated lignin particles can soften and relax to the structure of the surface. Similar to latex coatings, once the water has evaporated, those lignin micro particles merged into larger structures, even films at room temperature. Due to the coverage of these hydrophobic lignin particles or films, the coated surface demonstrated improvement on their hydrophobic properties. However, the surface did not retain the microstructured roughness from the dispersed compounds. Hence the roughness resulted from the substrate below the lignin film, which would explain why the smooth glass surface had the lowest contact angle. On the surface of films, there was still a small fraction of lignin particles not fully relaxed (**Figure 6d**); the diameter for these particles were around 2 μm. This result was in agreement with our previous dynamic light scattering data (**Figure 4**). Overall, ethyl-oleate lignin coated wood, paper, and glass showed increased hydrophobic properties.

CONCLUSION

In this study, a nature inspired lignin-based hydrophobic coating material was developed by esterification of lignin with a plant based fatty acids. The free phenolics were first hydroxyethylated using ethylene carbonate and subsequently,

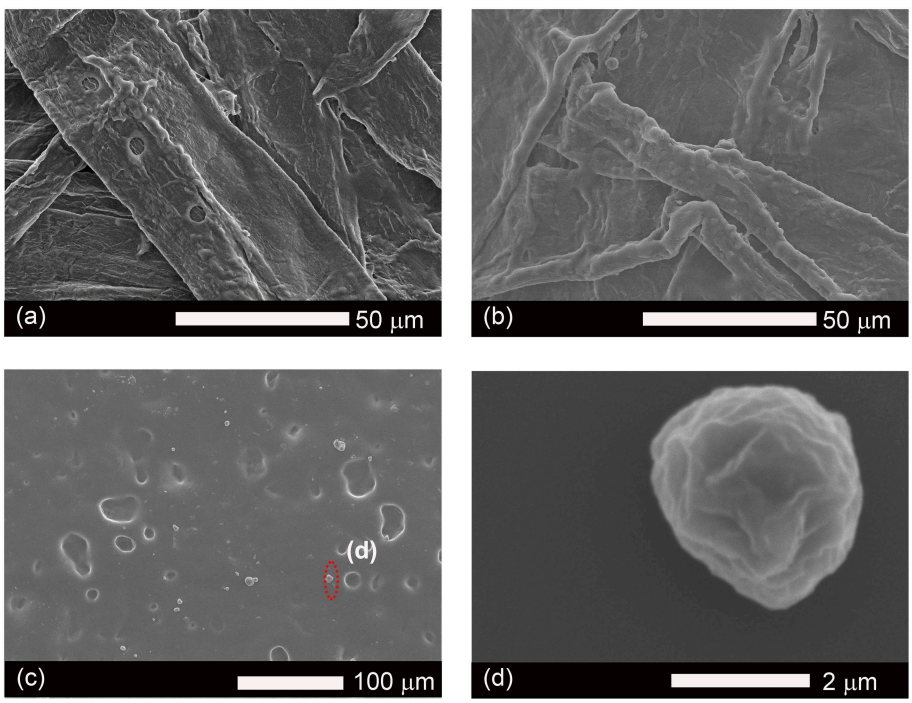

FIGURE 6 | SEM images of surfaces of original paper **(a)**, coated paper **(b)**, coated glass **(c)**, and micro particles of lignin **(d)**.

the aliphatic hydroxyls were esterified with oleic acid. Reaction conditions with and without added strong acid as a catalyst provided a derivative with high substitution levels; Utilizing the oleate ethyl-lignin derivative without added acid, lignin micro-particle suspensions were then prepared by controlled precipitation. The oleate HElignin particle showed a particle size centered at 1 μm. By spray or spin coating, this lignin aqueous solution could successfully improve the hydrophobic properties of solid wood and pulp paper with a contact angle above 120°. The low glass transition of the lignin derivative provided the ability of the microparticles to transform on the surface, a dynamic process, conforming to the inherent surface roughness. This renewable coating material helps to advance the field of simple methods to utilize technical lignin in relevant applications for packaging and construction material protection.

DATA AVAILABILITY

The datasets generated for this study are available on request to the corresponding author.

AUTHOR CONTRIBUTIONS

QH, L-YL, and SR designed the experiment. QH and L-YL generated and analyzed the experimental data. The manuscript was written by QH, L-YL, and SR. MK obtained AFM and SEM images and provided analysis. SR has supervised and finalized the final version of the manuscript.

ACKNOWLEDGMENTS

Funding support from Alberta Innovation (Alberta Bio Future Lignin Challenge 1.0 grant No. BFL18010), the MRPF, and the Paul and Edwina Heller Memorial Fund. The Canada Research Chairs Program is also acknowledged for supporting SR's program in Advanced Renewable Materials. Mehrnegar Mirvakili is acknowledged for her help on the particle size distribution analysis using DLS.

SUPPLEMENTARY MATERIAL

The Supplementary Material for this article can be found online at: https://www.frontiersin.org/articles/10.3389/fchem.2019.00515/full#supplementary-material

Figure S1 | The preparation of aqueous lignin micro particles solution using dialysis to exchange THF and water.

Figure S2 | ^{31}P NMR spectrum of **(A)** lignin and **(B)** HELignin. Peak (1) internal standard, (2) aliphatic OH groups, (3) aromatic OH groups, 4) COOH groups.

Figure S3 | ^{13}C NMR spectrum of **(A)** lignin, **(B)** HELignin, **(C)** Oleate esterified HELignin with 1% H_2SO_4, and **(D)** Oleate esterified HELignin.

Figure S4 | ^{1}H NMR spectrum of **(A)** lignin, **(B)** HELignin, and **(C)** oleate HELignin.

Figure S5 | GPC traces of oleate HELignin with 1% H_2SO_4 as catalysts.

Figure S6 | AFM images of aqueous lignin mico particles solution.

Video S1 | The surface properties of uncoated pulp.

Video S2 | The surface properties of coated pulp.

REFERENCES

Abbati de Assis, C., Greca, L. G., Ago, M., Balakshin, M. Y., Jameel, H., Gonzalez, R., et al. (2018). Techno-economic assessment, scalability, and applications of aerosol lignin micro- and nanoparticles. *ACS Sustain. Chem. Eng.* 6, 11853–11868. doi: 10.1021/acssuschemeng.8b02151

Ago, M., Huan, S., Borghei, M., Raula, J., Kauppinen, E. I., and Rojas, O. J. (2016). High-throughput synthesis of lignin particles (approximately 30 nm to approximately 2 mum) via aerosol flow reactor: size fractionation and utilization in pickering emulsions. *ACS Appl. Mater. Interfaces* 8, 23302–23310. doi: 10.1021/acsami.6b07900

Antonsson, S., Henriksson, G., Johansson, M., and Lindström, M. E. (2008). Low Mw-lignin fractions together with vegetable oils as available oligomers for novel paper-coating applications as hydrophobic barrier. *Ind. Crop. Prod.* 27, 98–103. doi: 10.1016/j.indcrop.2007.08.006

Argyropoulos, D. S. (1995). 31P NMR in wood chemistry: a review of recent progress. *Res. Chem. Intermed.* 21, 373–395. doi: 10.1007/BF03052265

Balakshin, M. Y., Capanema, E. A., Santos, R. B., Chang, H.-M., and Jameel, H. (2016). Structural analysis of hardwood native lignins by quantitative 13C NMR spectroscopy. *Holzforschung* 70, 95–108. doi: 10.1515/hf-2014-0328

Cho, M., Karaaslan, M. A., Renneckar, S., and Ko, F. (2017). Enhancement of the mechanical properties of electrospun lignin-based nanofibers by heat treatment. *J. Mater. Sci.* 52, 9602–9614. doi: 10.1007/s10853-017-1160-0

Clark, J. H., Farmer, T. J., Hunt, A. J., and Sherwood, J. (2015). Opportunities for bio-based solvents created as petrochemical and fuel products transition towards renewable resources. *Int. J. Mol. Sci.* 16, 17101–17159. doi: 10.3390/ijms160817101

Cui, C., Sadeghifar, H., Sen, S., and Argyropoulos, D. S. (2013). Toward thermoplastic lignin polymers; Part II: thermal & polymer characteristics of kraft lignin & derivatives. *BioResources* 8, 864–886. doi: 10.15376/biores.8.1.864-886

Cusola, O., Kivistö, S., Vierros, S., Batys, P., Ago, M., Tardy, B. L., et al. (2018). Particulate coatings via evaporation-induced self-assembly of polydisperse colloidal lignin on solid interfaces. *Langmuir*. 34, 5759–5771. doi: 10.1021/acs.langmuir.8b00650

Eriksson, K.-E. L., Blanchette, R. A., and Ander, P. (2012). *Microbial and Enzymatic Degradation of Wood and Wood Components*. Berlin; Heidelberg: Springer Science & Business Media.

Foster, E. J., Moon, R. J., Agarwal, U. P., Bortner, M. J., Bras, J., Camarero-Espinosa, S., et al. (2018). Current characterization methods for cellulose nanomaterials. *Chem. Soc. Rev*. 47, 2609–2679. doi: 10.1039/C6CS00895J

Franke, R., and Schreiber, L. (2007). Suberin–a biopolyester forming apoplastic plant interfaces. *Curr. Opin. Plant Biol.* 10, 252–259. doi: 10.1016/j.pbi.2007.04.004

Geissler, A., Chen, L., Zhang, K., Bonaccurso, E., and Biesalski, M. (2013). Superhydrophobic surfaces fabricated from nano- and microstructured cellulose stearoyl esters. *Chem. Commun.* 49, 4962–4964. doi: 10.1039/c3cc41568f

Gillet, S., Aguedo, M., Petitjean, L., Morais, A. R. C., Da Costa Lopes, A. M., Łukasik, R. M., and Anastas, P.T. (2017). Lignin transformations for high value applications: towards targeted modifications using green chemistry. *Green Chem.* 19, 4200–4233. doi: 10.1039/C7GC01479A

Gordobil, O., Herrera, R., Llano-Ponte, R., and Labidi, J. (2017). Esterified organosolv lignin as hydrophobic agent for use on wood products. *Progr. Organ. Coatings* 103, 143–151. doi: 10.1016/j.porgcoat.2016.10.030

Hu, Z., and Deng, Y. (2010). Superhydrophobic surface fabricated from fatty acid-modified precipitated calcium carbonate. *Industr. Eng. Chem. Res.* 49, 5625–5630. doi: 10.1021/ie901944n

Hult, E.-L., Koivu, K., Asikkala, J., Ropponen, J., Wrigstedt, P., Sipilä, J., et al. (2013). Esterified lignin coating as water vapor and oxygen barrier for fiber-based packaging. *Holzforschung* 67, 899–905. doi: 10.1515/hf-2012-0214

Jiang, F., and Hsieh, Y.-L. (2014). Super water absorbing and shape memory nanocellulose aerogels from TEMPO-oxidized cellulose nanofibrils via cyclic freezing–thawing. *J. Mater. Chem. A* 2, 350–359. doi: 10.1039/C3TA13629A

Jiang, F., Li, T., Li, Y., Zhang, Y., Gong, A., Dai, J., et al. (2018). Wood-based nanotechnologies toward Sustainability. *Adv. Mater.* 30:1703453. doi: 10.1002/adma.201703453

Koivu, K. A. Y., Sadeghifar, H., Nousiainen, P. A., Argyropoulos, D. S., and Sipilä, J. (2016). Effect of fatty acid esterification on the thermal properties of softwood kraft lignin. *ACS Sustain. Chem. Eng.* 4, 5238–5247. doi: 10.1021/acssuschemeng.6b01048

Kouisni, L., Holt-Hindle, P., Maki, K., and Paleologou, M. (2012). The lignoforce systeme^{TM}: a new process for the production of high-quality lignin from black liquor. *J. FOR* 2, 6–10.

Lange, H., Rulli, F., and Crestini, C. (2016). Gel permeation chromatography in determining molecular weights of lignins: critical aspects revisited for improved utility in the development of novel materials. *ACS Sustain. Chem. Eng.* 4, 5167–5180. doi: 10.1021/acssuschemeng.6b00929

Liu, L.-Y., Cho, M., Sathitsuksanoh, N., Chowdhury, S., and Renneckar, S. (2018). Uniform chemical functionality of technical lignin using ethylene carbonate for hydroxyethylation and subsequent greener esterification. *ACS Sustain. Chem. Eng.* 6, 12251–12260. doi: 10.1021/acssuschemeng.8b02649

Liu, L.-Y., Hua, Q., and Renneckar, S. (2019). A simple route to synthesize esterified lignin derivatives. *Green Chem.* 21, 3682–3692. doi: 10.1039/C9GC00844F

Lv, N., Wang, X., Peng, S., Zhang, H., and Luo, L. (2018). Study of the kinetics and equilibrium of the adsorption of oils onto hydrophobic jute fiber modified via the sol-gel method. *Int. J. Environ. Res. Public Health* 15:969. doi: 10.3390/ijerph15050969

Marney, D. C. O., and Russell, L. J. (2007). Combined fire retardant and wood preservative treatments for outdoor wood applications—a review of the literature. *Fire Technol.* 44, 1–14. doi: 10.1007/s10694-007-0016-6

Mohammad, M. J. R., Whelan, M., and Coxford, R. (2018). "Canada's tall wood buildings demonstration projects," in *2018 World Conference on Timber Engineering* (Seoul).

Mohanty, A. K., Misra, M., and Drzal, L. T. (2002). Sustainable bio-composites from renewable resources: opportunities and challenges in the green materials world. *J. Polymers Environ.* 10, 19–26. doi: 10.1023/A:1021013921916

Mohanty, A. K., Vivekanandhan, S., Pin, J.-M., and Misra, M. J. S. (2018). Composites from renewable and sustainable resources: challenges and innovations. *Science.* 362, 536–542. doi: 10.1126/science.aat9072

Pu, Y., Cao, S., and Ragauskas, A. J. (2011). Application of quantitative 31P NMR in biomass lignin and biofuel precursors characterization. *Energy Environ. Sci.* 4, 3154–3156. doi: 10.1039/c1ee01201k

Salanti, A., Zoia, L., and Orlandi, M. (2016). Chemical modifications of lignin for the preparation of macromers containing cyclic carbonates. *Green Chem.* 18, 4063–4072. doi: 10.1039/C6GC01028H

Sheldon, R. A. (2007). The E Factor: fifteen years on. *Green Chem.* 9, 1273–1283. doi: 10.1039/b713736m

Thielemans, W., and Wool, R. P. (2005). Lignin esters for use in unsaturated thermosets: lignin modification and solubility modeling. *Biomacromolecules* 6, 1895–1905. doi: 10.1021/bm0500345

Urushihara, Y., and Nishino, T. (2005). Effects of film-forming conditions on surface properties and structures of diblock copolymer with perfluoroalkyl side chains. *Langmuir* 21, 2614–2618. doi: 10.1021/la047317n

Zhang, C., Garrison, T. F., Madbouly, S. A., and Kessler, M. R. (2017). Recent advances in vegetable oil-based polymers and their composites. *Progr. Polymer Sci.* 71, 91–143. doi: 10.1016/j.progpolymsci.2016.12.009

Zhao, W., Simmons, B., Singh, S., Ragauskas, A., and Cheng, G. (2016). From lignin association to nano-/micro-particle preparation: extracting higher value of lignin. *Green Chem.* 18, 5693–5700. doi: 10.1039/C6GC01813K

Zuo, J., Li, S., Bouzidi, L., and Narine, S. S. (2011). Thermoplastic polyester amides derived from oleic acid. *Polymer* 52, 4503–4516. doi: 10.1016/j.polymer.2011.08.002

Conflict of Interest Statement: The authors declare that the research was conducted in the absence of any commercial or financial relationships that could be construed as a potential conflict of interest.

frontiers in Materials

ORIGINAL RESEARCH
published: 24 July 2019
doi: 10.3389/fmats.2019.00178

Adsorption and Desorption of Organic Molecules From Thin Cellulose Films

Elias Henögl[1,2], *Viktoria Haberl*[1], *Jakob Ablasser*[1] *and Robert Schennach*[1,2]*

[1] *Institute of Solid-State Physics, Graz University of Technology, Graz, Austria,* [2] *CD-Laboratory for Mass Transport Through Paper, Graz University of Technology, Graz, Austria*

The debate on the environmental effects of everyday packaging materials has long reached the scientific community. The quest is on to design cheap but also sustainable and eco-friendly packaging solutions. A hot contestant material within the application is the ever-present wood-based paper. In addition to meeting logistic requirements, paper packaging must protect the packaged goods from environmental influences, while keeping aroma molecules in the food. To quantify both aspects in depth, exploration of adsorption of organic molecules on paper is required. As paper is a rather complex material, adsorption and desorption experiments can be notoriously difficult to interpret. This paper will demonstrate that the adsorption of organic molecules on a cellulose surface can be investigated simply by using temperature programmed desorption (TPD) experiments. The experiments show that both non-polar and polar molecules (n-decane and deuterated methanol) readily adsorb onto cellulose films. During desorption one finds the polar molecule bound to the cellulose surface more heavily than the non-polar molecule.

Keywords: temperature programmed desorption, adsorption, desorption, cellulose films, paper

OPEN ACCESS

Edited by:
Eero Kontturi,
Aalto University, Finland

Reviewed by:
Andreas Mautner,
University of Vienna, Austria
Koon-Yang Lee,
Imperial College London,
United Kingdom

***Correspondence:**
Robert Schennach
robert.schennach@tugraz.at

Specialty section:
This article was submitted to Thin Solid Films, a section of the journal Frontiers in Materials

Received: *18 January 2019*
Accepted: *08 July 2019*
Published: *24 July 2019*

Citation:
Henögl E, Haberl V, Ablasser J and Schennach R (2019) Adsorption and Desorption of Organic Molecules From Thin Cellulose Films. Front. Mater. 6:178. doi: 10.3389/fmats.2019.00178

INTRODUCTION

The discussion of benefits vs. environmental cost of packaging materials is constant. In this age of ever-rising environmental awareness, customers often reward "going green" and paper securely holds a spot at the forefront of the issue.

However, in order to be used as packaging material for food, paper has to fulfill a number of requirements. On one hand aroma molecules need to stay inside the food and on the other hand the package is put on to protect the food from environmental influences like oxygen or organic molecules that might trigger ripening or produce rotten flavors. With paper being a porous material, a key feature is the transport of molecules through the porous structure to gain insight and control over the aforementioned issues. One of the questions to be answered in this context is the extent to which molecules adsorb onto the walls of the pores. This makes adsorption studies of molecules on cellulosic surfaces all the more essential.

Literature research reveals a substantial number of studies on cellulosic materials in the wet state to remove pollutants from water (see e.g., Voisin et al., 2017). Also, the adsorption of polyelectrolytes on pulps has been investigated intensely (see e.g., Li et al., 2003; Neumann et al., 2018). The adsorption of smaller molecules has attracted less attention as was proven in a recent review (Lombardo and Thielemans, 2019). Adsorption of aromatic compounds onto cellulose

has been studied by Perez et al. (2004). Benzophenone adsorption was studied by Mazeau and Vergelati (2002) and Congo red adsorption by Mazeau and Wyszomirski (2012). Naphtalin and Pyrene adsorption were investigated by Tozuka et al. (1998, 2002). Urea adsorption has been investigated by Chen et al. (2017), to mention just a few examples. However, these articles are not relevant for the field of food packaging. We are therefore specifically investigating the adsorption of small molecules from the gas phase onto cellulosic surfaces. Within this context dynamic vapor sorption has been studied extensively (see e.g., Xie et al., 2011). Usually such studies take place under equilibrium conditions. When adsorption of small molecules occurs in paper packaging, it is unlikely that equilibrium conditions apply. We are rather proposing to investigate the adsorption of small molecules under high vacuum conditions far from the equilibrium. Unfortunately, such measurements are impossible using paper samples, as the paper cannot be heated directly in a vacuum chamber. This is why we must employ a model system in our case thin cellulose films. Despite the fact that such thin cellulose films are produced out of cellulose II instead of cellulose I, which is found in paper, it was shown that these films are a useful replacement model system for paper (Rohm et al., 2014). Thin cellulose films have also been used before as substrates for water adsorption (see e.g., Niinivaara et al., 2015, 2016; Hakalahti et al., 2017) and sugar adsorption (Hoja et al., 2014).

Within this study we present the **first** high vacuum-based adsorption and temperature programmed desorption spectroscopy studies of n-decane and deuterated methanol on thin cellulose films.

MATERIALS AND METHODS

Equipment and Control Systems

- Rotary vane pump:
  Leybold TRIVAC D 25 B
- Turbo molecular pump & control system:
  Oerlikon Leybold Vacuum, Turbovac type TMP151 & Turbo.Drive TD20 classic
- Quadrupole mass spectrometer & control software:
  Balzers Prisma type QME 200 (CF DN40) & Quadstar 32-Bit
- Power supply:
  HP DC Power Supply System 6261B
- Temperature control system
  PID (Proportional-Integral-Derivative) controller in National Instruments LabVIEW 7.0
- Bayard-Alpert gauge & control system:
  Leybold AG IE 414 (CF DN40) & IONIVAC IM 520
- Manual angle valve
  Balzers EVA 025 H (KF DN25)
- Gas inlet valve
  Pfeiffer Vacuum Gas Dosing Valve EVN 116 (KF DN16)
- Metal to glass connector doomed:
  GMA-KF16-KGD-152-TD13 (KF DN16).

The TPD-System

The main vacuum chamber is a stainless steel six-way crossing. The pumping system consists of a turbo molecular pump,

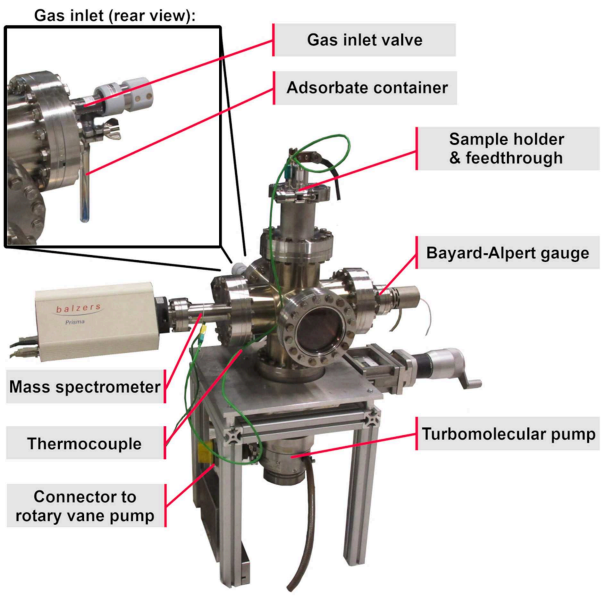

FIGURE 1 | TPD-System, overview.

attached to the bottom side of the main chamber (see **Figure 1**), followed by a rotary vane pump not shown in **Figure 1**. The quadrupole mass spectrometer and the Bayard-Alpert gauge are mounted onto the left and onto the right side of the chamber. The gas inlet valve is attached to the rear side and connected to a glass container holding the liquid organic molecules (see **Figure 1** rear view).

The top side of the six-way crossing is extended by an adapter to a DN63 CF-flange cover, which is fastened by a quick CF clamp chain providing faster sample change. The flange cover offers two electrical and one thermocouple feedthrough, as well as one borehole into the copper body of the cooling finger. The cooling finger, a hollow cylindrical copper piece, is mounted onto the inner side of this flange cover, extending down to the center of the chamber, merging into a flattened end piece, later referred to as the "sample holder" (**Figure 2**). Two sample holding benches are attached to this platform isolated by aluminum oxide spacers, which provide electrical isolation and heat conduction.

The sample substrate itself is a 1 × 1 cm stainless steel plate with two Ta wires for resistance heating and a K-Type thermocouple, spot welded to its backside. The substrate is mounted by clamping the heating wires into the sample holding benches, which are connected to the electrical feedthrough by copper cables.

In the middle section, the cooling finger also holds two aluminum oxide thermocouple mini connectors, which are plugged together. While the upper mini connector is permanently wired to the thermocouple feedthrough of the flange cover, the lower connector acts as a clamp board for the thermocouple wires coming from the backside of the sample (see **Figure 2**).

In order to increase the gas flow to the sample surface, a gas inlet pipe, which is connected to the gas inlet valve (see **Figure 3**), points at the sample surface at an angle of about 35° and ends

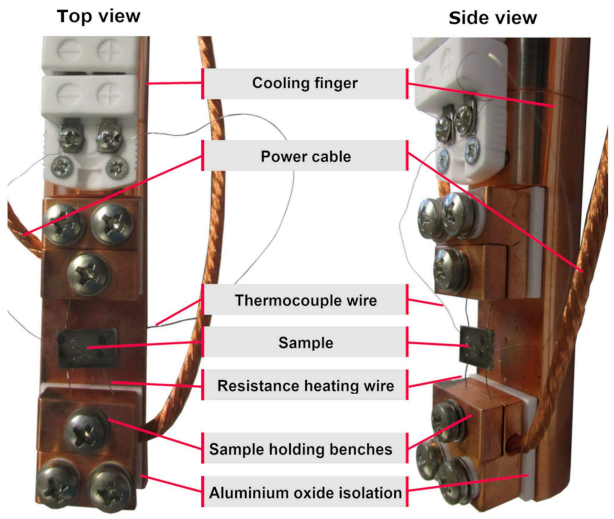

FIGURE 2 | Sample holder of the TPD-System, top view and side view.

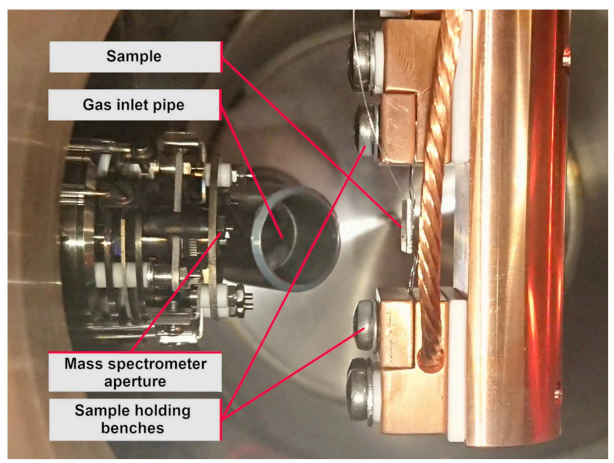

FIGURE 3 | Vacuum chamber inside geometry.

at a distance of about 3 cm from the sample surface. The mass spectrometer is positioned exactly opposite to the sample surface at the same distance.

Sample Preparation

The sample is prepared with the same standard procedure as proposed by Kontturi et al. (2003) and Rohm et al. (2014), with the substrate being coated by a thin cellulose film. The cellulose in question is trimethylsilyl cellulose (TMSC) with a degree of substitution of about 2.8 (Thüringisches Institut für Textil-und Kunstoff-Forschung e.V. (TITK), Germany) and dissolved in toluene with a concentration of about 1 mg/ml. The resulting solution is drop casted onto the polished metal surface of the sample and air-dried. Subsequently, a drop of 10% HCl is placed in a petri-dish and the sample is put right next to the HCl drop. The dish, including the sample setup is then covered with aluminum foil and left to react for 15 min.

According to Konturri and Djak this procedure results in a fully regenerated cellulose film with a thickness of about 50 nm (Kontturi et al., 2003; Djak et al., 2011). FTIR measurements of the films did not find any trimethylsilyl induced vibrations in the pure cellulose films. Mass 73 however, was found in thermal desorption which could correspond to the trimethyl silyl fragment. The amount of residual TMSC thus lies below the FTIR detection limit ($\sim 1 \times 10^{13}$ molecules) and above the detection limit of mass spectroscopy. The film thickness of several other samples was also measured by AFM. Afterwards these AFM samples were no longer used for desorption experiments to avoid the influence of the scratches caused by the AFM thickness measurements on the desorption behavior.

The films are completely amorphous; which is why we do not expect to see a porous structure in them. During AFM investigations of such films (Ganser et al., 2014, 2016; Rohm et al., 2014) no indication of pores has been found. This indicates that the density should be close to the one of regenerated cellulose. Nevertheless, porosity and density of the films were not measured within this study.

Experimental Procedure

Evacuation

The sample is mounted into the sample holding benches and the thermocouple is connected (see above). The sample holder is inserted into the vacuum chamber and the temperature monitoring is started. The flange cover is fastened by the quick CF clamp chain and the vacuum chamber is evacuated to the base pressure of about 5×10^{-9} mbar. Due to the filaments of the mass-spectrometer and the Bayard-Alpert gauge, the temperature of the sample inside the vacuum chamber levels at 55°C while the evacuation is performed.

Residual Gas Analysis

A residual gas analysis is performed by recording a mass spectrum from mass 1 to mass 100 (such a mass spectrum is shown in the supporting information (**SI Figure 1**) for evaluation of the starting conditions and the vacuum quality.

Cooling

Liquid nitrogen ($N_{2(l)}$) is now filled into the cooling finger repeatedly. Once the preset base temperature of the sample (−80°C) is reached, it is maintained by moderate, PID (Proportional-Integral-Derivative) controlled, resistance heating and further $N_{2(l)}$ cooling as needed.

Adsorption

The gas inlet valve is now opened carefully. Due to the vapor pressure at room temperature of the organic molecules inside the adsorbate container the vapor is dosed into the vacuum chamber. The sample is kept at −80°C during adsorption. The valve is adjusted until the inflow of the gaseous organic molecules and the pumping of the turbo molecular pump levels out at a steady state pressure of 5×10^{-6} mbar. This pressure is then maintained for a specified adsorption time of 6 min. After this time the gas inlet

valve is closed quickly, and the chamber pressure returns to the base pressure.

Desorption

It takes about 1 min to reach the base pressure and the thermal desorption process is started from −80°C. The PID controller heats the sample with a heating rate of 1°C/s to the upper temperature limit of 600°C. During desorption the intensity signals of preset masses are continuously recorded in respect to time by the mass spectrometer. At the same time the sample temperature is recorded as a function of time. Each mass intensity is then replotted as a function of temperature. This represents a fairly typical setup for TPD measurements (see e.g., Hohenegger et al., 1998).

Since only a limited number of mass-intensities can be recorded in a row, each mass represents a characteristic fragment of a participating molecule: mass 57 for n-decane, mass 34 for deuterated methanol (D_3COD), mass 44 for CO_2, and mass 18 for H_2O. While the first two masses are characteristic for the adsorbed species the latter two masses are characteristic for cellulose desorption.

Adsorbed Molecules

Aroma molecules usually are organic molecules with a rather high vapor pressure. One can encounter both polar and non-polar aroma molecules. To get a first idea about the adsorption behavior of such molecules on a cellulose thin film, we used n-decane as a non-polar molecule and deuterated methanol (D_3COD) as a polar molecule. Both molecules were obtained in p.a. grade from Sigma Aldrich (deuterated methanol ≥99%, isotope purity ≥99.8 atom % D, n-decane ≥99.5 %) and were cleaned *in situ* via several freeze and thaw cycles. The molecular mass of n-decane is 142 amu and the vapor pressure at 30°C is 3.17 hPa, which proved sufficient for adsorption. As the used quadrupole mass spectrometer has a maximum mass of 100 amu we had to look at mass 57 for the n-decane. In the end, this also happened to be the highest peak in the n-decane mass spectrum. Mass 57 also is of rather low intensity in the mass spectrum of the desorbing cellulose film. The mass spectrum of n-decane can be found in the supporting information (**SI Figure 2**). The n-decane mass spectrum remained unchanged over time and shows no evidence of contamination with lower hydrocarbons. Nevertheless, traces of nonane and octane contamination cannot be completely ruled out.

The molecular mass of deuterated methanol is 36 amu. The highest peak in the mass spectrum of deuterated methanol is at 34 amu. In our TPD measurements we used this mass as indicator as it does neither interfere with the mass spectrum of the desorbing cellulose film nor with the n-decane. The mass spectrum of the deuterated methanol during exposure can be found in the supporting information (**SI Figure 3**) as well. The vapor pressure of deuterated methanol at 20°C is 129 hPa.

RESULTS AND DISCUSSION

The exposed molecules not only adsorb onto the cellulose film, because adsorption is accomplished via the gas phase.

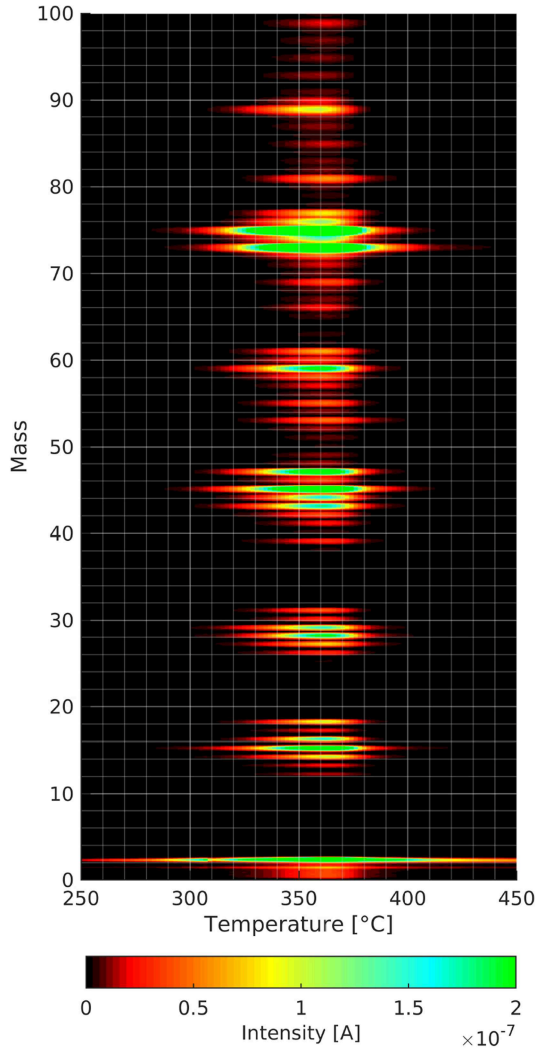

FIGURE 4 | Mass spectra as a function of temperature of the cellulose film decomposition and desorption. The intensities of the different masses are linked to the color code.

Therefore, a series of blind experiments was conducted to ensure that the effects found only stem from the cellulose films. In the blind regimen the clean substrate films with and without adsorption of n-decane and deuterated methanol were tested. These three experiments clearly show desorption peaks differing from the ones presented here. Without prior gas adsorption onto the cellulose films one finds (see **Figure 4**) several fragments desorbing in the same temperature range as shown by the TPD spectra below.

Cellulose Desorption/Decomposition Fingerprint

Figure 4 shows the result of a TPD experiment with a cellulose film without prior gas adsorption. In the three-dimensional plot one can see that the maximum intensity of the cellulose desorption fragments occurs at about 360°C. This is a lower

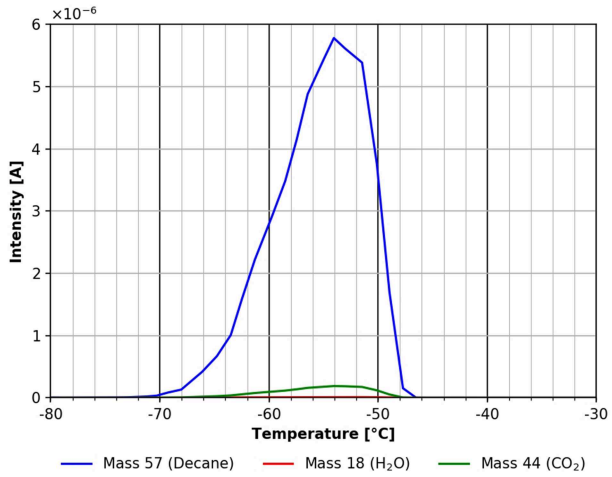

FIGURE 5 | Desorption of n-decane (mass 57, blue), carbon dioxide (mass 44, green) and water (mass 18, red) between −80 and −30°C.

temperature than the ones for the other TPD spectra shown later. The heating rate in the aforementioned experiment is only 0.1°C/s as opposed to 1°C/s in all the other experiments. The lower heating rate became necessary as the acquisition of a complete mass spectrum from 0 to 100 amu takes much longer than the 4 individual masses in the other experiments shown later.

One can see in **Figure 4** that both mass 18 and mass 44 desorb during cellulose decomposition and desorption. The most intense desorption peaks are at the masses 73 and 75 amu. While the peak at mass 73 fits to the trimethylsilyl group, one cannot explain mass 75 using this group as the Si isotope with mass 30 has only an occurrence of about 3%. Within this context, mass 75 could also stem from fragmentation of larger species that we are unable to detected due to the mass limitation (mass 100) of the mass spectrometer used. One can see several clusters of masses with a distance of about 10 amu, which is a common characteristic of mass spectra of organic molecules. Nevertheless, one needs to consider carefully which masses to track when doing thermal desorption experiments from cellulose films. This helps to distinguish the adsorbed species from the decomposing/desorbing cellulose film. We picked mass 57 for n-decane as this peak is the smallest of the cellulose peaks that could be used for n-decane. Deuterated methanol was employed, because its highest mass peak of 34 amu is not detected in the cellulose film desorption spectrum.

We also noted in preliminary experiments that heating to 150°C led to a marked change in the thin cellulose films shown by a significant change in the onset of the TPD spectra after repeated measurements on the same film (see **SI Figure 4**). In this work we present only data obtained with a virgin thin cellulose film. The desorption of the cellulose films is completed at about 600°C. Over time we found an accumulation of a carbon residue on the substrate, which was taken off by polishing the surface before film formation.

TPD-Spectra

The interpretation of TPD spectra in Surface Science follows the principle of microscopic equilibrium. An adsorbing species will thus take the same pathway during adsorption and desorption. As a reverse conclusion one can learn something about the adsorption process from desorption experiments (Somorjai, 1981). It has been shown that the shape of the desorption peak from a TPD experiment has a characteristic shape for desorption from both a multilayer for molecular desorption and for dissociative adsorption (Somorjai, 1981). Redhead proposed a simplified method to calculate the adsorption energy from the temperature at the peak maximum of a thermal desorption spectrum (Redhead, 1962). In this work we report adsorption energies for the adsorbed species calculated according to the Redhead formula. In any case one should keep in mind that this method was originally intended for simple molecule adsorption like CO or H_2. Under which circumstances the Redhead method also applies to organic molecules has not yet been investigated. In the end, the values do provide at least an idea about the adsorption energy. Different adsorption energies are commonly connected to different adsorption sites on the surface. This connection is used throughout this paper.

n-Decane Desorption

The asymmetric peak shape with the steep trailing edge of the desorption peak as demonstrated by **Figure 5** is a clear sign that the n-decane desorbs from a multilayer that was adsorbed at −80°C. The multilayer desorbs between about −70 and −52°C with an adsorption energy of about 60 kJ/mol. This value sits right between the heat of vaporization of 56 kJ/mol at −15°C (Carruth and Kobayashi, 1973) and 77 kJ/mol obtained by extrapolating the data from Majer and Scoboda (1985) to −70°C. This suggests that this desorption peak stems from a multilayer on the surface. Within the same temperature range also some desorption of CO_2 can be seen as well, which most likely stems from adsorption from the residual gas during cooling and during n-decane adsorption. A closer look at the same temperature range also shows a water desorption peak (see **Figure 6**).

The water desorption peak seen in the temperature range between −80 and about −52°C most likely is due to water adsorption from the residual gas during cooling and gas exposure. It might also partly stem from residual water in the cellulose film. To minimize the latter effect, the experiments shown here were only started when a background pressure of about 5×10^{-9} mbar was reached. The influence of the background pressure before adsorption is shown in the supporting information (**SI Figure 5**). **Figure 6** also shows another desorption feature from n-decane and water with a maximum at about −43°C. Even though this peak is small, please note, that all the figures are derived directly from raw data without any smoothing. For this reason, all peaks discussed in this paper show a good signal to noise ratio and all the features discussed have been experimentally reproduced several times.

This feature is shown in more detail in **Figure 7**. The desorption peak at around −43°C clearly suggests a more strongly bound n-decane species. Using the Redhead formula this corresponds to a binding energy of about 70 kJ/mol. A small peak

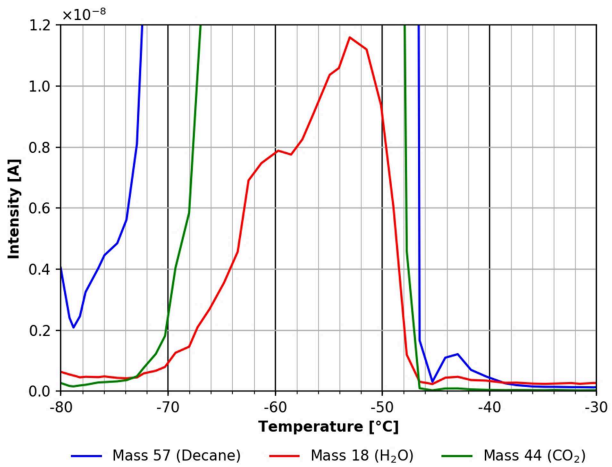

FIGURE 6 | Zoom into the TPD spectrum shown in **Figure 5**. n-decane (mass 57, blue), carbon dioxide (mass 44, green), and water (mass 18, red).

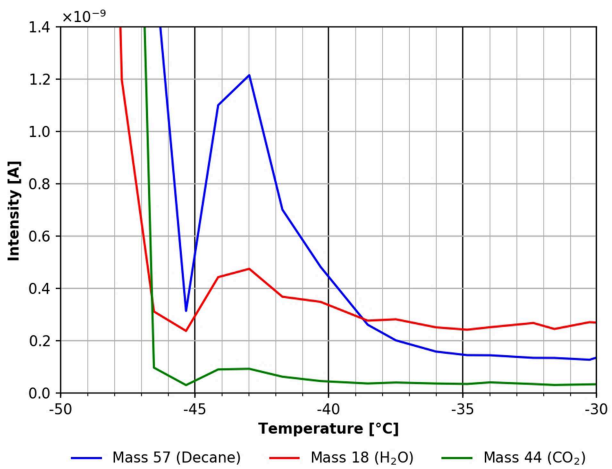

FIGURE 7 | Zoom into the TPD spectrum shown in **Figure 6**. n-decane (mass 57, blue), carbon dioxide (mass 44, green), and water (mass 18, red).

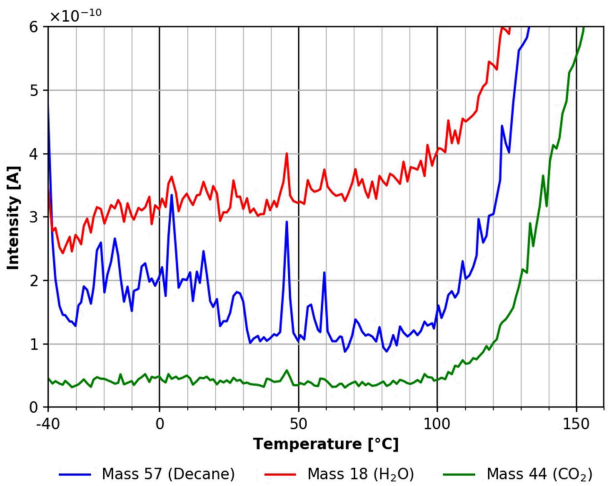

FIGURE 8 | Desorption of n-decane (mass 57, blue), carbon dioxide (mass 44, green) and water (mass 18, red) in the temperature range between −40 and +160°C.

of CO_2 and water is clearly visible in **Figure 7** still, indicating that these species find similar adsorption sites on the cellulose surface.

Going to higher temperatures one finds a small and broad desorption feature of n-decane between about −40 and +14°C (see **Figure 8**) corresponding to an adsorption energy of about 160 kJ/mol. This characteristic is not present in the CO_2 desorption trace, and is not clearly visible in the water desorption trace. The reason for the higher scattering in the data in **Figure 8** could have been caused by a heating rate which was not perfectly linear in this temperature range.

Figure 8 also shows that all three species start to desorb at different onset temperatures of about 80°C for water, 95°C for n-decane, and 100°C for CO_2. This is also the onset of the desorption/degradation of the cellulose film, as can be seen in **Figure 8**. Another strong indication that the cellulose film undergoes significant changes during heating can be seen in the difference between the onset of the desorption after repeated adsorption and desorption cycles without preparing a new film shown in the supporting information (**SI Figure 4**).

The largest desorption peak in **Figure 9** is the CO_2 peak followed by the water peak. Surprisingly, there is significant n-decane desorption visible still. This peak can also originate in part from the decomposition/desorption of the cellulose film. Unfortunately, these two possibilities cannot be distinguished from each other at this time. As mentioned above, a fragment at mass 57 can be seen in **Figure 4**. There probably is a 4th adsorption site for n-decane with a binding energy of about 180 kJ/mol. The degradation of cellulose takes place at about the same temperature range too. These results show that non-polar molecules readily adsorb on cellulose surfaces at room temperature and above.

A comparison of **Figures 9** and **10** shows that the final desorption of all species is influenced by the molecules adsorbed. In the case of n-decane adsorption three different desorption peaks for all three species investigated can be viewed in **Figure 9**. For deuterated methanol only one peak is observed in the same temperature region (**Figure 10**). This suggests, that the adsorbed species do have an influence on the cellulose decomposition and desorption.

Deuterated Methanol Desorption

Figure 10 shows the TPD spectrum from deuterated methanol over the whole temperature range. Evidently low temperature peaks are absent in this case. This is a strong indicator that the polar deuterated methanol is more strongly bound during adsorption than the n-decane. Nevertheless, the adsorption energy according to the Redhead equation is also about 180 kJ/mol. Clearly one has to keep in mind that the mass 57 desorption peak in the n-decane case is overlapping with mass

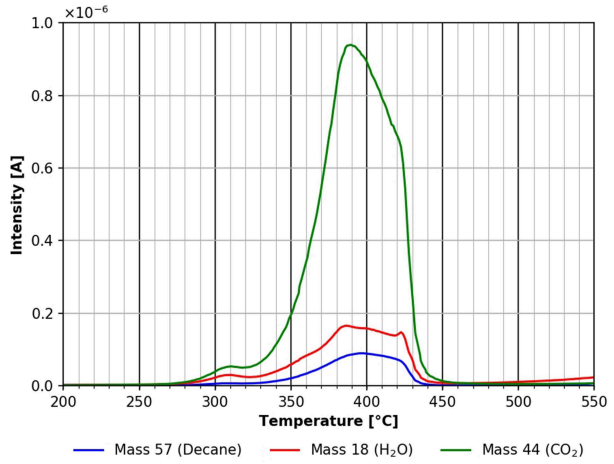

FIGURE 9 | Desorption of n-decane (mass 57, blue), carbon dioxide (mass 44, green) and water (mass 18, red) in the temperature range between 200 and 550°C.

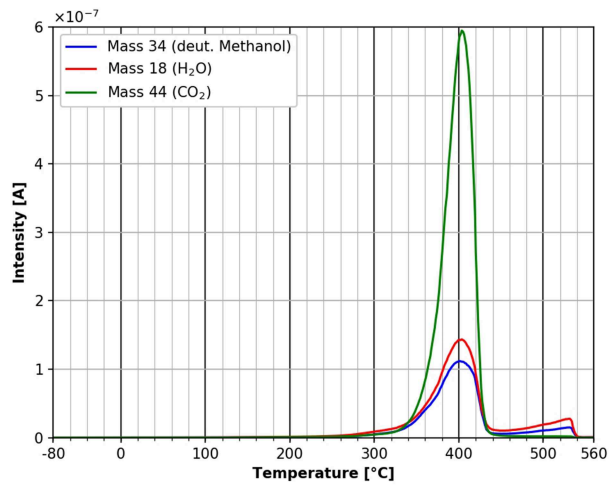

FIGURE 10 | Desorption of deuterated methanol (mass 34, blue), carbon dioxide (mass 44, green) and water (mass 18, red) in the temperature range between −80 and 560°C.

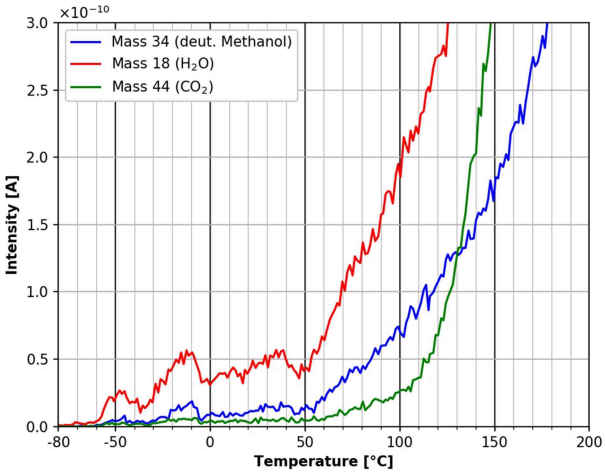

FIGURE 11 | Zoom into the desorption of deuterated methanol (mass 34, blue), carbon dioxide (mass 44, green) and water (mass 18, red) in the temperature range between −80 and 200°C.

57 from cellulose desorption/decomposition, which is not the case in the deuterated methanol desorption. All the mass 57 desorption takes place at lower temperatures and therefore lower adsorption energies are completely missing in the deuterated methanol case. Additionally, there seems to be a marked influence of the main adsorbed molecule on the adsorption of water and CO_2 from residual gas. The influence of the deuterated methanol on the cellulose film itself can be seen at the main peak at 400°C. In contrast to the n-decane case, there are no shoulders in the degradation/desorption peak after the adsorption of deuterated methanol. After adsorption of deuterated methanol, the small peak occurring at about 310°C after n-decane adsorption is missing, as well as the shoulders in the main desorption peak. We can also detect a small additional desorption of all three species at about 550°C, which was not seen after n-decane adsorption. Unfortunately, at this temperature an artifact of the copper sample holder cannot be ruled out completely.

The results presented in **Figures 9**, **10** show that the adsorption of polar molecules has a strong influence on the thin cellulose films, because the desorption spectra are significantly different.

Figure 11 shows the starting point of the TPD spectra after the adsorption of deuterated methanol in more detail. Water desorption starts at around −60°C. The fluctuations of the water desorption in this temperature range again is most likely due to small fluctuations in the linear heating rate. Interestingly, the desorption of deuterated methanol first starts at a temperature of about +40°C. This difference in desorption starting points between water and deuterated methanol can be attributed to different adsorption sites. Apparently, the methanol is more strongly bound to the cellulose film than the water. CO_2 desorption starts at about +60°C, marking the start of cellulose decomposition and desorption.

CONCLUSIONS

Within this study the adsorption and desorption of organic molecules on thin cellulose films was studied using temperature programmed desorption. It could be shown that the co-adsorption of water and CO_2 from the residual gas is also influenced by the adsorbed molecules. All species have a marked influence on the decomposition/desorption of the cellulose films. From the results presented here, it becomes clear that both non-polar and polar molecules adsorb readily

on a cellulose surface, with the polar molecule showing a higher binding energy.

Deuterated methanol shows a desorption peak at about 400°C and in the same temperature range cellulose desorption/decomposition takes place. As the adsorbed species desorb in the same range as the cellulose film the adsorption energy might actually be higher than the approximated 180 kJ/mol obtained from the Redhead equation.

In the future we plan to investigate different molecules as well as the possible influence of the cellulose film thickness on the adsorption and desorption of organic molecules.

AUTHOR CONTRIBUTIONS

EH planned and built the vacuum chamber and made experiments. VH conducted initial experiments. JA conducted initial experiments. RS had the idea of the research, of the vacuum chamber setup, and supervised the students.

ACKNOWLEDGMENTS

This work has been supported by the Christian Doppler Society, Austria. The financial support of the Austrian Federal Ministry for Digital and Economic Affairs and the National Foundation for Research, Technology and Development, Austria is gratefully acknowledged.

SUPPLEMENTARY MATERIAL

The Supplementary Material for this article can be found online at: https://www.frontiersin.org/articles/10.3389/fmats.2019.00178/full#supplementary-material

REFERENCES

Carruth, G. F., and Kobayashi, R. (1973). Vapor pressure of normal paraffins ethane through n-decane from their triple points to about 10 mm mercury. *J Chem Eng Data*. 18, 115–126. doi: 10.1021/je60057a009

Chen, P., Nishiyama, Y., Wohlert, J., Lu, A., Mazeau, K., and Ismail, A. E. (2017). Translational entropy and dispersion energy jointly drive the adsorption of urea to cellulose. *J. Phys. Chem. B* 121, 2244–2251. doi: 10.1021/acs.jpcb.6b11914

Djak, M., Gilli, E., Kontturi, E., and Schennach, R. (2011). Thickness dependence of reflection-absorption infrared spectra of supported thin polymer films. *Macromolecules* 44, 1775–1778. doi: 10.1021/ma102905v

Ganser, C., Hirn, U., Rohm, S., Schennach, R., and Teichert, C. (2014). AFM nanoindentation of pulp fibers and thin cellulose films at varying relative humidity. *Holzforschung* 68, 53–60. doi: 10.1515/hf-2013-0014

Ganser, C., Niegelhell, K., Czibula, C., Chemelli, A., Teichert, C., Schennach, R., et al. (2016). Topography effects in AFM force mapping experiments on xylan-decorated cellulose thin films. *Holzforschung* 70, 1115–1123. doi: 10.1515/hf-2016-0023

Hakalahti, M., Faustini, M., Boissiere, C., Kontturi, E., and Tammelin, T. (2017). Interfacial mechanisms of water vapor sorption into cellulose nanofibril films as revealed by quantitative models. *Biomacromolecules* 18, 2951–2958. doi: 10.1021/acs.biomac.7b00890

Hohenegger, M., Bechtold, E., and Schennach, R. (1998). Coadsorption of oxygen and chlorine on Pt(111). *Surf. Sci.* 412/413, 184–191.

Hoja, J., Maurer, R. J., and Sax, A. F. (2014). Adsorption of glucose, cellobiose, and cellotetraose onto cellulose model surfaces. *J Phys. Chemistry B* 118, 9017–9027. doi: 10.1021/jp5025685

Kontturi, E., Thüne, P. C., and Niemantsverdriet, J. W. (2003). Novel method for preparing cellulose model surfaces by spin coating. *Polymer* 44, 3621–3625. doi: 10.1016/S0032-3861(03)00283-0

Li, H., Du, Y., and Xu, Y. (2003). Adsorption and complexation of chitosan wet-end additives in papermaking systems. *J Appl Polymer Sci.* 91, 2642–2648. doi: 10.1002/app.13444

Lombardo, S., and Thielemans, W. (2019). Thermodynamics of adsorption on nanocellulose surfaces. *Cellulose* 26, 249–279. doi: 10.1007/s10570-018-02239-2

Majer, V., and Scoboda, V. (1985). Enthalpies of vaporization of organic compounds: a critical review and data compilation. *Blackwell Sci. Publications*. 1985:300.

Mazeau, K., and Vergelati, C. (2002). Atomistic Modeling of the Adsorption of benzophenone onto cellulosic surfaces. *Langmuir* 18, 1919–1927. doi: 10.1021/la010792q

Mazeau, K., and Wyszomirski, M. (2012). Modelling of Congo red adsorption on the hydrophobic surface of cellulose using molecular dynamics. *Cellulose* 19, 1495–1506. doi: 10.1007/s10570-012-9757-6

Neumann, R. D., Berg, J. M., and Claesson, P. M. (2018). Direct measurement of surface forces in papermaking and paper coating systems. *Nordic Pulp Paper Res. J.* 8, 96–104. doi: 10.3183/npprj-1993-08-01-p096-104

Niinivaara, E., Faustini, M., Tammelin, T., and Kontturi, E. (2015). Water vapor uptake of ultrathin films of biologically derived nanocrystals: quantitative assessment with quartz crystal microbalance and spectroscopic ellipsometry. *Langmuir* 31, 12170–12176. doi: 10.1021/acs.langmuir.5b01763

Niinivaara, E., Faustini, M., Tammelin, T., and Kontturi, E. (2016). Mimicking the humidity response of the plant cell wall by using two-dimensional systems: the critical role of amorphous and crystalline polysaccharides. *Langmuir* 32, 2032–2040. doi: 10.1021/acs.langmuir.5b04264

Perez, D. D. S., Ruggiero, R., Morais, L. C., Machado, A. E. H., and Mazeau, K. (2004). Theoretical and experimental studies on the adsorption of aromatic compounds onto cellulose. *Langmuir* 20, 3151–3158. doi: 10.1021/la0357817

Redhead, P. A. (1962). Thermal desorption of gases. *Vacuum* 12, 203–211, doi: 10.1016/0042-207X(62)90978-8

Rohm, S., Hirn, U., Ganser, C., Teichert, C., and Schennach, R. (2014). Thin cellulose films as a model system for paper fibre bonds. *Cellulose* 21, 237–249. doi: 10.1007/s10570-013-0098-x

Somorjai, G. A. (1981). *Chemistry in Two Dimensions: Surfaces*. Ithaca, NY: Cornell University Press.

Tozuka, Y., Tashiro, E., Yonemochi, E., Oguchi, T., and Yamamoto, K. (2002). Solid-state fluorescence study of naphthalene adsorptionon porous material. *J. Colloid Interface Sci.* 248, 239–243. doi: 10.1006/jcis.2001.8142

Tozuka, Y., Yonemochi, E., Oguchi, T., and Yamamoto, K. (1998). Fluorometric studies of pyrene adsorptionon porous crystalline cellulose. *J Colloid Interface Sci.* 205, 510–515.

Voisin, H., Bergström, L., Liu, P., and Mathew, A. P. (2017). Nanocellulose-based materials for water purification. *Nanomaterials* 7:57. doi: 10.3390/nano7030057

Xie, Y., Hill, C. A. S., Jalaludin, Z., and Sun, D. (2011). The water vapour sorption behaviour of three celluloses: analysis using parallel exponential kinetics and interpretation using the Kelvin-Voigt viscoelastic model. *Cellulose* 18, 517–530. doi: 10.1007/s10570-011-9512-4

Conflict of Interest Statement: The authors declare that the research was conducted in the absence of any commercial or financial relationships that could be construed as a potential conflict of interest.

frontiers in Chemistry

REVIEW
published: 30 July 2019
doi: 10.3389/fchem.2019.00535

Cellulose Nano-Films as Bio-Interfaces

Vikram Singh Raghuwanshi and Gil Garnier**

Bioresource Processing Research Institute of Australia (BioPRIA), Monash University, Clayton, VIC, Australia

Cellulose, the most abundant polymer on earth, has enormous potential in developing bio-friendly, and sustainable technological products. In particular, cellulose films of nanoscale thickness (1–100 nm) are transparent, smooth (roughness <1 nm), and provide a large surface area interface for biomolecules immobilization and interactions. These attractive film properties create many possibilities for both fundamental studies and applications, especially in the biomedical field. The three liable—OH groups on the monomeric unit of the cellulose chain provide schemes to chemically modify the cellulose interface and engineer its properties. Here, the cellulose thin film serves as a substrate for biomolecules interactions and acts as a support for bio-diagnostics. This review focuses on the challenges and opportunities provided by engineering cellulose thin films for controlling biomolecules interactions. The first part reviews the methods for preparing cellulose thin films. These are by dispersing or dissolving pure cellulose or cellulose derivatives in a solvent to coat a substrate using the spin coating, Langmuir-Blodgett, or Langmuir-Schaefer method. It is shown how different cellulose sources, preparation, and coating methods and substrate surface pre-treatment affect the film thickness, roughness, morphology, crystallinity, swelling in water, and homogeneity. The second part analyses the bio-macromolecules interactions with the cellulose thin film interfaces. Biomolecules, such as antibodies and enzymes, are adsorbed at the cellulose-liquid interface, and analyzed dry and wet. This highlights the effect of film surface morphology, thickness, crystallinity, water intake capacity, and surface pre-treatment on biomolecule adsorption, conformation, coverage, longevity, and activity. Advance characterization of cellulose thin film interface morphology and adsorbed biomolecules interactions are next reviewed. X-ray and neutron scattering/reflectivity combined with atomic force microscopy (AFM), quartz crystal microbalance (QCM), microscopy, and ellipsometer allow visualizing, and quantifying the structural morphology of cellulose-biomolecule interphase and the respective biomolecules conformations, kinetics, and sorption mechanisms. This review provides a novel insight on the advantages and challenges of engineering cellulose thin films for biomedical applications. This is to foster the exploration at the molecular level of the interaction mechanisms between a cellulose interface and adsorbed biomolecules with respect to adsorbed molecules morphology, surface coverage, and quantity. This knowledge is to engineer a novel generation of efficient and functional biomedical devices.

Keywords: cellulose, thin film, biomolecule, interface, diagnostics, characterization

OPEN ACCESS

Edited by:
Stefan Spirk,
Graz University of Technology, Austria

Reviewed by:
Artur J. M. Valente,
University of Coimbra, Portugal
Tamilselvan Mohan,
University of Maribor, Slovenia

****Correspondence:***
Vikram Singh Raghuwanshi
vikram.raghuwanshi@monash.edu
Gil Garnier
gil.garnier@monash.edu

Specialty section:
This article was submitted to Polymer Chemistry, a section of the journal Frontiers in Chemistry

Received: *20 April 2019*
Accepted: *12 July 2019*
Published: *30 July 2019*

Citation:
Raghuwanshi VS and Garnier G (2019) Cellulose Nano-Films as Bio-Interfaces. Front. Chem. 7:535. doi: 10.3389/fchem.2019.00535

INTRODUCTION

This review presents the methods and characterization techniques to engineer and quantify the properties of thin and smooth cellulose nanofilms. These model bio-interfaces aim to characterize the bio-molecule morphology and interaction with cellulose for biomedical applications, especially as diagnostics.

Cellulose is the most abundant polymer on the planet with plants producing 180 billion ton per year by photosynthesis from the conversion of CO_2 and water. Cellulose has widely been used for 2 centuries in commodity and industrial products such as pulp and paper, textile, and coatings. Available on all the inhabited continents, cellulose is biodegradable, non-toxic, sustainable, easy to functionalize, wettable, and flexible (Atalla and Vanderhart, 1984; Habibi et al., 2010b). These properties make cellulose an attractive material for engineering advanced applications such as low-cost, biodegradable, and disposable biodiagnostics (Su et al., 2012; Arcot et al., 2015), point of care analytical devices (Cranston et al., 2010), and membranes (Sukma and Culfaz-Emecen, 2018) for separation (dialysis). Currently, the main biomedical applications of cellulose include biodiagnostics, such as blood typing (Guan et al., 2014; Li et al., 2014; Casals-Terre et al., 2018), and pregnancy tests (Halpern et al., 2008; Koczula and Gallotta, 2016), tissue engineering (Courtenay et al., 2018; Torgbo and Sukyai, 2018; Curvello et al., 2019), scaffolds (Novotna et al., 2013; Modulevsky et al., 2014; Demitri et al., 2016; Courtenay et al., 2017; O'donnell et al., 2018), eye care solutions (Vehige et al., 2003; Luchs, 2010; Nguyen and Latkany, 2011; Racic et al., 2019), coatings (Jimenez et al., 2017; Spera et al., 2017; Sharif Hossain et al., 2018), packaging (Czaja et al., 2007; Sunasee et al., 2016; Shaghaleh et al., 2018), and sensors (Zhu et al., 2014; Ummartyotin and Manuspiya, 2015; Chen et al., 2018).

Cellulose is a hierarchical material. Cellulose fibers from plants are made up of bundles regrouping smaller units of linear monomer chains (Dufresne, 2013). The chain consists of both crystalline and amorphous regions. The crystalline/amorphous phase ratio determines the water intake capacity of the cellulose structure (Kontturi et al., 2011a, 2013). Each cellulose monomeric unit has 3 liable -OH groups which allow cellulose interfaces to be functionalized easily.

The cellulose fiber bundles can be fibrillated to fibrils of nanoscale thickness and length (1–100 nm) by mechanical (Bhatnagar and Sain, 2005; Bandera et al., 2014; Menon et al., 2017), enzymatic (Hu et al., 2018; Narkpiban et al., 2019), or chemical treatment (Sacui et al., 2014; Syafri et al., 2018; Tibolla et al., 2018). The resulting cellulose nanofibers (CNF) are 20–100 nm thick and 1–2 μm long, while the cellulose nanocrystals (CNC) are 5–10 nm in diameter with length ranging between 30 and 100 nm (Xu et al., 2013; Kim et al., 2015; Blanco et al., 2018). Engineered materials from CNF and CNC show high mechanical strength, optical transparency, and thermal stability compared to their original bulk counterparts. Therefore, CNF and CNC are used to produce transparent sheets, hydrogels, and as nanoscale thin film coatings.

Most disposable bio-diagnostics are currently made of polyolefin materials. Their major drawbacks are not being biodegradable which leads to accumulation and environmental toxicity, poor wettability, and difficulty to functionalize. In the last decade, cellulose based papers have been used as substrate in bio-diagnostic to identify pathogens, and to quantify biomolecules interactions (Then and Garnier, 2013). Cellulose based bio-diagnostics are typically used as dipstick (Free et al., 1957; Hosseini et al., 2017), or microfluidics (Martinez et al., 2010; Uddin et al., 2019) to interact with biomolecules. In particular, cellulose paper for blood typing takes half a minute to provide direct evidence, and visual readout outcome of blood groups (Then et al., 2015). In a typical reaction, the blood antigens interact with the pre-adsorbed biomolecules at the cellulose paper interface.

The main challenge associated with using cellulose based paper bio-diagnostics is engineering functionalized surface interacting with the targeted biomolecule for a specific biomedical application. Another issue is to maintain biomolecules activity efficiency over time by preventing their premature aging upon adsorption and immobilization on a surface. Other drawbacks of paper are controlling the fiber mesh network, pore size, and fiber strength. These variables significantly affect diffusion and biomolecules loss in the fiber network, and its activity (Derikvand et al., 2016; Huang et al., 2017; Prathapan et al., 2018). Such challenges can be overcome by engineering cellulose nanoscale thin film as substrate for biomolecules immobilization.

Cellulose thin films 5–100 nm thick with a roughness <3 nm provide a large surface area for biomolecules to interact, and for interface functionalization. This large available surface allows biomolecules to interact, adsorb, and remain immobilized at high density, and hopefully under controlled morphology onto the cellulose interface (**Figure 1**).

Cellulose thin films can be prepared with cellulose fibers (CNF, CNC) from plants, and bacteria or by using cellulose derivatives. Different cellulose sources, preparation procedures and coating methods result in film of different morphologies, and crystallinity. Kontturi et al. (2006) reviewed a detailed procedure to prepare cellulose thin film. The formed cellulose film adhere directly or indirectly (pre modified surface) with the substrate by forming electrostatic, van der Waal or hydrophobic forces, and covalent bonds (Eriksson et al., 2007).

The properties of cellulose thin film interface can be optimize by: (i) functionalization of the interface by taking advantage of the 3 liable -OH groups per cellulose monomer, (ii) controlling the ratio of crystalline and amorphous phase (iii) controlling CNF/CNC assembly/organization using magnetic field (Sugiyama et al., 1992; Revol et al., 1994), shear alignment (Yoshiharu et al., 1997; Ebeling et al., 1999), and electric field alignment (Bordel et al., 2006), (iv) engineering different surface morphology, thickness, roughness, and topography.

The interface functionalization leads to specific binding of targeted biomolecules. The controlled crystalline/amorphous phase ratio provides different film swelling behavior which is useful to optimize the liquid content in films (Aulin et al., 2009). The advantage of anisotropically ordered cellulose fiber thin film or anisotropic film surface morphology is the directional

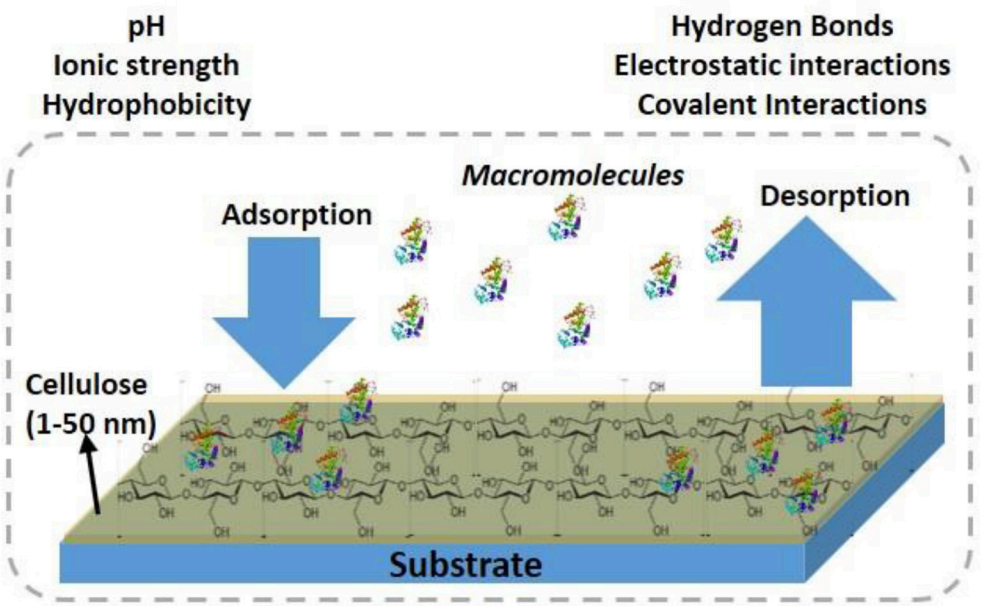

FIGURE 1 | Schematic of antibodies adsorption/desorption at the cellulosic thin film interface.

distribution and functionality of the adsorbed biomolecules (Prathapan et al., 2018).

This review focuses on the preparation, characterization and the biomedical applications of cellulose thin film interfaces. It provides insight on the best procedures for the consistent preparation of cellulose thin film of controlled structure and morphology. Further it highlights on optimization of film interface properties by surface functionalization. We hope this review will provide the foundation to researchers from academics and industries for developing better biodiagnostics, sensors, coatings, and substrates.

CELLULOSE FILM FORMATION

There are two general approaches used to prepare thin cellulose films; these rely on coating a dissolved cellulose derivative solution or a dispersed suspension of cellulose nanofibers (CNF), or cellulose nanocrystal (CNC) onto a surface. The prepared suspension is coated directly onto an interface or indirectly onto a chemically pre-modified substrate. The cellulose derivative coating requires regeneration into pure cellulose by chemical cleaving and substituting the derivative groups for hydroxyls. Dispersed or modified CNF/CNC coatings do not require a post treatment chemical conversion into cellulose. A chemically pre-modified substrate interface is used to control the adhesion and surface coverage of cellulose film by forming electrostatic, hydrogen or covalent bonds.

Different coating methods exist to cast smooth and uniform cellulose thin films (5–100 nm) on a substrate. These methods include spin coating (SC) (Emslie et al., 1958; Larson and Rehg, 1997; Kontturi et al., 2007), Langmuir-Schaefer (LS) (Aulin et al., 2009; Basavaraja et al., 2011), and Langmuir Blodgett (LB) (Sakakibara et al., 2006; Cohen-Atiya et al., 2007). In SC, a cellulose derivative or a cellulose suspension is applied over a flat substrate followed by substrate spinning at a controlled velocity. This produces smooth, homogenous thin films rapidly (in less than a minute). However, SC requires a flat solid substrate. A large amount of material is wasted during spinning, which needs a fast evaporating organic solvent to produce a good quality film. The solvent evaporation rate and the suspension spreading over the substrate during spinning define the film thickness and its homogeneity.

In LB and LS methods, a cellulose monolayer phase is first formed at the liquid/air interface. The resulting cellulose monolayer is either transferred to a vertically submerged solid substrate forming LB films or onto a horizontally emerged substrate forming LS films, as shown in **Figure 2** (Rubinger et al., 2006). However, the deposited films are slow to fabricate and require quick drying in a clean room to prevent impurities deposition. The LB and LS methods have produced nice cellulose films used in many classical studies but they retain some challenging inherent issues.

While cellulose films present many advantages, there are challenges in depositing, and characterizing the cellulose film interface. A first challenge is the dissolution of cellulose or cellulose derivatives in a proper solvent to easily coat a substrate. Acetone and toluene are good volatile solvents for cellulosic solutions, as they evaporate sufficiently fast to produce smooth, and homogeneous films. Cellulose can also be dissolved homogeneously in ionic liquids (IL) but their low vapor pressure hinder coating of smooth and homogenous films (Raghuwanshi et al., 2018). The pure cellulose regeneration process using acid

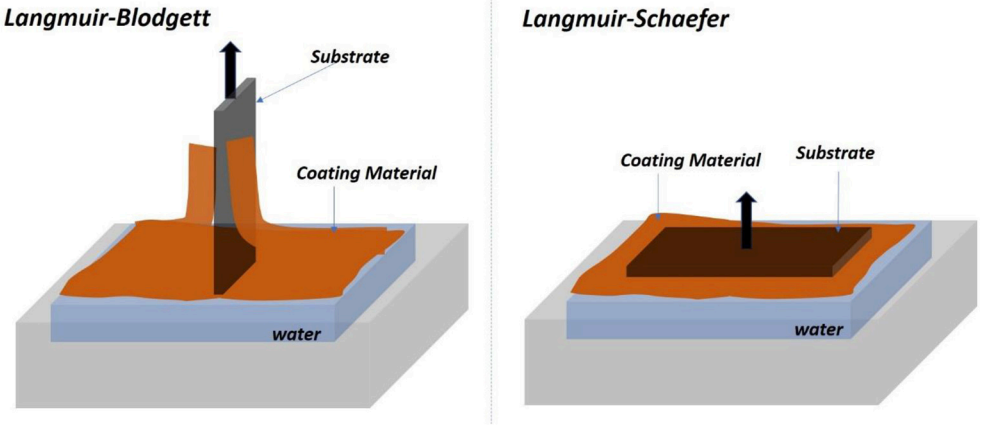

FIGURE 2 | Schematic of the Langmuir-Blodgett **(Left)** and Langmuir-Schaefer **(Right)** set of forming film from the air/water interface.

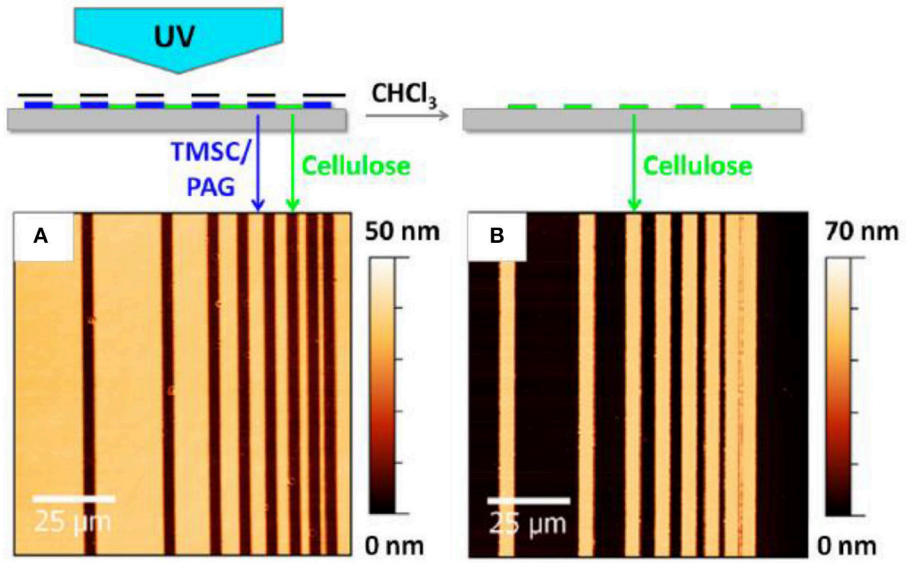

FIGURE 3 | Atomic force microscope image of the cellulose thin before **(A)** and after **(B)** regeneration. Reproduced with permission from Wolfberger et al. (2014).

hydrolysis for removing the unwanted derivatives also affect film quality by increasing roughness.

A second challenge in the cellulose film preparation is the formation of cellulose aggregates over the substrate which produces rough and heterogeneous distribution of cellulose at the interface. A homogenous cellulose suspension with a fast drying process are required to hinder the formation of cellulose fibers or crystal aggregates.

Another issue is the chemical modification of CNF, CNC, or the substrate surface is often required for adhering cellulose chains at high surface coverage. The chemical modification might bring toxicity, and add impurities at the interface, affecting surface properties, and biomolecules interaction with cellulose. The interaction between cellulose and modifier polymer depends on the polymer type, functional groups, charge density, and molecular weight (Wagberg, 2000; Ahola et al., 2008).

Films From Cellulose Derivatives

Trimethylsilyl cellulose (TMSC) is a preferred cellulose derivative for cellulose thin films (Klebe and Finkbeiner, 1969; Cooper et al., 1981; Heinze et al., 2018). Dissolving TMSC in toluene and coating on a substrate (silicon, gold coated) results in thin and homogeneous TMSC films. Exposing the TMSC film surface to HCl acid vapor for 10–15 min substitutes the trimethylsilyl (TMS) groups into hydroxyl groups, regenerating a pure cellulose film (Mohan et al., 2014).

The degree of substitution (DS) is defined as the average number of hydroxyl group per anydroglucosidic unit (3) that has been chemically reacted. It determines the extent of chemical

functionalization for cellulose derivatives (Samaranayake and Glasser, 1993). Full derivatization of cellulose into TMSC with a DS 3 is an easy reaction to proceed and to control, which results in a derivative fully soluble into tetrahydrofuran (THF). By contrast, cellulose acetate of DS = 2 is required for full solubility into acetone; interrupting the reaction midway or hydrolyzing cellulose triacetate back to cellulose diacetate (DS = 2) are reactions more challenging to control.

The neutron reflectivity and AFM measurements of the TMSC based cellulose films indicate the formation of a 20 nm thick film with a roughness of 0.5 nm. The measured volume fraction of cellulose in the film is about 80% (Kontturi et al., 2011b). Grazing incidence X-ray diffraction (GI-XRD) measurement shows the film to be amorphous with little traces of cellulose II and III crystallites. The film thickness, roughness, and crystallinity remain unchanged during the swelling and drying process.

Sprik et al. reported a photo regeneration of cellulose film obtained from spin coating a TMSC solution onto a silica substrate (Wolfberger et al., 2014). TMSC was dissolved at 1 wt% in a chloroform solution containing 2 wt% of *n*-Hydroxynaphtalimide triflate (NHT). The formed TMSC derivative films are 60 nm thick. Upon exposing the film surface to ultra-violet (UV) ($\lambda < 400$ nm) for 10 min, the NHT produces triflic acid (CF_3SO_3H) which regenerates TMSC films into cellulose by substituting the trimethylsilyl group for hydroxyls. The Fourier transform infra-red (FTIR) spectra confirmed removal of the Si-O-C band. The presence of NHT does not affect the quality and properties of the cellulose film which is about 60–70 nm thick as measured by atomic force microscopy (AFM) (**Figure 3**). This is the finest resolution of cellulose patterns achieved.

The TMSC based cellulose films were used to make structured pattern (Mohan et al., 2013; Niegelhell et al., 2016). Rupert Kargl et al. prepared the cellulose pattering by pressing the cellulose thin film (regenerated from spin coated TMSC film) on a glass slide supporting the polydimethylsiloxane (PDMS) microchannel mold. Immediately after pressing, the microchannel were filled with the enzyme cellulase. The cellulose area exposed to cellulase was digested while the non-exposed part creates a pattern. In a second method, the TMSC film was covered with an aluminum mask with a 16 squared pattern holes. The film was exposed to HCl for regeneration into cellulose followed by cellulase exposure to remove the regenerated cellulose. Upon removing aluminum mask, the substrate surface retained the pattern of TMSC film which was finally regenerated to cellulose by acid hydrolysis (Kargl et al., 2013; Bracic et al., 2014).

Orelema et al. made cellulose films from a TMSC solution using the LS method on a polystyrene precoated gold interface (Orelma et al., 2011). The desilylation in acid vapor regenerated cellulose into films 18 nm thick and of 0.5 nm roughness with 53% crystallinity. Schaub et al. produced cellulose ultra-thin films from TMSC multilayers (Schaub et al., 1993). TMSC was prepared by reacting cellulose in dimethylacetamide/lithium chloride with hexamethyldisilazane solvent. The synthesized TMSC in *n*-hexane was spread on the water surface to form TMSC multilayers onto the silicon substrate using the LB method. X-ray reflectivity on 22 multilayers of TMSC film revealed a thickness of 19.7 nm and a roughness of 0.5 nm (**Figure 4**). Exposing a multilayer film to 10% HCl vapor for 30 s cleaves the TMS side groups and regenerates cellulose film 7.8 nm thick with roughness of 0.8 nm. Infra-red spectroscopy confirmed the removal of TMS side group as the characteristic Si-CH_3, and Si-O-C vibration bands disappeared.

Cellulose thin films were also made by spin coating on a silicon substrate a solution of cellulose acetate (DS = 2) dissolved in acetone (Su et al., 2015). The acetone evaporates quickly to form a homogenous hydrophobic cellulose acetate layer on the substrate. The cellulose film was regenerated by exposing the coated cellulose acetate film to methanol-sodium methoxide (1:50) for 12 h. AFM surface analysis showed different film surface morphology before and after regeneration. AFM combined with X-ray and neutron reflectivity revealed films to be homogeneous, smooth, and 20 nm thick with a roughness <3 nm.

Films From Native Cellulose

Cellulose thin films can be prepared by dissolving native cellulose processed from pulp and bacteria sources. Su et al. dissolved bacterial cellulose [generated from Gluconacetobacter xylinus (Römling and Galperin, 2015)] in 1-butyl-3-methylimidazolium chloride ionic liquid (Su et al., 2016). The dissolved cellulose forms silane derivatives in solution. Later, the ionic liquid was replaced with toluene. The cellulose/toluene solution produced a smooth hydrophobic film upon spin coating on a silicon substrate. Pure cellulose film is regenerated by exposing the derivative film interface to HCl vapors for 5 min which cleaves the silane derivative groups and regenerates the hydroxyl groups. Attenuated total reflectance FTIR (ATR-FTIR) confirms the substitution of all silane groups for hydroxyls (Su et al., 2016; Raghuwanshi et al., 2017b).

AFM and neutron reflectivity measurements indicate the formation of smooth and homogeneous cellulose films, about 10 nm thick with roughness <2 nm (**Figure 5**). The film swells to 2–3 times its original thickness (up to 30 nm) and revealed an absorbed water content of 70%.

Deuterated cellulose thin films of different deuteration levels were produced by dissolving deuterated bacterial cellulose (DBC). The bacterial cellulose grown in the D_2O water environment lead to the formation of DBC, replacing all the -OH and -CH with -OD and -CD groups. The deuterating cellulose thin film interface provides significant neutron scattering length difference (SLD or contrast) between cellulose and adsorbed biomolecules. This greatly helps in visualizing and quantifying the adsorbed biomolecules at the cellulose interface (Raghuwanshi et al., 2017a).

Microcrystalline cellulose (MCC) dissolved in dimethylacetamide and lithium chloride (DMAc/LiCl) was spin coated onto silica substrates precoated with cationic polyacrylamide (CPAM) (Eriksson et al., 2005). Rinsing with the Milli-Q water and heating for 1 h at 150°C produces a cellulose film strongly adhering to the substrate. The CPAM precoating enhances the adhesion of cellulose thin film at the substrate. Ellipsometer and AFM investigations show the cellulose film to be 30 nm thick with a RMS roughness of 5 nm. The film is

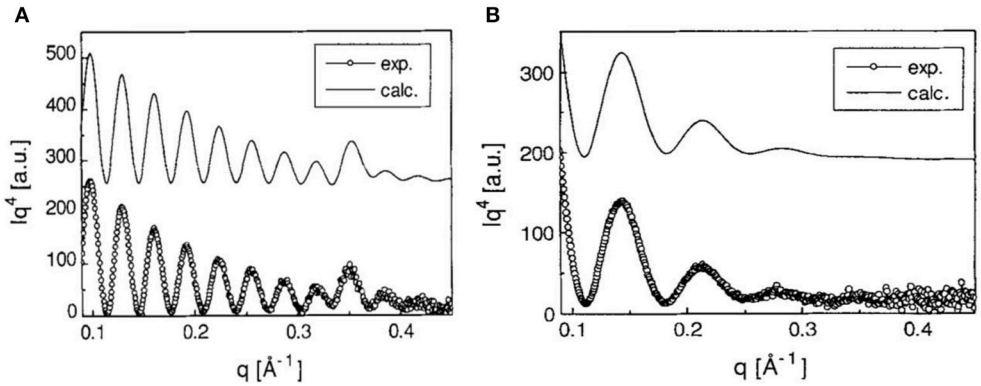

FIGURE 4 | (A) X-ray reflectivity curves of multilayers of TMSC films at the Si substrate. **(B)** X-ray reflectivity curves are from the cellulose thin film regenerated from TMSC by HCl acid hydrolysis. Dotted are the experimental curves and solid line are the modeling curves. Reproduced with permission from Schaub et al. (1993).

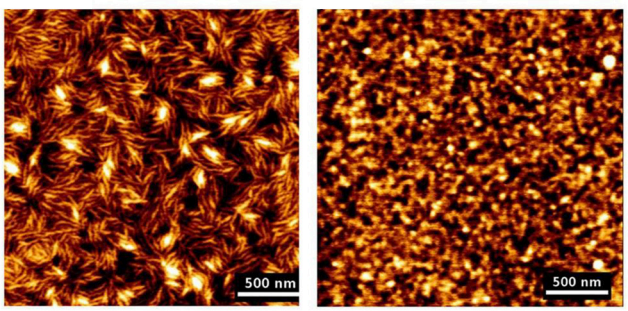

FIGURE 5 | (A) AFM image of the deuterated bacterial cellulose (DBC) film dissolved in the ionic liquid. **(B)** AFM image of the cellulose film regenerated from the DBC in the HCl acid hydrolysis. Reproduced with permission from Su et al. (2016).

isotropic, and free of solvents, and structure artifacts. In the aqueous media, the thin film swells to about 3 times its original dry thickness (up to 90 nm).

Cellulose nanofibers (CNF) and cellulose nanocrystals (CNC) suspensions can be coated onto a substrate. The coated film does not require any post cellulose regeneration process. As CNF and CNC are negatively charged, a surface pre-treatment (cationic) of the substrate is required. CNF films were produced by spin coating a 0.148 wt% CNF aqueous suspension onto silica and gold substrates (Ahola et al., 2008; Orelma et al., 2012). To increase the CNF coverage, 3-aminopropyltrimethoxysilane (APTS) was used as anchoring ligand for silica while polyvinyl amine (PVAm) was selected for gold substrate. Quartz crystal microbalance (QCM) and surface plasmon resonance (SPR) results show the anchoring substances to have no effect on the CNF film properties.

CNC has a low aspect ratio (diameter 5–10 nm, length 30–100 nm) compared to CNF (diameter 30–100 nm, length 1–2 μm). Prathapan et al. spin coated a CNC layer on a uniaxially stretched polydimethylsiloxane (PDMS) precoated with poly(ethylene oxide) (PEO) (Prathapan et al., 2018). The uniaxially stretched PDMS created a surface with well-aligned grooves and low roughness. The CNC coating was transferred (wet stamped) to the poly (amino amide) epichlorohydrin (PAE)-coated glass substrate. The transferred PAE-CNC layer was heated at 105°C for 5 min which initiates covalent interactions between PAE and CNC, and creates strongly adhesion onto the glass substrate. The films formed are transparent and AFM image analysis reveals the CNC coating to be 35 nm thick layer with a RMS roughness of 5 nm. These CNC films do not swell in aqueous environments which reduces the diffusion of adsorbed biomolecules into the film structure. This technique produces patterned strips of CNC crystals 50 nm wide, 100 to 200 nm thick and of variable, and controlled periodicity ranging from 450 to 670 nm.

Eriksson et al. compared CNF and CNC films prepared by spin coating using 3 different procedures (Eriksson et al., 2007). The films showed different crystallinity ratio, morphology, and quality varying upon preparation procedure. First, CNC films were prepared by spin coating colloidal CNC suspension on a polyvinylamine (PVAm) pre-coated silicon wafers (Eriksson et al., 2007). Heat treatment at 90°C for 4 h removed the sulfur impurities from the film. Ellipsometry and XRD revealed the film to be 120 nm thick and made of cellulose I phase (Edgar and Gray, 2003; Eriksson et al., 2007).

Second, cellulose films were made by dissolving cellulose pulp in *n*-methylmorpholine *n*-oxide (NMMO), and dimethylsulfoxide (DMSO) followed by spin coating the cellulose suspension on a precoated PVAm silicon wafer. Ellipsometer showed the film to be 30 nm thick. XRD revealed the formation of a cellulose II phase with 50% crystallinity (Gunnars et al., 2002; Falt et al., 2004). In the third procedure, the cellulose film was produced by dissolving pulp in a water-methanol solution. Later, the suspension was solvent exchanged with dimethylacetamide (DMAc), and mixed with a 110°C pre-heated DMAc/LiCl suspension. The cooled clear suspension was spin coated onto the pre-coated cationic PVAm silicon wafers. The final films were obtained by washing the film surface with Milli-Q water to remove any excess LiCl. Ellipsometry showed

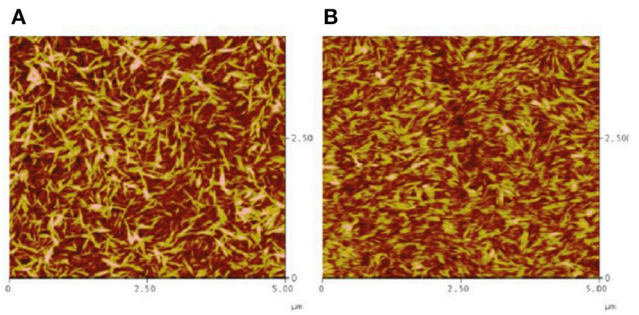

FIGURE 6 | AFM height images of LS films of CNC transferred at different surface pressures, **(A)** 45 mN/m and **(B)** 60 mN/m. Reproduced with permission from Habibi et al. (2010a).

the formation of an amorphous cellulose phase 44 nm thick (Berthold et al., 2004).

Habibi et al. created cellulose films by depositing CNC onto a thiolated gold coated substrate using the LS method (Habibi et al., 2010a). A cationic surfactant dioctadecyldimethylammonium bromide, (DODA)-Br was used as an intermediate for the adsorption/adhesion of negatively charged CNC onto the negatively charged gold substrate. In the film preparation, DODA was spread over the aqueous suspension of CNC placed in a Langmuir trough equipped with a Wilhelmy film balance. After stabilization, the surface pressure was created by reducing the distance between the trough. The DODA/gold substrate was contacted horizontally with the compressed surface to generate the CNC-DODA film.

AFM and ellipsometry revealed the formation of a 10 nm thick CNC film having an average roughness of 3.7 nm. The films are stable, smooth, and strongly attached to the gold/DODA interface. Interestingly, AFM images showed that the CNC transferred to the gold/DODA at 45 mN/m pressure led the formation of an isotropic randomly distributed structure of the CNC-DODA complex. However, at even higher surface pressure (60 mN/m), the CNC-DODA complex transit into more ordered nematic anisotropic structures (**Figure 6**). XPS measurements of films clearly showed the carbon and oxygen peaks correspond to the pure cellulose structure. Other C-H, C-O, and sulfur XPS peaks resemble the presence of DODA and the thiol group at the gold interface. Compelling and detailed morphology quantification of cellulose phase transitions in thin films reported in literature are rare.

Habibi used the same procedure to make cellulose films with the LB method (Habibi et al., 2007). In contrast to the LS films, the film interface was rinsed with chloroform, and NaOH after the film deposition to remove the adsorbed DODA and sulfur groups. Ellipsometry and AFM measurements showed the formation of a 10 nm thick CNC-DODA film before rinsing. After chloroform rinsing, the film thickness reduced to 9.2 nm indicating removal of the 0.8–1 nm thick DODA layer. The rinsed film roughness was about 3 nm. XPS investigation showed the presence of 4 kinds of bonds: C-O, C-H, C-C, and O-C-O. The C-O bonds correspond to the cellulose structure while the C-C bond (without O) corresponds to the DODA group. The XPS spectra clearly indicate the removal of any DODA traces after washing with chloroform and NaOH (**Figure 7**). Both LB and LS film preparation techniques produced smooth and stable thin film interfaces useful for biomolecules interactions.

CELLULOSE FILM CHARACTERIZATION

Characterization of nano scale thick cellulose films is a challenging task (Foster et al., 2018). The characterization of cellulose thin film includes quantification of composition, swelling, morphology, homogeneity, thickness, and roughness. Only a few characterization methods can measure thickness, roughness, and composition of coated films (Wenzel et al., 2005; Kassavetis et al., 2012). In many cases, the information/signals from the base substrate dominates the required characteristics from the film interface. This is due to the low volume fraction of film producing less signals compared to the dominating substrate signals.

X-ray/neutron reflectivity is a non-destructive method which determines the film thickness, roughness, and composition (Russell, 1990; Daillant and Gibaud, 2009). However, a pre-knowledge and extensive scattering curve modeling is required to extract relevant information. Swelling behavior of cellulose thin film spin coated at the silicon substrate was revealed by monitoring variations in film thickness by neutron reflectivity (Cheng et al., 2011; Raghuwanshi et al., 2017a). The cellulose film swells by 2–3 times its initial thickness of 8–10 nm. Furthermore, neutrons are sensitive to the large scattering length density (SLD) of hydrogen (H) and deuterium (D) (Shu et al., 2000; Ashkar et al., 2018). This difference can be exploited to visualize and quantify the biomolecules adsorbed at the cellulose thin film interface. Su et al. produced deuterated cellulose thin film from deuterated bacterial cellulose in which the liable –CH and -OH groups of the cellulose thin film were replaced by –CD and –OD groups. The deuterated cellulose interface provided significant SLD difference (contrast) between cellulose and adsorbed biomolecules (IgG and HRP) (Su et al., 2016). NR revealed the IgG layer to be adsorbed in the standing conformation, to have a thickness of 12.6 nm, a volume fraction of 15–20% and a surface coverage of 2.5 mg/m^2 (Raghuwanshi et al., 2017a).

Ellipsometer is another non-destructive scattering method to measure film thickness by evaluating the refractive index of the film (Barth and Keilmann, 1993; Tompkins and Irene, 2005). Karabiyik et al. used ellipsometer to determine the refractive index (RI) of thin films of TMSC (RI: 1.46), regenerated cellulose (RI: 1.51), and cellulose nanocrystals (RI:1.51) (Karabiyik et al., 2009). The PVAm-NFC bilayer thickness on a PDMS substrate was measured to be 2.2 nm and the refractive index in the range 1.56–1.52 was measured by variable angle (50–70°) spectroscopic ellipsometer. The layer was modeled with the Cauchy model (Eita et al., 2011).

Atomic force microscopy (AFM) is a powerful method to quantify surface morphology, film thickness, and roughness of cellulose nanoscale thin films (Dufrêne, 2002; Lahiji et al., 2010).

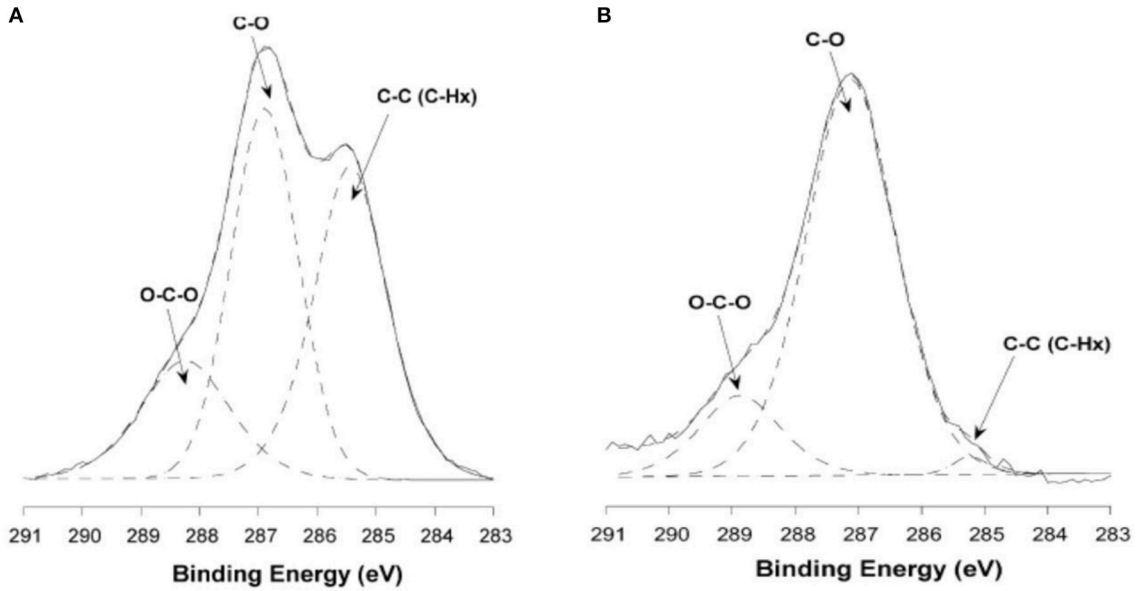

FIGURE 7 | X-ray photoelectron carbon spectra of untreated **(A)** and washed ramie **(B)** cellulose nanocrystalline films. Reproduced with permission from Habibi et al. (2007).

A cantilever is scanned continuously or tapped over the film surface; it measures surface forces in nano-newtons, and provides film surface topography within the resolution of 0.2 nm. Notley et al. used AFM to measure surface forces between cellulose thin films (120 nm thickness), and amorphous cellulose spheres (Notley and Wagberg, 2005; Notley et al., 2006). Tina Maver characterized regenerated cellulose thin film produced by TMSC on a silicon substrate. AFM image analysis revealed the TMSC spin coated film is 54 nm thick; after regeneration by acid, the film thickness decreased to 19 nm (Maver et al., 2015). Tammelin et al. used AFM to differentiate the surface morphology of the cellulose thin films (thickness 33 nm) prepared by LS and SC methods (Tammelin et al., 2015). The LS method produces highly crystalline film with a RMS roughness of 0.5 nm while the SC method generates amorphous film with RMS roughness of 3.4 nm. The LS films are much smoother than the SC films which is clearly seen in the AFM images (**Figure 8**).

Fourier transform infra-red (FTIR) spectroscopy is a convenient technique to determine the different chemical functionalities present in the cellulose thin film by adsorption of IR radiation (Müller and Schmitt, 1997). For characterizing thin films of nanometer thickness, attenuated total reflectance FTIR (ATR-FTIR) is used. FTIR spectra indicate chemical bonds, functional groups and help in identifying organic molecular groups and compounds, side chains and cross links which correspond to the characteristic vibrational frequencies in the IR range.

ATR-FTIR investigation is used to track and confirm the generation process of TMSC films into cellulose film upon acid hydrolysis. **Figure 9** shows TMSC film before and after regeneration (Maver et al., 2015). TMSC film spectra show C-Si vibration at 844 and 1,253 cm^{-1}. In the regeneration process, the Si-C bond disappears confirming the removal of Si-C groups. Moreover, the appearance of –OH bonds at 3,351 cm^{-1} combined with other peaks (between 1,200 and 1,000 cm^{-1}) reveal a cellulose film. Su et al. performed ATR-FTIR on the deuterated cellulose thin film to confirm the replacement of the –CH groups of cellulose chain by –CD groups. ATR-FTIR showed the C-H stretching at 2,900 cm^{-1} from the hydrogenated

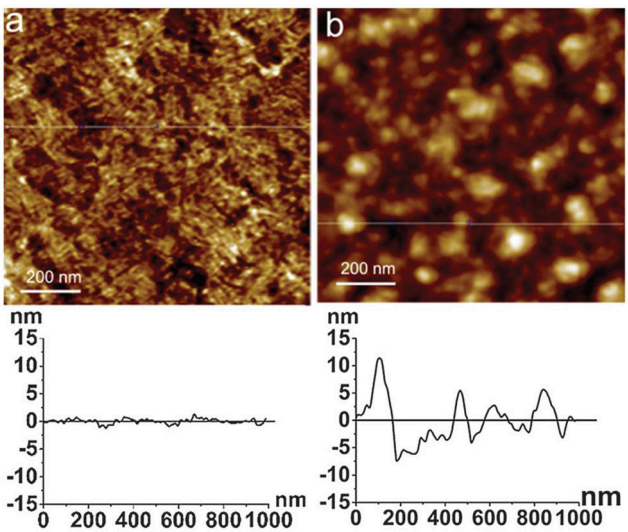

FIGURE 8 | AFM images and the corresponding surface profiles for **(a)** mostly crystalline cellulose film, **(b)** amorphous cellulose film on polystyrene coated gold substrates. The scan size is 1 mm^2 and the z-range is 15 nm. Reproduced with permission from Tammelin et al. (2015).

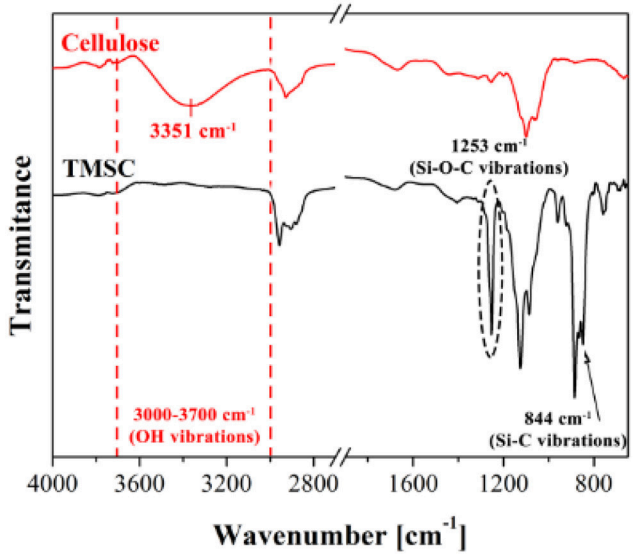

FIGURE 9 | ATR-FTIR spectra of cellulose and TMSC films showing different vibrational bonds. Reproduced with permission from Maver et al. (2015).

cellulose is shifted to 2,100 cm^{-1} which corresponds to the C-D stretching (Su et al., 2016).

Quartz crystal microbalance with dissipation (QCM-D) is a surface sensitive method to measure the variation in the cellulose thin film morphology and its interaction with the biomolecules in nanograms and in real time (Marx, 2003). The dissipation mode of the QCM-D reveals the rigidity of the adsorbed biomolecules layer at an interface (Turon et al., 2008). Raghuwanshi et al. characterized the adsorbed IgG layer at the cellulose thin film interface. They measured the adsorbed IgG layer to be 140 nm thick with a volume fraction of 25% and a surface coverage of 4 mg/m^2 (Raghuwanshi et al., 2017a).

Enzymatic digestion of cellulose thin film 24.2 nm thick was also monitored by QCM-D. Investigation showed the loss of 117 ng/cm^2 of cellulose from the sensor surface after 15 h of enzymatic treatment (Cheng et al., 2011). Kittle relied on QCM-D to investigate the equilibrium water content of cellulose films by solvent exchange (Kittle et al., 2011). QCM-D experiments were performed to compare the water content in films of regenerated cellulose (RC), sulfonated nanocrystalline cellulose (SNC), and desulfonated nanocrystalline cellulose (DNC). QCM-D showed the RC exhibit 5 water molecules per anhydroglucose unit, while both SNC, and DNC retained five time more water in the films. Tammelin et al. relied on QCM-D to characterize the swelling and water uptake/release behavior of amorphous and crystalline cellulose thin films (33 nm thick). QCM-D showed the crystalline films absorb more water than the amorphous cellulose film (**Figure 10**), where the mass change (ΔF) in the crystalline film are higher than for the amorphous film. The degree of swelling for the crystalline film is 72% compared to 4.8% for the amorphous film. QCM-D results indicate that the crystalline films have a nano-porosity structure and a higher surface area than the amorphous film which bind a large amount of water molecules (Tammelin et al., 2015).

X-ray photoelectron spectroscopy (XPS) is a quantitative method to determine the surface composition and impurities of the cellulose thin film interface (Johansson and Campbell, 2004). In XPS, the bombarded X-rays photons eject core, and valence band electrons from the film surface which are analyzed for the composition of the film (Swartz, 1973). XPS determined the composition of cellulose thin films prepared by dissolving microcrystalline cellulose in 50%wt water/*n*-methylmorpholine-n-Oxide (NMMO) at 115°C, and then coated onto silica and gold substrates. The cellulose film is anchored by polyvinylamine polymer. XPS spectra shows no peak from the nitrogen (400 eV) of NMMO which reveals the cellulose film to be solvent free. The carbon emission spectra of the XPS spectra shows the significant contribution from the bonded carbon atoms (O/C ratio is 0.85; O-C-O/C-O ratio is 0.22) in the cellulose film structure (Song et al., 2009).

Kontturi studied the hydrolysis of trimethylsilyl cellulose (TMSC) and its conversion in pure cellulose film by XPS (Kontturi et al., 2003). XPS survey spectra show the removal of the Si group upon the hydrolysis of TMSC film which reveals the cleaving of –SiO bonds (**Figure 11**). The detailed XPS carbon spectra of the TMSC film show the presence of O-C and O-C-O and C-Si bonds coming from the TMSC structure. The XPS carbon spectra after 5 min of HCl hydrolysis reveal the complete removal of the C-Si bond; and the O-C and O-C-O bonds corresponding to the cellulose remains.

CELLULOSE THIN FILM: SURFACE FUNCTIONALIZATION AND BIOMOLECULES INTERACTIONS

Engineering the specific and non-specific adsorption of biomolecules at the cellulosic film interface is critical in designing effective and biodegradable diagnostics and low-cost sensors. The negative surface charge of cellulose, with its 3 liable -OH groups (per monomer), can be used to modify the interface for specific biomolecules interaction, and functionality. Biomolecules interact with the cellulose film by forming physical and chemical bonds. The physical bonds are due to the van der Waal, ionic, and electrostatic interactions, and the chemical bonds are by covalent interactions.

Cellulose thin film of large surface/volume ratio, low porosity and able to form hydrogen bonds at the interface can overcome many challenges of bulk cellulose materials such as paper and textile. The limiting issues with bulk cellulose interacting with nanoscale biomolecules are their high water absorption, high roughness, and high porosity. The structure of paper and textile is also complex and presents heterogeneous morphologies. This means a high fraction of biomolecules disappears by absorption into the bulk of cellulose. Also, the biomolecules adsorb on the external surface into a plethora of conformations which can causes an important distribution of available functionalities and interaction with the molecules

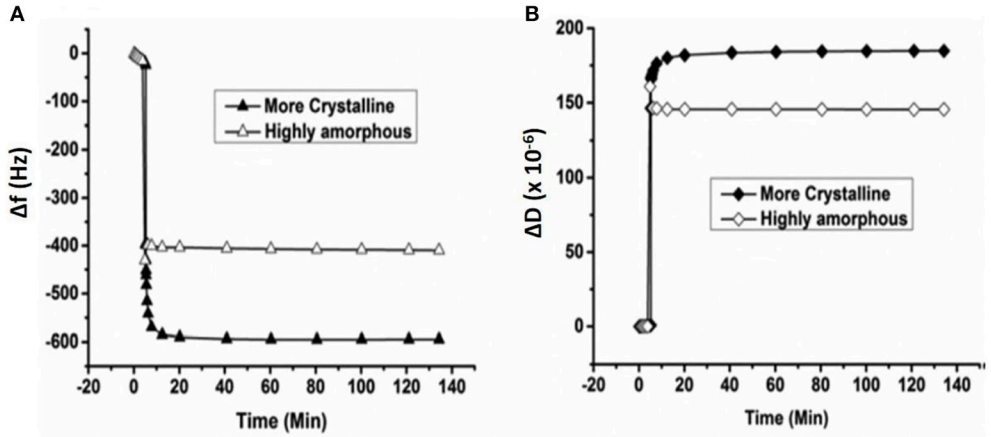

FIGURE 10 | QCM-D measurement of the water absorption in amorphous and crystalline cellulose using thin films. Change in frequency **(A)** and change in dissipation **(B)** as a function of time upon exposure to water for more crystalline and highly amorphous cellulose films. (f_0 = 5 MHz, n = 3, f_3/n). Reproduced with permission from Tammelin et al. (2015).

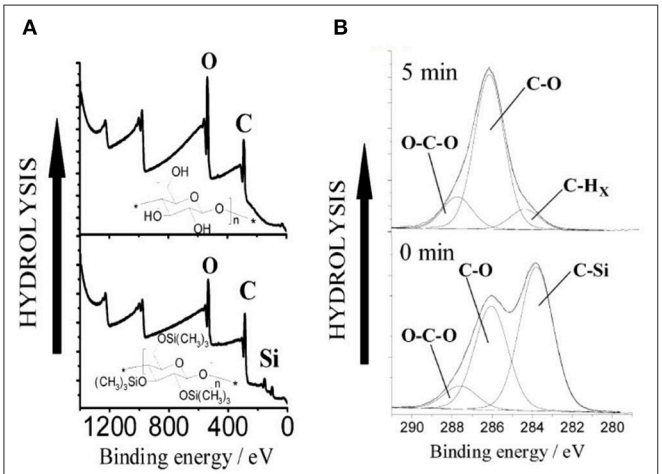

FIGURE 11 | (A) XPS wide scans from trimethylsilylcellulose (TMSC) and cellulose films hydrolyzed from TMSC with 2 M HCl for 1 min. **(B)** Hydrolysis of TMSC films with 0.5 M HCl followed with XPS. The carbon emission is resolved to contributions illustrating the decline of silicon bonded carbon from TMSC, as the hydrolysis proceeds. Reproduced with permission from Kontturi et al. (2003).

probed by paper/threads diagnostics. The low porosity of nanoscale thin films hinders the diffusion of biomolecules within the film structure as they remain at the interface for their specific functionality.

The essential requirements and characteristics of effective cellulose thin films to interact with nano sized biomolecules are:

(a) Controllable thickness in the nanometre range (1–200 nm) for films of large surface area.
(b) Smooth film interface of roughness lower than the biomolecule critical dimension (< 1 nm) for accurate size measurement and ensuring homogeneous biomolecules conformation.
(c) Low porosity for limited water intake capacity (if hydrophobic) for increased biomolecules longevity at the interface.
(d) An interface which is easy to functionalize to adsorb large amounts of specific biomolecules for selective activity with target molecules.
(e) Transparent and controllable wettability.

Mohan et al. studied the unspecific bovine serum albumin (BSA) adsorption at the cellulose interface with films modified with cationic cellulose derivatives: cellulose 4-([*nnn*-trimethylammonium] butyrate chlorides) with different degree of substitution (DS) of $NMe^{3+}Cl^{-}$ (Mohan et al., 2014). QCM-D (wet mass) combined with MP-SPR (dry mass) show 2 times higher adsorption of fluorescently labeled BSA molecules on the modified cellulose interface (BSA wet mass: 42 mg/m^2, Dry Mass: 3.9 mg/m^2) compared to the pure cellulose (BSA wet mass: 20 mg/m^2, Dry mass:1.6 mg/m^2) at pH 5.0. Higher BSA adsorption indicates higher amount of positive surface charges induced by the cationic cellulose derivative at the cellulose interface. However, the non-fluorescently labeled BSA molecules might show different mass adsorption and conformation at variable pH. The fluorescent labeling can alter the native conformation of BSA at a particular pH and result in a large BSA adsorption at an interface.

Eriksson et al. studied the degradation of 30 nm thick cellulose film exposed to active and inactive enzymes (Eriksson et al., 2005). Cellulases were adsorbed directly at the cellulose interface without any surface pre-modification. An inactive enzyme D10N was adsorbed at 3 mg/m^2, forming an enzyme monolayer 2.5 nm thick. However, no film degradation was observed by inactive enzymes as the mass over the substrate remained unchanged. In contrast, exposing the film surface to an active cellulase (GH45) embedded with carbohydrate-binding module (CBM) simultaneously starts adsorbing onto and degrading the film interface. The overall film mass first increases due to enzyme adsorption and later decreases as cellulose degrades. High

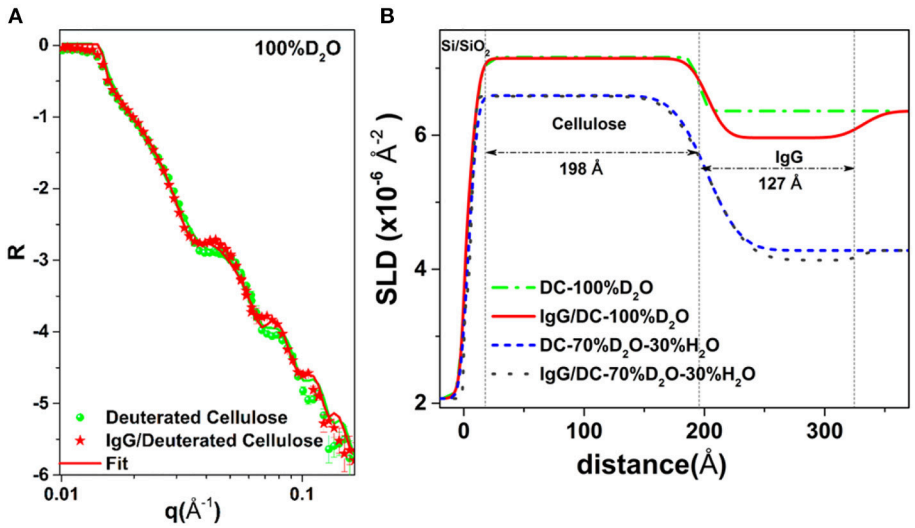

FIGURE 12 | (A) NR curves of deuterated cellulose and IgG adsorbed deuterated cellulose. **(B)** SLD profile with thickness from the substrate interface obtained by fitting the NR curves. Reproduced with permission from Raghuwanshi et al. (2017a).

enzyme concentration leads to large adsorption and faster film degradation. In the absence of CBM, no adsorption of active enzymes was observed on the film interface and no cellulose degradation occurred.

Raghuwanshi et al. adsorbed two types of biomolecules: an immunoglobulin G (IgG, antibody) and horseradish peroxidase (HRP, enzyme) onto deuterated cellulose films to create air-solid and liquid-solid interfaces. Deuterated cellulose films had all the hydrogen groups of the anhydroglucose replaced by deuterium (Raghuwanshi et al., 2017b). The replaced deuterium induces a large neutron SLD difference between the cellulose and biomolecules, providing high contrast by neutron reflectometry (NR) or scattering. In D_2O, the SLD of deuterated cellulose (7.1×10^{-6} Å^{-2}) and IgG (4.1×10^{-6} Å^{-2}) clearly show the differences in the NR curves (**Figure 12**). The SLD of hydrogenated cellulose is 3.56×10^{-6} Å^{-2}, which is close to the SLD of IgG and HRP (3.9×10^{-6} Å^{-2}), and does not provide sufficient contrast to differentiate cellulose from proteins. The IgG and HRP biomolecules might also contain a variable number of liable hydrogens in their structure. Dispersion of biomolecules in D_2O replaces the liable hydrogens by deuterium which alters their SLD. Determining the deuteration level of biomolecules can further increase accuracy in the quantification of adsorbed biomolecules in neutron-based experiments.

NR combined with QCM-D quantifies the conformation of the IgG molecules adsorbed at the cellulose interface as a monolayer of thickness 12.7 nm, surface coverage of 4.2 mg/m^2 and forming 25% of the interphase volume fraction. The HRP molecules also adsorbed as a monolayer of thickness 9.8 nm with volume fraction of 20%; this corresponds to partial surface coverage of HRP.

A water resistant nanofibrillated cellulose thin film was functionalized by carboxylated groups using the TEMPO oxidation method (Isogai and Kato, 1998). This converts the –OH groups of the cellulose C6 hydroxyl into a -COOH functionality. Conductometric titration indicates −72 μeq/g of charge on the pure NFC film, which increases by a factor 3, up to −237 μeg/g after 5 min TEMPO oxidation (Orelma et al., 2012).

The –COOH groups of the film interface were further modified into amine reactive sites by EDC/NHS coupling reaction for BSA and IgG adsorption. QCM-D shows the oxidation increases the film water intake capacity with a film wet mass of about 25 mg/m^2 (**Figure 13**). Modification of surface charge with NHS-ester reduces the water intake and produced no desorption of NHS-esters. The amount of water in the film structure can significantly affect the conformation and adsorption of biomolecules at the cellulosic interface. Therefore, quantification of water within the film structure, before and after adsorption of biomolecules, is an important factor.

The BSA adsorbed at the unmodified film interface had a surface coverage of 1.6 mg/m^2. The adsorbed BSA molecules show irreversible binding upon rinsing with 10 mM NaCl at pH 10. In contrast, the oxidized film interface reversibly adsorbed BSA at 6.8 mg/m^2; rinsing with 10 mM NaCl at pH 10 desorbed all BSA molecules. However, an initial BSA adsorption of 9.8 mg/m^2 was achieved onto the EDC/NHS modified film surface. Upon rinsing, the unbounded BSA molecules were removed and the only irreversible bounded BSA (4.9 mg/m^2) remained at the film interface.

Fluorescence imaging was used to track the adsorption of FITC-stained anti human IgG molecules on unmodified films. It shows a weak fluorescence intensity of 1.8. Rinsing with NaCl completely removed the IgG from the unmodified CNF interface. However, the EDC/NHS modified film interface showed a fluorescence 10 times stronger with an intensity of 18.76. NaCl rinsing had no effect on the adsorbed IgG as the

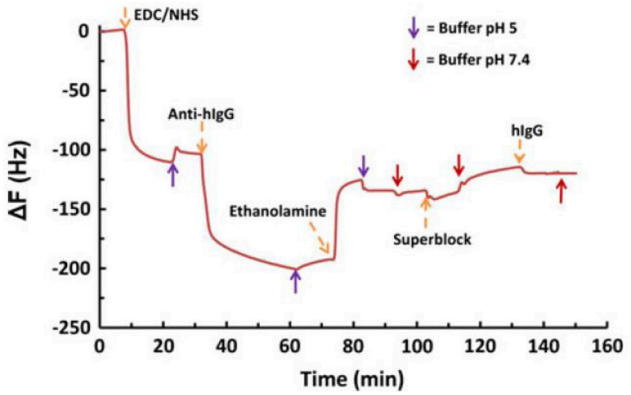

FIGURE 13 | QCM-D data for the adsorption of human IgG on EDC/NHS activated NFC-film in the presence of conjugated antihuman IgG. Conjugation of IgG resulted in a small shift in frequency. Reproduced with permission from Orelma et al. (2012).

molecules remained at the film interface with a surface coverage of 18 mg/m^2.

Prathapan et al. studied the drying profile of blood stains on CNC films (35 nm thick) coated onto a glass substrate. AFM and contact angle measurements quantified the roughness and wettability of the dried blood stains onto the CNC interface (**Figure 14**). Blood antibody and antigen tests proved the CNC layer capability to provide high selectivity for blood testing diagnostics (Prathapan et al., 2018).

Comparison of a CNC film with a cellulose film regenerated from cellulose acetate (Su et al., 2016) reveals significantly less swelling for CNC due to its crystalline structure. The regenerated cellulose is amorphous and swells up to 2–3 times in water. Biomolecules are prompt to diffuse into the swollen layer forming a gel or easily detach from the interface. The non-swelling CNC coating improves visualization of the blood stain reacting with an antibody during typing testing. Post hydrophobic chemical modifications of the cellulose film interface can hinder water penetration in the film structure and reduce its swelling, which can benefit further in visualization and quantification of biomolecules at film interface.

Huang et al. tested the functionality and longevity of physically adsorbed IgG and IgM antibodies on cellulose acetate films and compared those with regenerated cellulose thin films on glass substrate (Huang et al., 2017). X-ray and neutron reflectivity revealed the cellulose films to be 20.8 nm thick and swells to twice of their original thickness in water.

The adsorbed IgG and IGM antibodies were dried on cellulose acetate and regenerated cellulose film interfaces. The effect of aging on antibodies functionality was monitored by measuring the red blood cell (RBC) size agglutinates using image analysis for 30 days. Antibody aging was directly related to surface hydrophobicity by recording water droplet contact angle over the surface of antibody dried and aged onto the cellulosic films. The study revealed that both IgG, and IgM survive longer on the cellulose acetate film than on a cellulose film. This increased biomolecule longevity is due to a more favorable molecular conformation of the adsorbed antibodies as the hydrophobic cellulose acetate restricts hydrogen bonding interactions between antibody and surface which retain the original conformation of the native antibody (Huang et al., 2017).

However, IgM loses its functionality faster than IgG at both cellulosic interfaces, which might be due to the higher carboxyl content of IgM. The drop-in antibody functionality during aging is explained by the formation of antibody-surface hydrogen bonds which alter the biomolecule conformation and also rotate hydrophobic groups toward the air interface. The increased hydrophobicity of the antibody layer also delays wetting and rehydration by blood and buffers, slowing down the response of the test for analysis.

The human immunoglobulin G (h-IgG) and BSA interaction with chitosan and carboxymethyl cellulose (CMC) modified cellulose interfaces were studied by QCM-D combined with SPR measurements (Orelma et al., 2011). Both h-IgG and BSA adsorbed onto the modified cellulose interfaces (**Figure 15**).

CMC and chitosan adsorbed on cellulose at 53 mg/m^2 and 4.4 mg/m^2 (wet mass), respectively. The dry mass evaluated for the adsorbed CMC was 2 mg/m^2 and 0.7 mg/m^2 for chitosan. The CMC modified cellulose interface adsorbed 97% of water on hydration, which is higher than the chitosan modified surface (83%). Near the isoelectric point (pH 5.0), BSA adsorption at the unmodified cellulose interface is 1.7 mg/m^2, which increases to 3.5 mg/m^2 on the chitosan modified interface. However, BSA adsorption does not change much at the CMC modified interface as compared to the unmodified interface.

Similarly, at pH 5.0, h-IgG also showed enhanced adsorption at the chitosan modified interface (about 10 mg/m^2) as compared to the CMC modified (about 5 mg/m^2) and unmodified cellulose (2.2 mg/m^2). At higher pH 7.4, the adsorption of both BSA and h-IgG decreases for all the interfaces studied. The surface modification induces surface charges at the cellulose interface which play an important role in controlling the adsorption of biomolecules due to varying electrostatic interaction at the different pH values.

Multiple factors can affect the biomolecules interactions, longevity and functionality at the cellulosic thin film interface. These include the cellulose thin film morphology, its water intake capacity and swelling behavior, substrate types, cellulose surface chemistry/modification, surrounding pH and ionic strength, and initial biomolecules conformation and its ability to interact with the cellulosic thin film interface.

SUMMARY AND PERSPECTIVES

The review aims at engineering biodegradable and cost effective cellulosic thin films or interfaces of controlled properties. The applications of interest range from measuring macromolecule interactions onto cellulose and quantifying biomolecule conformation at interfaces to optimizing biomedical applications. Native cellulose from different sources or cellulose derivatives can be used to form cellulose thin film by the spin coating, Langmuir-Schaefer and Langmuir Blodgett coating

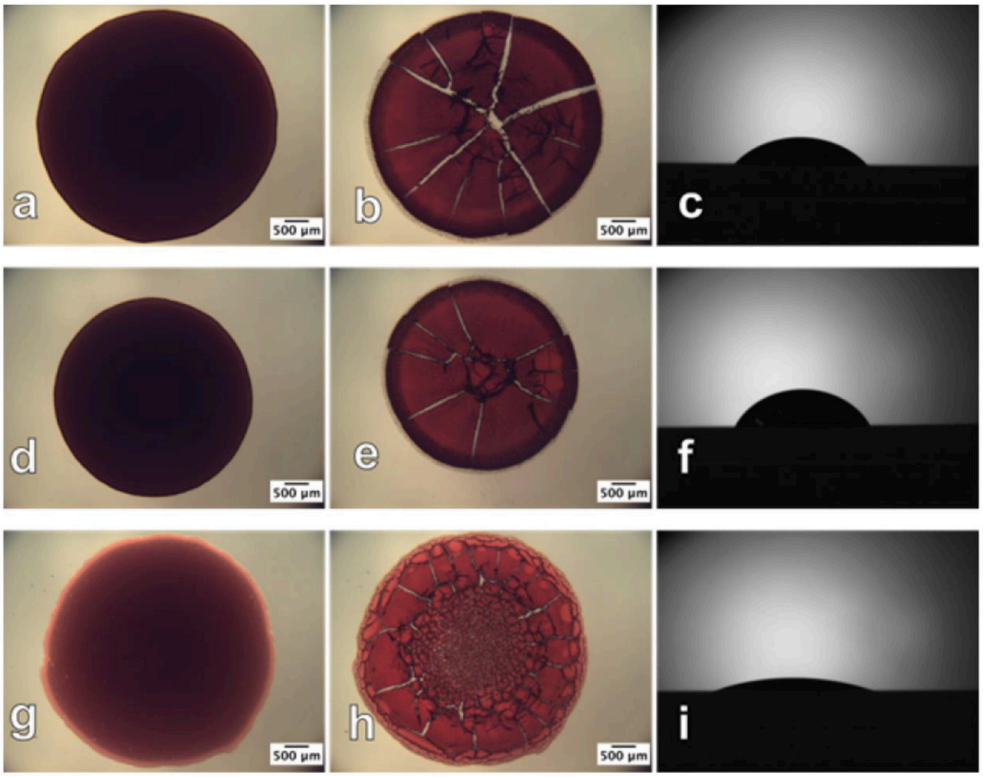

FIGURE 14 | Optical images of human blood before (left) and after (middle) drying and the contact angle sessile drop image (right), respectively, on the **(a–c)** glass slide surface; **(d–f)** cellulose acetate surface; **(g–i)** regenerated cellulose surface. The before and after drying images were taken in transmittance mode. Reproduced with permission from Prathapan et al. (2018).

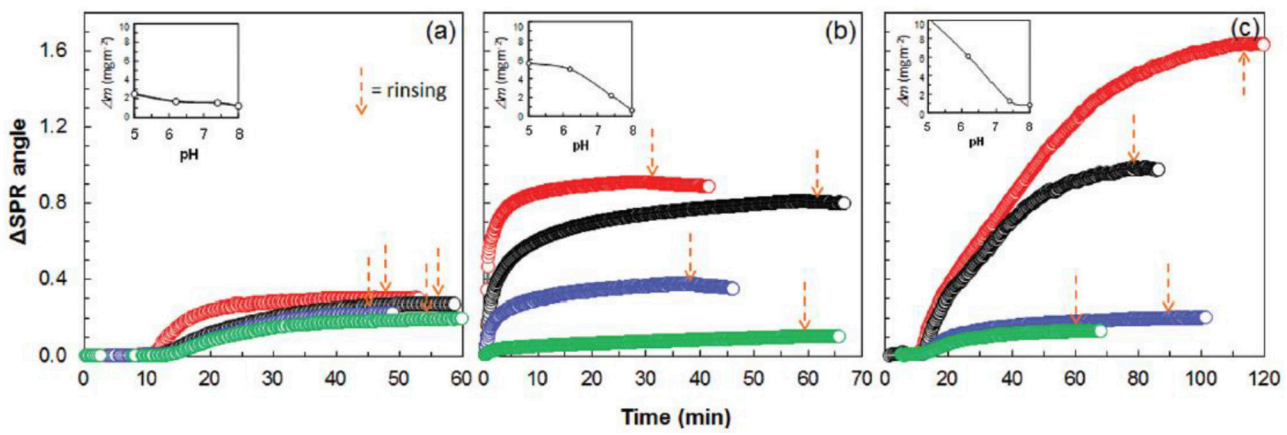

FIGURE 15 | SPR sensogram on the adsorption of 0.1 mg/mL human IgG on cellulose. **(a)** CMC-modified cellulose **(b)**, and chitosan modified cellulose **(c)**, from aqueous solutions of pH 5.0, 6.2, 7.4, and 8.0 (the respective curves follow the same order from top down). Corresponding calculated adsorbed mass is indicated as a function of pH in the inserts (calculated from SPR data modeling). Reproduced with permission from Orelma et al. (2011).

methods. Cellulose films can be coated directly onto a substrate or indirectly using chemical pre-modification. For measuring biomolecules interactions, the coated cellulose thin film surface requires film thickness between 2 and 100 nm and having a roughness of about 1 nm. This is to fulfill the requirements of advanced characterization surfaces technique (thickness) while being able to distinguish biomolecules from the film roughness. Smooth and ultra-thin films enable to accurately modify the cellulose surface and to increase surface area for optimizing biomolecules activity at interfaces. Cellulose surfaces can be easily

functionalized to selectivity retain or increase the activity of specific bio-molecules. This enables cellulose thin films to be optimized for biomedical applications, such as blood typing, pregnancy test and adhesion of specific cell at the interface.

The current review encourages engineering smooth and ultra-thin cellulosic interfaces to specific applications. These interfaces are low cost and enable multiple functionality by reacting the cellulose hydroxyls into carboxylic or amine groups. Currently, only a few applications using biomolecules at cellulose thin film interfaces have been developed. Many questions and challenges remain to reproducibly prepare nanocellulose film and best control their interactions with biomolecules. A limiting step has long been the ability to prepare smooth cellulose film from the pre-functionalized CNF/CNC. Advance characterization can further be developed to visualize and quantify the adsorbed biomolecules at the film interface. This will enable to control the biomolecules adsorption at the cellulosic interface and their conformational changes at any pH, ionic strength and temperature required.

AUTHOR CONTRIBUTIONS

VR and GG both wrote the manuscript and equally contributed.

FUNDING

Financial support was from Australian Research Council (ARC), Australian paper, Circa, Norske Skog, Orora, and Visy through the Industry Transformation Research Hub grant IH130100016.

REFERENCES

Ahola, S., Myllytie, P., Österberg, M., Teerinen, T., and Laine, J. (2008). Effect of polymer adsroption on cellulose nanofibril water binding capacity and aggregation. *Bioresources* 3, 1315–1328.

Arcot, L. R., Chen, X., Wenchao, X., Johansson, L. S., and Rojas, O. J. (2015). Paper-based plasmon-enhanced protein sensing by controlled nucleation of silver nanoparticles on cellulose. *Cellulose* 22, 4027–4034. doi: 10.1007/s10570-015-0783-z

Ashkar, R., Bilheux, H. Z., Bordallo, H., Briber, R., Callaway, D. J. E., Cheng, X. L., et al. (2018). Neutron scattering in the biological sciences: progress and prospects. *Acta Crystal. Sect. D Struct. Biol.* 74, 1129–1168. doi: 10.1107/S2059798318017503

Atalla, R. H., and Vanderhart, D. L. (1984). Native cellulose - a composite of 2 distinct crystalline forms. *Science* 223, 283–285. doi: 10.1126/science.223.4633.283

Aulin, C., Ahola, S., Josefsson, P., Nishino, T., Hirose, Y., Osterberg, M., et al. (2009). Nanoscale cellulose films with different crystallinities and mesostructures-their surface properties and interaction with water. *Langmuir* 25, 7675–7685. doi: 10.1021/la900323n

Bandera, D., Sapkota, J., Josset, S., Weder, C., Tingaut, P., Gao, X., et al. (2014). Influence of mechanical treatments on the properties of cellulose nanofibers isolated from microcrystalline cellulose. *React. Funct. Polym.* 85, 134–141. doi: 10.1016/j.reactfunctpolym.2014.09.009

Barth, K. L., and Keilmann, F. (1993). Far-infrared ellipsometer. *Rev. Sci. Instruments* 64, 870–875. doi: 10.1063/1.1144135

Basavaraja, C., Jo, E. A., and Huh, D. S. (2011). Fabrication and transport properties of poly(N-vinylcarbazole)-cellulose triacetate langmuir-schaefer films. *Polymer Comp.* 32, 79–88. doi: 10.1002/pc.21020

Berthold, F., Gustafsson, K., Berggren, R., Sjoholm, E., and Lindstrom, M. (2004). Dissolution of softwood kraft pulps by direct derivatization in lithium chloride/N,N-dimethylacetamide. *J. Appl. Polym. Sci.* 94, 424–431. doi: 10.1002/app.20697

Bhatnagar, A., and Sain, M. (2005). Processing of cellulose nanofiber-reinforced composites. *J. Reinforced Plast. Comp.* 24, 1259–1268. doi: 10.1177/0731684405049864

Blanco, A., Monte, M. C., Campano, C., Balea, A., Merayo, N., and Negro, C. (2018). "Chapter 5 - nanocellulose for industrial use: cellulose nanofibers (CNF), cellulose nanocrystals (CNC), and bacterial cellulose (BC)," in *Handbook of Nanomaterials for Industrial Applications,* ed C. Mustansar Hussain (Elsevier), 74–126.

Bordel, D., Putaux, J. L., and Heux, L. (2006). Orientation of native cellulose in an electric field. *Langmuir* 22, 4899–4901. doi: 10.1021/la0600402

Bracic, M., Mohan, T., Kargl, R., Griesser, T., Hribernik, S., Kostler, S., et al. (2014). Preparation of PDMS ultrathin films and patterned surface modification with cellulose. *RSC Adv.* 4, 11955–11961. doi: 10.1039/C3RA 47380E

Casals-Terre, J., Farre-Llados, J., Zuniga, A., Roncero, M. B., and Vidal, T. (2018). Novel applications of nonwood cellulose for blood typing assays. *J. Biomed. Mater. Res. B. Appl. Biomater.* 107, 1533–1541. doi: 10.1002/jbm.b.34245

Chen, Y., Potschke, P., Pionteck, J., Voit, B., and Qi, H. S. (2018). Smart cellulose/graphene composites fabricated by in situ chemical reduction of graphene oxide for multiple sensing applications. *J. Mater. Chem. A* 6, 7777–7785. doi: 10.1039/C8TA00618K

Cheng, G., Liu, Z. L., Murton, J. K., Jablin, M., Dubey, M., Majewski, J., et al. (2011). Neutron reflectometry and QCM-D study of the interaction of cellulases with films of amorphous cellulose. *Biomacromolecules* 12, 2216–2224. doi: 10.1021/bm200305u

Cohen-Atiya, M., Vadgama, P., and Mandler, D. (2007). Preparation, characterization and applications of ultrathin cellulose acetate Langmuir-blodgett films. *Soft Matter* 3, 1053–1063. doi: 10.1039/B701255A

Cooper, G. K., Sandberg, K. R., and Hinck, J. F. (1981). Trimethylsilyl cellulose as precursor to regenerated cellulose fiber. *J. Appl. Polym. Sci.* 26, 3827–3836. doi: 10.1002/app.1981.070261129

Courtenay, J. C., Johns, M. A., Galembeck, F., Deneke, C., Lanzoni, E. M., Costa, C. A., et al. (2017). Surface modified cellulose scaffolds for tissue engineering. *Cellulose* 24, 253–267. doi: 10.1007/s10570-016-1111-y

Courtenay, J. C., Sharma, R. I., and Scott, J. L. (2018). Recent advances in modified cellulose for tissue culture applications. *Molecules* 23:E654. doi: 10.3390/molecules23030654

Cranston, E. D., Gray, D. G., and Rutland, M. W. (2010). Direct surface force measurements of polyelectrolyte multi layer films containing nanocrystalline cellulose. *Langmuir* 26, 17190–17197. doi: 10.1021/la1030729

Curvello, R., Raghuwanshi, V. S., and Garnier, G. (2019). Engineering nanocellulose hydrogels for biomedical applications. *Adv. Colloid Interface Sci.* 267, 47–61. doi: 10.1016/j.cis.2019.03.002

Czaja, W. K., Young, D. J., Kawecki, M., and Brown, R. M. Jr. (2007). The future prospects of microbial cellulose in biomedical applications. *Biomacromolecules* 8, 1–12. doi: 10.1021/bm060620d

Daillant, J., and Gibaud, A. (2009). *X-Ray and Neutron Reflectivity: Principles and Applications.* Heidelberg; Berlin: Springer-Verlag.

Demitri, C., Raucci, M. G., Giuri, A., De Benedictis, V. M., Giugliano, D., Calcagnile, P., et al. (2016). Cellulose-based porous scaffold for bone tissue engineering applications: assessment of hMSC proliferation and differentiation. *J. Biomed. Mater. Res. Part A* 104, 726–733. doi: 10.1002/jbm.a.35611

Derikvand, F., Yin, D. T., Barrett, R., and Brumer, H. (2016). Cellulose-based biosensors for esterase detection. *Anal. Chem.* 88, 2989–2993. doi: 10.1021/acs.analchem.5b04661

Dufrêne, Y. F. (2002). Atomic force microscopy, a powerful tool in microbiology. *J. Bacteriol.* 184, 5205–5213. doi: 10.1128/JB.184.19.5205-5213.2002

Dufresne, A. (2013). Nanocellulose: a new ageless bionanomaterial. *Mater. Today* 16, 220–227. doi: 10.1016/j.mattod.2013.06.004

Ebeling, T., Paillet, M., Borsali, R., Diat, O., Dufresne, A., Cavaille, J. Y., et al. (1999). Shear-induced orientation phenomena in suspensions of

cellulose microcrystals, revealed by small angle X-ray scattering. *Langmuir* 15, 6123–6126. doi: 10.1021/la990046+

Edgar, C. D., and Gray, D. G. (2003). Smooth model cellulose I surfaces from nanocrystal suspensions. *Cellulose* 10, 299–306. doi: 10.1023/A:1027333928715

Eita, M., Arwin, H., Granberg, H., and Wagberg, L. (2011). Addition of silica nanoparticles to tailor the mechanical properties of nanofibrillated cellulose thin films. *J. Colloid Interface Sci.* 363, 566–572. doi: 10.1016/j.jcis.2011.07.085

Emslie, A. G., Bonner, F. T., and Peck, L. G. (1958). Flow of a viscous liquid on a rotating disk. *J. Appl. Phys.* 29, 858–862. doi: 10.1063/1.1723300

Eriksson, J., Malmsten, M., Tiberg, F., Callisen, T. H., Damhus, T., and Johansen, K. S. (2005). Model cellulose films exposed to H-insolens glucoside hydrolase family 45 endo-cellulase - the effect of the carbohydrate-binding module. *J. Colloid Interface Sci.* 285, 94–99. doi: 10.1016/j.jcis.2004.10.042

Eriksson, M., Notley, S. M., and Wagberg, L. (2007). Cellulose thin films: degree of cellulose ordering and its influence on adhesion. *Biomacromolecules* 8, 912–919. doi: 10.1021/bm061164w

Falt, S., Wagberg, L., Vesterlind, E. L., and Larsson, P. T. (2004). Model films of cellulose II - improved preparation method and characterization of the cellulose film. *Cellulose* 11, 151–162. doi: 10.1023/B:CELL.0000025403.23775.75

Foster, E. J., Moon, R. J., Agarwal, U. P., Bortner, M. J., Bras, J., Camarero-Espinosa, S., et al. (2018). Current characterization methods for cellulose nanomaterials. *Chem. Soc. Rev.* 47, 2609–2679. doi: 10.1039/C6CS00895J

Free, A. H., Adams, E. C., Kercher, M. L., Free, H. M., and Cook, M. H. (1957). Simple specific test for urine glucose. *Clin. Chem.* 3, 163–168.

Guan, L. Y., Cao, R., Tian, J. F., Mcliesh, H., Garnier, G., and Shen, W. (2014). A preliminary study on the stabilization of blood typing antibodies sorbed into paper. *Cellulose* 21, 717–727. doi: 10.1007/s10570-013-0134-x

Gunnars, S., Wagberg, L., and Stuart, M. (2002). Model films of cellulose: I. method development and initial results. *Cellulose* 9, 239–249. doi: 10.1023/A:1021196914398

Habibi, Y., Foulon, L., Aguie-Beghin, V., Molinari, M., and Douillard, R. (2007). Langmuir-blodgett films of cellulose nanocrystals: preparation and characterization. *J. Colloid Interface Sci.* 316, 388–397. doi: 10.1016/j.jcis.2007.08.041

Habibi, Y., Hoeger, I., Kelley, S. S., and Rojas, O. J. (2010a). Development of langmuir-schaeffer cellulose nanocrystal monolayers and their interfacial behaviors. *Langmuir* 26, 990–1001. doi: 10.1021/la902444x

Habibi, Y., Lucia, L. A., and Rojas, O. J. (2010b). Cellulose nanocrystals: chemistry, self-assembly, and applications. *Chem. Rev.* 110, 3479–3500. doi: 10.1021/cr900339w

Halpern, V., Ogunsola, F., Obunge, O., Wang, C. H., Onyejepu, N., Oduyebo, O., et al. (2008). Effectiveness of cellulose sulfate vaginal gel for the prevention of HIV infection: results of a phase III trial in Nigeria. *PLoS ONE* 3:e3784. doi: 10.1371/journal.pone.0003784

Heinze, T., El Seoud, O. A., and Koschella, A. (2018). *Cellulose Derivatives: Synthesis, Structure, and Properties*. Springer International Publishing.

Hosseini, S., Vazquez-Villegas, P., and Martinez-Chapa, S. O. (2017). Paper and fiber-based bio-diagnostic platforms: current challenges and future needs. *Appl. Sci. Basel* 7:863. doi: 10.3390/app7080863

Hu, J. G., Tian, D., Renneckar, S., and Saddler, J. N. (2018). Enzyme mediated nanofibrillation of cellulose by the synergistic actions of an endoglucanase, lytic polysaccharide monooxygenase (LPMO) and xylanase. *Sci. Rep.* 8:3195. doi: 10.1038/s41598-018-21016-6

Huang, Z. R., Raghuwanshi, V. S., and Garnier, G. (2017). Functionality of immunoglobulin g and immunoglobulin M antibody physisorbed on cellulosic films. *Front. Bioeng. Biotechnol.* 5, 2–10. doi: 10.3389/fbioe.2017.00041

Isogai, A., and Kato, Y. (1998). Preparation of polyglucuronic acid from cellulose by TEMPO-mediated oxidation. *Cellulose* 5, 153–164. doi: 10.1023/A:1009208603673

Jimenez, A. S., Jaramillo, F., Hemraz, U. D., Boluk, Y., Ckless, K., and Sunasee, R. (2017). Effect of surface organic coatings of cellulose nanocrystals on the viability of mammalian cell lines. *Nanotechnol. Sci. Appl.* 10, 123–136. doi: 10.2147/NSA.S145891

Johansson, L.-S., and Campbell, J. M. (2004). Reproducible XPS on biopolymers: cellulose studies. *Surface Interface Analy.* 36, 1018–1022. doi: 10.1002/sia.1827

Karabiyik, U., Mao, M., Roman, M., Jaworek, T., Wegner, G., and Esker, A. R. (2009). Optical characterization of Cellulose films via multiple incident media ellipsometry, model cellulosic surfaces, in *ACS Symposium Series*, ed M. Roman (Washington, DC: American Chemical Society), 137–155. doi: 10.1021/bk-2009-1019.ch006

Kargl, R., Mohan, T., Kostler, S., Spirk, S., Doliska, A., Stana-Kleinschek, K., et al. (2013). Functional patterning of biopolymer thin films using enzymes and lithographic methods. *Adv. Funct. Mater.* 23, 308–315. doi: 10.1002/adfm.201200607

Kassavetis, S., Gravalidis, C., and Logothetidis, S. (2012). "Thin film deposition and nanoscale characterisation techniques," in *Nanostructured Materials and Their Applications,* ed S. Logothetidis (Berlin; Heidelberg: Springer Berlin Heidelberg), 105–129.

Kim, J.-H., Shim, B. S., Kim, H. S., Lee, Y.-J., Min, S.-K., Jang, D., et al. (2015). Review of nanocellulose for sustainable future materials. *Int. J. Precision Eng. Manufact.Green Technol.* 2, 197–213. doi: 10.1007/s40684-015-0024-9

Kittle, J. D., Du, X. S., Jiang, F., Qian, C., Heinze, T., Roman, M., et al. (2011). Equilibrium water contents of cellulose films determined via solvent exchange and quartz crystal microbalance with dissipation monitoring. *Biomacromolecules* 12, 2881–2887. doi: 10.1021/bm200352q

Klebe, J. F., and Finkbeiner, H. L. (1969). Silyl celluloses: a new class of soluble cellulose derivatives. *J. Polymer Sci. Part A-1.* 7, 1947–1958. doi: 10.1002/pol.1969.150070733

Koczula, K. M., and Gallotta, A. (2016). Lateral flow assays. *Essays Biochem.* 60, 111–120. doi: 10.1042/EBC20150012

Kontturi, E., Johansson, L. S., Kontturi, K. S., Ahonen, P., Thune, P. C., and Laine, J. (2007). Cellulose nanocrystal submonolayers by spin coating. *Langmuir* 23, 9674–9680. doi: 10.1021/la701262x

Kontturi, E., Suchy, M., Penttila, P., Jean, B., Pirkkalainen, K., Torkkeli, M., et al. (2011a). Amorphous characteristics of an ultrathin cellulose film. *Biomacromolecules* 12, 770–777. doi: 10.1021/bm101382q

Kontturi, E., Suchy, M., Penttila, P., Jean, B., Pirkkalainen, K., Torkkeli, M., et al. (2011b). Correction to amorphous characteristics of an ultrathin cellulose film. *Biomacromolecules* 12, 3352–3352. doi: 10.1021/bm201109q

Kontturi, E., Tammelin, T., and Osterberg, M. (2006). Cellulose - model films and the fundamental approach. *Chem. Soc. Rev.* 35, 1287–1304. doi: 10.1039/B601872F

Kontturi, E., Thune, P. C., and Niemantsverdriet, J. W. (2003). Cellulose model surfaces-simplified preparation by spin coating and characterization by X-ray photoelectron spectroscopy, infrared spectroscopy, and atomic force microscopy. *Langmuir* 19, 5735–5741. doi: 10.1021/la0340394

Kontturi, K. S., Kontturi, E., and Laine, J. (2013). Specific water uptake of thin films from nanofibrillar cellulose. *J. Mater. Chem. A* 1, 13655–13663. doi: 10.1039/c3ta12998e

Lahiji, R. R., Xu, X., Reifenberger, R., Raman, A., Rudie, A., and Moon, R. J. (2010). Atomic force microscopy characterization of cellulose nanocrystals. *Langmuir* 26, 4480–4488. doi: 10.1021/la903111j

Larson, R. G., and Rehg, T. J. (1997). "Spin Coating," in *Liquid Film Coating: Scientific Principles and Their Technological Implications*, eds S. F. Kistler and P. M. Schweizer. (Dordrecht: Springer Netherlands), 709–734.

Li, L. Z., Huang, X. L., Liu, W., and Shen, W. (2014). Control performance of paper-based blood analysis devices through paper structure design. *ACS Appl. Mater. Interfaces* 6, 21624–21631. doi: 10.1021/am506618c

Luchs, J. (2010). Efficacy of hydroxypropyl cellulose ophthalmic inserts (HCOI) in dry eye syndrome (DES) at all levels of severity. *Invest. Ophthalmol. Vis. Sci.* 51:6262.

Martinez, A. W., Phillips, S. T., Whitesides, G. M., and Carrilho, E. (2010). Diagnostics for the developing world: microfluidic paper-based analytical devices. *Anal. Chem.* 82, 3–10. doi: 10.1021/ac9013989

Marx, K. A. (2003). Quartz crystal microbalance: a useful tool for studying thin polymer films and complex biomolecular systems at the solution–surface interface. *Biomacromolecules* 4, 1099–1120. doi: 10.1021/bm020116i

Maver, T., Maver, U., Mostegel, F., Griesser, T., Spirk, S., Smrke, D. M., et al. (2015). Cellulose based thin films as a platform for drug release studies to mimick wound dressing materials. *Cellulose* 22, 749–761. doi: 10.1007/s10570-014-0515-9

Menon, M. P., Selvakumar, R., Kumar, P. S., and Ramakrishna, S. (2017). Extraction and modification of cellulose nanofibers derived from biomass for environmental application. *RSC Adv.* 7, 42750–42773. doi: 10.1039/C7RA06713E

Modulevsky, D. J., Lefebvre, C., Haase, K., Al-Rekabi, Z., and Pelling, A. E. (2014). Apple derived cellulose scaffolds for 3D mammalian cell culture. *PLoS ONE* 9:e97835. doi: 10.1371/journal.pone.0097835

Mohan, T., Niegelhell, K., Zarth, C. S. P., Kargl, R., Kostler, S., Ribitsch, V., et al. (2014). Triggering protein adsorption on tailored cationic cellulose surfaces. *Biomacromolecules* 15, 3931–3941. doi: 10.1021/bm500997s

Mohan, T., Ristic, T., Kargl, R., Doliska, A., Kostler, S., Ribitsch, V., et al. (2013). Cationically rendered biopolymer surfaces for high protein affinity support matrices. *Chem. Commun.* 49, 11530–11532. doi: 10.1039/c3cc46414h

Müller, M., and Schmitt, F.-J. (1997). Quantitative atr-ftir spectroscopy at polymer surfaces: sorption and molecular conformation. *Macromol. Symp.* 119, 269–276. doi: 10.1002/masy.19971190128

Narkpiban, K., Sakdaronnarong, C., Nimchua, T., Pinmanee, P., Thongkred, P., and Poonsawat, T. (2019). The effect of mechano-enzymatic treatment on the characteristics of cellulose nanofiber obtained from kenaf (*Hibiscus cannabinus* L.) bark. *Bioresources* 14, 99–119. doi: 10.15376/biores.14.1.99-119

Nguyen, T., and Latkany, R. (2011). Review of hydroxypropyl cellulose ophthalmic inserts for treatment of dry eye. *Clin. Ophthalmol.* 5, 587–591. doi: 10.2147/OPTH.S13889

Niegelhell, K., Sussenbacher, M., Jammernegg, K., Ganner, T., Schwendenwein, D., Schwab, H., et al. (2016). Enzymes as biodevelopers for nano- and micropatterned bicomponent biopolymer thin films. *Biomacromolecules* 17, 3743–3749. doi: 10.1021/acs.biomac.6b01263

Notley, S. M., Eriksson, M., Wagberg, L., Beck, S., and Gray, D. G. (2006). Surface forces measurements of spin-coated cellulose thin films with different crystallinity. *Langmuir* 22, 3154–3160. doi: 10.1021/la052886w

Notley, S. M., and Wagberg, L. (2005). Morphology of modified regenerated model cellulose II surfaces studied by atomic force microscopy: effect of carboxymethylation and heat treatment. *Biomacromolecules* 6, 1586–1591. doi: 10.1021/bm050005u

Novotna, K., Havelka, P., Sopuch, T., Kolarova, K., Vosmanska, V., Lisa, V., et al. (2013). Cellulose-based materials as scaffolds for tissue engineering. *Cellulose* 20, 2263–2278. doi: 10.1007/s10570-013-0006-4

O'donnell, N., Okkelman, I. A., Timashev, P., Gromovykh, T. I., Papkovsky, D. B., and Dmitriev, R. I. (2018). Cellulose-based scaffolds for fluorescence lifetime imaging-assisted tissue engineering. *Acta Biomater.* 80, 85–96. doi: 10.1016/j.actbio.2018.09.034

Orelma, H., Filpponen, I., Johansson, L. S., Laine, J., and Rojas, O. J. (2011). Modification of cellulose films by adsorption of CMC and chitosan for controlled attachment of biomolecules. *Biomacromolecules* 12, 4311–4318. doi: 10.1021/bm201236a

Orelma, H., Filpponen, I., Johansson, L. S., Osterberg, M., Rojas, O. J., and Laine, J. (2012). Surface functionalized nanofibrillar cellulose (nfc) film as a platform for immunoassays and diagnostics. *Biointerphases* 7:61. doi: 10.1007/s13758-012-0061-7

Prathapan, R., Mcliesh, H., Garnier, G., and Tabor, R. (2018). Surface engineering of transparent cellulose nanocrystal coatings for biomedical applications. *ACS Applied Bio Mater.* 1, 728–737. doi: 10.1021/acsabm.8b00193

Racic, A., Calija, B., Milic, J., Milasinvic, N., and Krajisnik, D. (2019). Development of polysaccharide-based mucoadhesive ophthalmic lubricating vehicles: the effect of different polymers on physicochemical properties and functionality. *J. Drug Deliv. Sci. Technol.* 49, 50–57. doi: 10.1016/j.jddst.2018.10.034

Raghuwanshi, V. S., Cohen, Y., Garnier, G., Garvey, C. J., Russell, R. A., Darwish, T., et al. (2018). Cellulose dissolution in ionic liquid: ion binding revealed by neutron scattering. *Macromolecules* 51, 7649–7655. doi: 10.1021/acs.macromol.8b01425

Raghuwanshi, V. S., Su, J. L., Garvey, C. J., Holt, S. A., Holden, P. J., Batchelor, W. J., et al. (2017a). Visualization and quantification of IgG antibody adsorbed at the cellulose-liquid interface. *Biomacromolecules* 18, 2439–2445. doi: 10.1021/acs.biomac.7b00593

Raghuwanshi, V. S., Su, J. L., Garvey, C. J., Holt, S. A., Raverty, W., Tabor, R. F., et al. (2017b). Bio-deuterated cellulose thin films for enhanced contrast in neutron reflectometry. *Cellulose* 24, 11–20. doi: 10.1007/s10570-016-1108-6

Revol, J. F., Godbout, L., Dong, X. M., Gray, D. G., Chanzy, H., and Maret, G. (1994). Chiral nematic suspensions of cellulose crystallites - phase-separation and magnetic-field orientation. *Liquid Crystals* 16, 127–134. doi: 10.1080/02678299408036525

Römling, U., and Galperin, M. Y. (2015). Bacterial cellulose biosynthesis: diversity of operons, subunits, products, and functions. *Trends Microbiol.* 23, 545–557. doi: 10.1016/j.tim.2015.05.005

Rubinger, C. P. L., Moreira, R. L., Cury, L. A., Fontes, G. N., Neves, B. R. A., Meneguzzi, A., et al. (2006). Langmuir-blodgett and langmuir-schaefer films of poly (5-amino-1-naphthol) conjugated polymer. *Appl. Surf. Sci.* 253, 543–548. doi: 10.1016/j.apsusc.2005.12.096

Russell, T. P. (1990). X-ray and neutron reflectivity for the investigation of polymers. *Mater. Sci. Rep.* 5, 171–271. doi: 10.1016/S0920-2307(05)80002-7

Sacui, I. A., Nieuwendaal, R. C., Burnett, D. J., Stranick, S. J., Jorfi, M., Weder, C., et al. (2014). Comparison of the properties of cellulose nanocrystals and cellulose nanofibrils isolated from bacteria, tunicate, and wood processed using acid, enzymatic, mechanical, and oxidative methods. *ACS Appl. Mater. Interfaces* 6, 6127–6138. doi: 10.1021/am500359f

Sakakibara, K., Ifuku, S., Tsujii, Y., Kamitakahara, H., Takano, T., and Nakatsubo, F. (2006). Langmuir–blodgett films of a novel cellulose derivative with dihydrophytyl group: the ability to anchor β-carotene molecules. *Biomacromolecules* 7, 1960–1967. doi: 10.1021/bm060083x

Samaranayake, G., and Glasser, W. G. (1993). Cellulose derivatives with low Ds. 2. *Carbohydrate Polymers* 22, 79–86. doi: 10.1016/0144-8617(93)90069-G

Schaub, M., Wenz, G., Wegner, G., Stein, A., and Klemm, D. (1993). Ultrathin films of cellulose on silicon-wafers. *Adv. Mater.* 5, 919–922. doi: 10.1002/adma.19930051209

Shaghaleh, H., Xu, X., and Wang, S. F. (2018). Current progress in production of biopolymeric materials based on cellulose, cellulose nanofibers, and cellulose derivatives. *RSC Adv.* 8, 825–842. doi: 10.1039/C7RA11157F

Sharif Hossain, A. B. M., Uddin, M. M., Fawzi, M., and Veettil, V. N. (2018). Nano-cellulose biopolymer based nano-biofilm biomaterial using plant biomass: an innovative plant biomaterial dataset. *Data Brief* 17, 1245–1252. doi: 10.1016/j.dib.2018.02.053

Shu, F., Ramakrishnan, V., and Schoenborn, B. P. (2000). Enhanced visibility of hydrogen atoms by neutron crystallography on fully deuterated myoglobin. *Proc. Natl. Acad. Sci. U.S.A.* 97, 3872–3877. doi: 10.1073/pnas.060024697

Song, J. L., Liang, J., Liu, X. M., Krause, W. E., Hinestroza, J. P., and Rojas, O. J. (2009). Development and characterization of thin polymer films relevant to fiber processing. *Thin Solid Films* 517, 4348–4354. doi: 10.1016/j.tsf.2009.03.015

Spera, M. B. M., Taketa, T. B., and Beppu, M. M. (2017). Roughness dynamic in surface growth: layer-by-layer thin films of carboxymethyl cellulose/chitosan for biomedical applications. *Biointerphases* 12:04E401. doi: 10.1116/1.4986057

Su, J. L., Al-Tamimi, M., and Garnier, G. (2012). Engineering paper as a substrate for blood typing bio-diagnostics. *Cellulose* 19, 1749–1758. doi: 10.1007/s10570-012-9748-7

Su, J. L., Garvey, C. J., Holt, S., Tabor, R. F., Winther-Jensen, B., Batchelor, W., et al. (2015). Adsorption of cationic polyacrylamide at the cellulose-liquid interface: a neutron reflectometry study. *J. Colloid Interface Sci.* 448, 88–99. doi: 10.1016/j.jcis.2015.02.008

Su, J. L., Raghuwanshi, V. S., Raverty, W., Garvey, C. J., Holden, P. J., Gillon, M., et al. (2016). Smooth deuterated cellulose films for the visualisation of adsorbed bio-macromolecules. *Sci. Rep.* 6:36119. doi: 10.1038/srep36119

Sugiyama, J., Chanzy, H., and Maret, G. (1992). Orientation of cellulose microcrystals by strong magnetic-fields. *Macromolecules* 25, 4232–4234. doi: 10.1021/ma00042a032

Sukma, F. M., and Culfaz-Emecen, P. Z. (2018). Cellulose membranes for organic solvent nanofiltration. *J. Memb. Sci.* 545, 329–336. doi: 10.1016/j.memsci.2017.09.080

Sunasee, R., Hemraz, U. D., and Ckless, K. (2016). Cellulose nanocrystals: a versatile nanoplatform for emerging biomedical applications. *Expert Opin. Drug Deliv.* 13, 1243–1256. doi: 10.1080/17425247.2016.1182491

Swartz, W. E. (1973). X-ray photoelectron spectroscopy. *Analyt. Chem.* 45, 788A−800A. doi: 10.1021/ac60331a001

Syafri, E., Kasim, A., Abral, H., Sudirman, Sulungbudi, G. T., Sanjay, M. R., et al. (2018). Synthesis and characterization of cellulose nanofibers (CNF) ramie reinforced cassava starch hybrid composites. *Int. J. Biol. Macromol.* 120, 578–586. doi: 10.1016/j.ijbiomac.2018.08.134

Tammelin, T., Abburi, R., Gestranius, M., Laine, C., Setala, H., and Osterberg, M. (2015). Correlation between cellulose thin film supramolecular structures and interactions with water. *Soft Matter* 11, 4273–4282. doi: 10.1039/C5SM00374A

Then, W. L., and Garnier, G. (2013). Paper diagnostics in biomedicine. *Rev. Analyt. Chem.* 32, 269–294. doi: 10.1515/revac-2013-0007

Then, W. L., Li, M., Mcliesh, H., Shen, W., and Garnier, G. (2015). The detection of blood group phenotypes using paper diagnostics. *Vox Sang.* 108, 186–196. doi: 10.1111/vox.12195

Tibolla, H., Pelissari, F. M., Martins, J. T., Vicente, A. A., and Menegalli, F. C. (2018). Cellulose nanofibers produced from banana peel by chemical and mechanical treatments: characterization and cytotoxicity assessment. *Food Hydrocoll.* 75, 192–201. doi: 10.1016/j.foodhyd.2017.08.027

Tompkins, H. G., and Irene, E. A. (2005). *Handbook of Ellipsometry.* New York, NY; Heidelberg: William Andrew Publishing; Springer-Verlag GmbH & Co, 1–870.

Torgbo, S., and Sukyai, P. (2018). Bacterial cellulose-based scaffold materials for bone tissue engineering. *Appl. Mater. Today* 11, 34–49. doi: 10.1016/j.apmt.2018.01.004

Turon, X., Rojas, O. J., and Deinhammer, R. S. (2008). Enzymatic kinetics of cellulose hydrolysis: a QCM-D study. *Langmuir* 24, 3880–3887. doi: 10.1021/la7032753

Uddin, K. M. A., Jokinen, V., Jahangiri, F., Franssila, S., Rojas, O. J., and Tuukkanen, S. (2019). Disposable microfluidic sensor based on nanocellulose for glucose detection. *Global Challenges* 3:1800079. doi: 10.1002/gch2.201800079

Ummartyotin, S., and Manuspiya, H. (2015). A critical review on cellulose: from fundamental to an approach on sensor technology. *Renew. Sustain. Energy Rev.* 41, 402–412. doi: 10.1016/j.rser.2014.08.050

Vehige, J. G., Simmons, P. A., Anger, C., Graham, R., Tran, L., and Brady, N. (2003). Cytoprotective properties of carboxymethyl cellulose (CMC) when used prior to wearing contact lenses treated with cationic disinfecting agents. *Eye Contact Lens* 29, 177–180. doi: 10.1097/01.ICL.0000074106.82322.17

Wagberg, L. (2000). Polyelectrolyte adsorption on cellulose fibres– a review. *Nordic Pulp Paper Res. J.* 15, 586–597. doi: 10.3183/npprj-2000-15-05-p586-597

Wenzel, C., Wetzig, K., Thomas, J., Hecker, M., and Brückner, W. (2005). "Thin film preparation and characterization technique," in *Metal Based Thin Films for Electronics*, eds K. Wetzig and C. M. Schneider (Weinheim: Wiley-VCH GmbH & Co), 121–203. doi: 10.1002/3527602534.ch3

Wolfberger, A., Kargl, R., Griesser, T., and Spirk, S (2014). Photoregeneration of trimethylsilyl cellulose as a tool for microstructuring ultrathin cellulose supports. *Molecules* 19, 16266–16273. doi: 10.3390/molecules191016266

Xu, X., Liu, F., Jiang, L., Zhu, J. Y., Haagenson, D., and Wiesenborn, D. P. (2013). Cellulose nanocrystals vs. cellulose nanofibrils: a comparative study on their microstructures and effects as polymer reinforcing agents. *ACS Appl. Mater. Interfaces* 5, 2999–3009. doi: 10.1021/am302624t

Yoshiharu, N., Shigenori, K., Masahisa, W., and Takeshi, O. (1997). Cellulose microcrystal film of high uniaxial orientation. *Macromolecules* 30, 6395–6397. doi: 10.1021/ma970503y

Zhu, Y. H., Xu, X. W., Brault, N. D., Keefe, A. J., Han, X., Deng, Y., et al. (2014). Cellulose paper sensors modified with zwitterionic poly(carboxybetaine) for sensing and detection in complex media. *Anal. Chem.* 86, 2871–2875. doi: 10.1021/ac500467c

Conflict of Interest Statement: The authors declare that the research was conducted in the absence of any commercial or financial relationships that could be construed as a potential conflict of interest.

frontiers in Chemistry

ORIGINAL RESEARCH
published: 06 August 2019
doi: 10.3389/fchem.2019.00562

Reactivity of Isocyanate-Functionalized Lignins: A Key Factor for the Preparation of Lignin-Based Polyurethanes

Mareike Zieglowski[1], Simon Trosien[1], Jochen Rohrer[2], Sabrina Mehlhase[1], Simone Weber[1], Kerstin Bartels[1], Gregor Siegert[1], Taina Trellenkamp[3], Karsten Albe[2] and Markus Biesalski[1]*

[1] Laboratory of Macromolecular Chemistry and Paper Chemistry, Ernst-Berl Institute of Chemistry, Technische Universität Darmstadt, Darmstadt, Germany, [2] Fachgebiet Materialmodellierung, Institute of Material Science, Technische Universität Darmstadt, Darmstadt, Germany, [3] UPM Biochemicals, Augsburg, Germany

Using isocyanate-functionalized Kraft lignin as a reactive macromonomer for the preparation of polyurethane foams by a prepolymer technique is a well-known strategy to incorporate the biomacromolecule into a higher value polymer material. However, as of today the mechanical properties of the resulting materials are still insufficient for a number of possible applications. One reason for this limitation is that the reaction pathway and the morphological arrangement of such foams is of uttermost complexity and depends on a large number of influencing material-intrinsic factors. One important parameter is the reactivity of the functionalized lignin, which has a great impact on the interphase reaction kinetics and thus, on the geometry and mechanical properties of the resulting polyurethane foams. The reactivity is implied, amongst others, by the electron affinity of the isocyanate moiety. Herein, we investigate the reactivity of Kraft lignin modified with different commercially used isocyanates in the reaction with conventional polyols. Therefore, differently reactive prepolymers were synthesized, characterized and polyurethane foams were prepared thereof by using these compounds and the foam formation kinetics, morphological as well as mechanical properties were investigated. Finally, the results were supported by quantum mechanical calculations of the electron affinities of representative model compounds for the lignin-based prepolymers. This work gives rise to a better understanding of the effect of the reactivity and isocyanate structure linked to Kraft lignin on the polyurethane formation and enables rational choice of the isocyanate for pre-functionalization of lignin to prepare materials with better mechanical performance.

Keywords: kraft lignin, polyurethanes, polyurethane foams, isocyanates, bio-based materials

OPEN ACCESS

Edited by:
Eero Kontturi,
School of Chemical Technology,
Aalto University, Finland

Reviewed by:
Aleksander Hejna,
Gdańsk University of Technology, Poland
Marlene Kienberger,
Graz University of Technology, Austria

***Correspondence:**
Markus Biesalski
biesalski@tu-darmstadt.de
Simon Trosien
trosien@cellulose.tu-darmstadt.de

Specialty section:
This article was submitted to Polymer Chemistry, a section of the journal Frontiers in Chemistry

Received: *15 February 2019*
Accepted: *23 July 2019*
Published: *06 August 2019*

Citation:
Zieglowski M, Trosien S, Rohrer J, Mehlhase S, Weber S, Bartels K, Siegert G, Trellenkamp T, Albe K and Biesalski M (2019) Reactivity of Isocyanate-Functionalized Lignins: A Key Factor for the Preparation of Lignin-Based Polyurethanes. Front. Chem. 7:562. doi: 10.3389/fchem.2019.00562

INTRODUCTION

Polyurethanes (PUs) are a class of highly interesting materials due to their versatility that makes them valuable for various fields of day-to-day applications, such as coatings, flame retardants, insulations, adhesives, paints and foams (Chattopadhyay and Raju, 2007). Especially PU foams show unique material characteristics, such as thermal insulating, low volumetric weight and

versatile mechanical properties (Singh and Jain, 2008; Yang et al., 2015; Liu et al., 2017). Chemically, polyurethanes are products of an addition reaction of a polyol and a (poly)isocyanate, respectively, and it can be considered as phase separated polymer blends which consist of alternating hard and soft segments linked to each other by different chemical as well as physical interaction means (Petrovic and Ferguson, 1991). However, the formation of such polymers is highly complex because it is influenced by a plethora of parameters. It is obvious that the molecular structure (e.g., molecular mass and geometric structure) of the single precursor components plays an important role. However, of similar importance are interactions between the individual molecules based on secondary forces (e.g., hydrogen bonds), which could influence for example the crystallinity, the phase separation, and the interphase connections of the segments, and thus, predefine the morphological structure, which greatly influences the addition reaction (Erekkath and Sreejalekshmi, 2018). For the formation of polyurethane foams, in addition to the urethane formation, a so-called blowing reaction is induced by the addition of water, which aims to generate a gas that foams the reactive mixture (most commonly CO_2). To obtain the desired foam structure providing good material properties, urethane formation (crosslinking) of the polymer and vitrification occurs *in situ* during the blowing reaction, with an immobilized blow structure in the end. Therefore, perfectly harmonizing diffusion, reaction kinetics of the single processes (blow reaction vs. crosslinking reactions) and thermodynamic properties (e.g., glass transition/vitrification) are a crucial requirement (Delebecq et al., 2013).

To date, the primary raw materials for polyurethane production are derived from petrochemical refining of crude oil and coals (Gama et al., 2018). With increasing attention to environmental concerns about the use of fossil resources the need to find bio-based alternatives grew rapidly over the last decades (Sawpan, 2018). For this reason, much efforts were made to exploit by-products of plant materials such as lignocellulosic biomass (crops, crops residues or forestry biomass) to extract sustainable raw materials (e.g., lignin), which can be used for synthesis of the high-value PU polymer (Furtwengler and Avérous, 2018). Lignin is an amorphous, cross-linked aromatic heteropolymer which provides structural integrity and confines water transport to distinct parts of the cells in plants. Moreover, it is the second most abundant natural polymer after cellulose and accounts for nearly 30% of organic carbon in the biosphere (Boerjan et al., 2003). Fifty million tons of lignin are produced annually only in the pulp and paper industry, using different pulping processes (mainly Kraft process and sulfite process), which makes it inexpensive and readily available in bulk quantities (Türk, 2014). Although it exhibits various modification sites with different types of hydroxyl and arene moieties which are predestined to be used for the synthesis of polymeric materials (Laurichesse and Avérous, 2014), as of today only a small amount of 2 % is used to generate value-added products and chemicals (Upton and Kasko, 2016).

To incorporate lignin into polyurethane foams, up to now several approaches have been published starting from the middle of the last century (Moorer et al., 1970). Most simply, unmodified lignin was used for the foam formation and combined with an diisocyanate and an additional polyol in a single step (one-shot process) (Mahmood et al., 2016). Because the OH groups of the non-lignin polyol usually react much faster than the corresponding OHs of the lignin, a prepolymer of methylene diisocyanate (MDI) and the polyol may be formed, which would react with the lignin in a subsequent step. This sequence would greatly influence the lignin distribution. [Note that for investigation of the reaction kinetics of the polyurethane formation using unmodified lignin in the one-shot process, Barreiro and co-workers developed an elegant method. Therein, lignin was treated with MDI and a polyol [different polycaprolactones (PCL)] and the disappearance of the NCO band at ∼2,270 cm^{-1} was monitored (Cateto et al., 2008, 2011)]. As a result, the obtained properties of materials made by this approach are commonly not satisfactory. One method to improve the reactivity of the lignin, is tailoring the lignin with more nucleophilic groups, e.g., via hydroxypropylation (Glasser et al., 1982; Nadji et al., 2005), modification with caprolactones (Hatakeyama et al., 2002) or introduction of additional hydroxyl groups at the arene core (Huo et al., 2012). An alternative way to gain better control of the reaction sequence and to get more efficient interphase linkage is to functionalize the lignin with a diisocyanate first and using this electrophilic precursor polymer for polyurethane foam formation (so-called prepolymer approach). The foams, which are generated by using this method, provide a significantly better performance (Chauhan et al., 2014; Gómez-Fernández et al., 2017). However, up to now, for formation of polyurethane foams with these electrophilic lignin-based prepolymers, just few studies have been published and the influence of the reactivity of the introduced isocyanate has not been investigated in detail, mainly due to non-trivial characterization of the processes and materials obtained.

Addressing the latter open questions, we were interested in investigating the influence of the molecular isocyanate structure of the corresponding lignin prepolymers on the properties of PU foams made thereof. Therefore, MDI-modified lignin (KL-MDI) as well as significantly less reactive 2,4-toluene diisocyanate (TDI)-modified lignin (KL-TDI, position 4 is bound to the lignin) and hexamethylene diisocyanate (HDI)-modified lignin (KL-HDI) providing the lowest reactivity were synthesized, characterized and incorporated into a commercial polyurethane foam formulation, respectively (for kinetic studies on the reactivity of the sole diisocyanates, see Coutinho and Rocha, 1991). The experimental results were supported by quantum mechanical calculations of the electron affinities and ionization potentials of representative model compounds. Finally, the morphology and the mechanical properties of the foams were investigated in detail to obtain better understanding of the relationship between reactivity and material properties.

MATERIALS AND METHODS

In the following section, only the most relevant materials and methods for understanding are described. A complete list of all chemicals including purity grades and suppliers of the

single compounds, details about computational methods, as well as detailed information of all analytical methods used [nuclear magnetic resonance spectroscopy (NMR), infrared spectroscopy (IR), SEC (size exclusion chromatography), potentiometric titration, elemental analysis, DSC (differential scanning calorimetry), compression tests, SEM (scanning electron microscopy), and TGA (thermogravimetric analysis)] including original spectra of all synthesized compounds, further details of experimental and theoretical methods and a list of all instruments are shown in detail in **Supplementary Material**.

Reagents and Materials

Kraft lignin was obtained from UPM Biochemicals (UPM Biopiva^{TM} 100, Batch 06.10.2015). All chemicals and solvents were purchased from Fisher Scientific, Sigma-Aldrich, Bernd Kraft GmbH, Tosoh, Evonic Industries AG and Grüssing and used as received unless otherwise stated. For preparation of the polyurethane foams, commercially available MDI-based isocyanate formulation (Desmodur CD-S, Covestro) and polyether-based polyol (Desmophen, 10WF15, Covestro) were used (for more details see **Supplementary Material**). Solvents were dried, if necessary, by using standard methods.

Characterization of the Kraft Lignin

The used Kraft lignin was characterized via SEC, elemental analysis, DSC, IR, and ^{31}P NMR for OH number determination of Argyropoulos (Granata and Argyropoulos, 1995) by using *endo-N*-hydroxy-5-norbornene-2,3-dicaroboximide as internal standard (Zawadzki and Ragauskas, 2001). Most important material characteristics of the lignin used herein are summarized in **Table 1** (for further details see **Supplementary Material**).

Synthesis and Characterization of Isocyanate-Modified Lignins

General Protocol for Synthesizing the Prepolymers KL-MDI, KL-TDI, and KL-HDI

The synthesis of the isocyanate-modified lignins was performed according to the method of Singh and co-workers (Chauhan et al., 2014): To the desired diisocyanate (40 mmol) a solution of Kraft lignin (10 g, 59 mmol of OH groups) in dry THF (tetrahydrofuran) was added drop wise over 15–20 min at 66°C under argon atmosphere. After stirring at 66°C for 90 min the mixture was cooled to room temperature and the crude product was precipitated in 1.2 l of dry toluene. The product is centrifuged for 5 min at 4,500 rpm and the obtained supernatant is decanted. The product is washed 5 times with dry toluene (5 × 300 ml) and centrifuged at 4,500 rpm for 5 min in order to remove all non-reacted isocyanate molecules. The product was finely ground and dried at 40°C *in vacuo* overnight and stored under argon atmosphere. By using this method, the prepolymers KL-MDI, KL-TDI, and KL-HDI were synthesized and in the following further examined (**Figure 1**).

Characterization of the Isocyanate-Modified Lignins

The chemically modified lignins were characterized via elemental analysis, IR, DSC, potentiometric titrations and gravimetrical means under argon atmosphere (for details see **Supplementary Material**).

Quantum Mechanical Calculations of Model Compounds of the Prepolymers

Ionization potentials and electron affinities were computed using electronic structure calculations on the level of the generalized gradient approximation (GGA [REF_PBE]) of density functional theory (DFT) [REF_GPAW] by comparing charge neutral and charged systems (for details, we refer to **Supplementary Material**). Therefore, as model compounds the addition products of model lignin **ML** (1,3-diarylpropan-1,2-diol derivative) and the corresponding isocyanate (MDI, TDI, and HDI) were used (see **Figure 2**).

Preparation and Characterization of the Lignin-Based Polyurethane Foams

General Protocol for Preparation of the Lignin-Based PU Foams

Desmophen 10WF15 (178.8 g), Monoethyleneglycol (18.0 g), Teda L 33 E (2.0 g, gel catalyst), DABCO BL11 (1.0 g, 70% bis-(dimethylaminoethyl)ether and 30% dipropyleneglycol, blowing agents) and water (2.0 g, blowing agent) were mixed vigorously in

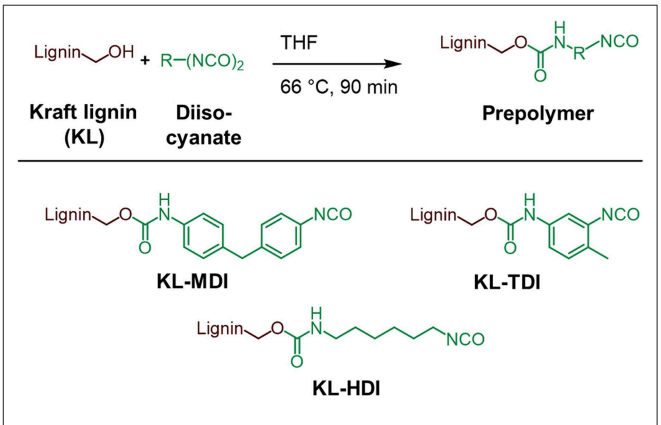

FIGURE 1 | Schematic illustration of the synthesis of lignin-isocyanate prepolymers.

TABLE 1 | Important lignin characteristics.

Mw [g/mol]	Mn [g/mol]	Dispersity	N content* [mol.-%]	Hydroxy groups [mmol/g]	Tg [°C]
4,780	2,075	2.30	0.26	5.90	151

**Determined via elemental analysis.*

a plastic beaker by using a KPG apparatus for 5 min. The resulting mixture was used as polyol component. To the polyol component (33.80 g) isocyanate-modified lignin (optimized amount of 5.7 wt.-%, 3.42 g) was added and the mixture was stirred for 10 s by using a KPG apparatus. Subsequently, the isocyanate Desmodur CD-L (22.8 g) was added. After stirring for further 10 s, the stirrer was removed. During the reaction, the start and overall foaming times were recorded.

Characterization of the Lignin-Based Polyurethane Foams

The foams were characterized via compression tests according to DIN standards (DIN ISO 3386-1:2015-10, 2015) (see **Supplementary Material**). Therefore, the foams were cut into rectangulars of 5.0 × 5.0 × 2.5 cm and compressed with a defined speed, while measuring the force and the distance. Furthermore, SEM, DSC, and gravimetric measurements were performed (for details see **Supplementary Material**).

RESULTS AND DISCUSSION

Chemical Structure of the Functionalized Lignins

The amount of diisocyanate molecules, which have reacted with the OH groups of the lignin after transformation to the prepolymers, were determined by investigation of the nitrogen content of the compounds obtained by elemental analysis (see **Table 2**). In case of MDI-functionalization 1.89 mmol/g of the lignin's hydroxyl groups were modified with the diisocyanate molecules, which corresponds to a conversion of 32 mol.-% of the theoretical yield. When lignin was functionalized with TDI a lower NCO content of 1.14 mmol/g is obtained and in KL-HDI 0.97 mmol/g isocyanate moieties were linked to the lignin. This trend is caused by the fact that lignin is a highly heterogeneous biomolecule providing differently reactive hydroxyl groups. Sixteen percent of the OH groups can easily be transformed by each diisocyanate. When this amount has been abreacted, two factors are the cause that significantly more unreactive OH groups can be functionalized by using MDI than by using TDI, which both are caused by the low reactivity of the NCO group in position 2 of the TDI (Bailey et al., 1956): First, the concentration of isocyanates in solution is decreased during the reaction of the TDI, second, the reactivity of the second NCO may not be high enough to further react intramolecularly with the lignin. To investigate the impact of the latter reaction (lignin-lignin homo-crosslinking), we investigated the amount of free isocyanate groups via potentiometric titration. By this, we demonstrated that the degree of undesired crosslinking is the highest in case of synthesis of KL-MDI (free NCO = unbound NCO groups divided by amount of total diisocyanate (from elemental analysis) = 56 mol.-%, **Table 2**) because of the highest reactivity of the prepolymer. The reactivity of the NCO group in position 2 of TDI can be considered as low, once the other NCO group (in position 4) is abreacted. Consequently, the crosslinking of KL-TDI is negligible (free NCO = 100%, **Table 2**). HDI can be generally considered as unreactive and homo-crosslinking is expected to be negligible. Contrary to the expectations, a significant amount of crosslinking was determined (free NCO = 66 mol.-%) (**Table 2**). The reasons might be that HDI (i) provides no arene moieties, which could limit the degrees of freedom through arene-arene interactions with the lignin core and (ii) exhibits a distance and much more flexible bonds than the other isocyanates, and therefore, is capable to circumvent sterical limitations of the bulky lignin. These effects could expedite intermolecular homo-crosslinking.

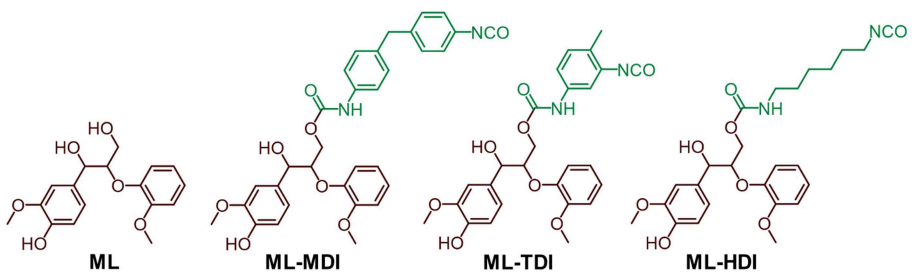

FIGURE 2 | Model compounds used for DFT calculations.

TABLE 2 | NCO contents of the (partially crosslinked) modified lignins by titration and elemental analysis.

Compound	Total NCO amount[a] [mmol/g]	Conversion[c] [mol.-%]	Free NCO[b] [mmol/g]	Free NCO [mol.-%]	Tg [°C]
KL-MDI	1.89 ± 0.01	32.03 ± 0.13	1.06 ± 0.04	56	72
KL-TDI	1.14 ± 0.01	19.32 ± 0.19	1.14 ± 0.18	100	82
KL-HDI	0.97 ± 0.07	16.44 ± 1.15	0.64 ± 0.04	66	75

[a] *Total amount of NCO bound to the lignin determined via elemental analysis.*
[b] *Determined by potentiometric titration.*
[c] *Molar percentage of OH groups which have reacted based on the results of elemental analysis; solubility in 0.1 M NaOH solution.*

Furthermore, we were interested in the investigation of the reaction kinetics of the transformation of the synthesized lignin-based prepolymers to carbamates using a common polyol providing primary hydroxyl groups. To this end, we investigated the kinetics of the transformation of the lignin prepolymers via FTIR spectroscopy according to the method of Barreiro and co-workers (Cateto et al., 2008, 2011). To proceed according to the literature-known protocol and receive comparable results, we utilized the same polyol compound (PCL) as was used in the literature (see **Supplementary Material**). Interestingly, in the work of Barreiro and co-workers, the reactions between lignin, MDI and PCL are completed after about 30 min, whereas the reaction of KL-MDI takes more than 2 h. The reason might be that in the literature the reaction mixture contains small unbound MDI molecules, which could be able to generate a more flexible system so that diffusion of the polyol to the NCO plays a minor role. However, because the process is highly complex and depends on a large number of parameters, at present, the given experiments should only be discussed in qualitative manner.

Quantum Mechanical Calculations

To support the different reactivities, we calculated the ionization potentials and the electron affinities of the model compounds ML-MDI, ML-TDI, and ML-HDI. As a result, the theoretical data correlate with our experimental findings, as expected: ML-MDI provides the highest calculated electron affinity (A_{ML-MDI} = 0.44 eV), whereas ML-TDI exhibits the second (A_{ML-TDI} = 0.39) and ML-TDI the lowest (A_{ML-HDI} = 0.37) value (**Figure 3**). The ionization potentials show the same tendency: I_{ML-MDI} = 6.56 eV, I_{ML-TDI} = 6.68 eV, and I_{ML-HDI} = 6.82 eV.

Preparation and Characterization of Polyurethane Foams Using Isocyanate-Functionalized Lignins

To investigate the macroscopic effects of the different reactivities, in the next step, the synthesized isocyanate-modified lignins were used for preparation of polyurethane foams using a commercially available polyether/MDI-based formulation (for further details see **Supplementary Material**) and the influence on the PU foaming times were determined. In particular, the cream time (i.e., the time at which the foam begins to grow) and the rise time (i.e., the time at which the change of the foam volume stops) were analyzed (see **Figure 4A**). As expected, the cream and rise times of the formulations correlate with the reactivity of the isocyanate compound: the reaction of the reference foam, containing MDI as isocyanate component, is faster than the foaming process of all prepolymer-based systems: The foam formation with the MDI-modified lignin starts and stops significantly faster than the reaction of KL-TDI, respectively. KL-HDI reacts even slower, which supports the hypothesis that steric effects of the lignin molecule imply lower degrees of lignin-lignin homo coupling reactions. Caused by the slow crosslinking of KL-TDI and KL-HDI, the cell-walls of the foam ruptured before the crosslinking, and the blown structures of foams made of these compounds macroscopically collapsed before the final foam structure was set. As a result, the volume weight (density) of the KL-TDI as well as KL-HDI-based foam is distinctly higher than of the foam based on KL-MDI (see **Figure 4B**, for further details see **Supplementary Material**). However, the reference foam without any lignin provided the lowest volume weight (like also observed in the recent literature; Gómez-Fernández et al., 2017). This is caused by the fact that bubble formation, which occurs during the blow reaction, is faster than the CO_2 generation in the lignin-based foams, which might be caused by the different viscosities of the formulations. Although it would be very interesting, determination of the viscosities during the foam formation is not trivial, due to the highly dynamic processes, low dripping times and high temperature gradients. To investigate this in more detail requires extensive method developments/adaptions and it would extend the scope of this manuscript.

Note that we have focused on the investigation of the reactivity of differently modified lignins. Since no homogeneous lignin distribution could be obtained at higher lignin contents, because of high viscosity and coagulation, we used an optimized (i.e., highest) lignin content of 5.7 wt.-% within the foam formulations. The latter was observed during empirical pre-trials (data not shown).

To understand the structure, which the foaming behavior implies in more detail, the foams were cut into small pieces and the cross-section was analyzed by scanning electron microscopy (SEM) (for further details see **Supplementary Material**). The lignin distribution in the foam made of KL-MDI is highly homogeneous and the foam geometry is comparable with the neat foam (**Figure 5**). Because of the low reactivity of KL-TDI and KL-HDI in the foams made of these prepolymers, large unreacted lignin domains (up to several hundred micrometers in diameter) were formed by phase separation, which obviously did not have reacted with the formulation and affect the foam structure. The collapse of the PU foam at the generation process causes a distinct distortion of the cell geometry, especially in case of the KL-HDI-based foam (**Figure 5**). Additionally, the cell size of these foams appears to be larger when compared with the material made of KL-MDI and the distribution of the cell size

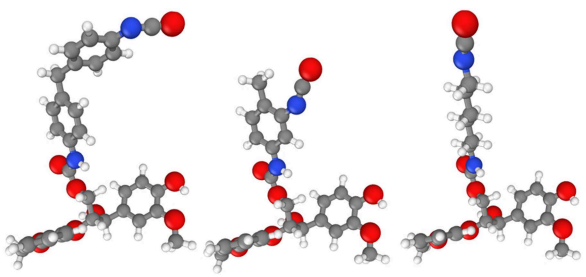

	ML-MDI	ML-TDI	ML-HDI
A [eV]	0.44	0.39	0.37
I [eV]	6.56	6.68	6.82

FIGURE 3 | Electron affinities A and ionization potentials I for model compounds for lignin-based prepolymers determined by quantum mechanical calculations (DFT).

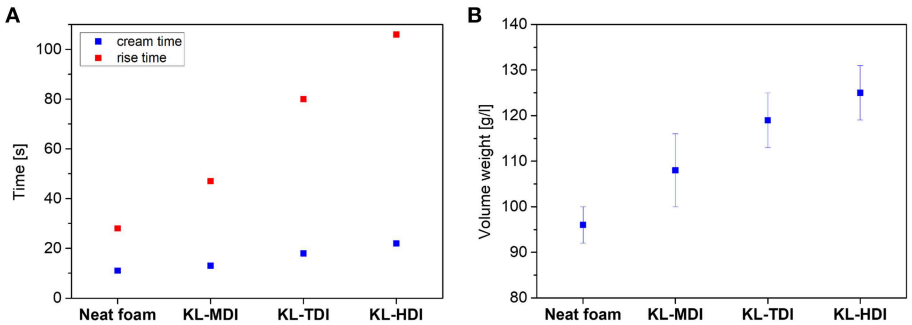

FIGURE 4 | (A) Foaming times of different lignin-isocyanate prepolymers (cream time is the time when foaming reaction starts, rise time is the time until the volume of the foam changes); **(B)** Volume weight of polyurethane foams made of different lignin-isocyanate prepolymers.

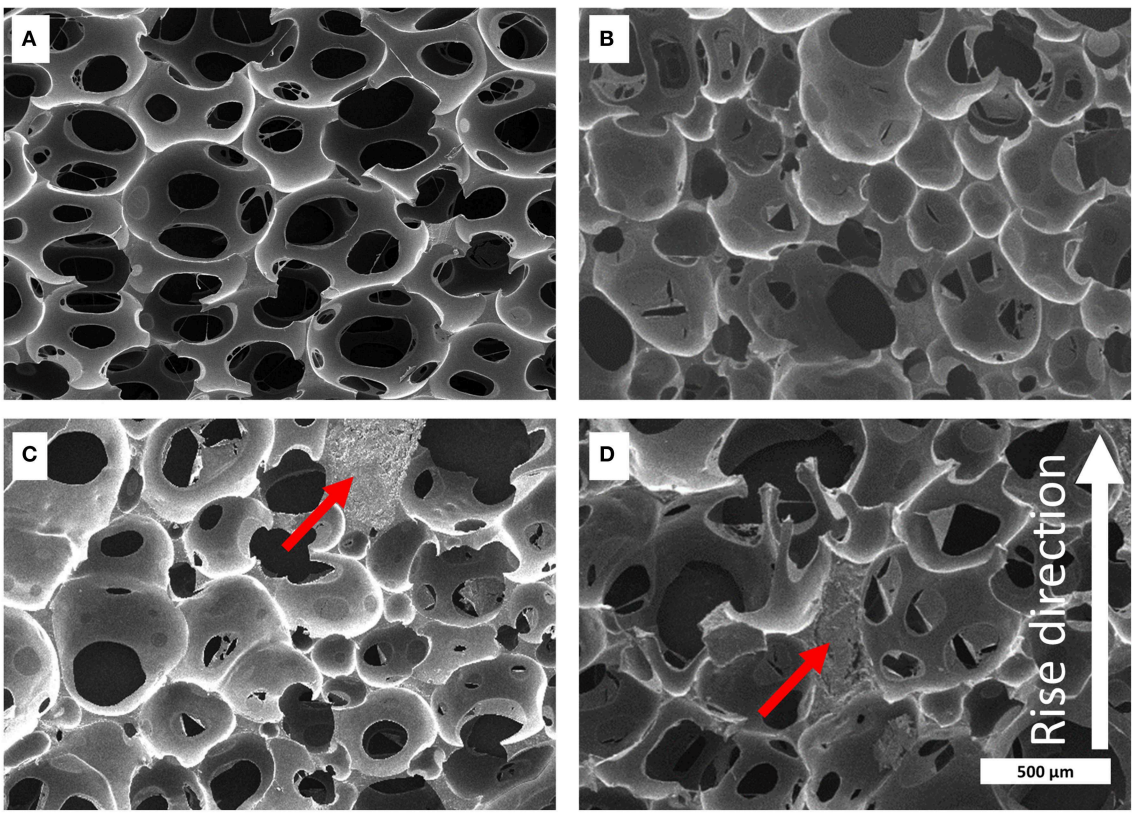

FIGURE 5 | Microscopic structure of the polyurethane foams captured by SEM. Foams consisting of **(A)** neat foam, **(B)** KL-MDI, **(C)** KL-TDI, **(D)** KL-HDI. Examples of large lignin coagulates are marked with a red arrow. The foaming rise direction is shown as white arrow in **(D)** of the figure.

is much less homogeneous. The foam with KL-MDI provides cell sizes of 283 ± 8 µm diameter, whereas foams made of KL-TDI exhibits cell sizes of 394 ± 21 µm and KL-HDI 433 ± 13 µm. Note that the distorted cell structures of KL-TDI and KL-HDI limit the accuracy of the cell size determination, because of the assumption that cells are spherical. However, qualitatively the cell sizes of the latter foams are larger and the size distribution is broader.

The foam morphologies also imply the mechanical properties. To analyze this influence in detail, samples of the foams were analyzed via compression tests according to DIN standards (EN ISO 3386), after conditioning of the samples at norm climate (23°C, 50% rel. humidity) for 2 days (see **Supplementary Material**). During the first deformation curve, at which first 5 to 10% of compression (decrease of the foam volume) takes place, usually the bending of cell struts occurs (actual elastic region). In this state, each lignin-based foam provides a higher elastic modulus than the neat foam (E_{neat} = 0.30 MPa) (as expected from similar lignin-based PU foams; Chauhan et al., 2014). The elastic modulus of the KL-MDI-based material is the most flexible and provides a modulus of 0.40 MPa. As expected, the foams providing an

inhomogeneous lignin distribution (foams made of KL-TDI and KL-HDI) are distinctly less flexible (E_{KL-TDI} = 1.30 and E_{KL-HDI} = 0.70 MPa) (**Figure 6**). This is caused by the coagulated lignin domains, which may provide a reinforcement effect (**Figure 5**). The fact that the flexibility of the KL-TDI-based foam is lower than the KL-HDI-based foam can be explained by the strongly ruptured cell geometry of the latter materials.

As a result of the lignin-reinforcement and the ruptured cell geometry, the compressive strength of the initial elastic region (proportional limit σ_{PL}) correlates not linearly with the volume weight (see **Figure 7A**). This is particularly noticeable in case of the KL-HDI-based foam, which provides the highest volume weight but not the highest proportional limit: $\sigma_{PL,KL-HDI}$ = 0.056 MPa and $\sigma_{PL,KL-TDI}$ = 0.067 MPa, while the volume weights are δ_{KL-TDI} = 115 and δ_{KL-HDI} = 125 g/l. Once the foams have been compressed, the effects of the cell geometry and reinforcement of the material by lignin domains are extinguished. Consequently, if the so-called plateau stress of the materials is compared according to DIN standards at

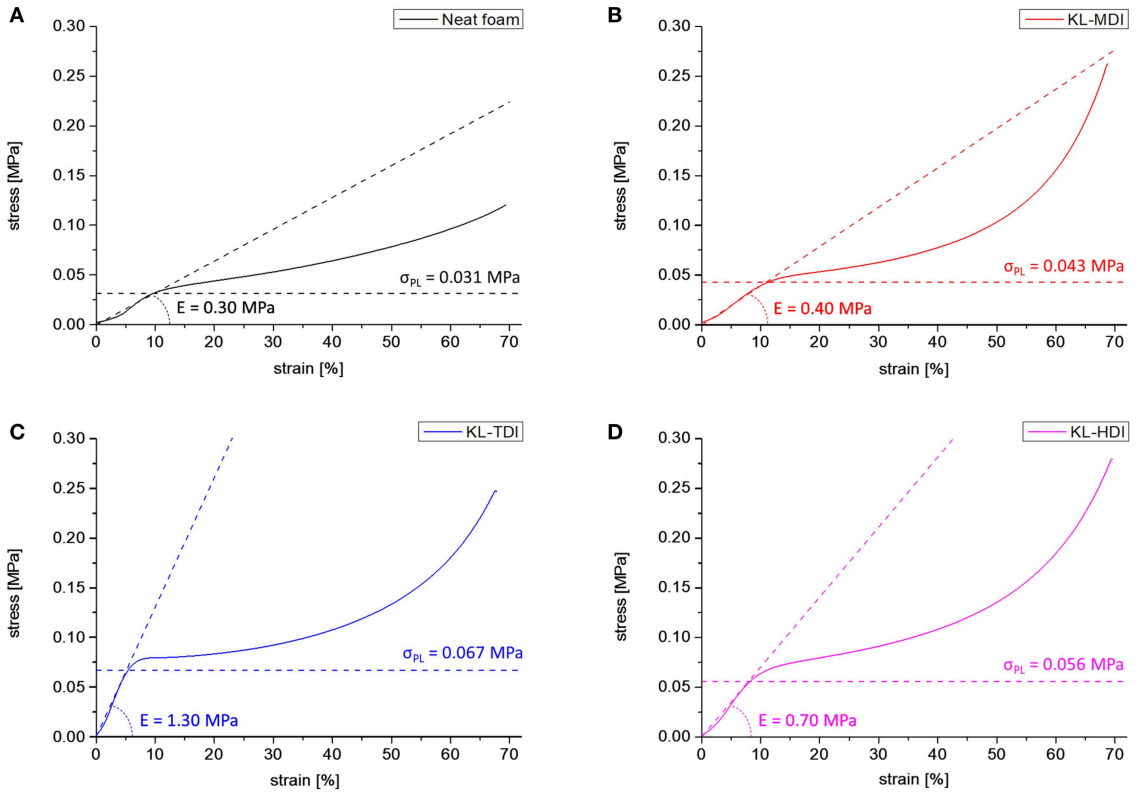

FIGURE 6 | First compression curves of foams made of different lignin-based prepolymers as well as the neat foam formulation: **(A)** Neat foam, **(B)** KL-MDI-based foam, **(C)** KL-TDI-based foam, **(D)** KL-HDI-based foam. Elastic modulus of the actual elastic region as well as the proportional limit σ_{PL} are shown as dashed lines.

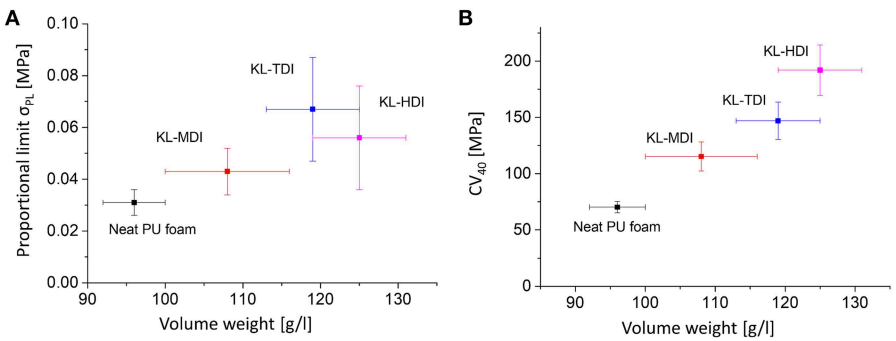

FIGURE 7 | (A) Proportional limit σ_{PL} of the different foams vs. the volume weight. **(B)** CV_{40} values of the different foams vs. the volume weight.

the 4th compression cycle (i.e., the CV_{40} value = the force which is needed to compress the foam volume to 40%), the results clearly correlate with the volume weights (see **Figure 7B**): For compression of the neat foam, providing the lowest volume weight, the lowest force is needed ($CV_{40,neat}$ = 70.1 N). The lignin-based foam with the lowest volume weight containing KL-MDI possesses the lowest CV_{40} value for the foams obtained from lignin prepolymers ($CV_{40,KL-MDI}$ = 115.3 N), whereas the KL-HDI-based foam needs most force to be compressed to 40% ($CV_{40,KL-HDI}$ = 192.0 N; in between the value of the KL-TDI-based foam: $CV_{40,KL-TDI}$ = 147.0 N) (see **Figure 7B**).

In the final stages of deformation, densification takes place. At this point the stress rises steeply and the cell walls are finally crushed (Ashby, 2006), which leads to an irreversible deformation of the material. In particular, 4.3% of the foam made of KL-MDI were irreversibly deformed, in case of KL-TDI 5.0%, and in case of the KL-HDI-based foam 6.9% (complete mechanical testing curves including hysteresis curves are shown in **Supplementary Material**), respectively.

CONCLUSION

In conclusion, we prepared different lignin-based isocyanates by treatment of Kraft lignin with various diisocyanates and analyzed the impact of the molecular structure of the diisocyanate moieties on the reactivity of the resulting prepolymers. To this end, different macromonomers were synthesized by treatment of Kraft lignin with different diisocyanates and fully characterized. As a result, the structure of the different prepolymer differs vastly with regard to the extent of intra- and intermolecular lignin-lignin homo coupling (i.e., degree of crosslinking/amount of reactive NCO groups), which occurs during the synthesis of the compounds, implied by the reactivity of the NCO moieties. The results are in good agreement with the electron affinity and the ionization potential, which were determined for representative model compounds of the prepolymers. Furthermore, the compounds were used for preparation of PU foams and the influence of the reactivity on their macroscopic properties was determined. By this, the relationship between molecular structure, foaming kinetics, volume weight, lignin distribution, cell geometry and mechanical properties of the resulting materials was investigated. As expected, the foaming times and the density of the foams correlate with the reactivity of the utilized lignin prepolymer. Furthermore, the morphological as well as the mechanical properties of the different materials differ distinctly because of the diverging kinetics of the interphase reactions. This work gives rise to a better understanding of the relationship between molecular structure and macroscopic properties of lignin-based polyurethane foams and therefore, enables the rational preparation of foams with tailor-made macroscopic properties.

DATA AVAILABILITY

All datasets generated for this study are included in the manuscript and/or the **Supplementary Files**.

AUTHOR CONTRIBUTIONS

All authors listed, have made substantial, direct, and intellectual contribution to the work. MZ, SW, KB, and GS performed the experiments and characterized the materials. SM, ST, and MZ analyzed the data, reviewed the literature, and wrote the manuscript. JR and KA coordinated and performed the quantum mechanical calculations. MB and ST set-up and coordinated the project. All authors discussed and reviewed the results. All authors discussed, reviewed, and approved the manuscript.

FUNDING

This project has received funding from the Bio Based Industries Joint Undertaking under the European Union's Horizon 2020 research and innovation programme under grant agreement No 669065 (ValChem). The manuscript reflects only the author's view and the JU is not responsible for any use that may be made of the information it contains.

ACKNOWLEDGMENTS

Valuable technical support of Martina Ewald and Heike Herbert is gratefully acknowledged. JR acknowledges computing resources provided by the Lichtenberg HPC cluster of the Hochschulrechenzentrum at TU Darmstadt. Furthermore, we thank Cynthia Cordt for help with the SEM images as well as Max Pfeifer and Erik Uhlein for support with DSC measurements.

SUPPLEMENTARY MATERIAL

The Supplementary Material for this article can be found online at: https://www.frontiersin.org/articles/10.3389/fchem.2019.00562/full#supplementary-material

REFERENCES

Ashby, M. F. (2006). The properties of foams and lattices. *Philos. Transac. Ser. A Math. Phys. Eng. Sci.* 364, 15–30. doi: 10.1098/rsta.2005.1678

Bailey, M. E., Kirss, V., and Spaunburgh, R. G. (1956). Reactivity of organic isocyanates. *Ind. Eng. Chem.* 48, 794–797. doi: 10.1021/ie5056a035

Boerjan, W., Ralph, J., and Baucher, M. (2003). Lignin biosynthesis. *Ann. Rev. Plant Biol.* 54, 519–546. doi: 10.1146/annurev.arplant.54.031902.134938

Cateto, C. A., Barreiro, M. F., and Rodrigues, A. E. (2008). Monitoring of lignin-based polyurethane synthesis by FTIR-ATR. *Ind. Crops Prod.* 27, 168–174. doi: 10.1016/j.indcrop.2007.07.018

Cateto, C. A., Barreiro, M. F., Rodrigues, A. E., and Belgacem, M. N. (2011). Kinetic study of the formation of lignin-based polyurethanes in

bulk. *React. Funct. Polym.* 71, 863–869. doi: 10.1016/j.reactfunctpolym.2011.05.007

Chattopadhyay, D. K., and Raju, K.V.S.N. (2007). Structural engineering of polyurethane coatings for high performance applications. *Progress Polymer Sci.* 32, 352–418. doi: 10.1016/j.progpolymsci.2006.05.003

Chauhan, M., Gupta, M., Singh, B., Singh, A. K., and Gupta, V. K. (2014). Effect of functionalized lignin on the properties of lignin–isocyanate prepolymer blends and composites. *Eur. Polym. J.* 52, 32–43. doi: 10.1016/j.eurpolymj.2013.12.016

Coutinho, F.M.B., and Rocha, M.C.G. (1991). Kinetic study of the reactions between hydroxylated polybutadiene and isocyanates in chlorobenzene—IV. Reactions with tolylene diisocyanate, 3-isocyanatomethyl-3, 5, 5-trimethylcyclohexyl isocyanate and hexamethylene diisocyanate. *Eur. Polymer J.* 27, 213–216. doi: 10.1016/0014-3057(91)90226-E

Delebecq, E., Pascault, J. P., Boutevin, B., and Ganachaud, F. (2013). On the versatility of urethane/urea bonds: reversibility, blocked isocyanate, and non-isocyanate polyurethane. *Chem. Rev.* 113, 80–118. doi: 10.1021/cr300195n

Erekkath, S., and Sreejalekshmi, K. G. (2018). Theoretical predictions on microphase separation in polyurethane: combinatorial design, synthesis and demonstration of shape memory property. *Mater. Today Commun.* 16, 71–80. doi: 10.1016/j.mtcomm.2018.04.007

Furtwengler, P., and Avérous, L. (2018). Renewable polyols for advanced polyurethane foams from diverse biomass resources. *Polym. Chem.* 9, 4258–4287. doi: 10.1039/C8PY00827B

Gama, N. V., Ferreira, A., and Barros-Timmons, A. (2018). Polyurethane foams: past, present, and future. *Materials* 11:E1841. doi: 10.3390/ma11101841

Glasser, W. G., Saraf, V. P., and Newman, W. H. (1982). Hydroxy propylated lignin-isocyanate combinations as bonding agents for wood and cellulosic fibers. *J. Adhes.* 14, 233–255. doi: 10.1080/00218468208073206

Gómez-Fernández, S., Ugarte, L., Calvo-Correas, T., Peña-Rodríguez, C., Corcuera, M. A., and Eceiza, A. (2017). Properties of flexible polyurethane foams containing isocyanate functionalized kraft lignin. *Ind. Crops Prod.* 100, 51–64. doi: 10.1016/j.indcrop.2017.02.005

Granata, A., and Argyropoulos, D. S. (1995). 2-Chloro-4,4,5,5-tetramethyl-1,3,2-dioxaphospholane, a reagent for the accurate determination of the uncondensed and condensed phenolic moieties in lignins. *J. Agric. Food Chem.* 43, 1538–1544. doi: 10.1021/jf00054a023

Hatakeyama, T., Izuta, Y., Hirose, S., and Hatakeyama, H. (2002). Phase transitions of lignin-based polycaprolactones and their polyurethane derivatives. *Polymer* 43, 1177–1182. doi: 10.1016/S0032-3861(01)00714-5

Huo, S.-P., Nie, M.-C., Kong, Z.-W., Wu, G.-M., and Chen, J. (2012). Crosslinking kinetics of the formation of lignin-aminated polyol-based polyurethane foam. *J. Appl. Polym. Sci.* 125, 152–157. doi: 10.1002/app.35401

Laurichesse, S., and Avérous, L. (2014). Chemical modification of lignins: towards biobased polymers. *Prog. Polym. Sci.* 39, 1266–1290. doi: 10.1016/j.progpolymsci.2013.11.004

Liu, H., Dong, M., Huang, W., Gao, J., Dai, K., Guo, J., et al. (2017). Lightweight conductive graphene/thermoplastic polyurethane foams with ultrahigh compressibility for piezoresistive sensing. *J. Mater. Chem. C* 5, 73–83. doi: 10.1039/C6TC03713E

Mahmood, N., Yuan, Z., Schmidt, J., and Xu, C. (2016). Depolymerization of lignins and their applications for the preparation of polyols and rigid polyurethane foams: a review. *Renew. Sustain. Energy Rev.* 60, 317–329. doi: 10.1016/j.rser.2016.01.037

Moorer, H. H., Dougherty, W. K., and Ball, F. J. (1970). *Method of Producing Synthetic Lignin-Polyisocyanate Resin.* US Patent 3.519.581. Westvaco Corporation.

Nadji, H., Bruzzèse, C., Belgacem, M. N., Benaboura, A., and Gandini, A. (2005). Oxypropylation of lignins and preparation of rigid polyurethane foams from the ensuing polyols. *Macromol. Mater. Eng.* 290, 1009–1016. doi: 10.1002/mame.200500200

Petrovic, Z. S., and Ferguson, J. (1991). Polyurethane elastomers. *Prog. Polym. Sci.* 16, 695–836. doi: 10.1016/0079-6700(91)90011-9

Sawpan, M. A. (2018). Polyurethanes from vegetable oils and applications: a review. *J Polym Res* 25:91. doi: 10.1007/s10965-018-1578-3

Singh, H., and Jain, A. K. (2008). Ignition, combustion, toxicity, and fire retardancy of polyurethane foams: a comprehensive review. *J. Appl. Polym. Sci.* 111, 1115–1143. doi: 10.1002/app.29131

Türk, O. (2014). *Stoffliche Nutzung Nachwachsender Rohstoffe*. Wiesbaden: Springer Fachmedien Wiesbaden.

Upton, B. M., and Kasko, A. M. (2016). Strategies for the conversion of lignin to high-value polymeric materials: review and perspective. *Chem. Rev.* 116, 2275–2306. doi: 10.1021/acs.chemrev.5b00345

Yang, C., Fischer, L., Maranda, S., and Worlitschek, J. (2015). Rigid polyurethane foams incorporated with phase change materials: a state-of-the-art review and future research pathways. *Energy Buildings* 87, 25–36. doi: 10.1016/j.enbuild.2014.10.075

Zawadzki, M., and Ragauskas, A. (2001). N-hydroxy compounds as new internal standards for the 31P-NMR determination of lignin hydroxy functional groups. *Holzforschung* 55:175. doi: 10.1515/HF.2001.047

Conflict of Interest Statement: The authors declare that the research was conducted in the absence of any commercial or financial relationships that could be construed as a potential conflict of interest.

frontiers in Chemistry

ORIGINAL RESEARCH
published: 06 September 2019
doi: 10.3389/fchem.2019.00581

Affinity of Serum Albumin and Fibrinogen to Cellulose, Its Hydrophobic Derivatives and Blends

Rupert Kargl[1,2], Matej Bračič[1], Matic Resnik[3], Miran Mozetič[3], Wolfgang Bauer[2], Karin Stana Kleinschek[1,4] and Tamilselvan Mohan[1]*

[1] Laboratory for Characterization and Processing of Polymers, Faculty of Mechanical Engineering, University of Maribor, Maribor, Slovenia, [2] Faculty of Technical Chemistry, Chemical and Process Engineering, Biotechnology, Institute of Paper, Pulp and Fibre Technology (IPZ), Graz University of Technology, Graz, Austria, [3] Department of Surface Engineering and Optoelectronics, Jožef Stefan Institute, Ljubljana, Slovenia, [4] Faculty of Technical Chemistry, Chemical and Process Engineering, Biotechnology, Institute of Inorganic Chemistry, Graz University of Technology, Graz, Austria

This work describes the preparation of spin-coated thin polymer films composed of cellulose (CE), ethyl cellulose (EC), and cellulose acetate (CA) in the form of bi- or mono-component coatings on sensors of a quartz crystal microbalance with dissipation monitoring (QCM-D). Depending on the composition and derivative, hydrophilicity can be varied resulting in materials with different surface properties. The surfaces of mono- and bi-component films were also analyzed by atomic force microscopy (AFM) and large differences in the morphologies were found comprising nano- to micrometer sized pores. Extended protein adsorption studies were performed by a QCM-D with 0.1 and 10 mg mL^{-1} bovine serum albumin (BSA) and 0.1 and 1 mg mL^{-1} fibrinogen from bovine plasma in phosphate buffered saline. Analysis of the mass of bound proteins was conducted by applying the Voigt model and a comparison was made with the Sauerbrey wet mass of the proteins for all films. The amount of deposited proteins could be influenced by the composition of the films. It is proposed that the observed effects can be exploited in biomaterial science and that they can be used to extent the applicability of bio-based polymer thin films composed of commercial cellulose derivatives.

Keywords: cellulose acetate, ethyl cellulose, fibrinogen, albumin, hydrophilicity, quartz crystal microbalance, protein adsorption

OPEN ACCESS

Edited by:
Tiina Nypelö, Chalmers University of Technology, Sweden

Reviewed by:
Andreas Dahlin, Chalmers University of Technology, Sweden
Hannes Orelma, VTT Technical Research Centre of Finland Ltd., Finland

****Correspondence:***
Rupert Kargl
rupert.kargl@um.si

Specialty section:
This article was submitted to Polymer Chemistry, a section of the journal Frontiers in Chemistry

Received: *19 March 2019*
Accepted: *02 August 2019*
Published: *06 September 2019*

Citation:
Kargl R, Bračič M, Resnik M, Mozetič M, Bauer W, Stana Kleinschek K and Mohan T (2019) Affinity of Serum Albumin and Fibrinogen to Cellulose, Its Hydrophobic Derivatives and Blends. Front. Chem. 7:581. doi: 10.3389/fchem.2019.00581

INTRODUCTION

Synthetic and bio-based polymeric biomaterials are widely used for biomedical devices including those which are in contact with human blood, plasma, serum, or protein solutions. Applications for such materials are, among others, bio-separation techniques (Jungbauer, 2005) such as dialysis (Roumelioti et al., 2018), affinity chromatography (Burnouf and Radosevich, 2001), and electrophoresis (Rocco, 2005). For most of these applications knowledge on the interaction of blood, plasma, or serum proteins with the surfaces of materials is important. This knowledge allows drawing conclusion about the biocompatibility (Wang et al., 2013), coagulative properties (Vikinge et al., 2000), or separation performance (Zou et al., 2001) and finally determines their applicability. Commercial and research based separation columns or disposable biomedical materials are usually composed of very different synthetic or bio-based polymers and their derivatives. Among these bio-based polymers are cellulose and its esters and ethers (Klemm et al., 2005; Arca et al., 2018). Many authors therefore investigated the interaction of proteins with surfaces of polymers and

elucidated its relation to hydrophilicity (Fujimori et al., 1998; Alves et al., 2010), charge (Edwards et al., 2012), morphology or solvation (Lu et al., 2007). Such studies were also conducted for cellulose and surface modified materials composed of it (Solin et al., 2019). Investigations on the interaction of proteins also included those with cellulose derivatives. Examples are published by Lv et al. (2017) who studied the protein binding and performance of cellulose nano-crystal modified cellulose acetate membranes and found that less albumin adsorbs with higher crystal content. Raghuwanshi et al. (2017) describe the interaction of immunoglobulins (IgG) at the solid liquid cellulose interface and Hong et al. (2008) used cellulose to efficiently separate proteins. Many studies describe the use of ethyl cellulose (EC) as particles, capsules or coatings for the controlled release and targeted delivery of drugs (Graves et al., 2005; Rogers and Wallick, 2012; Adebisi and Conway, 2014; Fan et al., 2014). Polymer blends with EC were used to control and retard the release of drugs from polymer based nanoparticles (Lecomte et al., 2005; Hasan et al., 2007). Although it is essential for drug delivery and the application of EC as biomaterial, adsorption of proteins on EC was surprisingly less frequently studied (Casilla and Eley, 1975; Bruck, 1976; Abu-Lzza and Lu, 1998; Hoffart et al., 2007). This work therefore aims at investigating and comparing the interaction of the proteins bovine serum albumin (BSA) and fibrinogen (FIB) on commercially available celluloses and their derivatives in the form mono- and bi-component thin films using a quartz crystal microbalance with dissipation monitoring (QCM-D). Both proteins are essential in the assessment of biocompatibility and blood coagulation and any material composed of these polymers that comes into contact with full blood or plasma will be initially covered by these proteins as confirmed by QCM-D and surface plasmon resonance (SPR) (Mohan et al., 2013, 2014, 2017). Films are prepared by spin coating trimethylsilyl cellulose (TMSC) in combination with cellulose acetate (CA) or ethyl cellulose (EC) on sensors of a QCM-D. Cleavage of the trimethylsilyl protecting groups by acid vapor hydrolysis results in blends composed of cellulose and either contain CA or EC. Bi-component blends were also prepared from CA-EC. Static water contact angle measurements are performed to assess the hydrophilicity of the blend films and morphological studies by atomic force microscopy (AFM) are included. Understanding protein adsorption on mono- and bi-component films of cellulose and its derivatives should allow for a basic understanding of their surface properties and result in alternative applications for these bio-based polymers.

MATERIALS AND METHODS

Film Preparation

Trimethylsilyl cellulose (TMSC, DS_{TMS}: 2.8, Mw: 149 kDa, derived from Avicel PH-101) was purchased from Thüringisches Institut für Textil- und Kunststoffforschung e.V. (TITK, Rudolstadt, Germany). Cellulose acetate (CA, acetyl content 38 wt.% Mw: 30 kDa, Sigma-Aldrich, Austria) and ethyl cellulose (EC, viscosity 100 cP, 5% in toluene/ethanol 80:20, extent of labeling: 48% ethoxyl, Sigma-Aldrich Austria) were used as received. For mono-component films, polymers were dissolved at 1 wt.% in tetrahydrofuran p. a. (THF, Sigma Aldrich Austria). For bi-component films of CA-EC both polymers were dissolved each at 0.5 wt.% in the same solvent and solution. For blend films containing cellulose (CE) the TMSC precursor concentration in the spinning solution was 1.13 wt.% since cleavage and removal of TMS groups during regeneration into cellulose causes a mass loss of 55.8 wt.%. Concentration of the other component (CA or EC) was 0.5 wt.%. Films were made by dropping 50 μL polymer solution on the static QCM-D crystals with a gold electrode layer (QSX-301, LOT-Oriel, Germany) and spin coating them at 4,000 rpm and an acceleration of 2,500 rpm sec^{-1}. Prior to coating QCM-D crystals were immersed into a mixture of H_2O/H_2O_2 (30 wt.%)/NH_4OH (5:1:1; v/v/v) for 10 min at 70°C, then immersed in a "piranha" solution containing H_2O_2 (30 wt.%)/H_2SO_4 (1:3; v/v) for 40 s, and then rinsed with water and finally blown dry with N_2 gas.

Films obtained were composed of TMSC, CA, EC, TMSC-CA 1.1:0.5 w/w, TMSC-EC 1.1:0.5 w/w, and CA-EC 1:1 w/w. Films containing TMSC were placed into a 20 mL polystyrene petri-dish (4 cm in diameter) and 2 mL 10 wt.% HCl was dropped next to the QCM-D crystals and the petri-dish was covered with its cap. HCl vapors deprotected the cellulose hydroxyl groups by acid catalyzed hydrolysis of TMS groups leading to a mass loss of 55.6 wt.% for TMSC within 30 min and cellulose (CE) was obtained in the film (Mohan et al., 2017) resulting in a polymer blend mass ratio of 1:1 (CE-EC; CE-CA). Bi-component films then containing cellulose instead of TMSC were labeled CE-CA, CE-EC.

Atomic Force Microscopy

Surface morphology was analyzed by Atomic Force Microscopy (AFM, Solver PRO, NT-MDT, Moscow, Russia) in semi-contact mode in air. The sample surfaces were scanned by a standard silicon cantilever with a force constant of 16 N/m at a resonance frequency of 325 kHz. Cantilevers' tip radius was 10 nm, the tip length was 95 μm and the scan rate was set at 1.56 Hz. At least three different areas of each sample were measured. The average root mean square surface roughness (Sq) was calculated from representative images on 5 × 5 μm^2 areas, with the Nova AFM software provided be the manufacturer.

Infrared Spectroscopy

Infrared transmission spectra (Perkin Elmer FTIR Spectrum GX spectrometer with ATR-IR attachment and diamond crystal) were measured on the coated QCM-D crystals at room temperature and humidity with 16 scans and a resolution of 4 cm^{-1}.

Contact Angle

Static water contact angle measurements were performed using an OCA15+ contact angle measurement system from Dataphysics (Germany). All measurements were conducted at room temperature and humidity without conditioning of the environment on at least two independent surfaces on QCM-D crystals with a drop volume of 3 μl. Each contact angle value was the average of at least four drops of liquid per surface. For contact

angle measurements water (>18 MΩ cm) from a Milli-Q-water system (Millipore, USA) was used.

Quartz Crystal Microbalance

A QCM-D instrument (model E4) from Q-Sense (Gothenburg, Sweden) was used. The instrument simultaneously measures decreases/increases in the resonance frequency (Δf) and increases/decreases in energy dissipation (ΔD) when the mass of an oscillating piezoelectric crystal increases/decreases due to deposition/removal of material. Dissipation refers to the frictional losses that lead to damping of the oscillation depending on the viscoelastic properties of the material. For a rigid adsorbed layer that is fully coupled to the oscillation of the crystal, Δfn is given by the Sauerbrey Equation (1) (Sauerbrey, 1959).

$$\Delta m = C\frac{\Delta f_n}{n} \tag{1}$$

where Δf_n is the observed frequency shift, C is the Sauerbrey constant (-0.177 mg Hz^{-1} m^{-2} for a 5 MHz crystal), n is the overtone number ($n = 1, 3, 5$, etc.) and Δm is the change in mass of the crystal due to the adsorbed or desorbed layer. The mass of a soft (i.e., viscoelastic) film is not fully coupled to the oscillation and the Sauerbrey relation is not valid since energy is dissipated in the film during the oscillation. The energy dissipation (D) is defined as (2):

$$D = \frac{E_{diss}}{2\pi E_{stor}} \tag{2}$$

where E_{diss} is the energy dissipated and E_{stor} is the total energy stored in the oscillator during one oscillation cycle.

For protein adsorption studies, bovine serum albumin (BSA, 0.1 and 10 mg mL^{-1}) and fibrinogen from bovine plasma (FIB, 0.1 and 1 mg mL^{-1}) were gently dissolved in a 10 mM PBS buffer at pH 7.4 and room temperature. Both proteins and the PBS were from Sigma Aldrich, Austria.

Quartz crystal microbalance with dissipation monitoring (QCM-D) crystals coated with the thin films were mounted in the QCM-D flow cell and equilibrated with MilliQ-water and 10 mM PBS buffer solution until a stable frequency signal was established. BSA or FIB were pumped through the QCM-D cell for 40 min, followed by the PBS solution for 25 min and water for 30 min. The flow rate was kept at 0.1 mL min^{-1} and the temperature at 21°C throughout all experiments. All adsorption experiments were performed in two parallels and a mean value of the third overtone of dissipation (D_3) and frequency (f_3) was displayed. The overtones (f_3-f_{11}) were separately displayed for one measurement per sample. ***Viscoelastic modeling:*** The viscoelastic Voigt model was applied for calculating the adsorbed mass (Γ_{QCM}), film thickness (h_{f}), viscosity (η_{f}), and elastic shear modulus (μ_{f}) of the adsorbed BSA and FIB layer. In this model, the adsorbed layer was treated as a viscoelastic layer between the quartz crystal and a semi-infinite Newtonian liquid layer. More details on the Voigt modeling can be found elsewhere (Voinova et al., 1999; Höök et al., 2001). For data evaluation or fitting the different overtones (n = 3, 5, 7, 9, 11, and 13) of frequency and dissipation were used. All calculations were carried out using the software package QTools 3.0.12 (Q-Sense).

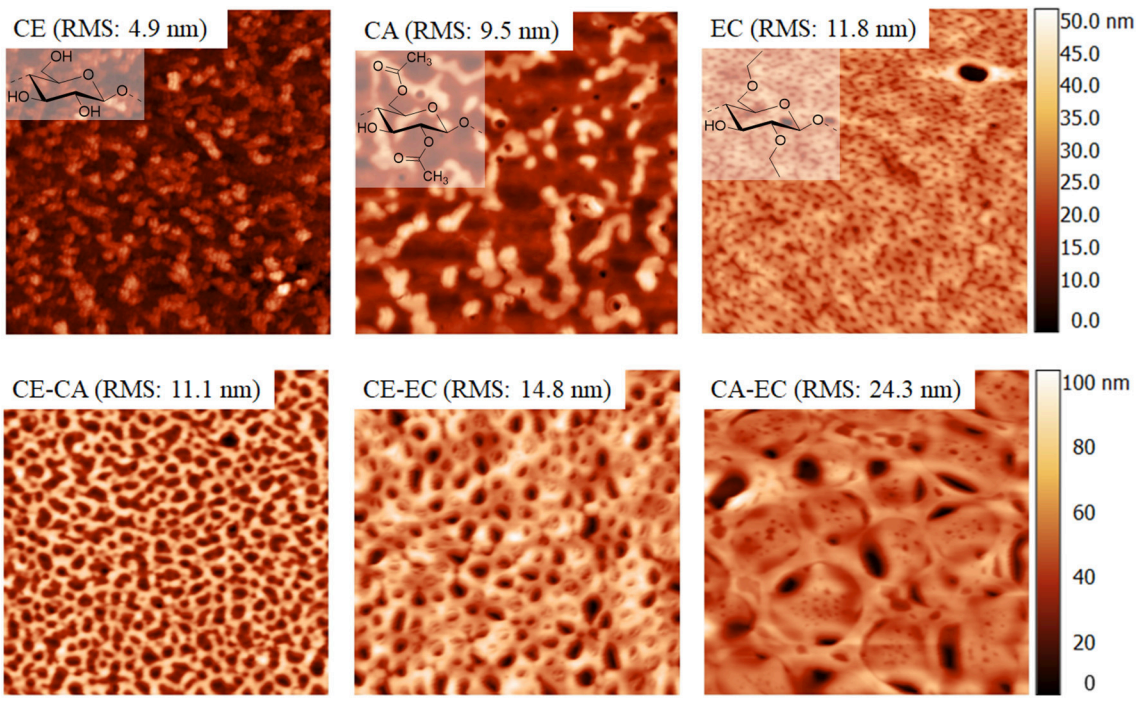

FIGURE 1 | Atomic force microscopy height image of cellulose (CE), cellulose acetate (CA), ethyl cellulose (EC), and their blends. Image size is 5 × 5 μm^2.

The fitting parameters used for the modeling are: viscosity, from 1×10^{-4} to 0.01 $N{\cdot}s{\cdot}m^{-2}$; elastic shear modulus, from 1×10^{4} to 1×10^{8} $N{\cdot}m^{-2}$; and thickness, from 1×10^{-10} to 1×10^{-6} m. It is worth noting that the values of h_f and ρ_f were not independent variables. In order to calculate the effective thickness and adsorbed mass (Equation 3), the density ρ_f values was varied between 1,000 and 1,130 kg m^{-3}. It turned out that no mass change for BSA/FIB coated layer occurred by changing the density value and therefore a density (ρ_f) of 1,000 kg m^{-3} was used for all calculations (Equation 3).

$$\Gamma_{QCM} = h_f \rho_f \quad (3)$$

RESULTS AND DISCUSSION

Morphology and Composition of the Films

Figure 1 shows $5 \times 5\,\mu m^2$ AFM height images of all films investigated. According to root mean square roughness calculations the smoothest coatings are obtained from cellulose. Significant differences in structural features can be seen. Most notably a pore sizes in the nanometer range and a concomitant surface roughness increase for blend films and a maximum for CA-EC is observed. Interestingly, pore size distribution is relatively uniform for the films. Care must be taken that the surface morphology and accessibility of the films for water and protein are considered with respect to the QCM-D and contact angle results. Since these materials are very different form a morphological and chemical point of view, attempts to perfectly quantify the amount of retained protein by QCM-D can be challenging (Vikinge et al., 2000; Reviakine et al., 2011).

The infrared transmission spectra of the films are given in **Figure 2**. For clarity reasons also a neat trimethylsilyl cellulose film (TMSC) is shown. The materials show all expected peaks according to literature values (Shi et al., 2008; Kargl et al., 2012). Most importantly for films containing cellulose (CE) a deprotection of the trimethyl silyl groups could be confirmed by the absence of peaks at 1,252 and 848 cm^{-1} representative for the Si-C vibrations (Mohan et al., 2011).

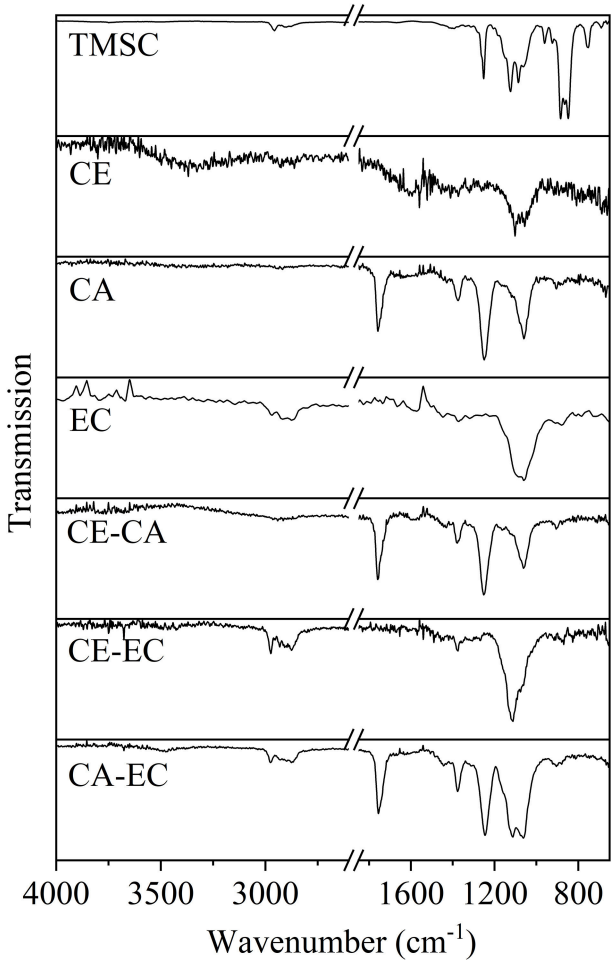

FIGURE 2 | Infrared transmission spectra for trimethylsilyl cellulose (TMSC), cellulose (CE), cellulose acetate (CA), ethyl cellulose (EC), and blends thereof on QCM-D gold crystals.

Hydrophilicity of the Films

Figure 3 depicts the static water contact angles of mono- and bi-component thin films. As expected from the molecular structure, cellulose (CE) is the most hydrophilic polymer with a contact angle of 31.9 ± 0.2°. Compared to ethyl cellulose (EC, 85.3 ± 2.9°), cellulose acetate (CA, 54.4 ± 3.4°) is a less hydrophobic material owing to its ability to act as a hydrogen bond acceptor over the electron lone pairs of the carboxyl oxygen atoms and as a donor and acceptor at unsubstituted hydroxyl groups. Blending hydrophobic cellulose derivatives in bi-component films with cellulose, results in more hydrophilic surfaces (CE-CA 38.5 ± 0.4°) confirming the exposure of cellulose R-OH groups and the ability to interact with larger amounts of water. Blending EC with CA however, gives surfaces with an intermediate hydrophobicity (CA-EC, 76.6 ± 2.6°). A static water contact angle of 55.2 ± 1.5° is observed by combining the most hydrophilic material CE with the most hydrophobic cellulose derivative (EC). As a result, a variety of thin films composed of the glycan chain of cellulose but with different substituents is available, whose hydrophilicity and number of available hydrogen bond acceptor and donor groups can be adjusted by simple blending of the polymers. These films were subjected to interaction studies with different concentrations of bovine serum albumin and fibrinogen from bovine plasma in phosphate buffered saline at pH 7.4 and 21°C.

Interaction of Bovine Serum Albumin With the Films

Figure 4 depicts frequency (f_3) and dissipation (D_3) changes from QCM-D experiments on CE, CA, and EC films and the blends CE-CA, CE-EC, and CA-EC. A BSA concentration of 0.1 mg mL^{-1} (upper row) and 10 mg mL^{-1} (lower row) in PBS (pH 7.4) was used. Initial rinsing of the films with buffer reduces the frequency and increases the damping of the oscillation due to a higher density of PBS compared to water. Subsequent introduction of the protein solution results in a negative frequency and positive dissipation shift which is caused

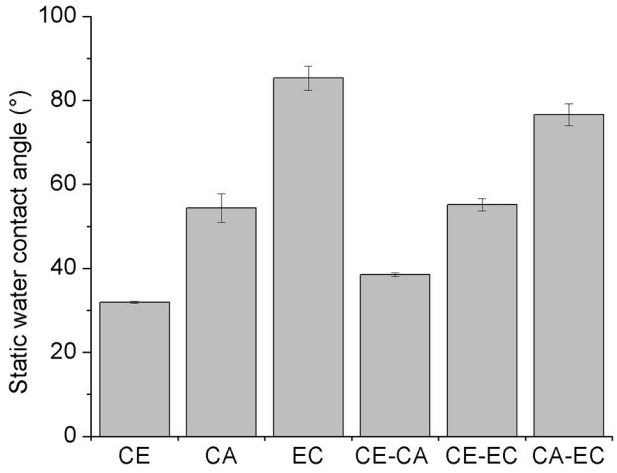

FIGURE 3 | Static water contact angles of spin-coated films composed of cellulose (CE), cellulose acetate (CA), and ethyl cellulose (EC) or their blends (CE-CA, CE-EC, CA-EC). All blend films are composed of 50 wt.% for each polymer.

by: (a) adsorption of the protein and (b) a higher viscosity and density of the solution in contact with the film on the crystal. For 0.1 mg mL^{-1} BSA no significant difference in the f_3 and D_3 response can be observed for neat and blend films during contact with the protein and rinsing with PBS or water. Final values after rinsing almost reach the initial stage. For 10 mg mL^{-1} BSA significant differences are observed for neat films with CA showing a lower response than CE and EC for all stages of adsorption and rinsing. QCM-D signals on blend films a significantly different for CE-EC, the material which contains a combination of the most and the least hydrophilic polymer. This feature obviously allows for a better interaction of the protein with the film.

A spread in the response of the different overtones of oscillation and dissipation (**Figures S1**, **S2** is observed for all films at 10 mg mL^{-1} BSA demonstrating the viscoelastic behavior of the protein layer and solution. This spread almost disappears upon the final rinsing with water leading to the qualitative statement that the retained protein layer has a more compact, less swollen form on all films.

A summary of the frequency and dissipation shifts after BSA adsorption and final rinsing with water is given in **Figure 5**, displaying the Sauerbrey and Voigt wet mass of adsorbed protein per unit area. For a low protein concentration of 0.1 mg mL^{-1} only CE and blends composed of CA-EC and CE-CA have a significantly higher protein affinity. For 10 mg mL^{-1} BSA the highest affinity was found for blends composed of cellulose and its ethyl derivative. Again, it is hypothesized that this mixed blend of the most hydrophilic with the most hydrophobic material allows BSA to attached more efficiently and irreversibly. The Voigt wet mass per unit area, as calculated by modeling the data from six overtones, is higher for all measurements but follows the same trend as the Sauerbrey mass calculated from the linear relation of frequency and deposited mass. It is important to note that the same surface area is assumed for all films for this calculation.

Interaction of Fibrinogen With the Films

Fibrinogen adsorption on biomaterials is essential in processes involving blood clot formation. The binding of this protein at concentrations similar to those found in human plasma is therefore of interest in biomaterial research. **Figure 6** shows the interaction of fibrinogen in PBS (0.1 and 1 mg mL^{-1}) with neat (CE, CA, EC) and blend (CE-CA, CE-EC, CA-EC) polysaccharide thin films.

At 0.1 mg mL^{-1} already differences in the affinity of FIB toward the cellulose derivatives can be observed. The largest frequency shift and presumably strongest interaction is seen on cellulose acetate (CA). Upon rinsing with PBS and water, all films show a similar response in f_3. CA however gives higher D_3 leading to the conclusion than only minor amounts of FIB are retained on all films with a maximum on cellulose acetate.

When 1 mg mL^{-1} fibrinogen in PBS are introduced the strongest QCM-D response can be found for cellulose films. Upon rinsing with PBS minor desorption is observed. Rinsing with water however reveals that only on the most hydrophobic ethyl cellulose (EC) larger amounts of FIB are retained that incorporate water and substantially increase the D_3 value. Swelling and water retention is so strong that f_3 even decreases in contrast to all other films. Since pure water is used for rinsing, this also strongly increases the osmotic pressure in the film and adsorbed layer upon ion exchange, resulting in such a pronounced swelling. Interestingly in blends with other materials this behavior is not observed for EC demonstrating that the second polymer cellulose or its acetate ester in the bi-component film suppresses FIB interaction and retention. The spread in the response of the different overtones of oscillation and dissipation (**Figures S3**, **S4**) is more pronounced for 1 mg mL^{-1} FIB but is significantly lowered after rinsing with water, similar to the results from BSA.

Figure 7 depicts a summary of the retained fibrinogen wet masses per unit area for all films investigated. The Sauerbrey relation and the Voigt model were used to calculate these wet masses. For 0.1 mg mL^{-1} fibrinogen the largest retention can be found on cellulose acetate even though overall the amounts are similarly low for all films. Fibrinogen deposition is however more significant than serum albumin retention on the same materials in terms of overall mass which can also be attributed to the much higher molecular mass of FIB. As already discussed above, significant differences are observed for 1 mg mL^{-1} fibrinogen on ethyl cellulose (EC) which is also the most hydrophobic materials. Again, this significant impact of EC diminished in blends with the other polymers.

CONCLUSION

It was shown that the commercial cellulose derivatives trimethylsilyl cellulose, cellulose acetate and ethyl cellulose can be blended and shaped into thin films by spin coating on sensors of a quartz crystal microbalance. The trimethylsilyl cellulose in the films can be regenerated to cellulose by exposure to vapors

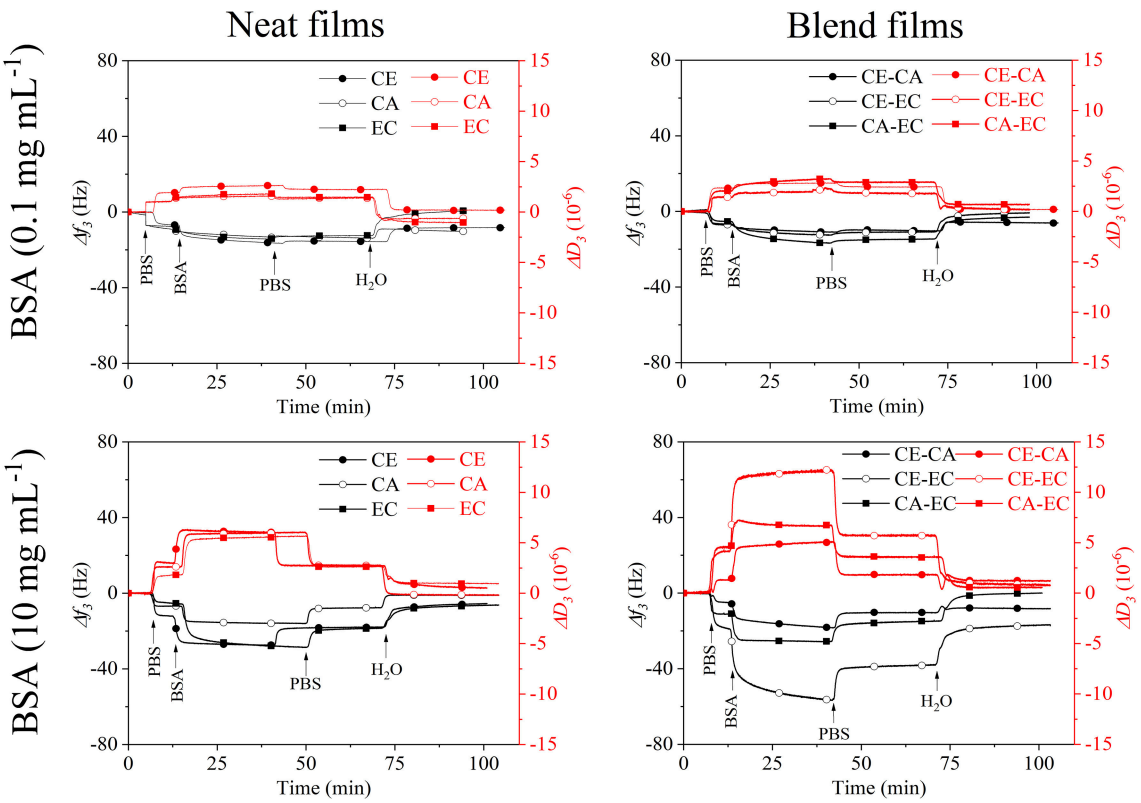

FIGURE 4 | QCM-D frequency (f_3) and dissipation change (D_3) during rinsing with 0.1 and 10 mg mL^{-1} bovine serum albumin over cellulose (CE), cellulose acetate (CA), and ethyl cellulose (EC) and their 50:50 wt.% blends (CE-CA, CE-EC, CA-EC) in PBS followed by rinsing with PBS and water.

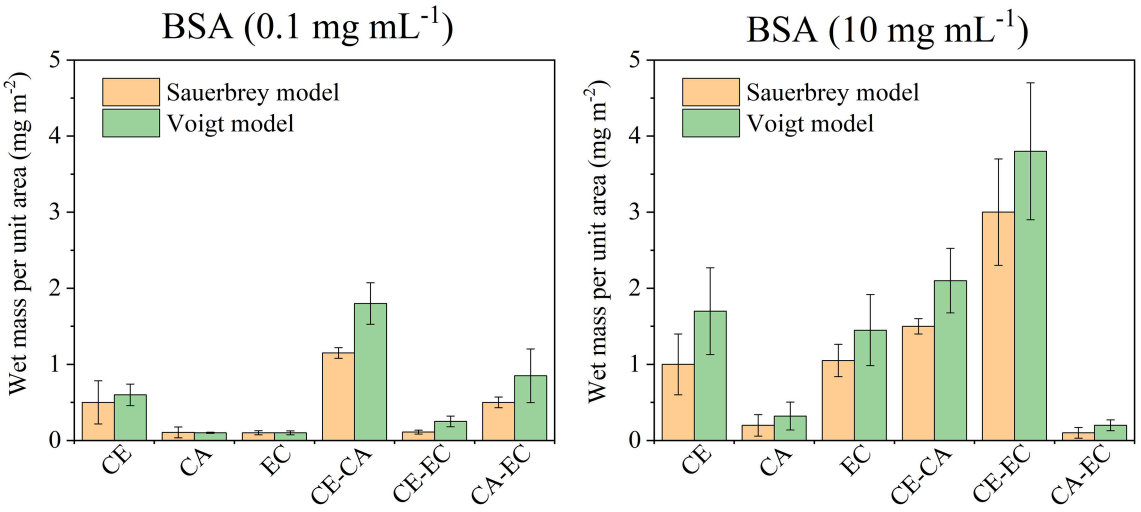

FIGURE 5 | Wet mass of retained BSA per unit area as calculated from the Sauerbrey equation or Voigt model after films were in contact with 0.1 or 10 mg mL^{-1} protein in PBS and subsequently rinsed with PBS and water. Deposited protein masses are shown for cellulose (CE), cellulose acetate (CA), ethyl cellulose (EC), and their blends (CE-CA; CE-EC, CA-EC).

of hydrochloric acid as confirmed by infrared transmission measurements. The surface morphology and roughness of blend films containing a mass ratio of 50% of each polymer strongly varies between different blends. Nano- to micrometric features with relatively regular pore sizes can be obtained. Those films that contain cellulose are hydrophilic and hydrophobicity

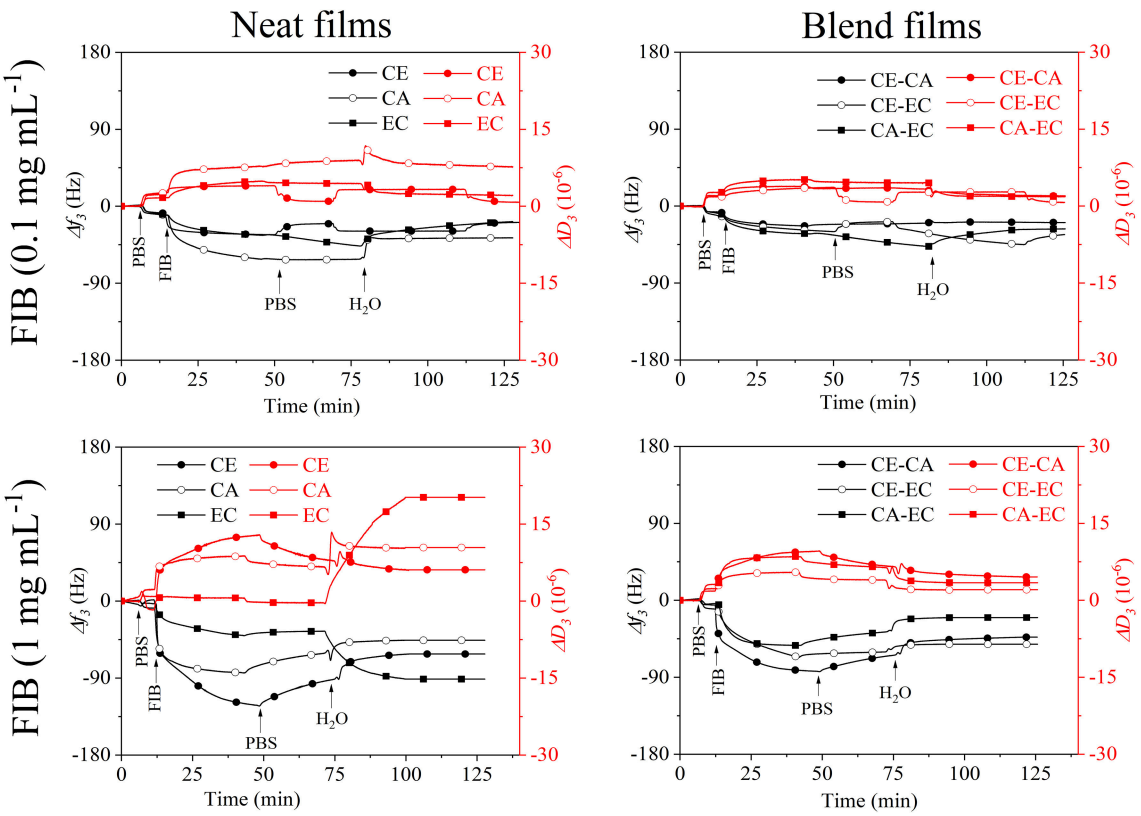

FIGURE 6 | QCM-D frequency (f_3) and dissipation change (D_3) during rinsing with 0.1 and 1 mg mL^{-1} fibrinogen (FIB) from bovine plasma in PBS over cellulose (CE), cellulose acetate (CA), and ethyl cellulose (EC) and their 50:50 wt.% blends (CE-CA, CE-EC, CA-EC) followed by rinsing with PBS and water.

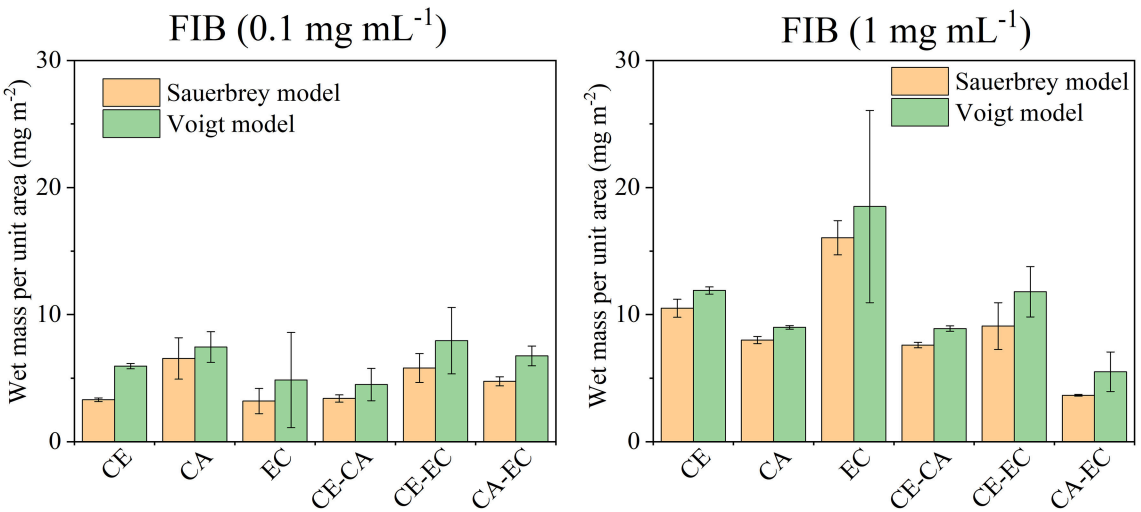

FIGURE 7 | Wet mass of retained fibrinogen (FIB) per unit area as calculated from the Sauerbrey equation or Voigt model after films were in contact with 0.1 or 1 mg mL^{-1} protein in PBS and subsequently rinsed with PBS and water. Deposited protein masses are shown for cellulose (CE), cellulose acetate (CA), ethyl cellulose (EC), and their blends (CE-CA, CE-EC, CA-EC).

increases for cellulose acetate and is the highest for ethyl cellulose. The wetting of blend films with water reflects the composition and the static water contact angles are on average in between those of the single component materials. Quartz crystal microbalance with dissipation monitoring showed, that blend films composed of cellulose and ethyl cellulose significantly bind more bovine serum albumin than all other films at an initial protein concentration of 10 mg mL^{-1}. Fibrinogen is however

retained most significantly on the most hydrophobic polymer ethyl cellulose, already at initial concentrations of 1 mg mL^{-1}. Sauerbrey and Voigt models of the retained protein masses reveal similar amounts which is also reflected in a minor spread of the overtones of oscillation.

DATA AVAILABILITY

The datasets generated for this study are available on request to the corresponding author.

AUTHOR CONTRIBUTIONS

RK contributed to experimental planning, data analysis and writing. MB performed the QCM-D experiments, analyzed and interpreted the data and contributed to the manuscript. MR performed the atomic force microscopy measurements and calculation. MM interpreted the surface analytical results and contributed to the writing. WB contributed to the overall concept and manuscript revision. KS guided the work, scientifically interpreted it and contributed to manuscript writing. TM oversaw all experimental planning, data analysis, and writing.

FUNDING

This work has received funding from the Marie Skłodowska-Curie Intra European Fellowship (IEF) POLY-INTER-FACES, Grant agreement ID: 331600.

ACKNOWLEDGMENTS

Support from the Slovenian Ministry of Education, Science and Sport, contract C3330-19-952004 Bacteriostatic properties of medical implants and project core funding from the Slovenian Research Agency No. Z2-9216 are acknowledged.

SUPPLEMENTARY MATERIAL

The Supplementary Material for this article can be found online at: https://www.frontiersin.org/articles/10.3389/fchem.2019.00581/full#supplementary-material

REFERENCES

Abu-Lzza, K. A., and Lu, D. R. (1998). Effect of gastrointestinal protein adsorption on the *in vitro* release of azt from ethylcellulose microspheres. *Pharm. Dev. Technol.* 3, 495–501. doi: 10.3109/10837459809028631

Adebisi, A. O., and Conway, B. R. (2014). Lectin-conjugated microspheres for eradication of helicobacterpylori infection and interaction with mucus. *Int. J. Pharm.* 470, 28–40. doi: 10.1016/j.ijpharm.2014.04.070

Alves, C. M., Reis, R. L., and Hunt, J. A. (2010). The competitive adsorption of human proteins onto natural-based biomaterials. *J. R. Soc. Interface* 7, 1367–1377. doi: 10.1098/rsif.2010.0022

Arca, H. C., Mosquera-Giraldo, L. I., Bi, V., Xu, D., Taylor, L. S., and Edgar, K. J. (2018). Pharmaceutical applications of cellulose ethers and cellulose ether esters. *Biomacromolecules* 19, 2351–2376. doi: 10.1021/acs.biomac.8b00517

Bruck, S. D. (1976). Polymeric materials in the physiological environment. *Pure Appl. Chem.* 46, 221–226. doi: 10.1016/B978-0-08-020975-3.50019-0

Burnouf, T., and Radosevich, M. (2001). Affinity chromatography in the industrial purification of plasma proteins for therapeutic use. *J. Biochem. Biophys. Methods* 49, 575–586. doi: 10.1016/S0165-022X(01)00221-4

Casilla, R. C., and Eley, D. D. (1975). Adhesive interaction with lignin and various cellulose monolayers. *J. Chem. Soc. Faraday Transact.* 71, 1469–1475. doi: 10.1039/F19757101469

Edwards, J. V., Castro, N. J., Condon, B., Costable, C., and Goheen, S. C. (2012). Chromatographic and traditional albumin isotherms on cellulose: a model for wound protein adsorption on modified cotton. *J. Biomater. Appl.* 26, 939–961. doi: 10.1177/0885328210390542

Fan, T., Feng, J., Ma, C., Yu, C., Li, J., and Wu, X. (2014). Preparation and characterization of porous microspheres and applications in controlled-release of abamectin in water and soil. *J. Porous Mater.* 21, 113–119. doi: 10.1007/s10934-013-9754-7

Fujimori, A., Naito, H., and Miyazaki, T. (1998). Adsorption of complement, cytokines, and proteins by different dialysis membrane materials: evaluation by confocal laser scanning fluorescence microscopy. *Artif. Organs* 22, 1014–1017. doi: 10.1046/j.1525-1594.1998.06083.x

Graves, R. L., Makoid, M. C., and Jonnalagadda, S. (2005). The effect of coencapsulation of bovine insulin with cyclodextrins in ethylcellulose microcapsules. *J. Microencapsul.* 22, 661–670. doi: 10.1080/02652040500161917

Hasan, A. S., Socha, M., Lamprecht, A., Ghazouani, F. E., Sapin, A., Hoffman, M., et al. (2007). Effect of the microencapsulation of nanoparticles on the reduction of burst release. *Int. J. Pharm.* 344, 53–61. doi: 10.1016/j.ijpharm.2007.05.066

Hoffart, V., Maincent, P., Lamprecht, A., Latger-Cannard, V., Regnault, V., Merle, C., et al. (2007). Immunoadsorption of alloantibodies onto erythroid membrane antigens encapsulated into polymeric microparticles. *Pharm. Res.* 24, 2055–2062. doi: 10.1007/s11095-007-9340-2

Hong, J., Ye, X., Wang, Y., and Zhang, Y. H. P. (2008). Bioseparation of recombinant cellulose-binding module-proteins by affinity adsorption on an ultra-high-capacity cellulosic adsorbent. *Anal. Chim. Acta* 621, 193–199. doi: 10.1016/j.aca.2008.05.041

Höök, F., Kasemo, B., Nylander, T., Fant, C., Sott, K., and Elwing, H. (2001). Variations in coupled water, viscoelastic properties, and film thickness of a Mefp-1 protein film during adsorption and cross-linking: a quartz crystal microbalance with dissipation monitoring, ellipsometry, and surface plasmon resonance study. *Anal. Chem.* 73, 5796–5804. doi: 10.1021/ac0106501

Jungbauer, A. (2005). Chromatographic media for bioseparation. *J. Chromatogr. A* 1065, 3–12. doi: 10.1016/j.chroma.2004.08.162

Kargl, R., Mohan, T., Bračič, M., Kulterer, M., Doliška, A., Stana-Kleinschek, K., et al. (2012). Adsorption of carboxymethyl cellulose on polymer surfaces: evidence of a specific interaction with cellulose. *Langmuir* 28, 11440–11447. doi: 10.1021/la302110a

Klemm, D., Heublein, B., Fink, H.-P., and Bohn, A. (2005). Cellulose: fascinating biopolymer and sustainable raw material. *Angew. Chem. Int. Ed.* 44:3358. doi: 10.1002/anie.200460587

Lecomte, F., Siepmann, J., Walther, M., MacRae, R. J., and Bodmeier, R. (2005). pH-sensitive polymer blends used as coating materials to control drug release from spherical beads: importance of the type of core. *Biomacromolecules* 6, 2074–2083. doi: 10.1021/bm0500704

Lu, J. R., Zhao, X., and Yaseen, M. (2007). Protein adsorption studied by neutron reflection. *Curr. Opin. Colloid Interface Sci.* 12, 9–16. doi: 10.1016/j.cocis.2007.02.001

Lv, J., Zhang, G., Zhang, H., and Yang, F. (2017). Exploration of permeability and antifouling performance on modified cellulose acetate ultrafiltration membrane with cellulose nanocrystals. *Carbohydr. Polym.* 174, 190–199. doi: 10.1016/j.carbpol.2017.06.064

Mohan, T., Findenig, G., Höllbacher, S., Cerny, C., Ristić, T., Kargl, R., et al. (2014). Interaction and enrichment of protein on cationic polysaccharide surfaces. *Colloids Surf. B Biointerfaces* 123, 533–541. doi: 10.1016/j.colsurfb.2014.09.053

Mohan, T., Kargl, R., Doliška, A., Vesel, A., Ribitsch, V., and Stana-Kleinschek, K. (2011). Wettability and surface composition of partly and fully regenerated cellulose thin films from trimethylsilyl cellulose. *J. Colloid Interface Sci.* 358, 604–610. doi: 10.1016/j.jcis.2011.03.022

Mohan, T., Niegelhell, K., Nagaraj, C., Reishofer, D., Spirk, S., Olschewski, A., et al. (2017). Interaction of tissue engineering substrates with serum proteins and its influence on human primary endothelial cells. *Biomacromolecules* 18, 413–421. doi: 10.1021/acs.biomac.6b01504

Mohan, T., Ristic, T., Kargl, R., Doliska, A., Köstler, S., Ribitsch, V., et al. (2013). Cationically rendered biopolymer surfaces for high protein affinity support matrices. *Chem. Commun.* 49, 11530–11532. doi: 10.1039/C3CC46414H

Raghuwanshi, V. S., Su, J., Garvey, C. J., Holt, S. A., Holden, P. J., Batchelor, W. J., et al. (2017). Visualization and quantification of IgG antibody adsorbed at the cellulose-liquid interface. *Biomacromolecules* 18, 2439–2445. doi: 10.1021/acs.biomac.7b00593

Reviakine, I., Johannsmann, D., and Richter, R. P. (2011). Hearing what you cannot see and visualizing what you hear: interpreting quartz crystal microbalance data from solvated interfaces. *Anal. Chem.* 83, 8838–8848. doi: 10.1021/ac201778h

Rocco, R. M. (2005). Joachim Kohn (1912–1987) and the origin of cellulose acetate electrophoresis. *Clin. Chem.* 51, 1896–1901. doi: 10.1373/clinchem.2005.056572

Rogers, T. L., and Wallick, D. (2012). Reviewing the use of ethylcellulose, methylcellulose and hypromellose in microencapsulation. Part 1: materials used to formulate microcapsules. *Drug Dev. Indust. Pharmacy 38*, 129–157. doi: 10.3109/03639045.2011.590990

Roumelioti, M.-E., Trietley, G., Nolin, T. D., Ng, Y.-H., Xu, Z., Alaini, A., et al. (2018). Beta-2 microglobulin clearance in high-flux dialysis and convective dialysis modalities: a meta-analysis of published studies. *Nephrol. Dial. Transplant.* 33, 1025–1039. doi: 10.1093/ndt/gfx311

Sauerbrey, G. (1959). Verwendung von Schwingquarzen zur Wägung dünner Schichten und zur Mikrowägung. *Z. Phys.* 155, 206–222. doi: 10.1007/bf01337937

Shi, P., Li, Y., and Zhang, L. (2008). Fabrication and property of chitosan film carrying ethyl cellulose microspheres. *Carbohydr. Polym.* 72, 490–499. doi: 10.1016/j.carbpol.2007.09.021

Solin, K., Orelma, H., Borghei, M., Vuoriluoto, M., Koivunen, R., and Rojas, O. J. (2019). Two-dimensional antifouling fluidic channels on nanopapers for biosensing. *Biomacromolecules* 20, 1036–1044. doi: 10.1021/acs.biomac.8b01656

Vikinge, T. P., Hansson, K. M., Sandström, P., Liedberg, B., Lindahl, T. L., Lundström, I., et al. (2000). Comparison of surface plasmon resonance and quartz crystal microbalance in the study of whole blood and plasma coagulation. *Biosens. Bioelectr.* 15, 605–613. doi: 10.1016/s0956-5663(00)00125-1

Voinova, M. V., Rodahl, M., Jonson, M., and Kasemo, B. (1999). Viscoelastic acoustic response of layered polymer films at fluid-solid interfaces: continuum mechanics approach. *Phys. Scripta* 59:391. doi: 10.1238/Physica.Regular.059a00391

Wang, M., Yuan, J., Huang, X., Cai, X., Li, L., and Shen, J. (2013). Grafting of carboxybetaine brush onto cellulose membranes via surface-initiated ARGET-ATRP for improving blood compatibility. *Colloids Surf. B Biointerfaces* 103, 52–58. doi: 10.1016/j.colsurfb.2012.10.025

Zou, H., Luo, Q., and Zhou, D. (2001). Affinity membrane chromatography for the analysis and purification of proteins. *J. Biochem. Biophys. Methods* 49, 199–240. doi: 10.1016/s0165-022x(01)00200-7

Conflict of Interest Statement: The authors declare that the research was conducted in the absence of any commercial or financial relationships that could be construed as a potential conflict of interest.

Advantages of publishing in Frontiers

OPEN ACCESS
Articles are free to read for greatest visibility and readership

FAST PUBLICATION
Around 90 days from submission to decision

HIGH QUALITY PEER-REVIEW
Rigorous, collaborative, and constructive peer-review

TRANSPARENT PEER-REVIEW
Editors and reviewers acknowledged by name on published articles

Frontiers
Avenue du Tribunal-Fédéral 34
1005 Lausanne | Switzerland

Visit us: www.frontiersin.org
Contact us: info@frontiersin.org | +41 21 510 17 00

REPRODUCIBILITY OF RESEARCH
Support open data and methods to enhance research reproducibility

DIGITAL PUBLISHING
Articles designed for optimal readership across devices

FOLLOW US
@frontiersin

IMPACT METRICS
Advanced article metrics track visibility across digital media

EXTENSIVE PROMOTION
Marketing and promotion of impactful research

LOOP RESEARCH NETWORK
Our network increases your article's readership